The Biophysical Characteristics of Extracellular Vesicle Production and Transport

BY

STEPHEN LENZINI
B.S., Northwestern University, 2015
M.S., Northwestern University, 2016

THESIS

Submitted as partial fulfillment of the requirements
for the degree of Doctor of Philosophy in Bioengineering
in the Graduate College of the
University of Illinois at Chicago, 2021

Chicago, Illinois

Defense Committee:

Jae-Won Shin, Chair and Advisor
James Lee, Bioengineering
Eben Alsberg, Bioengineering
Dolly Mehta, Pharmacology
Yulia Komarova, Pharmacology
Richard Minshall, Pharmacology

This thesis is dedicated to Richard Sheldon and Barbara Scott Sheldon.

ACKNOWLEDGEMENTS

I would like to sincerely thank my advisor, Dr. Jae-Won Shin, for providing the opportunity to complete this dissertation under his guidance. To Dr. Shin, you taught me the true meaning of dedication and the pursuit of quality in work. All that I approach in life from here will be affected profoundly by what I learned from your guidance. I was fortunate to share an experience with you in the beginnings of a research laboratory that is now very successful. I wish the best to you and your laboratory for the future and will always remember my time spent there.

I would like to thank Dr. David Giljohann for first introducing me to research and being supportive of my future goals. I would like to thank Dr. Keith Tyo and Dr. Joshua Leonard for providing me opportunities to further my research career. To Dr. Leonard, your passion and dedication for teaching and training aspiring researchers was always incredibly inspiring to me. I will always remember the effort that you expended to teach me, and I look back fondly on my years as a student at Northwestern in large part due to you as a role model. I would also like to thank Dr. Michelle Hung for providing invaluable guidance at Northwestern.

I would like to thank my thesis committee – Dr. James Lee, Dr. Eben Alsberg, Dr. Yulia Komarova, and Dr. Richard Minshall – for their unwavering support and assistance. I would also like to thank Dr. Sing Wan Wong, who helped me numerous times in many different aspects of this work and made several contributions. To Dr. Wong, the bond that I developed working with you is something that I will always cherish. I would also like to acknowledge Gina Chung, Raymond Bargi, and Angie Song, who made contributions to this work. A number of other individuals assisted me at various points, and I would like to thank them as well. At UIC, Dr. Peter Toth and the Fluorescence Imaging Core; Dr. Balaji Ganesh and the Flow Cytometry

Core; Tara Foroozan and Jacek Lechowicz at the Nanotechnology Core Facility; Tao Teng at the Department of Bioengineering; Jing Li and Alan Tseng at the Department of Pharmacology; Figen Seiler at the Electron Microscopy Core. At Northwestern University, Alexandra Kolot of the ANTEC facility. At Duke University, Dr. Brenton Hoffmann. At the University of Virginia, Dr. Liheng Cai. Others who were helpful include the administrative staff at the UIC Department of Bioengineering and UIC Department of Pharmacology.

To my family, you are the rock that grounds me in all that I do. To my parents, your unwavering love and support will always be remembered and appreciated. You allowed me to pursue anything that I thought valuable – I hope it pays off someday! To my sister and brother – I will always be there for you both.

Lastly, I would like to thank Allison Tomek, without whom this work would certainly never have been accomplished.

CONTRIBUTION OF AUTHORS

For the following statements, full citations of the relevant work are provided at the beginning of the appropriate section as well as in Appendix K. Chapter 1 contains a Figure 1.1 that was included in a published review article of which I was the first author and primary writer. Daniel Devine and my advisor Dr. Jae-Won Shin also made contributions to this article. Chapter 2, section 3 contains brief information used in two separate manuscripts of which I was a co-author. Dr. Sing Wan Wong, Madeline Cooper, Dr. David Mooney, Daniel Devine, Vishwaarth Vijayakumar, Dr. Peter Newman, and my advisor Dr. Jae-Won Shin also made contributions to these works. Chapter 3 represents a published manuscript of which I was the first author and sole driver of research. Raymond Bargi, Gina Chung, and my advisor Dr. Jae-Won Shin also made contributions to this work.

TABLE OF CONTENTS

LIST OF FIGURES

FIGURE PAGE

LIST OF APPENDICES

LIST OF ABBREVIATIONS

3D/2D	Three-dimensional/Two-dimensional
AAD	Adipic acid dihydrazide
ANOVA	Analysis of variance
Arp2/3	Actin-related protein 2/3 complex
AQP1	Aquaporin-1
ATP	Adenosine triphosphate
CI	Confidence interval
DNA	Deoxyribonucleic acid
mtDNA	Mitochondrial deoxyribonucleic acid
DMEM	Dulbecco's modified eagle medium
DS	Degree of substitution
EBA	Evans blue albumin
ECM	Extracellular matrix
ELISA	Enzyme-linked immunosorbent assay
ESC	Embryonic stem cell
ESCRT	Endosomal sorting complex required for transport
EV	Extracellular vesicle
FAK	Focal adhesion kinase
FITC	Fluorescein isothiocyanate
FBS	Fetal bovine serum
GTPase	Guanosine triphosphate hydrolase
HBSS	Hanks' buffered salt solution
HEK293T	Human embryonic kidney-293T cell
HUVEC	Human umbilical vein endothelial cell
IF	Interstitial Fluid
IgG	Immunoglobulin G
IVIS	Intravital imaging system

K2S	Katushka2S
LPS	Lipopolysaccharides
MCA	Membrane-to-cortex attachment
MSC	Mesenchymal stromal cell
MSD	Mean squared displacement
MVB	Multivesicular body
MW	Molecular weight
NP	Nanoparticle
NTA	Nanoparticle tracking analysis
PBS	Phosphate-buffered saline
PEG	Polyethylene glycol
PEG-DA	Polyethylene glycol-diacrylate
PCR	Polymerase chain reaction
qPCR	Quantitative polymerase chain reaction
RGD	Arginine-glycine-aspartate
RhoA	Ras homolog family member A
RNA	Ribonucleic acid
mRNA	Messenger ribonucleic acid
miRNA	Micro ribonucleic acid
rRNA	Ribosomal ribonucleic acid
siRNA	Silencing ribonucleic acid
SD	Standard deviation
SEM	Standard error of the mean
TIRF	Total internal reflection fluorescence
TLN	Talin
TNFα	Tumor necrosis factor alpha
YAP	Yes-associated protein

SUMMARY

Extracellular vesicles (EVs) produced by mesenchymal stromal cells (MSCs) are cell-secreted nanoparticles with broad potential to treat tissue injuries by delivering cargo to program target cells. Understanding fundamental mechanisms by which the extracellular microenvironment regulates EV production and resulting EV transport will lend a significant insight towards translating EVs as therapeutics. To this end, we show that MSCs produce significantly more EVs on softer substrates due to less integrin activation. MSCs produce EVs more rapidly if adhesion time on substrates is limited to a briefer period. Substrate mechanical properties direct EV number per cell without altering EV size, morphology, therapeutic content, or therapeutic efficacy against a murine model of acute lung injury. Mechanistically, intracellular $CD63^+$ multivesicular bodies (MVBs) transport faster within MSCs on softer hydrogels with less adhesion time, leading to an increased frequency of MVB fusion with the plasma membrane to secrete more exosomes. Furthermore, we show that EVs transport through matrix environments despite being larger than the average nanoporous mesh. Water permeation through aquaporin-1 on the surface of EVs mediates their deformability, allowing navigation through the dense matrix. Matrix stress relaxation further facilitates EVs to overcome confinement, and matrix stiffness leads to a fluctuating transport motion. The combination of water permeation, matrix stress relaxation and matrix stiffness results in a greatly enhanced EV transport through matrix. In sum, this thesis elucidates the regulation by the biophysical environment of MSC-EV production and transport and presents novel approaches to understand fundamental mechanisms of EV-matrix interactions and informs potential strategies to improve translation of EVs as promising therapeutics.

1. INTRODUCTION

Note: The Figure 1.1 in this chapter was originally published in Frontiers in Bioengineering and Biotechnology: Lenzini S., Devine D., and Shin J.-W. Leveraging biomaterial mechanics to improve pluripotent stem cell applications for tissue engineering. Front. Bioeng. Biotechnol. 2019; 10. (See Appendix K).

1.1 BACKGROUND

1.1.1 EXTRACELLULAR VESICLES

Extracellular vesicles (EVs) are nano-sized particles derived from cells. They were first discovered in the 1980s using electron microscopy, described as vesicles 'jettisoned' from reticulocytes [1, 2]. Due to their presence in endosomal compartments and involvement in protein recycling [3], many researchers believed that these particles were simply cellular waste products. As a result, they were considered 'cell dust' or 'cell debris' [4] that existed to regulate the waste homeostasis of cells. However, in subsequent studies, other researchers began to show that EVs are readily secreted and taken up by other cells [5]. This appeared to question previous conclusions, because it is not entirely clear why cells would readily take up the waste products from other cells. Some posited that EVs served as packages to send signals between cells and thus, scientists posed the hypothesis that EVs constituted a medium of intercellular communication. As nano-sized particles composed of a lipid bilayer, EVs can contain several different biological components such as RNA, protein, lipids, and DNA, all at the same time [5]. Due to their lipid bilayer, EVs have the potential to shield these internal cargoes from the outside

environment, potentially prolonging their half-life and thereby providing the ability to travel over longer distances [6]. Because EVs can contain several distinct cargoes at the same time, they also can potentially deliver more complex signals to recipient cells, where multiple distinct components of the complex signal are packaged together. For these reasons, EVs were recognized as a potentially important intercellular communication system.

The potential for EV-mediated intercellular communication began to be studied and demonstrated in a few landmark studies. In 1996, Raposo *et al* used immunogold labeling in electron microscopy to show that EVs secreted from B lymphocytes contain major histocompatibility complex II [7]. When T cells were treated with these EVs, they exhibited a proliferative response as if they were cultured directly with B lymphocytes. This was observed with B cell derived EVs but not EVs derived from another cell type. This study was the first to demonstrate cellular phenotypic changes resulting from EV treatment. In 2007, Valadi *et al* isolated EVs from mast cells and showed that they contain over 1000 distinct RNA transcripts including mRNA and miRNA [8]. Furthermore, these EVs were able to transfer RNA from mouse cells to recipient human cells, which later were shown to contain transcribed mouse proteins. This study was the first to definitively show EV-mediated transfer of functional biological material. In 2015, Zomer *et al* used the genetic Cre-loxP system to visualize EV transfer from cancer cells *in vivo* [9]. Cells taking up EVs from cancer cells *in vivo* exhibited a detectable fluorescent signal as a result of Cre-mediated activation, a cancerous phenotype, and a metastatic potential. This could occur even when cells were located distantly across the mouse body, demonstrating the capacity for long-range functional EV communication *in vivo*.

Since EVs were shown to contain cellular contents and deliver them to other cells, their ability to act as important paracrine signaling agents became more appreciated. Cell therapy, the

ability to utilize aspects of cells to achieve a therapeutic effect against diseases, has become a popular therapeutic direction in recent years, and it is driven partly by paracrine signaling functions of cells [10]. EVs can be considered a reduced form of cell therapy since cell therapy itself will involve EVs secreted by cells in some cases. However, cell therapy has some major barriers to becoming a true therapeutic avenue. Primarily, there are significant risks regarding latent tumor formation and immune rejection by the host [11, 12]. EVs derived from cells have some advantages over cells as therapies. First, EVs do not proliferate, so they cannot form tumors by themselves. Second, EVs have shown to exhibit lower toxicity than cells, due to less risk of cytokine release syndrome [13], or other nanocarriers, presumably due to recognition by the host [14, 15]. Third, EVs likely face less regulation in manufacturing, and can be readily stored and transported while maintaining a clinical effect [16], allowing more versatility in distribution.

A popular cell source for therapeutic EVs are mesenchymal stromal cells (MSCs), as there are currently over 80 clinical trials involving MSC-EVs [17]. Indeed, EVs from MSCs have shown efficacy in several preclinical disease models with diverse scope, including acute lung injury [18], lung fibrosis [19], liver fibrosis [20], and kidney fibrosis [21], myocardial infarction [22], neurodegenerative disease such as multiple sclerosis [23], among several others [24]. In one early example, MSC-EVs showed efficacy against graft versus host disease in humans [25] – this particular example highlights the fact that EVs show a low toxicity in human patients. Since then, EVs have shown high tolerance in patients against several other disease indications in clinical settings [24].

However, there are two substantial issues with the translation of EVs as therapeutics. First, efforts to produce enough EVs for a therapeutic dose have elucidated issues with scaling up

production and manufacturing large quantities of EVs [26]. Conventional substrate-based cell culture requires a significant area for cells to expand without optimizing the number of EVs per cell, which demands large quantities of costly culture materials such as tissue culture-treated plastic and culture reagents. Furthermore, administration of EVs will require primary cells derived from patients, which can be costly to obtain, increasing the need to maximize the number of EVs obtained per cell. Crucially, though, efforts to enhance EV production per cell must not compromise the therapeutic efficacy of EVs on a per EV basis. Though significant progress has been made regarding using EVs as therapeutics in preclinical settings, addressing these manufacturing issues will be required to ultimately translate EVs as a therapeutic in widespread clinical settings.

This issue is accentuated by a lack of understanding regarding how the culture environment affects the biogenesis and secretion of EVs from cells. Issues with suboptimal EV manufacturing can be addressed in part by redesigning manufacturing environments inspired by better understanding how cells produce EVs in native environments. EVs are generally classified into subtypes by the cellular pathway by which they are generated. The EV subgroup microvesicles (or ectosomes) are produced by budding directly from the membrane [27], while exosomes are produced by inward budding within late endosomes that form multivesicular bodies (MVBs) [5]. Exosomes are released from cells when the MVB fuses with the plasma membrane. Exocytosis and endocytosis are highly regulated cellular processes that involve the cell membrane, protein machinery, and cytoskeletons. In the case of exosomes, for example, endosome and MVB formation, trafficking and fusion all are presumed to affect exosome production. For example, the endosomal sorting complex required for transport (ESCRT) proteins are involved in EV production for some exosome populations but not others [28].

Furthermore, Rab GTPases involved in MVB trafficking to the membrane have differential regulatory roles depending on cell type, and the precise mechanisms of regulation are still unknown [29]. However, the role of the culture environment in EV production remains unknown and understanding this role will facilitate the development of strategies to maximize EV production for therapeutic purposes.

The second substantial issue is that EVs are cleared very rapidly *in vivo* after administration. Studies show a range of EV biodistribution patterns after systemic administration with accumulations mainly in the spleen and liver [30, 31], though patterns are sensitive to mode of systemic administration and cell source [32]. For example, EVs administered intravenously show even more enhanced accumulation in the liver compared to intraperitoneal or subcutaneous administration, which show enhanced accumulation in the gastrointestinal tract. The circulation half-time of EVs is reported to be in the range of several hours [30, 33]. Some efforts have enhanced EV retention to an extent, but they require modification of EVs that may result in functional comprises. For example, EVs can be engineered to exhibit extended clearance time by decorating their surface with polyethylene glycol [34]. This strategy also offers the ability to incorporate targeting peptides or other molecules on the surface of EVs to improve targeting [35], though it is unclear if these methods will provide enough retention and uptake to show substantial clinical improvements. Eventually, more sophisticated targeting systems, potentially combinatorial systems based on the above studies, can be developed and utilized to enhance delivery of EVs to target tissues – but these will require EVs to remain in circulation long enough to find the target, or EVs to be injected directly to the tissue of interest.

Issues related to clearance and uptake are accentuated by a lack of understanding of how EVs transport and distribute within the body. For example, it is possible that rapid EV clearance

is partly associated with significant EV uptake within interstitial tissues, rather than degradation or excretion. EVs derived from plasma are heterogenous, and their compositions suggest that they originate from a diverse range of tissues [36], implying that EVs from different tissues readily navigate to the bloodstream. Indeed, EVs are known to be present in tissues in matrix-bound form [37], where they are presumably secreted by cells embedded within the tissues. Some studies suggest that EVs show the ability to remodel the extracellular environment [38] by directly secreting or activating latent matrix remodeling enzymes. However, it remains unknown whether some population of EVs are secreted by cells within tissues to transport and excrete from tissues to travel elsewhere in the body. It also remains largely unknown whether EVs readily transport across biological interfaces, though it was shown that EVs are present surrounding the endometrium [39], and some studies claim that EVs can cross the blood-brain barrier [40]. Interestingly, EVs can affect vascular permeability through delivery to cells [41, 42], suggesting a feedback mechanism that allows their entry past the barrier and into the interstitial spaces. Thus, if EVs are administered systemically, their ability to transport across barriers and enter tissues must be further elucidated. After this entry, or if EVs are to be administered directly to tissues, EVs must be able to navigate the interstitial space that likely includes an extracellular matrix (ECM) in order to reach target cells. In sum, to optimize EVs as a therapeutic medium, it is important to know and understand mechanisms of EV transport and uptake in ECM within tissues.

1.1.2 THE MICROENVIRONMENT AND MECHANOBIOLOGY

Cells exist within a physical environment, and therefore they react to physical cues within the environment and respond with physical forces. Adherent cells attach physically to the

surrounding ECM or other cells. Both the attaching cell and surrounding cells sense the physical properties of their environment. Suspended cells also sense the forces in their environment, including shear stresses and pressure [43]. Mechanobiology is a field that describes how mechanical properties of cells and the surrounding microenvironment affect cell phenotypes.

Cells use membrane protein complexes called integrins to form attachments with the environment [44], which are known as focal adhesions. In 1997, it was first observed that the properties of focal adhesions are dependent on the mechanical properties of the environment, as focal adhesions became larger on stiffer substrates [45]. In 2004, McBeath *et al* used a substrate patterning approach to demonstrate that cell shape determined the fate of MSCs [46]. Cells forced to be rounded differentiated into adipocytes, and cells forced to be flattened differentiated into osteocytes – furthermore, this process depended on RhoA activation through actin-myosin-generated tension. In 2006, Engler *et al* showed that substrate stiffness alone determined MSC fate [47]. This phenomenon depended on activity of the motor protein myosin-II, which directly impacts cellular contractility and intracellular tension. Since these landmark studies, other studies have shown the mechanical regulation of other cell phenotypes such as spread area [48], motility [49], shape [50], and division [51] among others. Mechanics can also affect certain pathological conditions including cancer [52], fibrosis [53], and vascular disease [54].

Total cellular tension can be dissociated into membrane tension, cytoskeletal tension, and the attachment between membrane and cytoskeletal (termed the membrane-to-cortex attachment, MCA) [55]. Indeed, the total cellular tension alone is highly significant since manipulation of tension through cell volume by osmotic pressure is sufficient to determine MSC fate [56]. Membrane tension is affected by both the total area of membrane and the composition of that membrane. However, cells may hold these factors generally constant as evidenced by extensive

membrane ‘reservoirs’ [57] that exist independent of spread area, and it is unclear the extent to which cells alter their membrane composition. In contrast, the cytoskeleton consists of actin filaments, intermediate filaments, microtubules, and motor proteins, all of which are known to contribute to total cellular tension [58]. The actin cortex, located near to the plasma membrane, is a significant contributor to cellular tension [59] and is the site by which the plasma membrane connects to the cytoskeleton through the MCAs. In general, cells sense the physical environment through their integrins and focal adhesions on the plasma membrane, and transduce this sensation through the cortex and cytoskeleton, eventually resulting in phenotypic changes. Phenotypic changes can occur at the level of cytoskeleton structure, protein translation, or even gene regulation -- for example, through the YAP/TAZ mechanotransduction pathway [60]. However, not all levels of this chain need be involved in any given phenotype. For example, Oakes *et al* showed that cell spreading through the lamellipodium is affected by substrate stiffness independent of myosin-II and transcriptional regulation [61]. Activation of this mechanotransduction train will likely depend on different downstream biological functions.

The influence of membrane channels on mechanobiological phenotypes such as intracellular tension and cell motility is beginning to be more appreciated. For example, voltage-gated ion channels such as Piezo1 can be mechanosensitive by responding to various types of force such as shear or stretch [62]. Additionally, water channels such as the aquaporin family regulate water influx and efflux in the cell which regulates their response to osmotic environment conditions. Osmotic conditions can affect intracellular pressure by affecting the density of the cytoplasm, which can then affect phenotypes such as cell fate decisions [56]. Aquaporins have also been implicated in cell motility, since knockdown of aquaporins lead to reduced cell motility in vitro [63]. The prevailing theory is that aquaporins can impact local volume gradients

within cells, which can affect lamellipodium turnover at either the leading or trailing edge. Interestingly, the water channel aquaporin-1 (AQP1) was found to exist within EVs derived from reticulocytes [64] and aquaporins have also been observed to exist in plasma membrane blebs in liver endothelial cells [65]. However, it remains to be studied whether membrane channels present within EV membranes affects their phenotypes, potentially in terms of their transport behaviors or biodistribution patterns.

The environments from which cells are derived contain a diverse range of physical properties and forces that have the ability to affect cell phenotypes. For example, the bone marrow from which MSCs are derived features orders of magnitude of different tissue stiffness (Young's modulus, *E*, from 0.1-100 kPa) [66]. To recapitulate salient features of the biophysical environment, biomaterials serve as an excellent tool that can be used to study the ways in which cells react to and respond to external physical cues. Importantly, some biomaterials such as alginate can be designed to recapitulate singular biophysical properties to isolate the contributions of different biophysical properties, in order to study how cells respond to them. For example, the stiffness of alginate hydrogels can be tuned independent of the resulting porosity of the material [67]. Broadly, material properties can be defined in two categories (Fig. 1.1): (1) intrinsic properties, which are irreducible and independent of scale, and (2) extrinsic properties, which are highly specific to scale [68]. Stiffness and porosity are examples of intrinsic material properties since they can be constant independent of scale. Another intrinsic property, stress relaxation, is related to viscoelasticity and can be tuned by using alginate hydrogels [69]. Most tissues exhibit a stress relaxing property [70], and thus the ability to control the extent of material stress relaxation highlights how biomaterials can be used to recapitulate biophysical characteristics of the physiological cellular microenvironment.

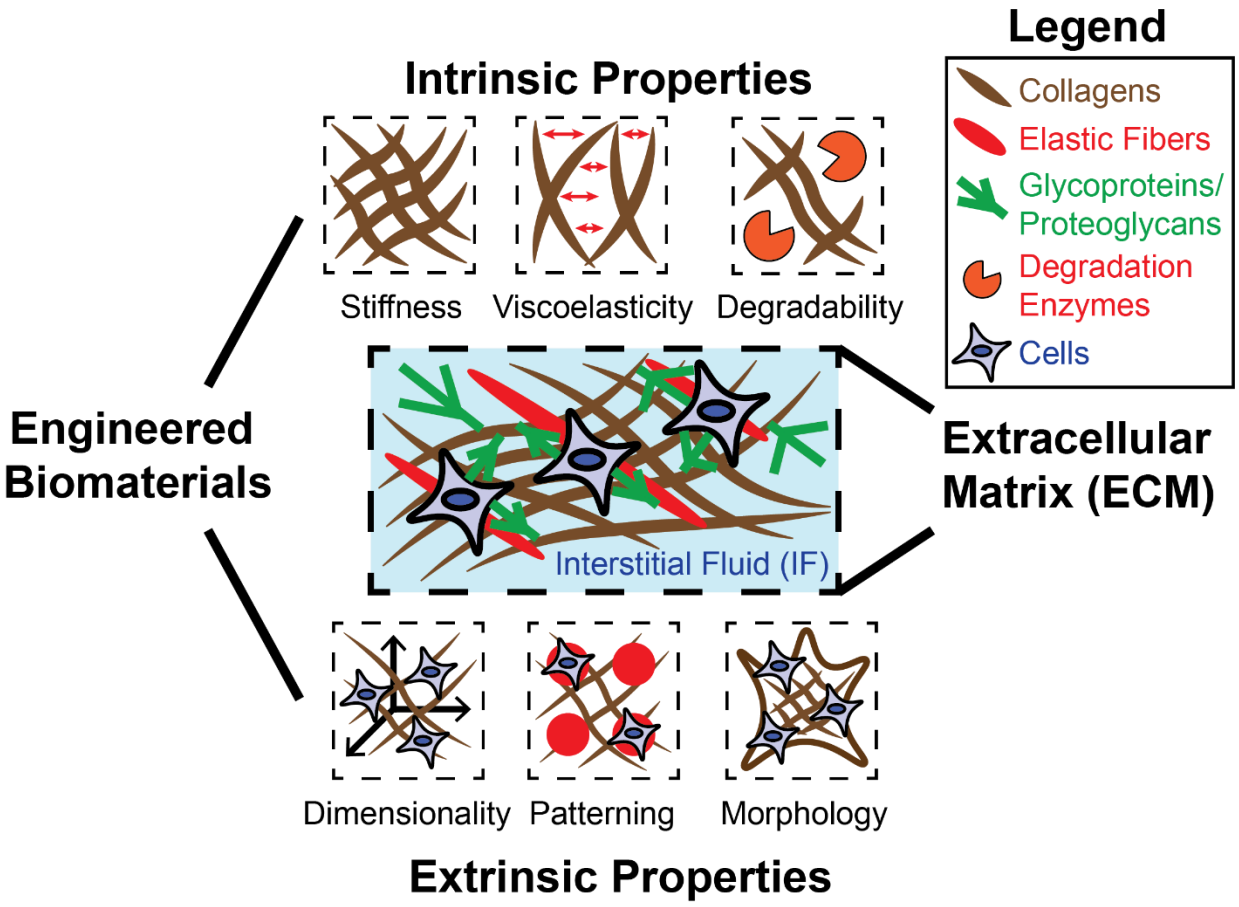

Figure 1.1. Engineered biomaterials exhibit intrinsic and extrinsic properties to recapitulate the native environment. Engineered biomaterials can be used to model diverse mechanical properties of ECM. The native ECM is composed of fibrous materials (collagen, elastic fibers) as well as glycoproteins and proteoglycans, which confer adhesion between cells and the ECM. The ECM and the IF that exists within can possess many distinct mechanical properties, each of which can be recapitulated individually or in combination using biomaterial design. Intrinsic properties include stiffness, viscoelasticity, and degradability, and are generally independent of scale. Extrinsic properties include dimensionality, patterning, and morphology/geometry, and are determined by scale.

Alginate hydrogels have been used to show that both stiffness and stress relaxation [69, 71] are key intrinsic biophysical properties that regulate cell phenotypes. Other intrinsic properties include porosity and degradability, the latter of which has been elegantly incorporated into many biomaterial systems [72]. Extrinsic properties have also been shown to be important in driving cellular behavior. The importance of dimensionality cannot be overstated, since cells *in vivo* exist in a 3D environment that is dramatically different than a 2D environment when considering cellular phenotypes [73, 74]. Furthermore, factors like substrate patterning and geometry play a key role in determining cell phenotypes; for example, a recent study created 3D 'microniches' with defined shapes to demonstrate that cell volume and morphology are critical in determining several phenotypes including focal contractility, transcriptional regulation and epigenetic phenomena [75]. In sum, advances in biomaterials drive advances in mechanobiology since they allow discovery of key mechanobiological insights.

Membrane dynamics involve intricate processes tied both to regulation of the cellular cytoskeleton as well as the biogenesis and secretion of EVs. Various studies suggest that intracellular tension drives biological processes that increase the plasma membrane surface area or mass, such as exocytosis [76]. Cytoskeletal components are well-known to be involved in intracellular trafficking [77, 78], including endosomal dynamics [79]. Though their involvement is clear, the extent that cytoskeletal components are required for endosomal trafficking remains to be fully elucidated. Furthermore, while some components are known to be associated with endosomal dynamics, it is possible that they serve to inhibit endosomal transport – for example, the actin cortex surrounding the cell membrane in some cases likely presents as a dense mesh that acts to sterically hinder transporting endosomes. However, it remains to be studied how biophysical properties of the microenvironment regulate EV production by cells.

Once released from cells, EVs will likely be either trapped within or transported through the matrix. One important consideration is the mesh size within the matrix, since EVs are larger as compared to the known mesh size of many biological matrices [80-82]. If cells produce large quantities of EVs *in vivo*, it is likely that EVs can accumulate to a significant extent within interstitial regions. Such accumulation would require a clearance mechanism to maintain normal tissue homeostasis. It is known that cells can manipulate their characteristic size to transport through tight spaces, such as during transmigration [83] or diapedesis [84]. Whether EVs can also transport through tight spaces in the extracellular matrix remains unclear. In addition, it remains unknown whether mechanical properties of the matrix or the composition of EVs themselves regulate this potential transport. One potential way to study EV transport within matrix would be to utilize multiple particle tracking, which broadly refers to methods that can be used track the transport behaviors of multiple particles within a medium over time [85]. These methods can estimate the size of particles or the viscosity of solutions containing particles [86]. Most notably, multiple particle tracking has been adapted to allow characterization of mechanical properties within cells, using a method termed microrheology [87]. However, particle tracking can also be performed in a matrix environment, as has been done in mucus environments to study nanoparticle penetration [88]. Though significant advances in studying nanoparticle transport have been achieved, direct tracking of biologically-derived particle transport within matrices with defined viscoelastic properties has yet to be achieved.

1.1.3 EXTRACELLULAR VESICLE-MATRIX INTERACTIONS

More recently, there has been an appreciation for different types of EVs that are defined by where they are located within or derived from the body. Though it has been extensively

reported that EVs can be found in a variety of different biological fluids such as serum and saliva [89], the presence of EVs existing bound within the ECM itself is more recently reported [37]. Matrix-derived or matrix-bound EVs are found within the ECM. In contrast, fluid-derived or fluid-phase EVs are found primarily within the blood serum. As EVs are becoming more promising candidates for both therapeutic and diagnostic applications, it is important to appreciate the existence these two distinct populations as they are presumably carrying out different functions by existing in different environments. For example, if diseased cells embedded in a matrix release EVs that can be considered disease biomarkers, it will be important to determine whether these EVs can be retrieved from the matrix or the fluid.

EVs have been shown to have express different contents depending on different conditions such as tissue source. Recently, it was demonstrated that matrix-bound and fluid-phase EVs contain different miRNA and lipid contents [90]. The contents of EVs are a potential reason for differences in matrix or fluid localization. For example, presence of matrix binding ligands on the surface of EVs, such as integrins [91] or lipid binding domains [92] will make them more likely to bind to matrix proteins and thus exist in the matrix. Furthermore, the lipid composition of vesicles may determine their mobility, as in the case of nanoparticles, where a composition leading to semi-elastic properties significantly assists their transport through a matrix environment [93]. For EVs specifically, membrane fluidity was shown to affect their bending modulus, which is dependent on disease state of the patient [94]. However, the effects of EV composition and mechanical properties on their status as matrix-bound or fluid-phase remains to be elucidated.

The properties of the matrix itself may be an important determinant of whether EVs localize in matrix or are released into fluid, since particle transport in matrix is known to be

dependent on matrix properties [95]. For example, the matrix should allow EV transport if the diameter of EVs is smaller than the mesh size. However, this assumes that interactions do not occur between EV and matrix. Even if the mesh size is larger than EVs and thus will lead to their confinement, affinity interactions will tend to slow EV transport and likely result in their embedding in the matrix as described above. Other potential interactions include ionic interactions and hydrophobic interactions, among others. Ionic interactions can occur between the negatively charged lipid bilayer on EVs and charged groups that may be present within the matrix; positively charged matrix groups will tend to attract EVs and negatively-charged matrix groups will tend to repel EVs. Furthermore, the mechanical properties of materials also may affect EV transport; however, this is yet to be studied.

Matrix degradability is a key feature that would allow EV transport through matrix, and the lack of matrix degradability is likely to retain EVs in the matrix. Indeed, the ability for cells to degrade surrounding matrix plays a key role in cell migration through matrix [96], particularly in cancer cell invasion [97, 98] and endothelial cell sprouting [99]. Interestingly, it was reported over 20 years ago that membrane shed vesicles from ovarian cancer cells could contain matrix metalloproteinases (MMPs) [100], enzymes that exhibit the ability to degrade matrix. Since then, some have reported that EVs can contain other matrix degradation proteins such as heparanases, hyaluronidases, and aggrecanases [38]. EVs that contain active matrix degradation enzymes are expected to more easily transport through matrix as the enzymes degrade their surroundings, which suggests that this population of vesicles is less likely to remain in a matrix-bound form. Despite many matrix degradation enzymes being detected in EVs, a direct EV-mediated matrix degradation is yet to be demonstrated. Interestingly, EVs are also found to be coated with matrix molecules themselves, including fibronectin [101] and hyaluronan [102], which are known to

affect phenotypes of recipient cells. The relative amounts of matrix versus matrix-degrading enzymes present within EVs should be elucidated to better understand population differences of matrix-bound or fluid-phase EVs.

It is possible that matrix-bound EVs and fluid-phase EVs can switch their state; in other words, EVs bound within the matrix can transport into the fluid, and EVs within the fluid can transport into the matrix. It is more likely that EVs will transport from fluid to matrix, since EVs totally trapped within matrix are unlikely to escape without the influence of a significant force or matrix degradation. In contrast, it seems plausible that EVs release into the fluid can transport into the matrix. However, a direct observation of this phenomenon is yet to be reported. There are several potential areas where such a transition would be regulated. First, the content of EVs released initially into the fluid could be targeted to the matrix by inclusion of affinity domains or other targeting mechanisms. Second, at the interface between the fluid and the matrix, the vascular barrier can often exhibit a tight barrier, such as in the blood brain barrier, which will restrict passage of larger particles though the vessel from the serum to the matrix. However, some vascular regions such as capillaries have looser junctions due to presence of fenestrations, which potentially allows EVs to cross the vascular barrier. Third, the ability for EVs to be retained in the fluid (and not be degraded or taken up by other cells) will increase their residence time in circulation, leading to a greater chance that they are able to cross into the matrix. In other words, a lack of uptake by other cells or a clearance by other means will mean that EVs are more likely to end up in matrix. An investigation into the transition between matrix-bound and fluid-phase EV states will serve to greatly increase knowledge of EV biology, as well as for potential EV theranostic purposes. For therapeutic purposes, it is important to develop an understanding of how systemically administered EVs will transport to desired disease sites. For diagnostic

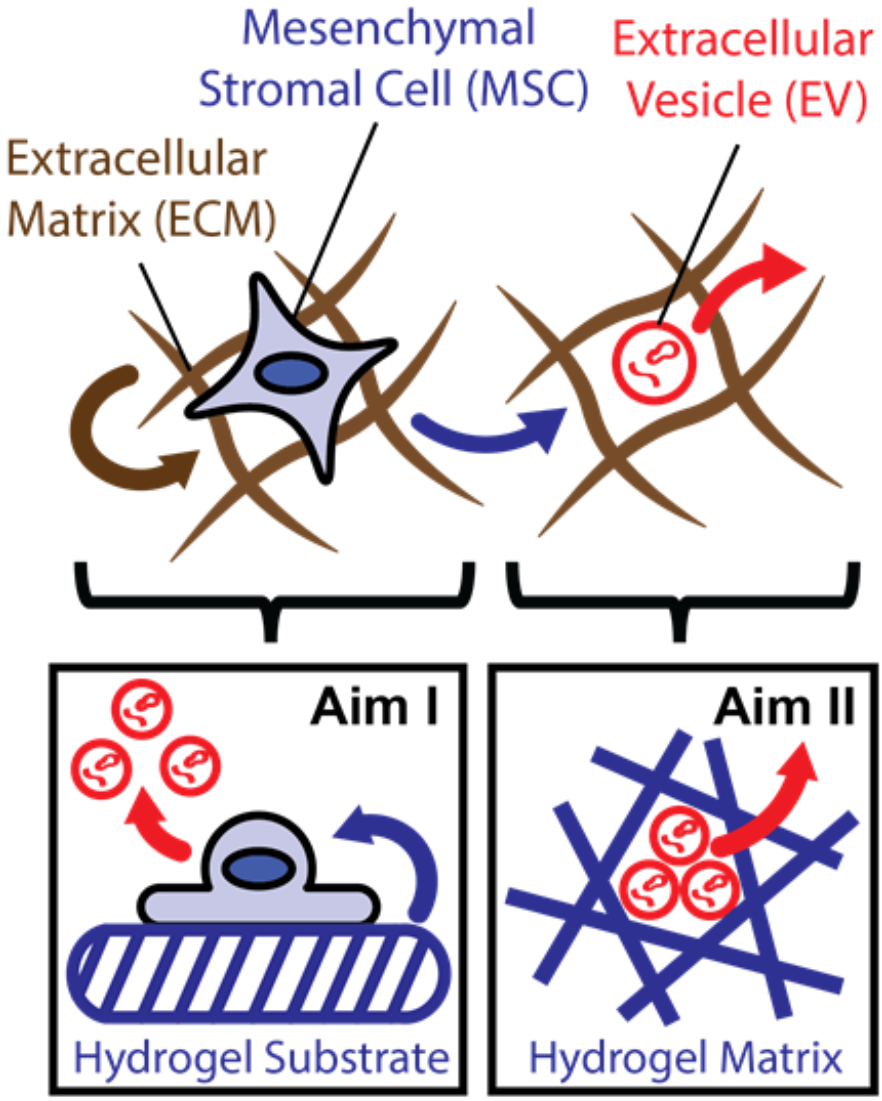

Figure 1.2. A hypothesis that matrix mechanics regulate EV production by cells and EV transport within the matrix. The purpose of this thesis can be understood by the proposition of two basic questions: (1) how does the matrix environment affect MSCs in their production of EVs, and (2) once they are produced, how do EVs navigate the matrix environment? These questions can be expanded into specific Aims, which are illustrated here.

purposes, it will be important to consider the fate of EVs, particularly whether they originated in the matrix or arrived there from an external source.

1.2 PURPOSE

MSCs produce EVs as a medium of communication with other cells. Through such communication, MSC-EVs are increasingly being shown to confer therapeutic benefits in preclinical disease models [24]. However, the translation of EVs as therapeutics remains premature due to an ineffective means of *ex vivo* production and an incomplete model to describe their *in vivo* biodistribution [103]. This is in part because mechanisms by which MSCs produce EVs and how EVs transport through their environment remain unclear. In this thesis, multidisciplinary approaches through biomaterial design, genetic engineering, quantitative modeling, and imaging were utilized to test the central hypothesis:

Matrix mechanics regulate EV production by cells and EV transport within the matrix.

Clarification of the phenomena behind this hypothesis, as presented in this thesis, lends significant insights as to the innate biological properties of EVs, and will also improve the ability to translate MSC-EVs as therapies. The specific aims of this thesis (Fig. 1.2) include:

Aim I: Determine the effects of matrix biophysical cues on EV production by MSCs.

Aim II: Evaluate whether EVs are able to transport in a 3D nanoporous extracellular matrix environment and outline the biophysical mechanisms and dependencies of such a phenomenon.

1.3 SIGNIFICANCE

Most therapies produced to date are drugs, which are relatively simple small molecules. Because of the complexity of certain diseases, the next era of medicine demands a higher complexity in therapeutics to treat such diseases. Cell therapy is a promising strategy to leverage the complexity of cells to generate groundbreaking treatments for complex diseases. However, challenges exist to realizing the full potential of cell therapy. EVs represent a medium between the complexity of cells and simplicity of small molecules. Direct treatment with cells can be expensive or undesired in some cases, and EVs from cells can potentially be sufficient to treat disease without causing complications. However, there are important issues in translating EVs as therapeutics – (1) production of functional EVs *in vitro* is limited and (2) EVs are cleared rapidly after administration in the body. These issues in large part can be attributed to our lack of understanding of how EVs are produced by cells and how they transport within the body. This thesis proposes that matrix biophysical mechanics play a significant role in the production and transport of EVs. Here, a novel approach is presented to study these phenomena by designing and creating hydrogels with specifically defined mechanical properties that mimic those found within a physiological environment. Additionally, state-of-the-art genetic engineering approaches are employed to convincingly define mechanisms behind uncovered phenomena. Advances in microscopy allow live imaging of nano-sized vesicular components within cells and the transport of EVs within nanoporous synthetic matrices. Sophisticated mathematical modeling accompanies empirical endeavors to enhance the quantitative basis of obtained results.

Producing enough EVs from cells for therapeutic doses in a manufacturing setting has proven challenging. However, a lack of complete understanding as to endogenous mechanisms by which cells produce EVs limits the efficiency of functional EV production on a per cell basis.

Since all production strategies will involve cells cultured on or within a material, a fundamental understanding of how materials affect EV production by cells is highly valuable in the quest to maximize EV production using those strategies. It follows that a study focusing on the impact of substrate mechanical properties, which can be generalizable across different materials used for EV production, will be useful for existing or future strategies to implement.

After either production or exogenous administration, EVs sometimes need to cross the interstitium to reach target cells. ECM compositions are heterogeneous and often nanoporous with network structures that approach the scale of nano-sized particles [80]. As particles become similar in size to the network, an infinite solvent assumption no longer applies, and interactions between particles and network becomes significant in defining particle transport properties [95]. As a result, although much is known about transport of molecular factors, it is unclear how nano-sized particles such as EVs transport within the ECM. It follows that in order to study EV transport through ECM, specific transport behaviors must be considered as a function of properties of the environments themselves. Thus, studying the ability of EVs to transport within a dense nanoporous matrix environment will lend great insights into the field of nanoparticle transport and tracking, as well as shed new light on exciting properties of EVs as biological nanoparticles. Furthermore, elucidating mechanisms of EV transport through ECM allows the potential to engineer endogenous EVs to better transport through tissues, thereby improving their therapeutic outlook. Lastly, results will suggest the possibility of developing a hydrogel-based technology that may efficiently deliver EVs to target tissues.

Studies presented in this thesis are the first attempts to describe and understand EV production and transport in a biophysical context. In Chapter 2, a novel dependency of EV production on substrate stiffness has been identified, and the mechanisms behind the

phenomenon are elucidated. Results provide a greater understanding of how microenvironments and mechanotransduction impact EV biogenesis from cells and suggest strategies for the optimal *ex vivo* production of EVs. In Chapter 3, the ability and mechanosensitivity of EV transport in nanoporous 3D matrices has been demonstrated and elaborated, while Chapter 4 further details mechanisms behind this finding by constructing a mathematical model. Results inform a novel direction to not only consider environmental mechanics for EV delivery but also to engineer various aspects of this relationship to optimally deliver EVs *in vivo* for the treatment of pathological conditions.

1.4 OUTLINE OF THESIS

The primary Aims of this thesis are (1) to study the biophysical interactions that regulate extracellular vesicle production by cells and (2) to study if and how extracellular vesicles can transport through the extracellular matrix environment. Thus, Chapter 2 presents a comprehensive study on the effect of substrate mechanical properties on the production of EVs by cells. Next, Chapter 3 shows that EVs exhibit the ability to transport through the matrix environment, and it furthermore details this ability as a function of matrix and vesicle properties. Finally, Chapter 4 provides a theoretical basis for the EV transport behaviors presented in Chapter 3. The document concludes by summarizing the major conclusions drawn from this work and providing an outlook for related future directions.

2. BIOPHYSICAL REGULATION OF EXTRACELLULAR VESICLE PRODUCTION

2.1 ABSTRACT

Exosomes are cell-secreted nanoparticles with broad potential to treat tissue injuries by delivering cargo to program target cells. However, improving the yield of functional exosomes remains challenging due to an incomplete understanding of how microenvironmental cues regulate exosome secretion. We show that mesenchymal stromal cells (MSCs) seeded sparsely (~25 cells/mm^2) on engineered hydrogels that mimic the elasticity of soft (~3 kPa) tissues with a lower (~0.16 mM) integrin ligand density secrete ~10-fold more exosomes per cell than MSCs seeded on a rigid plastic substrate, without compromising their therapeutic activity or cargo to resolve acute lung injury in mice. Mechanistically, intracellular CD63$^+$ multivesicular bodies (MVBs) transport faster within MSCs on softer hydrogels with less adhesion time, leading to an increased frequency of MVB fusion with the plasma membrane to secrete more exosomes. Actin-related protein 2/3 complex but not myosin-II limits MVB transport and exosome secretion from MSCs on hydrogels. The results provide a rational basis for biomaterial design to improve exosome secretion while maintaining their functionality.

2.2 INTRODUCTION

Extracellular vesicles (EVs) are small cell-derived particles composed of a lipid bilayer that are conventionally described as ranging from 50-500nm in diameter [104]. These particles carry various cargoes such as proteins, lipids and nucleic acids, which they can deliver to recipient cells. EVs are generally classified into subtypes by the cellular pathway by which they

are generated. The EV subgroup microvesicles (or ectosomes) are produced by budding directly from the membrane [27], while exosomes are produced by inward budding within late endosomes that form a multivesicular bodies (MVBs) [5]. Exosomes are released from cells when the MVB fuses with the plasma membrane. Recent studies have established exosomes as a critical paracrine secretion mechanism for cell-cell communication [105], including as potent regulators of the cellular microenvironment. Non-mechanical environmental cues such hypoxia [106], histamine [107] or Ca2+ levels [108] are known to affect exosome release. In turn, exosomes released by cells can alter the microenvironment directly, as in tumor cell migration [109], or indirectly, as in ECM deposition and remodeling [38], cardiomyocyte autophagy [110] and tissue regeneration [111], or angiogenesis [112].

Mesenchymal stromal cells (MSCs) derived from the bone marrow utilize paracrine mechanisms to mediate the biology of surrounding cells within their microenvironment [113]. Recent studies show that exosomes from MSCs contain therapeutic cargo with broad potential to treat various tissue injuries [24, 114]. Exosomes from MSCs have been investigated for their therapeutic efficacy in clinical trials by delivering bioactive contents to recipient cells and ameliorating diseases. Relevant bioactive contents that ameliorate lung injury, for example, include angiogenic factors [115, 116], growth [117] and transcription factors [118], anti-inflammatory factors [119-121] and mitochondrial contents such as mitochondrial DNA (mtDNA) [122]. It is well-known that biophysical properties influence MSC behaviors such as cell spreading [48], division [123] and differentiation [124] among others. Previous studies suggest that cellular tension regulates biological processes that affect the plasma membrane surface area or mass, such as exocytosis and endocytosis [55]. These processes are highly

regulated and involve cell membrane, protein machinery, and cytoskeletons. Although cells are highly sensitive to mechanical cues by the microenvironment, the role of these cues in mediating intercellular communication by exosome production remains unclear.

Because the bone marrow environment from which MSCs are derived presents a diverse range of biophysical environments [125], environmental cues can potentially play a role in determining a level of EV production most appropriate for specific environments. Thus, we hypothesized that biophysical cues of the microenvironment determine exosome production from MSCs. To test this hypothesis, we leveraged alginate hydrogels with a physiologically relevant range of substrate stiffness for MSC mechanosensing [70]. We show that softer hydrogels with less ligand density increase exosome production from MSCs. This occurs due to less integrin-ligand binding, as cells with less time to adhere to substrates produce exosomes more rapidly. Exosomes from cells seeded on substrates of different stiffness remain functionally similar, as they show similar efficacy against an animal model of acute lung injury in part through CD44. Through recombinant fluorescent protein expression and imaging, we elaborate that MSCs on softer hydrogels with less adhesion exhibit enhanced intracellular $CD63^+$ MVB transport, which is correlated with increased fusion of $CD63^+$ MVBs with the plasma membrane. Consistent with the notion that less well-developed actin cytoskeletons inhibit MVB trafficking and resulting fusion with the plasma membrane, inhibition of actin-related protein complex 2/3 (Arp2/3) restores MVB trafficking on the stiffer substrate.

2.3 MATERIALS AND METHODS

Note: Portions of this section were originally published:

Wong, S.W., Lenzini, S., Cooper, M.H., Mooney, D.J., Shin, J.-W. Soft extracellular matrix enhances inflammatory activation of mesenchymal stromal cells to induce monocyte production and trafficking. Science Advances, 2020. 6(15): p. eaaw0158. (See Appendix K)

Devine, D., Vijayakumar, V., Wong, S.W., Lenzini, S., Newman, P., Shin, J.-W. Hydrogel Micropost Arrays with Single Post Tunability to Study Cell Volume and Mechanotransduction. Adv Biosyst, 2020. 4(11): p. e2000012. (See Appendix K)

Material preparation and hydrogel formation

Raw sodium alginates with different molecular weights, low (10/60, ~120 kDa) and high (Manugel, ~240 kDa), were obtained from FMC Corporation. Alginate was purified through dialysis in a 3.5 kDa membrane submerged in water, followed by treatment with activated charcoal (Sigma) 0.5 g per gram alginate. It was then filtered, frozen and lyophilized to obtain a solid polymer. Conjugation of RGD (amino acid sequence GGGGRGDSP, Peptide 2.0) to alginate polymers was performed using a method involving carbodiimide chemistry described previously [126] at DS10 (0.8 μM) or DS2 (0.16 μM). Physically crosslinked hydrogels were formed as described previously [71]. Briefly, alginate solutions were mixed to be 1% Manugel and 1% 10/60 (2% total), added to a syringe and locked to another syringe with CaSO4 (Sigma) to achieve final calcium concentrations of 10 mM (softer) and 25 mM (stiffer). After mixing, the solutions were deposited under glass for 2 h to form a hydrogel. Covalently crosslinked hydrogels were formed using carbodiimide chemistry and adipic acid dihydrazide (AAD, Sigma) as described [127]. Alginate solution (1% Manugel and 1% 10/60) was mixed with 4.8mg/mL Hydroxybenzotriazole (Sigma), 50 mg/mL 1-Ethyl-3-(3-dimethylaminopropyl)carbodiimide

(Sigma), and either 1.5 mM (soft) or 6 mM (stiff) AAD. Solutions were incubated at RT under glass for 12-18 hr to form a hydrogel. Polyethylene diacrylate (PEG-DA) hydrogels were formed by adding the materials: 10 mM sodium L-ascorbate (Sigma), 4 mM tris(2-carboxyethyl)phosphine (Sigma), 1X phosphate-buffered saline (PBS), 0.8 or 0.16 mM RGD peptide (sequence CGGGRGDSP, Peptide 2.0), PEG-DA Mn 700 (Sigma) and lithium phenyl(2,4,6-trimethylbenzoyl)phosphinate (TCI Chemicals) in varying concentrations to achieve desired range in mechanical properties upon 365 nm ultraviolet light exposure.

Mechanical characterization of hydrogels

The mechanical properties of hydrogels or tissues were obtained using rheometry via Anton Paar MCR302. Storage (*G'*) and loss (*G''*) moduli were measured through a frequency sweep by lowering the geometry (Anton Paar PP08) to a 5% normal strain followed by a rotation that induced a 0.5% shear strain at an increasing frequency and finally measurement of the resulting shear stress. The complex shear modulus *G** was calculated [128]:

$$G^* = \sqrt{G'^2 + G''^2}\,. \qquad \text{(Equation 2.3.1)}$$

Young's Modulus (*E*) was calculated with the equation [129]:

$$E = 2G^*(1+\nu) \qquad \text{(Equation 2.3.2)}$$

using the value of *G** obtained at 1 Hz, with Poisson's ratio $\nu = 0.5$. To determine stress relaxation, the geometry was lowered at constant velocity (25 μm s^{-1}) through the linear elastic region until a 15% strain was reached, followed by measurement of normal force over time.

Cell culture

Cells were cultured at 37°C in 5% CO_2. Human MSCs (hMSCs) were derived by plastic adherence of mononucleated cells from human bone marrow aspirate (Lonza). After 3 days, adherent cells were cultured in the hMSC medium: α-minimal essential medium (αMEM, Thermo) supplemented with 20% fetal bovine serum (FBS, Atlanta Biologicals), 1% penicillin/streptomycin (Thermo Fisher Scientific), and 1% GlutaMAX (Thermo). After reaching 70~80% confluence at 10~14 days, cells were split, expanded in the hMSC medium and used at passage 3. D1 MSC cells (CRL-12424, ATCC) were cultured using high-glucose DMEM (Thermo) supplemented with 10% FBS, 1% penicillin/streptomycin (P/S, Thermo) and 1% GlutaMAX (Thermo) to 80% confluency before passaging, no more than 30 times. Cells were routinely tested for mycoplasma contamination and only used if no contamination was present.

Cell seeding on hydrogels

Hydrogel discs were placed in ultra-low binding polystyrene well plates (Corning) to ensure cells attach to hydrogels and not the plate surface. Hydrogels were washed with Hank's buffered salt solution (HBSS, Thermo) for at least 3 days before seeding cells. Cells were seeded at various densities and for various times to achieve conditions described in the manuscript. After seeding, hydrogels were washed thoroughly to remove unattached cells. N-cadherin blocking was achieved by adding a neutralizing N-cadherin antibody (50 μg/mL, GeneTex, GTX11340) or an IgG isotype control (BioLegend, 401403) to cell suspensions for 45 min at 4 °C followed by washing cells by centrifugation and seeding onto hydrogels. Drug treatments of 3 μM $MnCl_2$ (Fisher Scientific), 200 nM cilengitide (Cayman) and 5 μM CK-869 (Cayman) were applied during and after cell adhesion to substrates. To evaluate the number of live cells seeded on substrates, cells were detached by incubating with Accutase® Cell Detachment Solution

(Innovative Cell Technologies, Inc.) for 10 min at 37C. Cells were then washed by centrifugation and directly added to HBSS containing calcein AM (1:2000; Biotium), ethidium bromide (1:2000; Thermo Fisher Scientific), and a predefined number of allophycocyanin beads (BD). After incubation at RT for 10 min, the samples were analyzed for live and dead cell number by flow cytometry. To evaluate cell morphology on substrates, cells were washed with HBSS, incubated with calcein AM (1:2000) for 10 min at 37C, and imaged using a Nikon Eclipse Ts2R inverted fluorescence microscope. Cell circularity was calculated with the equation:

$$Circularity = \frac{4\pi(Area)}{Perimeter^2} . \qquad \text{(Equation 2.3.3)}$$

Particle size and number characterization

Particle size and number were obtained using Nanoparticle Tracking Analysis 3.2 (NTA) via NanoSight NS300 (Malvern) using a 405 nm laser. Samples were introduced by syringe pump at a rate 100 µL/min. Three thirty-second videos were acquired using camera level 14 followed by detection threshold 7. Camera focus, shutter, blur, minimum track length, minimum expected particle size and maximum jump length were set automatically by the software. Samples were diluted as needed to maintain particles per video from 100-2000. To ensure specificity, all samples were tested as compared to appropriate blank conditions.

Transmission electron microscopy

Samples were prepared by placing 10 µL onto a 300-mesh copper grid with carbon-coated formvar film (Electron Microscopy Sciences) and incubating for 2 min. Excess liquid was removed by blotting. Grids were placed briefly on 10 µL of 2% uranyl acetate, followed by blotting to remove excess liquid, and placed again. Grids were examined via JEOL JEM-1400F

transmission electron microscope, operating at 80 kV. Digital micrographs were acquired using an AMT NanoSprint1200-S CMOS Camera and AMT software (Version 701). Particle diameter and sphericity were determined manually from images using ImageJ. Circularity of particles was defined by Equation 6.

Exosome surface marker characterization

CD63 and CD9 expression were determined using in-house ELISA assays. Capture antibodies (CD63: BioLegend, 353014; CD9: BioLegend, 312102) were adhered to Nunc MaxiSorp™ flat-bottom coated plates (Invitrogen, 44-2404-21) overnight followed by blocking for 1 hour with 1% bovine serum albumin (Roche) in PBS. After washing, samples were incubated overnight followed by incubation with biotin-conjugated detection antibodies (CD63: GeneTex, GTX52381; CD9: Miltenyi, 130-103-989), incubation with Streptavidin-HRP (R&D Systems), and ELISA substrate (R&D Systems). Reactions were quenched with 1M HCl and absorbance read at 450 nm. Recombinant protein standards (Sino Biological) were used as comparisons for protein content. CD44 expression was determined using a commercially available ELISA assay (R&D systems, DY7045-05).

siRNA transfection

Scrambled siRNA (Dharmacon, D-001810-01-05) or siRNA against FAK (Ambion, 4427038) or TLN1 (Dharmacon, J-012949-05-0002) was diluted to 160 nM in unsupplemented Opti-MEM medium (Thermo) and combined 1:1 with Opti-MEM supplemented with 2% Lipofectamine RNAiMAX (Thermo) and incubated at room temperature for at least 20 min. Cells were washed with HBSS and fresh growth medium was added to cells. The transfection

solution was added dropwise for a final siRNA concentration of 4 nM to treat cells on hydrogels for 3 days followed by EV collection and measurement.

Exosome isolation and preparation

To isolate EVs from cells for cargo characterization and animal experiments, the cells were washed twice with HBSS followed by incubation with serum-free growth medium for 30 min. Afterwards, the medium was exchanged with fresh serum-free medium. After times as indicated in the manuscript, medium was centrifuged at 2,000*g* for 10 min to remove cell debris followed by centrifugation at 10,000*g* to remove particles larger than 500 nm [130]. Afterwards, the solution was added slowly to a 14 mL polystyrene ultracentrifuge tube (Beckman) containing 1.5 mL of 30% sucrose (Fisher Scientific) in PBS and centrifuged at 100,000*g* for 90 min. The upper non-sucrose layer was aspirated and washed with PBS followed by centrifugation at 100,000*g* for 90 min. The pellet was resuspended and confirmed to contain concentrated EVs using NanoSight NS300 (Malvern).

Exosome content characterization

Before extraction, for all samples, particles were incubated with DNase I (Thermo) to remove potential exogenous DNA not contained within particles. DNA samples were treated with RNase A (Qiagen) to remove RNA contaminants, and DNA was extracted using the DNeasy Blood and Tissue kit (Qiagen) followed by qPCR analysis. Total RNA was extracted from samples using the RNeasy Mini kit (Qiagen). Complementary DNA was reverse transcribed from RNA by SuperScript-III (Thermo Fisher Scientific). For both mRNA and miRNA, a random hexamer primer (Invitrogen) was used. For miRNA, an additional stem-loop

RT (SLRT) primer was included at 100 nM for each specific miRNA target (see Table S1 for sequences) as described [131]. Quantitative PCR was performed in the ViiA7 qPCR system with PowerSYBR Green master mix (Applied Biosystems). Samples were analyzed using primer concentrations of 100 nM each; for miRNA, the forward primer corresponds to the miRNA sequence and the reverse primer corresponds to the stem-loop sequence, which is universal for all targets. Relative gene expression was computed by the delta Ct method by comparing Ct values to a reference gene (*GAPDH* or *U6*). See Appendix J for a list of primers used. Samples were compared to a blank to ensure specificity of the assay (data not shown). To analyze rRNA contents, RNA samples were analyzed by Agilent TapeStation 4200 and 18S rRNA was considered as a peak in the range 1000-2000 nt as in Fig. 2.2b.

Lentiviral-mediated expression of CD63 fused with fluorescent proteins

Katushka2S was fused with CD63 in a lentiviral expression vector (CD63-K2S vector) and expressed in D1 MSCs as described previously [132]. The sequence for pHLuorin2 was synthesized by Genscript and exchanged with the Katushka2S in the same vector using restriction enzyme cloning. The resulting CD63-pHLuorin2 lentiviral vector was transduced in D1 MSCs in a similar method as the CD63-K2S vector. Cells were selected by treatment with 5 ug/mL puromycin over 3 days and confirmed to express fluorescent signal versus non-transduced cells.

TIRF imaging of cells on substrates

To covalently bond crosslinked PEG-DA hydrogel to a thin glass surface, acrylate groups were attached to glass coverslips by silanization [133]. A solution of 3% v/v 3-

(trimethoxysilyl)propyl acrylate (TCI Chemicals) and 5% v/v glacial acetic acid (Fisher Scientific) was prepared in methanol. No. 1 coverslips (Ted Pella) were incubated in the reaction solution for 45 minutes and thoroughly washed with methanol. The newly silanized coverslips were rinsed with ethanol and dried. A thin, flat (~40 μm) layer of PEG-DA hydrogel was formed on the coverslips, followed by cell seeding, both as described above. Before imaging, cells were stained with CellMask Green (Thermo) for Katushka2S experiments and CellMask Deep Red (Thermo) for pHLuorin2 experiments for 5 min at 37ºC followed by washing. Coverslip-hydrogels with seeded cells were mounted with immersion oil (Cargille) of refractive index 1.518 for Katushka2S experiments or 1.514 for pHLuorin2 experiments. Samples were imaged with a DeltaVision OMX SR microscope (GE) with an Olympus 60X Apo N objective. Dual channel 512 × 512-pixel (41 × 41 μm) images were obtained using the TIRF imaging mode with TIRF angle set at 80-90 degrees. For each cell, 250 images were obtained over 25 sec with frequency 100 ms per image.

CD63-Katushka2S data analysis

Using the IMARIS ‘Surfaces’ function, a custom tracking algorithm was created. Intracellular bodies were determined using Gaussian smoothing and local background intensity thresholding (with automatically determined thresholds) to detect surfaces followed by tracking their position (x, y) over time (*t*). To account for noise within images, bodies were discarded if they were constituted by less than 12 pixels (0.0768 μm^2). Tracks could continue if the body was undetectable for a single timepoint within the track but not for two or more consecutive timepoints. MVB area was computed for each time *t* and reported as the mean area across total

track time *T*. Tracks were then analyzed via a custom MATLAB program. Track MSD was calculated as

$$MSD(t) = [x(t) - x(t=0)]^2 += [y(t) - y(t=0)]^2 . \quad \text{(Equation 2.3.4)}$$

Ensemble-averaged track data were generated by averaging the *MSD* for each track *i* at every time *t* elapsed since the start of tracking:

$$< MSD(t) > = \frac{1}{N}\sum_{i=1}^{N} MSD_i(t) \quad \text{(Equation 2.3.5)}$$

where *N* is number of tracks. For ensemble-averaged tracks, a lower limit of 15 points (1.5 sec) and an upper limit of 180 points (18 sec) were defined to constrain the tracks considered for analysis, as uneven track sizes can bias the results. Consequently, the ensemble-averaged data are shown only up to the lower limit (t = 1.5 sec). Tracks were sorted into 'Slow' or 'Fast' populations using a threshold $D_{0.4s}$ = 0.001 μm^2/sec.

CD63-pHLuorin2 data analysis

Flashing events were determined from image sequences using a custom MATLAB program. Potential event regions were determined by subtracting each image from a rolling average of the 5 previous images. The resulting image was converted to a binary image using a threshold of 40% of the mean image intensity. Regions identified after thresholding containing greater than 20 pixels (0.128 μm^2) were considered. The total intensity within each region at the time of the event was then compared to the total intensity in the same region before the event (i.e., 5 images previous). A ratio of these intensities was taken, and the event was counted if the ratio exceeded three.

Animal model of acute lung injury

All animal procedures were performed in compliance with NIH and institutional guidelines approved by the ethical committee from the University of Illinois at Chicago. Female C57BL/6J mice were purchased from The Jackson Laboratory and housed in the University of Illinois at Chicago Biologic Resources Laboratory. At age 10-12 weeks, mice were treated with 10mg/kg lipopolysaccharides (LPS, Sigma) via intraperitoneal injection to induce acute lung injury. After 4 hours, mice were anesthetized using ketamine/xylazine (50/5 mg/kg) and 3 x 10^8 exosomes were administered by single dose intratracheal instillation. One day after LPS administration, mice were evaluated for lung vascular permeability and edema as described previously [134]. Briefly, mice were anesthetized using ketamine/xylazine (50/5 mg/kg) and a solution of Evans blue albumin (20 mg/kg) was applied via retro-orbital intravenous injection. After 20 min, mice were sacrificed and lung tissue was harvested along with a fraction of circulating blood. Right lung tissue was weighed initially (wet weight) and after 24h incubation at 65C (dry weight) to calculate wet/dry ratio. Left lung tissue was homogenized and Evans blue extracted with formamide. Evans blue content was measured by absorbance at 620 nm and normalized to that present in circulating blood. For CD44 blocking experiments, exosomes were incubated with 1 ug/mL of CD44 antibody (BE0039, BioXCell) or IgG control antibody (BioXCell, BE0090) for 30 min at 4^{o}C prior to administration.

Statistical evaluation

Statistics were performed as described in figure captions. All statistical analyses were performed using GraphPad Prism version 9.0.0. Unless otherwise noted, statistical comparisons

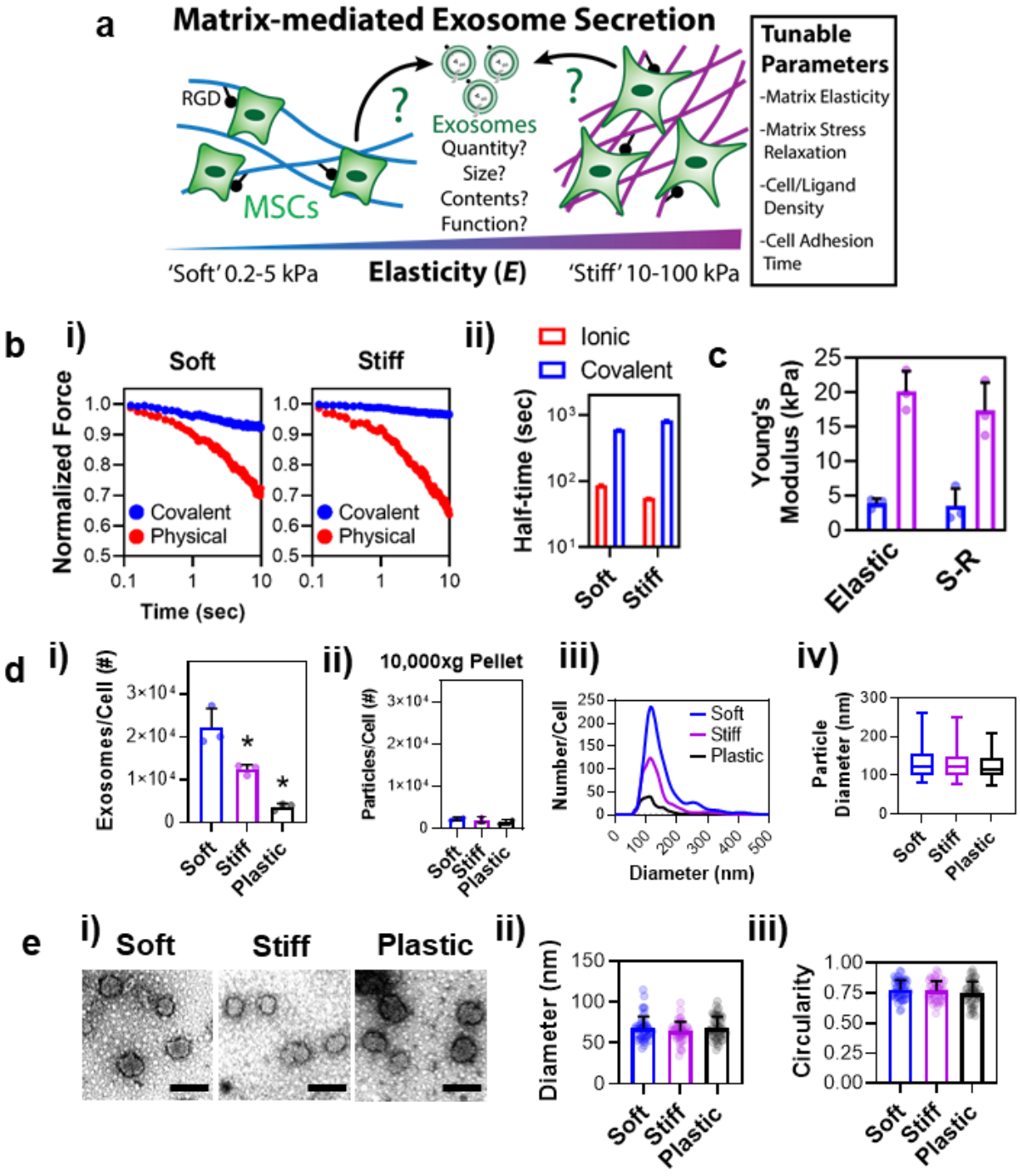
a
Matrix-mediated Exosome Secretion
RGD
MSCs
Exosomes
Quantity?
Size?
Contents?
Function?
'Soft' 0.2-5 kPa
Elasticity (E)
'Stiff' 10-100 kPa
Tunable Parameters
-Matrix Elasticity
-Matrix Stress Relaxation
-Cell/Ligand Density
-Cell Adhesion Time
b
i)
Soft
Stiff
Normalized Force
Covalent
Physical
Time (sec)
ii)
Ionic
Covalent
Half-time (sec)
Soft
Stiff
c
Young's Modulus (kPa)
Elastic
S-R
d
i)
Exosomes/Cell (#)
Soft
Stiff
Plastic
ii)
10,000xg Pellet
Particles/Cell (#)
iii)
Number/Cell
Soft
Stiff
Plastic
Diameter (nm)
iv)
Particle Diameter (nm)
e
i)
Soft
Stiff
Plastic
ii)
Diameter (nm)
iii)
Circularity

Figure 2.1. Substrate stiffness determines the amount of exosome secretion from MSCs. **(a)** Illustration of potential biophysical relationships and their impact on exosome secretion from MSCs. **(b)** (i) Stress relaxation properties of alginate hydrogels crosslinked ionically or covalently. Normal force is normalized to the initial normal force value for comparison. Data represent the mean of N = 3 hydrogels. (ii) Quantification of timescale at which stress is relaxed to half of the original value. Error bars denote 95% confidence interval (CI). **(c)** Young's modulus of alginate hydrogels. **(d)** (i) Primary human MSCs produce significantly more exosomes on softer elastic alginate hydrogels conjugated with 0.8 mM RGD. Data represent the mean of N = 3 experiments. *, $p = 0.0109$ (Soft *vs.* Stiff), $p = 0.0189$ (Stiff *vs.* Plastic) via one-way ANOVA with Tukey's post-test. (ii) Contents pelleted from samples after 10,000 g centrifugation show low particle numbers and no difference across substrates. N = 2 hydrogels per condition. (iii) Exosome size distributions by NTA. Data represent the mean of N = 3 particle samples per condition. (iv) Quantification of size distribution data in (ii). Line represents the median, box represents the 25^{th}-75^{th} percentile, and whiskers represent the 5^{th}-95^{th} percentile. **(e)** (i) Representative TEM images for secreted particles from human MSCs on substrates. Scale bar = 100nm. (ii) Quantification of particle diameter from TEM images. Data are per particle measured across N = 6 images per condition. (iii) Quantification of particle circularity for particles in (ii). For (b), (c), (d), data represent the mean of N = 3 experiments. For all, error bars indicate standard error of the mean (SEM).

were made from at least three independent experiments by one-way ANOVA followed by Tukey's multiple comparison test, and then were considered significant if $p < 0.05$.

2.4 RESULTS

To evaluate the effect of substrate mechanics on exosome secretion from MSCs (Fig. 2.1a), we engineered hydrogel substrates comprised of alginate polymer conjugated with the cell adhesion peptide Arg-Gly-Asp (RGD) that binds primarily to $\alpha_v\beta_3$ and $\alpha_5\beta_1$ integrins [135]. Alginate-RGD hydrogels can be formed either covalently through adipic acid dihydrazide or physically through divalent cations, resulting in elastic or stress-relaxing hydrogels, respectively [127] (Fig. 2.1b). For both types of hydrogels, we considered elastic modulus (Young's modulus, E) ~ 3 kPa 'soft' and E ~ 20 kPa 'stiff' (Fig. 2.1c). In contrast, E is ~GPa magnitude for conventional plastic substrates. We allowed primary human bone marrow MSCs to adhere to

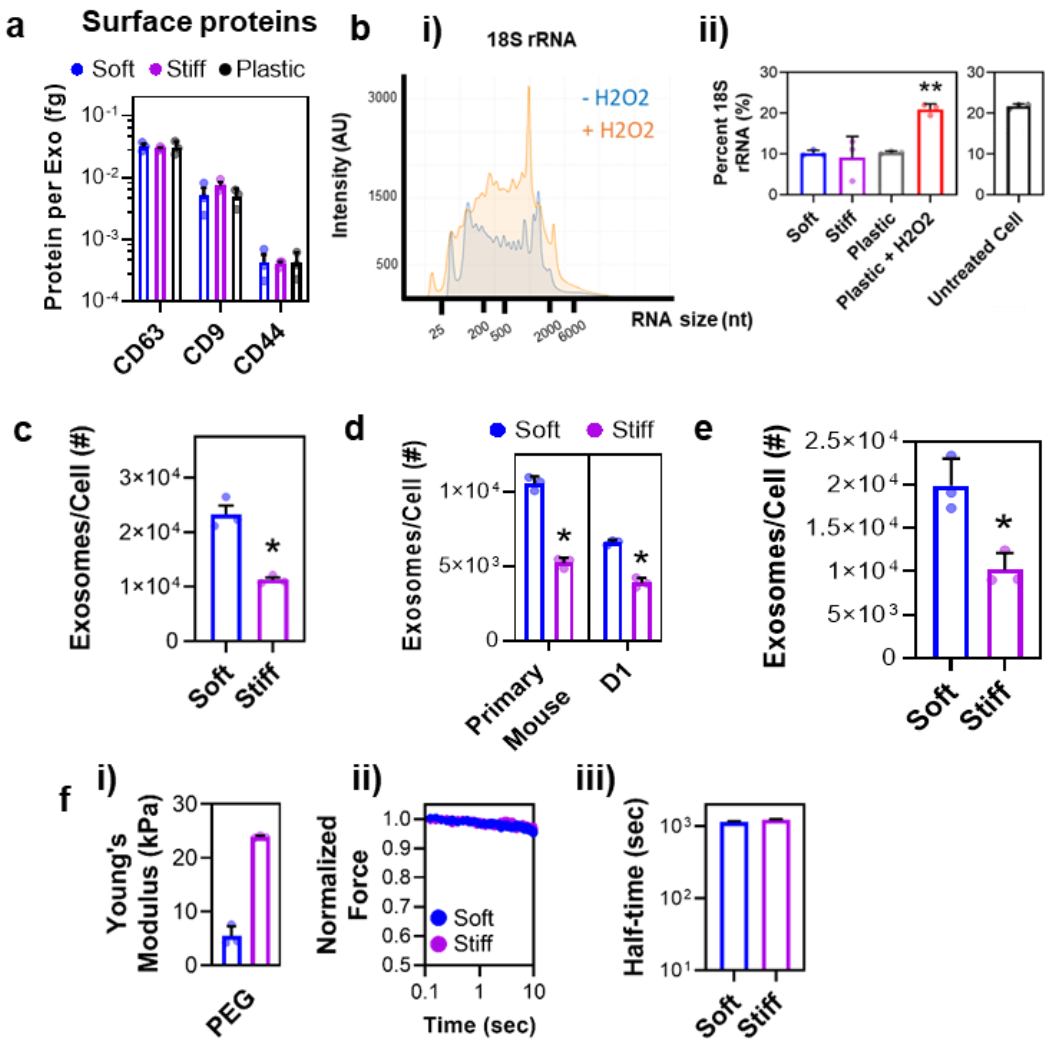

Figure 2.2. Characterization of hydrogel substrate stiffness-dependent exosome secretion. (a) Exosome marker protein content measured via ELISA. Data represent the mean of N = 3 experiments. **(b)** (i) Representative sample of RNA isolated from exosomes from primary human MSCs on plastic culture treated ± 1 mM H_2O_2 for 30 min to induce apoptosis. (ii) Particles from primary human MSCs treated with 1 mM H_2O_2 to induce apoptosis contain a significantly greater fraction of 18S ribosomal RNA (rRNA), similar to that of untreated cells. N = 3 RNA samples. **, $p = 0.0019$ via one-way ANOVA. **(c)** Exosome secretion from primary human MSCs on stress-relaxing alginate hydrogels is like elastic alginate hydrogels in Fig. 1B. *, $p = 0.0020$ via unpaired t-test. **(d)** Exosome secretion from primary mouse MSCs and D1 MSCs exhibit similar stiffness-dependent behavior as primary human MSCs. *, $p = 8.6 \times 10^{-5}$ (Mouse), $p = 2.0 \times 10^{-5}$ (D1) via unpaired t-test. **(e)** Exosome secretion from primary human MSCs on PEG-DA hydrogels is like on alginate hydrogels in Fig. 1B. **(f)** (i) Young's Modulus of PEG hydrogels are like alginate hydrogels in (b). (ii) Stress relaxation properties of PEG hydrogels as in (a). Data represent the mean of N = 3 hydrogels. *, $p = 0.01$ via unpaired t-test. (iii) Quantification of timescale at which stress is relaxed to half of the original value. Error bars denote 95% CI. For all, data represent the mean of N = 3 experiments. For all, error bars denote standard error of the mean (SEM).

substrates for 24 hours followed by washout and collection of the conditioned medium from MSCs after 24 hours. After centrifugation of the medium at 10,000 g to remove cell, apoptotic, and microvesicle fractions [130], particles in the medium were analyzed by nanoparticle tracking analysis. At lower cell density (~25 cells/mm^2) on elastic alginate hydrogels with 0.8 mM RGD, MSCs secreted significantly more particles on the soft hydrogel (~20,000 particles/cell) than on the stiff hydrogel (~10,000 particles/cell), while MSCs on a plastic substrate secreted 5-times less particles (~4,000 particles/cell) than MSCs on the soft hydrogel (Fig. 2.1d, i). Particles in the 10,000 g pellet showed no difference in number per cell, and in general were much lower per cell than the particles in the supernatant (Fig. 2.1d, ii). The particle size distribution remained similar across different substrates with median diameter ~120 nm, a size range typically associated with exosomes (Fig. 2.1d, ii and iii). Analysis of particle preparations by transmission electron microscopy (Fig. 2.1e, i) showed that particles exhibit mean diameter ~70 nm (Fig. 2.1e, ii) and circularity ~0.75 (Fig. 2.1e, iii) regardless of substrates, further confirming that particles are likely exosomes. Moreover, exosomes from different substrates expressed similar levels of CD63, CD9, and CD44 (Fig. 2.2a). Importantly, levels of ribosomal RNA in particle preparations were lower than that found in untreated MSCs or particles derived from H_2O_2-treated apoptotic MSCs (Fig. 2.2b), ruling out cell apoptosis as the cause of increased exosome secretion on the soft hydrogel. MSCs showed a similar level of exosome secretion on stress-relaxing alginate-RGD hydrogels as elastic hydrogels (Fig. 2.2c). The effect of substrate stiffness on exosome secretion was also observed for primary mouse bone marrow MSCs and clonally-derived D1 mouse MSCs [136] (Fig. 2.2d), as well as on RGD-bearing polyethylene glycol-diacrylate (PEG-DA) hydrogels (Fig. 2.2e) with similar mechanical properties to elastic alginate hydrogels (Fig. 2.2f). Thus, substrate stiffness is an important

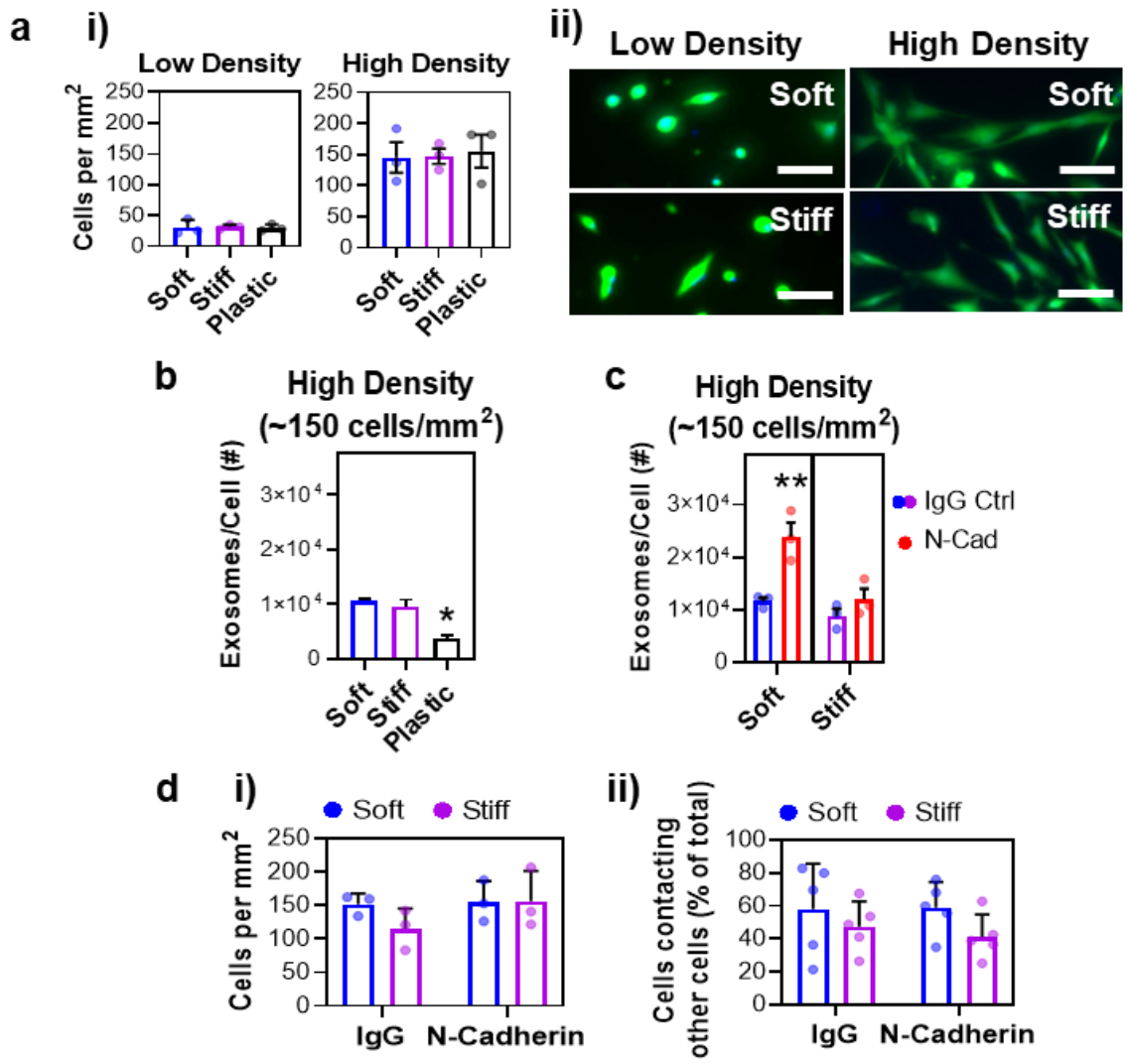

Figure 2.3. The effects of cell density and N-cadherin cell-cell interactions on exosome production. (a) (i) Primary human MSCs seeded at different densities to achieve relatively low- or high-density cultures. Data represent the mean of N = 3 experiments. (ii) Representative images for low- or high-density cultures stained with calcein AM. Scale bar is 100 μm. **(b)** Increased exosome secretion on softer elastic alginate hydrogel is suppressed in higher density culture. *, $p = 0.0021$ (Soft *vs.* Plastic), $p = 0.0049$ (Stiff *vs.* Plastic) via one-way ANOVA with Tukey's post-test. **(c)** Treating human MSCs with N-cadherin blocking antibody before adhesion restores increased exosome secretion on softer elastic hydrogels. **, $p = 0.012$ via unpaired t-test. **(d)** (i) Primary human MSC density for N-cadherin blocking experiments is like the high-density condition in (a). Data represent the mean of N = 3 experiments. (ii) Cells are counted from N = 5 images for each condition. For all, bars represent the mean and error bars denote SEM. For (a, i) and (d, i), primary human MSC number is evaluated by flow cytometry.

determinant of exosome secretion from MSCs without affecting vesicle size, morphology, or surface protein expression. While cell density can be increased to improve the yield of exosomes per substrate, it is possible that increased cell-cell interactions serve as a spatial or physical constraint to impede vesicular trafficking [137], potentially impacting exosome secretion. To test this idea, exosome secretion was measured after seeding human MSCs on elastic alginate-RGD hydrogels at higher cell density (~150 cells/mm^2) (Fig. 2.3a). Under this condition, MSCs on the soft hydrogel no longer secreted more exosomes per cell than MSCs on the stiff hydrogel, but exosome secretion per cell on both hydrogels was still higher than on plastic (Fig. 2.3b). We speculated that increased intercellular interaction masked the effect of substrate stiffness on exosome secretion. One way that mesenchymal cells are known to interact with each other is through N-cadherin homotypic interactions [138]. Thus, we incubated MSCs with an N-cadherin blocking antibody before seeding cells on hydrogels, and this restored exosome secretion per cell on the soft hydrogel to a level as if MSCs were seeded at lower density (Fig. 2.3c). The antibody did not impact the number of adhered cells or the fraction of MSCs that contact each other (Fig. 2.3d). Thus, N-cadherin limits the effect of soft hydrogels on exosome secretion in a higher cell density condition.

We next evaluated the role of integrin-mediated cell adhesions on exosome secretion for cells on hydrogel substrates. The binding of talin to the cytoplasmic domain of integrin β_3 activates integrin inside-out signaling, while ligand binding induces outside-in signaling via focal adhesion kinase (FAK) [139] (Fig. 2.4a). To test roles of talin and FAK in exosome secretion, we treated human MSCs on elastic alginate-RGD hydrogels with siRNA against talin or FAK over 3 days followed by evaluation of exosome secretion. The knockdown efficiency of talin and FAK

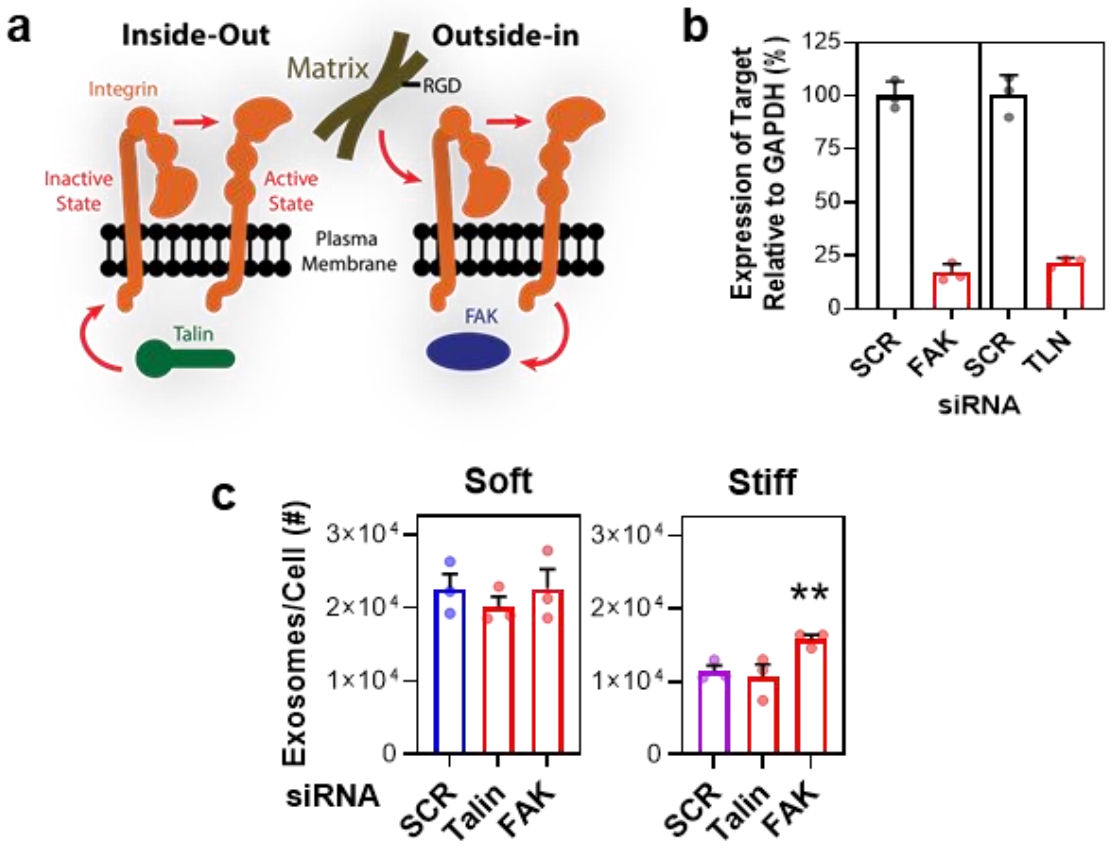

Figure 2.4. The outside-in integrin signaling mediator FAK regulates exosome production on stiff hydrogels. (a) Illustration of known interactions for integrin inside-out versus outside-in signaling. **(b)** Confirmation of FAK and TLN1 knockdown in primary human MSCs by siRNA. SCR = scrambled siRNA control. N = 3 qPCR reactions per condition. Error bars denote SD. **(c)** Treatment of primary human MSCs on substrates with 4 nM siRNA against talin and FAK. **, $p = 0.044$ (SCR *vs.* FAK) via one-way ANOVA followed by Tukey's post-test. Bars represent the mean of N = 3 experiments and error bars denote SEM.

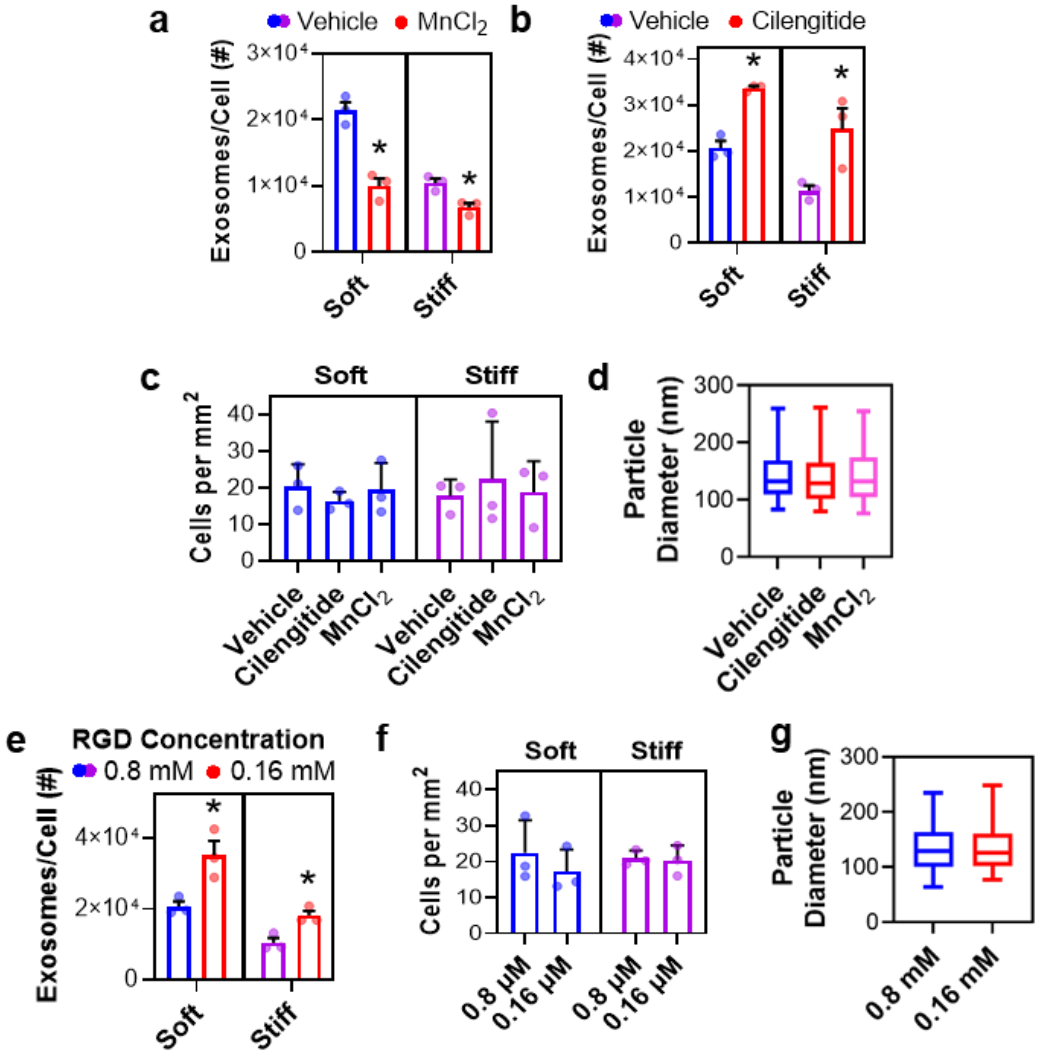

Figure 2.5. Cell adhesion to substrates through integrin-RGD interaction regulates exosome secretion. (a) Treatment of human MSCs with 3 μM $MnCl_2$ during and after adhesion to hydrogels inhibits exosome secretion. *, $p = 0.012$ (Soft), p = 0.015 (Stiff) via unpaired t-test. **(b)** Treatment of human MSCs with 200 nM cilengitide during and after adhesion to hydrogels inhibits exosome secretion. ***,** $p = 0.0010$ (Soft**),** p = 0.043 (Stiff) via unpaired t-test. **(c)** Live cell number is not different after treatments in (a) and (b). **(d)** Comparison of particle size from primary human MSCs on soft alginate hydrogels after treatments as in (a) and (b). **(e)** Decreasing the amount of RGD conjugated in hydrogels significantly increase exosome secretion. ***,** $p = 0.026$ (Soft), $p = 0.015$ (Stiff) via unpaired t-test. **(f)** Live cell number is not different with different RGD concentrations on alginate hydrogels in Fig. 2E. **(g)** Comparison of particle size from primary human MSCs on soft alginate hydrogels with different RGD concentration in Fig. 2E. For (d) and (g), data represent the mean of N = 3 particle samples per condition. Line represents the median, box represents the 25^{th}-75^{th} percentile, and whiskers represent the 5^{th}-95^{th} percentile. Unless stated otherwise, bars represent the mean of N = 3 experiments and error bars represent SEM.

was ~80% (Fig. 2.4b). While knockdown of talin expression had no effect, knockdown of FAK significantly increased exosome secretion per cell on the stiff hydrogel (Fig. 2.4c). These results support the notion that integrin ligand-mediated focal adhesions limit exosome secretion, which is enhanced on soft hydrogels (Fig. 2.4d) where focal adhesions are less developed [45].

We sought to understand whether changes in integrin-ligand interactions on substrates are sufficient to influence exosome secretion. When human MSCs were plated on elastic alginate-RGD hydrogels in the presence of 3 μM Mn^{2+}, a treatment known to increase integrin-ligand affinity [140], exosome secretion was decreased to a greater extent on the soft hydrogel than the stiff hydrogel (Fig. 2.5a). In contrast, treatment of MSCs with cilengitide, which interfere with integrin binding to RGD [141], significantly increased exosome secretion on both soft and stiff hydrogels (Fig. 2.5b). Neither treatment significantly affected the number of cells seeded on hydrogels (Fig. 2.5c) or particle size (Fig. 2.5d). Consistent with these results, decreasing RGD concentration from 0.8 to 0.16 mM increased exosome secretion per cell by ~2-fold on both soft and stiff hydrogels while also maintaining the number of adhered cells per substrate (Fig. 2.5e) and particle size (Fig. 2.5f, Fig. 2.5g). Thus, minimizing integrin-ligand interactions while maintaining cell adhesion promotes exosome secretion.

Since cell attachment, spreading, and adhesion are dynamic processes that occur when cells contact substrates [142], we tested the effect of cell adhesion time on exosome secretion by allowing human MSCs to adhere to elastic alginate hydrogels with 0.8 mM RGD for 4 hours *vs.* 24 hours, followed by washout and measurement of exosome secretion per cell at different time points. MSCs adhered for 4 hours showed less spreading area than when adhered for 24 hours

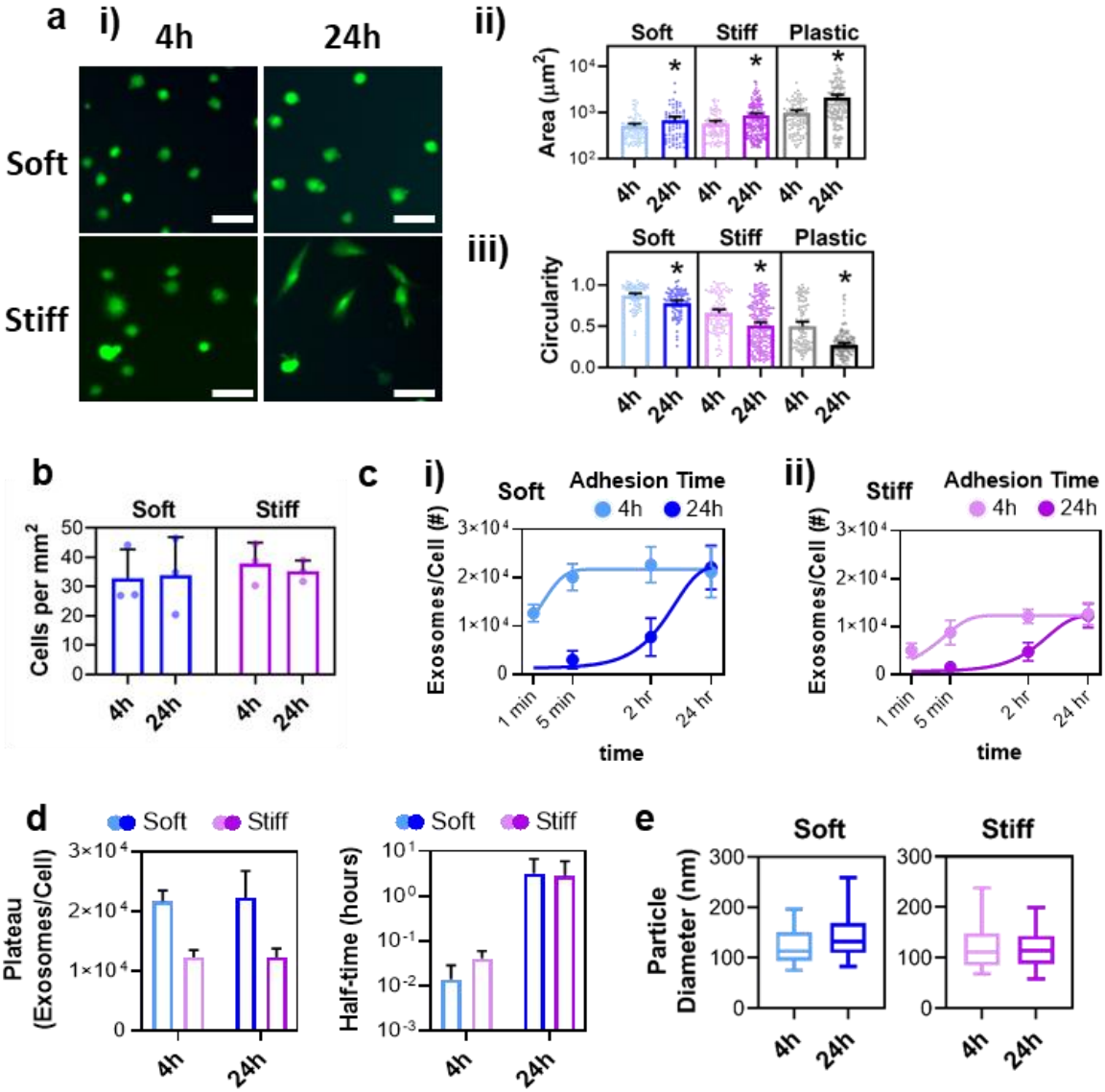
a
i)
4h
24h
Soft
Stiff
ii)
Soft
Stiff
Plastic
Area (μm²)
iii)
Circularity
b
Cells per mm²
c
i)
Soft
Adhesion Time
4h
24h
Exosomes/Cell (#)
time
1 min
5 min
2 hr
24 hr
ii)
Stiff
d
Plateau (Exosomes/Cell)
Half-time (hours)
e
Particle Diameter (nm)

Figure 2.6. Cell adhesion time to substrates regulates exosome secretion. (a) (i) Representative images of primary human MSCs seeded on alginate hydrogels after 4 or 24 hours stained with calcein AM. Scale bar is 100 μm. Quantification of cell area (ii) and circularity (iii) as a function of hydrogel stiffness and cell adhesion time. Data represent cells across N = 5 images for each condition. Soft 4h, N = 98 cells; 24h, N = 85 cells. Stiff 4h, N = 104 cells; 24h, N = 205 cells. Plastic 4h, N = 104 cells; 24h, N = 163 cells. For (i): *, $p = 0.02$ (Soft), $p = 6.1 \times 10^{-4}$ (Stiff), $p = 7.7 \times 10^{-8}$ (Plastic). For (ii), *, $p = 4.2 \times 10^{-5}$ (Soft), $p = 2.0 \times 10^{-6}$ (Stiff), $p = 1.0 \times 10^{-15}$ (Plastic) via unpaired t-test. **(b)** Live cell number is not different with different cell adhesion time on alginate hydrogels in Fig. 2F. **(c)** Exosome secretion kinetics of human MSCs on soft (Left) and stiff (Right) hydrogels as a function of cell adhesion time. **(d)** One-phase association fit values for plateau and half-time to plateau for data presented in Fig. 2F. Error bars denote 95% CI. **(e)** Comparison of particle size for primary human MSCs with different adhesion time on alginate hydrogels in Fig. 2F. Data are from 2 hours after the start of exosome collection. Line represents the median, box represents the 25^{th}-75^{th} percentile, and whiskers represent the 5^{th}-95^{th} percentile. Unless stated otherwise, bars represent the mean of N = 3 experiments and error bars represent SEM.

regardless of substrates (Fig. 2.6a). The number of adhered MSCs per substrate was similar between 4 and 24-hour adhesion conditions (Fig. 2.6b). Interestingly, exosome secretion reached the steady-state level ~10-times more rapidly when MSCs adhered to substrates for 4 hours than 24 hours regardless of substrate stiffness (Fig. 2.6c, Fig. 2.6d) without a significant effect on particle size (Fig. 2.6e). In contrast, substrate stiffness determined the steady-state level of secreted exosomes per cell regardless of how long cells adhered to substrates (Fig. 2.6c). The data suggest distinct roles of cell adhesion time and substrate stiffness in exosome secretion.

Our results collectively show that the combination of a soft (E ~ 3 kPa) hydrogel substrate (Fig. 2.1d) and a lower (0.16 mM) RGD concentration (Fig. 2.5e) results in a total ~10-fold increase in exosome secretion per cell than plastic culture. Thus, we next evaluated the potential impact of substrate on exosome content and functionality. MSC-derived exosomes are known to attenuate acute lung injury [18, 143]. Thus, we delivered a matched dose of exosomes (3×10^8 per 20g mouse) from primary mouse MSCs cultured on soft or stiff PEG-DA hydrogels

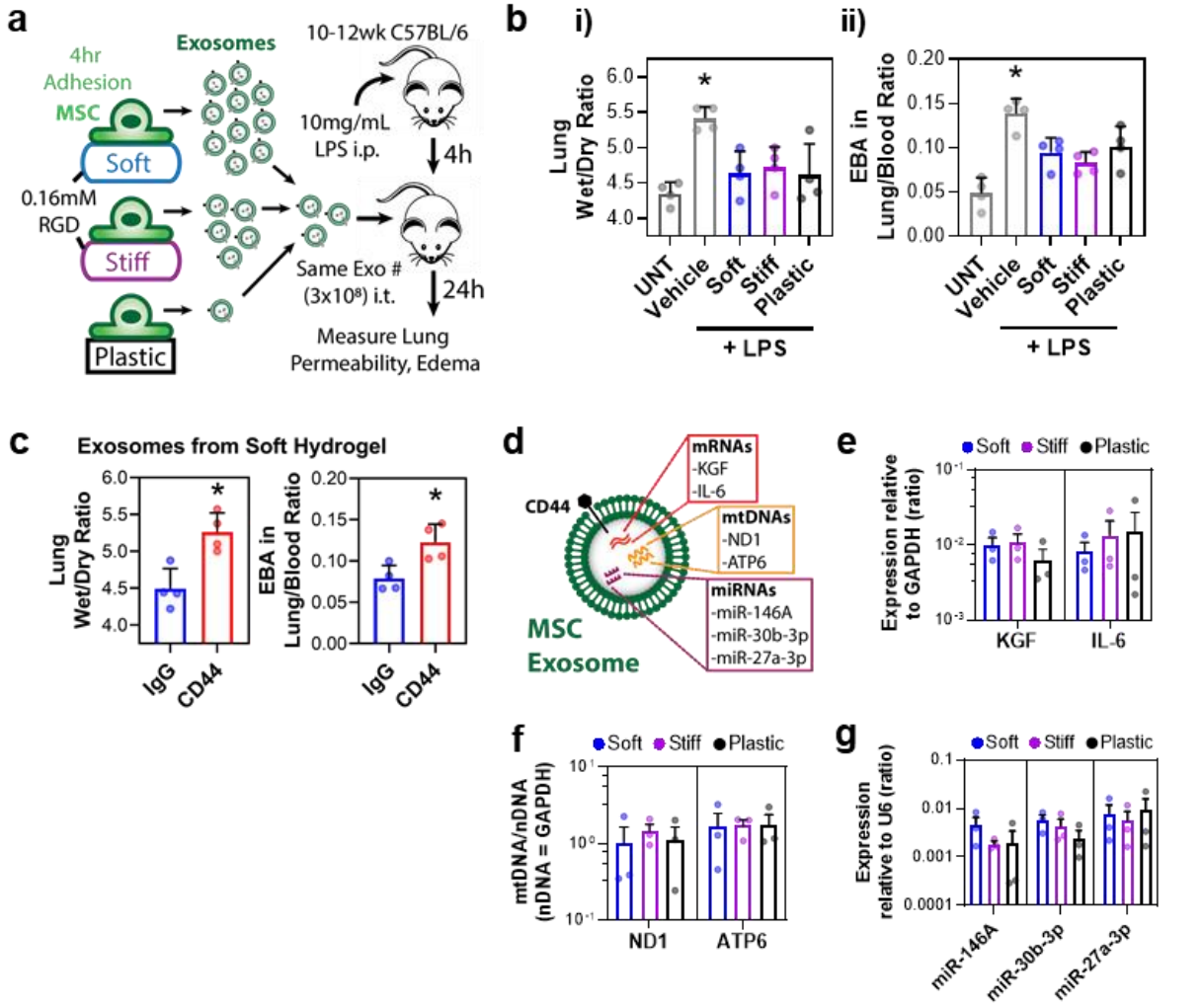

Figure 2.7. Substrate stiffness does not compromise the efficacy or cargo contents of MSC-derived exosomes to resolve tissue injury. (a) Overview of strategy to determine exosome therapeutic efficacy in a preclinical model of acute lung injury. Exosomes were collected after plating primary mouse MSCs on indicated substrates for 4 hours followed by 24 hours in culture. Exosomes (3 x 10^8 per 20g mouse) from each group were administered intratracheally (*i.t.*) 4 hours after intraperitoneal (*i.p.*) injection of lipopolysaccharides (LPS). **(b)** Measurements of (i) lung edema by quantifying lung wet-dry ratio and (ii) lung vascular permeability by quantifying Evans blue albumin (EBA) accumulation. *, $p = 0.0030$ (i), $p = 0.0008$ (ii) via Welch's one-way ANOVA. **(c)** CD44 blocking antibody reverses efficacy of exosomes from soft hydrogels. (Left) Lung edema measurements. (Right) Lung vascular permeability measurements. *, $p = 0.0066$ (Left), p = 0.017 (Right) via unpaired t-test. **(d)** Overview of cargo contents within exosomes known to affect therapeutic outcomes. **(e)** Expression of mRNAs in exosomes known to affect lung injury outcomes, measured by qPCR. **(f)** Presence of mtDNA (normalized to nDNA) in exosomes, measured by qPCR. **(g)** Presence of miRNAs (normalized to U6 RNA) in exosomes known to affect lung injury outcomes, measured by qPCR. For (b) and (c), N = 4 mice per condition and error bars denote SD. For (e-g), data represent the mean of N = 3 experiments each with N = 3 qPCR reactions per condition and error bars denote SEM.

with 0.16 mM RGD, or plastic culture intratracheally (*i.t.*) 4 hours after inducing lung injury in mice using lipopolysaccharides (LPS) (Fig. 2.7a). After 24 hours, a significant reduction in lung edema (Fig. 2.7b, i) and vascular permeability as shown by albumin accumulation in lung parenchyma (Fig. 2.7b, ii) was observed for mice treated with exosomes from all tested substrates. Blocking CD44 via antibody on exosomes secreted from MSCs on the soft hydrogel negated their therapeutic activity in terms of lung edema and permeability (Fig. 2.7c), as has been reported for exosomes from plastic substrates [119]. We also profiled exosome cargo composition from primary mouse MSCs in terms of different molecules known to ameliorate acute lung injury (Fig. 2.7d). Exosomes from different substrates showed a similar level of keratinocyte growth factor (KGF) [144] and interleukin-6 (IL-6) [145, 146] RNAs (Fig. 2.7e), mitochondrial DNAs [147] (Fig. 2.7f), and miRNAs [148-150] (Fig. 2.7g). Thus, soft hydrogels enhance exosome secretion without compromising functionality or cargo contents to resolve injury.

To understand how cell-substrate interactions mediate biological events that result in exosome secretion from MSCs, we tested the effect of substrate stiffness and cell adhesion time on intracellular trafficking of $CD63^+$ MVBs. To visualize $CD63^+$ MVBs within cells, we fused the red fluorescent protein Katushka2S (K2S) to CD63 and transduced CD63-K2S into D1 mouse MSCs as described [132]. We imaged CD63-$K2S^+$ MSCs on soft or stiff PEG-DA hydrogels with 0.8 mM RGD using total internal reflection fluorescence (TIRF) microscopy in order to quantify intracellular transport [151] (Fig. 2.8a). CD63-$K2S^+$ MVBs were tracked by calculating

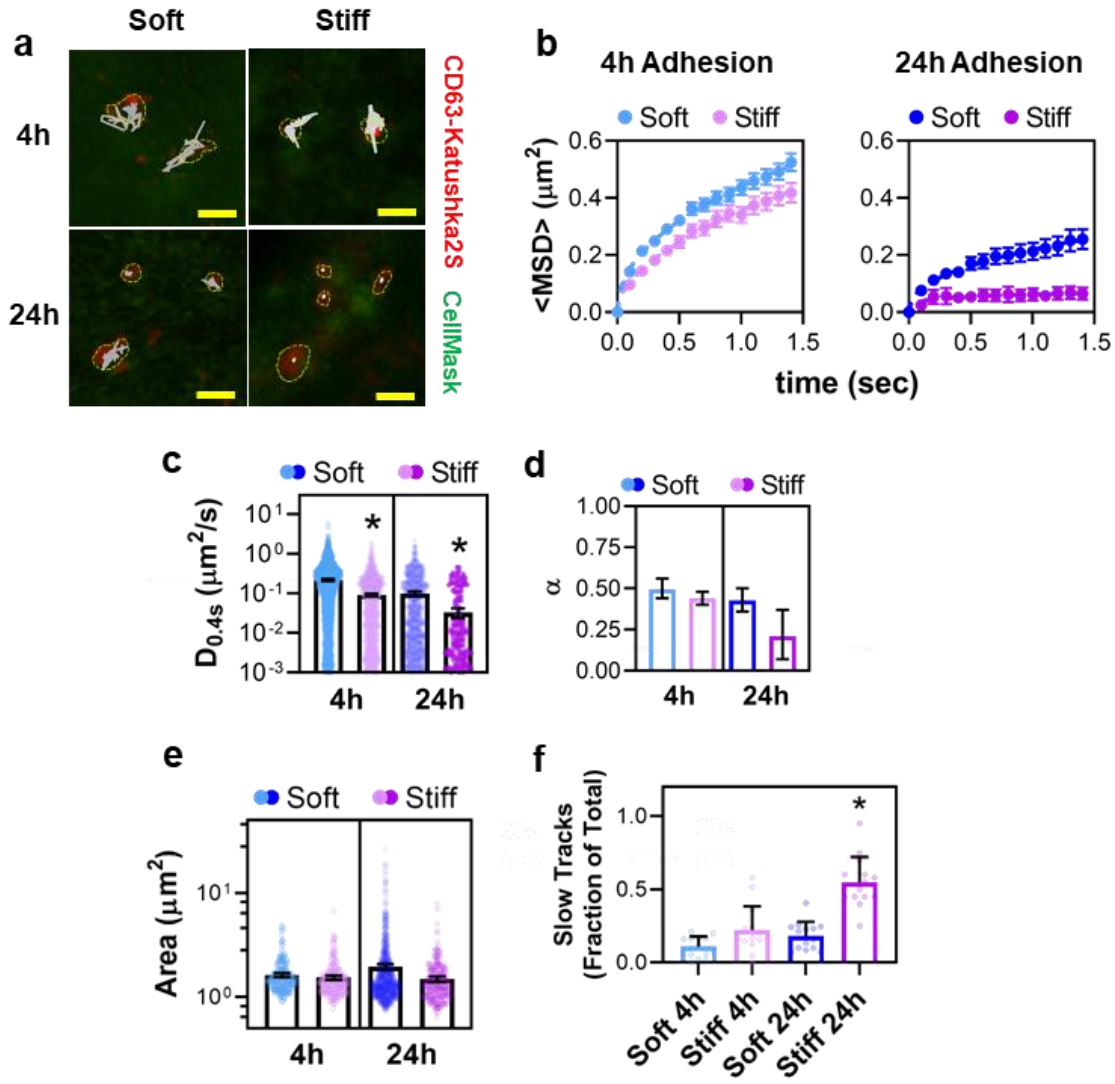

Figure 2.8. Softer hydrogel substrates and less adhesion time facilitate intracellular MVB trafficking. (a) Representative TIRF images of CD63-K2S^{+} MVBs in D1 mouse MSCs and their full 2D MSD tracks under tested conditions. Yellow circles indicate tracked CD63-K2S^{+} MVB regions. Scale bar = 0.5 μm. **(b)** Ensemble <*MSD*> vs time plots. Data are fit to Equation 1. **(c)** Values of $D_{0.4s}$ for tracks. *, $p < 1 \times 10^{-15}$ (Soft), $p = 1.4 \times 10^{-7}$ (Stiff) via unpaired t-test. **(d)** Values of exponent α for curves in (B). For all, track N are: Soft (4h), 3500 tracks; Soft (24h), 989 tracks; Stiff (4h), 2478 tracks; Stiff (24h), 282 tracks. Tracks for all conditions were obtained from N = 12 cells each. For all, error bars denote 95% confidence interval (CI). **(e)** Area of tracked CD63-K2S^{+} MVBs in D1 MSCs. Track *N* are: Soft (4h), 3500 tracks; Soft (24h), 989 tracks; Stiff (4h), 2478 tracks; Stiff (24), 282 tracks. Error bars denote 95% CI. **(f)** Fraction of 'slow' CD63-K2S^{+} MVB tracks with threshold $D_{0.4s}$ = 0.001 μm^2/sec. Data represent fractions for each cell. Error bars denote SD. *, $p = 1.7 \times 10^{-11}$ via one-way ANOVA followed by Tukey's post-test.

their ensemble-averaged mean squared displacement (*MSD*) over time (*t*). Data were collected every $\Delta t = 0.1$ sec and fit to the transport equation:

$$< MSD > = K_\alpha t^\alpha \,, \qquad \text{(Equation 2.4.1)}$$

with K_α as the transport coefficient and α as the transport exponent [152]. The transport exponent α is ~ 1 for Brownian motion when particle transport is unimpeded, and < 1 for sub-diffusive, or impeded, transport. We also calculated the two-dimensional effective diffusion coefficient D_τ of tracks:

$$D_\tau = MSD(\tau)/4\tau \,. \qquad \text{(Equation 2.4.2)}$$

Track D_τ were calculated over each time interval $\tau = 4\Delta t = 0.4$ sec as:

$$D_{0.4s} = MSD(\tau = 0.4s)/4(0.4s)\,. \qquad \text{(Equation 2.4.3)}$$

CD63-K2S$^+$ MVBs in MSCs transported more rapidly when MSCs adhere for 4 hours on the soft hydrogel than the stiff hydrogel as indicated by <*MSD*> vs *t* plots (Fig. 2.8b) and diffusion coefficient $D_{0.4s}$ (Fig. 2.8c). CD63-K2S$^+$ MVBs transport slowed further after 24 hours of cell adhesion, but MVBs still transported faster on the soft hydrogel. The transport exponent α across all the conditions was less than 1 (Fig. 2.8d), suggesting that MVB transport is passive and impeded by cytoplasmic contents—exponent α showed a decrease on the stiff hydrogel after 24-hour cell adhesion. Tracked MVB size was not significantly different across tested conditions (Fig. 2.8e). Sorting tracks into ‘slow’ or ‘fast’ subgroups reveals that more tracks are considered ‘slow’ for cells on the stiff hydrogel 24-hour adhesion condition (Fig. 2.8f). Thus, soft substrates and short adhesion times facilitate intracellular MVB transport.

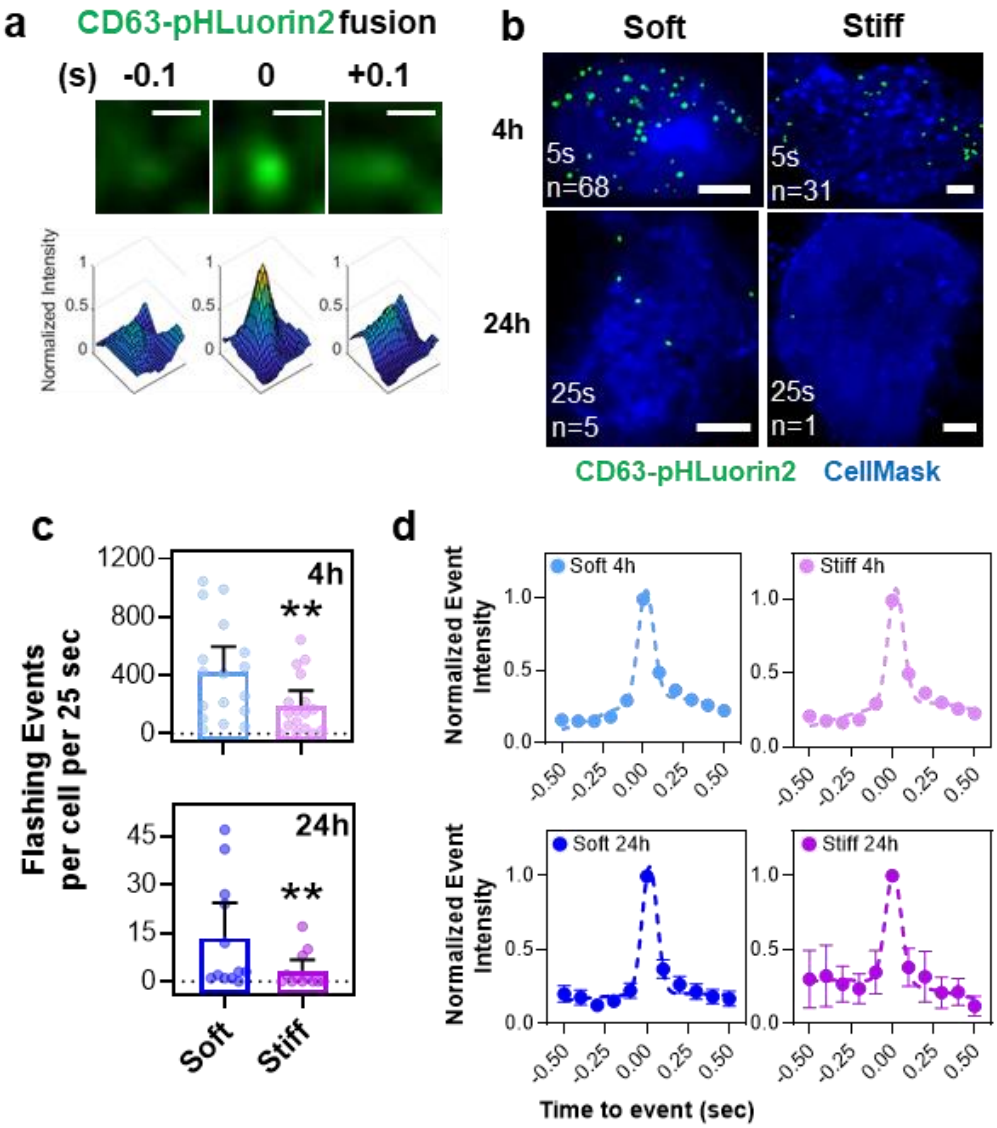

Figure 2.9. Softer hydrogel substrates and less adhesion time facilitate MVB fusion. (a) (Top) Representative image of event within a cell adhered for 24 hours on the soft hydrogel. Scale bar = 0.5 µm**.** (Bottom) Plot of normalized fluorescence intensity for above images; x-y axes represent image pixels. **(b)** Representative TIRF images of CD63-pHLuorin2^{+} D1 mouse MSCs for tested conditions. Cumulative events (*n*) up until the indicated time (sec) are projected on the image. Scale bars = 5 µm. **(c)** Number of MVB fusion events per cell is significantly increased for MSCs on soft *vs.* stiff hydrogels adhered for 4 hours (Top, N = 17 cells per condition) and 24 hours (Bottom, N = 12 cells per condition). **, $p = 0.0270$ (Top), $p = 0.026$ (Bottom) via unpaired Mann-Whitney test. **(d)** Intensity of CD63-pHLuorin2 flashing events normalized to peak intensity for all detected events in D1 MSCs on substrates for 4h and 24h adhesion. Event *N* are: Soft (4h), 7161 events; Soft (24h), 162 events; Stiff (4h), 3277 events; Stiff (24h), 40 events. Data are fit to a sum of two Gaussian curves. Error bars denote 95% CI.

We next evaluated the impact of cell-substrate interactions on the fusion of MVBs with the plasma membrane, an event that results in exosome secretion [5]. To accomplish this, we fused the pH-sensitive reporter pHLuorin2 to CD63 as described [107]. This reporter will turn on GFP fluorescence when pH changes from low (acidic) to high (neutral) as occurs when acidic $CD63^+$ MVBs carrying exosomes fuse with the plasma membrane and release exosomes into the pH-neutral extracellular space. After transducing CD63-pHLuorin2 into D1 mouse MSCs, we imaged MSCs seeded on soft or stiff PEG-DA hydrogels with 0.8 mM RGD over time using the same TIRF microscopy method every $\Delta t = 0.1$ sec with total time $T = 25$ sec. Flashing events were determined using a custom program (see Materials and Methods). The intensity for counted events exhibited a sharp increase followed by a rapid decrease (Fig. 2.9a). MSCs on the stiff hydrogel produced significantly less events than MSCs on the soft hydrogel independent of adhesion time (Fig. 2.9b-c)—however, MSCs adhered for 4 hours showed a dramatically increased number of flashing events than MSCs adhered for 24 hours. Substrate stiffness or cell adhesion time does not impact the kinetics of flashing events (Fig. 2.9d). Thus, soft hydrogels and short adhesion times enhance the frequency of MVB fusion with the plasma membrane, correlating with increased intracellular transport of MVBs.

Finally, we sought to understand mechanisms behind how biophysical regulation of cell-substate interactions impacts exosome secretion. Because myosin-II activity is known to mediate mechanosensing, we tested whether its inhibition would rescue exosome secretion from MSCs on stiff substrates. Surprisingly, 50 μM blebbistatin, an inhibitor of myosin-II ATPase, did not impact exosome secretion from human MSCs on either soft or stiff elastic alginate-RGD

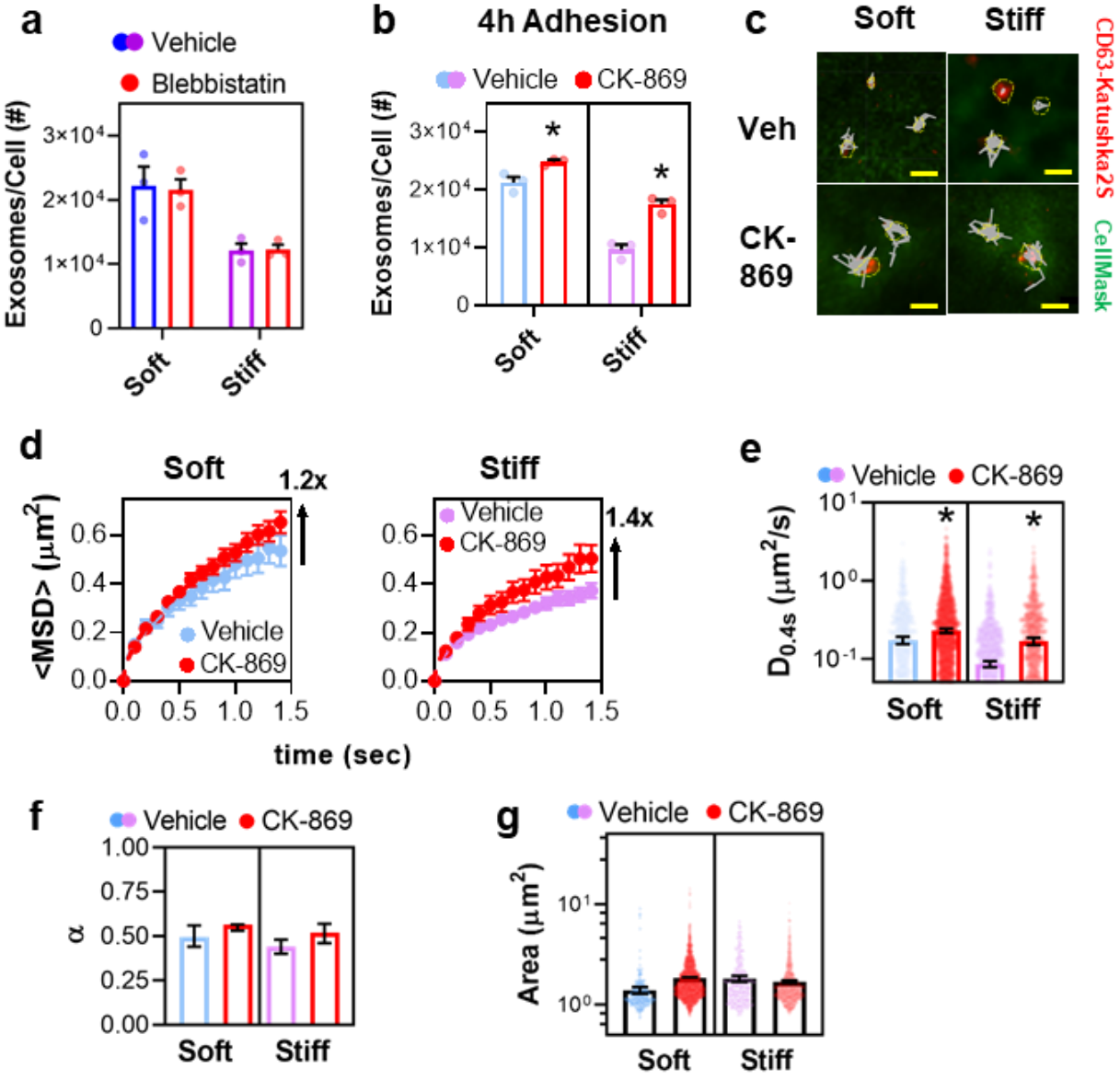
a
Vehicle
Blebbistatin
Exosomes/Cell (#)
3×10⁴
2×10⁴
1×10⁴
0
Soft
Stiff
b
4h Adhesion
Vehicle
CK-869
Exosomes/Cell (#)
3×10⁴
2×10⁴
1×10⁴
0
*
*
Soft
Stiff
c
Soft
Stiff
Veh
CK-869
CD63-Katushka2S
CellMask
d
Soft
1.2x
Stiff
1.4x
<MSD> (μm²)
0.6
0.4
0.2
0.0
Vehicle
CK-869
0.0 0.5 1.0 1.5
time (sec)
e
Vehicle
CK-869
D0.4s (μm²/s)
10¹
10⁰
10⁻¹
*
*
Soft
Stiff
f
Vehicle
CK-869
α
1.00
0.75
0.50
0.25
0.00
Soft
Stiff
g
Vehicle
CK-869
Area (μm²)
10¹
10⁰
Soft
Stiff

Figure 2.10. Arp2/3 limits exosome secretion from MSCs on hydrogels by inhibiting MVB transport. (a) Myosin-II inhibition does not impact exosome secretion from primary human MSCs. MSCs were seeded for 24 hours on soft or stiff elastic alginate-RGD hydrogels, followed by washout and treatment with vehicle (DMSO) or 50 μM blebbistatin for 24 hours, and nanoparticle tracking analysis to count secreted exosomes per cell. **(b)** Primary human MSCs treated with 5 μM CK-869 (Arp2/3 inhibitor) exhibit significantly increased exosome secretion. N = 3 experiments. *, $p = 0.024$ (Soft), $p = 0.0027$ (Stiff) via unpaired t-test. **(c)** Representative TIRF images of CD63-K2S$^+$ MVBs in D1 mouse MSCs and their full 2D MSD tracks. Yellow circles indicate tracked CD63-K2S$^+$ MVB regions. Scale bar = 0.5 μm. **(d)** Ensemble $<MSD>$ vs time plots. Data were fit to Equation 1. **(e)** Values of $D_{0.4s}$ for tracks. *, p = 6.2 x 10^{-5} (Soft), $p < 10^{-15}$ (Stiff) via unpaired t-test. **(f)** Values of exponent α for curves in (C). **(g)** Area of tracked CD63-K2S+ MVBs in D1 MSCs. For (d-g), track *N* are: Soft (Veh), 960 tracks; Soft (CK-869), 2921 tracks; Stiff (Veh), 1991 tracks; Stiff (CK-869), 1182 tracks. Unless stated otherwise, bars represent the mean of N = 3 experiments and error bars denote SEM.

hydrogels (Fig. 2.10a). Thus, substrate stiffness-mediated changes in exosome secretion do not require myosin-II contractility. The average mesh size of intracellular cytoskeleton networks in mesenchymal cell types is typically ~50 nm [153] on plastic culture, and hence likely impedes the transport of MVBs (Fig. 2.8a-d) that contain multiple exosomes. Since cells on softer substrates show more fluid-like, less dense actin cytoskeletons [154], which can be regulated independently of myosin-II [61], we investigated the role of actin networks in exosome secretion from MSCs on substrates. FAK is known to promote actin assembly by interacting with the actin related protein 2/3 (Arp2/3) complex [155], and inhibition of FAK rescues exosome secretion on the stiff hydrogel (Fig. 2.4c). Consistently, treatment of human MSCs with 5 μM CK-869, an Arp2/3 inhibitor, after 4 hours of cell adhesion increased exosome secretion on the stiff hydrogel, and the effect was also observed on the soft hydrogel to a lesser but significant extent (Fig. 2.10b). Arp2/3 inhibition did not change the size of tracked CD63-K2S$^+$ MVBs in MSCs on substrates (Fig. 2.10v). However, Arp2/3 inhibition significantly enhanced transport on either substrate as indicated by representative tracks (Fig. 2.10d), $<MSD>$ vs t plots (Fig. 2.5e), and

$D_{0.4s}$ (Fig. 2.10f), while transport exponent α remained unchanged at ~0.5 (Fig. 2.10g). Thus, Arp2/3 limits MVB transport and exosome secretion on hydrogels.

2.5 DISCUSSION

Extracellular vesicles, nano-sized particles composed of a lipid bilayer, are a critical medium of intercellular communication. Exosomes, a subset of extracellular vesicles, are produced by inward budding within late endosomes, forming MVBs which then fuse with the plasma membrane and thereby release exosomes into the extracellular space. MSCs employ exosomes to communicate with a diverse range of effector cells [156, 157], and the bone marrow environment in which MSCs are derived exhibits a diverse range of biophysical properties [125]. These properties affect cell phenotypes, including membrane dynamics and cytoskeletal organization, processes which are likely involved in exosome production and release. The results presented here establish a fundamental relationship between functional exosome secretion and cell-matrix interactions in the microenvironment. As cells adhere to substrates, integrins become increasingly activated, leading to cell spreading and a decrease in exosome production. Cells on softer substrates spread less and produce more exosomes than cells on stiffer or conventional plastic substrates. Despite the difference in number of exosomes released, exosomes remain similar in terms of their size, morphology, and presence of membrane markers CD63, CD9, and CD44. Mechanistically, we show that the decreased outside-in integrin activation on soft substrates promotes exosome secretion by enhancing intracellular MVB transport and fusion to the plasma membrane, while FAK and Arp2/3 inhibit exosome secretion (Fig. 2.11). Although exosome secretion is increased by cells adhered for a shorter time on a softer hydrogel substrate, exosomes retain similar cargo contents and efficacy in a mouse model of acute lung injury.

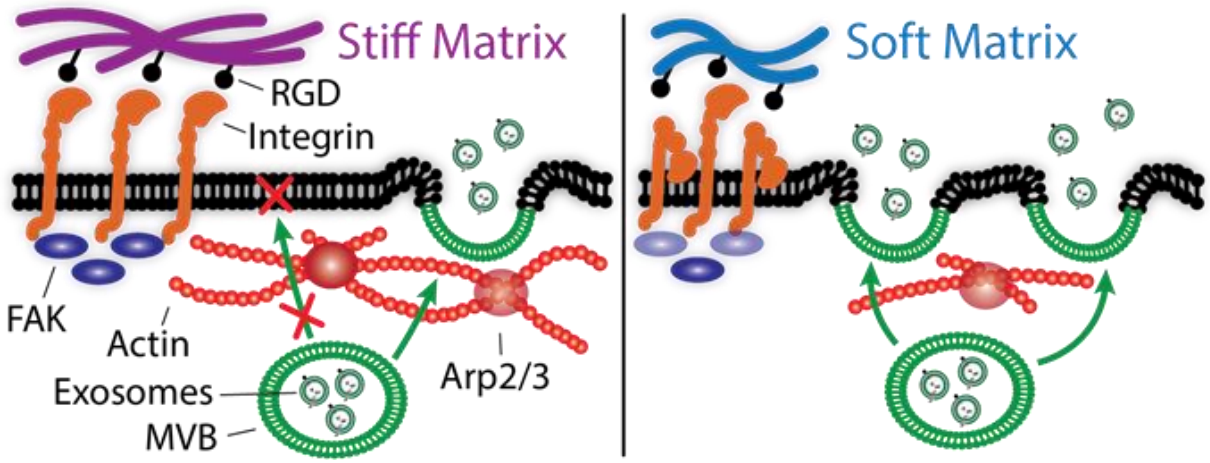

Figure 2.11. A model for biophysical regulation of exosome production. Rigid substrates increase outside-in integrin activation, focal adhesions, and Arp2/3-mediated actin network formation, resulting in less ability for exosome-containing MVBs to transport and fuse with the plasma membrane to release exosomes.

MSCs exist in a diverse biophysical environment within the bone marrow. Cells localized within various environments likely exhibit distinct functions that are constrained precisely by the biophysical properties of each environment. Since EVs are produced to communicate with other cells over longer ranges, it seems logical that cells in a perivascular environment characterized by a softer matrix will be more likely to secrete more EVs. In this environment, EVs are probably more likely to end up in the vasculature where they can be transported to effector cells such as hematopoietic cells, which are more often present in this environment. A recent paper expanded upon the known heterogeneity of EVs [158], including the delineation of other EV types (nanovesicles [NVs] and small EVs [sEVs]). Indeed, particles derived from cells on different substrates in this study appear similar in terms of size, morphology, and measured contents – resembling NVs and sEVs. Along these lines, results presented here support a mechanism by which substrate elasticity would determine the number of secreted exosomes and not necessarily their contents, size, or morphology, so that exosome communications could be tunable per environment. Future studies should elaborate precisely whether the particles resemble NVs or sEVs and whether more detailed properties such as lipid composition are affected by substrate stiffness.

Cells consist of a dense cytoplasm that is considered a viscous semi-solid. Other studies have characterized the typical transport properties of particles within the cytoplasm [159]. As the actin mesh becomes denser, particle transport is hindered, resulting in particle sub-diffusion. Cells on stiffer substrates are known to spread more and thus possess a denser actin mesh due to increased cytoskeletal activity. Thus, $CD63^{+}$ MVBs are likely constrained by this denser mesh within cells spreading on stiffer substrates. If MVBs are unable to transport freely, it follows that

they are less readily able to reach the plasma membrane to undergo fusion and release EVs as demonstrated here. In addition to the actin cortex, which surrounds the edge of the cell and is the primary driver of cell shape [59], the extent of membrane-cortex attachment likely plays a significant role in the ability of MVBs to transport and fuse with the plasma membrane. The membrane tension of cells correlates with substrate elasticity [47], and hence membrane tethers from the actin cortex attachment are less developed on softer substrates [160]. Thus, future studies will delineate a potential relationship between membrane tethers and MVB fusion and the impact of membrane-cortex attachment proteins such as ezrin, radixin, and moesin [161] in driving exosome release on soft substrates. Furthermore, the approach utilized here can be extended to study the role of extrinsic material properties [68], such as substrate dimensionality and geometry, as well as dynamically-tunable hydrogels [162] in functional exosome secretion.

Translation of exosomes as treatments against diseases from *in vitro* preclinical studies to therapeutics in clinical settings will require their efficient and scalable production *ex vivo*. Currently, limitations exist on the number of exosomes that can be produced for clinical studies, especially if studies require autologous exosomes [26]. Practically, it will be useful to investigate the implications of rapid exosome secretion from cells that contact with substrates for a briefer period of time and test how this observation can be leveraged to optimize clinical manufacturing of exosomes. Previous efforts to improve EV production for manufacturing purposes primarily involve cellular treatments such as by small molecules [163], culture methods such as scaffolds, membranes or fibers [164], or a combination of both strategies. Bioreactor systems, such as hollow-fiber bioreactors, feature cells seeded on fibers with small pores to allow exosome transport and subsequent collections [165]. Methods utilizing cell culture in three dimensional

spheroids have also been established [166]. More recently, a nanoporation technique significantly improved exosome production from cells in comparison to conventional culture methods [167]. However, these strategies require invasive cellular manipulation and/or expensive, complicated apparatus. Furthermore, existing strategies may not achieve an optimal level of exosome production and can be improved further by considering mechanisms by which cells regulate exosome production. Hydrogel-based strategies provide the advantage of recapitulating salient mechanical features of microenvironments from which cells are derived, thus promoting a more physiological cell phenotypes. Additionally, biomaterial strategies are in principle entirely compatible with bioreactor- or treatment-based strategies to further increase their yield. Thus, future studies should address whether existing exosome production strategies can further benefit by considering results presented here such as substrate elasticity, cell-cell interactions, and integrin activation.

In summary, this study describes the importance of matrix biophysical cues in determining the amount of functional exosome secretion and suggests new considerations for fundamental exosome release mechanisms and biomaterial-based strategies for therapeutic exosome production.

3. BIOPHYSICAL REGULATION OF EXTRACELLULAR VESICLE TRANSPORT WITHIN MATRICES

Note: the work described in this chapter was originally published: Lenzini, S., Bargi, R., Chung, G., Shin, J.-W. Matrix mechanics and water permeation regulate extracellular vesicle transport. Nat Nanotechnol 2020; 15: 217-223. (See Appendix K)

3.1 ABSTRACT

Cells release extracellular vesicles (EVs) to communicate over long distances, which requires EVs to traverse the extracellular matrix (ECM). However, given that the size of EVs is usually larger than the mesh size of the ECM, it is not clear how they can travel through the dense ECM. Here we show that, in contrast to synthetic nanoparticles, EVs readily transport through nanoporous ECM. Using engineered hydrogels, we demonstrate that the mechanical properties of the matrix regulate anomalous EV transport under confinement. Matrix stress relaxation allows EVs to overcome the confinement, and a higher crosslinking density facilitates a fluctuating transport motion through the polymer mesh, which leads to free diffusion and fast transport. Furthermore, water permeation through aquaporin-1 mediates the EV deformability, which further supports EV transport in hydrogels and a decellularized matrix. Our results provide evidence for the nature of EV transport within confined environments and demonstrate an unexpected dependence on matrix mechanics and water permeation.

3.2 INTRODUCTION

Extracellular vesicles (EVs) are cell-derived particles conventionally described as ranging from 50-500 nm in diameter [27]. Although EVs have been observed and described for many decades [168], their proposed functions have gained increasing attention in recent years. EVs contain a variety of proteins and RNAs, some of which serve as essential signals in intercellular communication [169]. Since EVs from some cell types are known to contain therapeutically useful molecules, they have also been investigated in preclinical studies against diseases [170]. EVs can be found in decellularized extracellular matrix (ECM) [37] and are proposed to be important functional elements of the ECM through direct interactions with ECM components [171]. However, the ECM is heterogeneous in its range of mechanical properties and often features average mesh sizes much smaller than EVs [80-82]**.** In these cases, particle transport remains poorly understood [95], and the extent by which EVs transport through the ECM has not been studied. Although EVs exist within ECM, their uncontrolled accumulation there can potentially lead to abnormal tissue mechanics or blockage of homeostatic fluid transport. Thus, we hypothesize that there may exist mechanisms for EVs to become cleared or transported through ECM. Mechanisms for EV transport through tissues would enable intercellular communications through ECM regions. Furthermore, as EVs become more prevalent in the study and treatment of disease in tissues, it becomes important to consider that in many cases therapeutically delivered EVs will require interaction with the ECM in order to reach target cells. Understanding how EVs transport through ECM will have a fundamental importance to EV biology and therapeutics. Thus, we sought to determine and investigate EV transport behaviors in matrices using a combination of biomaterial strategies, 3D particle tracking and molecular approaches.

3.3 MATERIALS AND METHODS

Particle size and number characterization

Particle size and number were obtained using a Nanoparticle Tracking Analysis 3.2 via a NanoSight NS300 (Malvern) with a 405 nm laser. Samples were introduced by a syringe pump at a rate 100 μl/min. Three 30 s videos were acquired using camera level 14 followed by detection threshold 7. Camera focus, shutter, blur, minimum track length, minimum expected particle size and maximum jump length were set automatically by the software. Samples were diluted as needed to maintain particles per video from 100 to 2,000.

Cell culture

All cells were cultured at 37 °C in 5% CO2. HeLa cells (CCL-2, ATCC) were a gift from A. Karginov at the University of Illinois at Chicago (UIC). D1 MSC cells (CRL-12424, ATCC), HeLa cells and HEK293T cells (CRL-3216, ATCC) were cultured using high-glucose DMEM (Thermo) supplemented with 10% FBS (Atlanta Biologicals), 1% penicillin/streptomycin (Thermo) and 1% GlutaMAX (Thermo) to 80% confluency before passaging, no more than 30 times. Human umbilical vein endothelial cells (HUVEC) (no. CC-2519, Lonza) were a gift from Y. Komarova at UIC. HUVEC were cultured using Ham's F-12K (Thermo) supplemented with 10% FBS, 1% P/S, 1% GlutaMAX, 0.1 mg/mL heparin (no. H3393, Sigma) and endothelial cell growth supplement (no. E2759, Sigma) at passage 5. Human MSCs (hMSCs) were derived by the plastic adherence of mononucleated cells from human bone marrow aspirate (Lonza). After 3 days, the adherent cells were cultured in the hMSC medium: α-minimal essential medium (Thermo) supplemented with 20% FBS, 1% P/S (Thermo Fisher Scientific) and 1% GlutaMAX

(Thermo). After reaching 70~80% confluence at 10~14 days, the cells were split, expanded in the hMSC medium and used at passage 3. Cells were routinely tested for mycoplasma contamination and only used if no contamination was present.

Lentiviral expression of CD63 fused with K2S

A DNA plasmid that contained K2S was synthesized in a pUC57-Kan backbone (GenScript). The K2S sequence was cloned into a lentiviral construct that contained CD63 (LV112335, Applied Biological Materials) so that K2S fused to CD63 on the C terminus of CD63. D1 MSCs were transduced with lentivirus that contained the CD63–K2S plasmid using standard techniques [172]. Briefly, lentiviral particles were produced with a second-generation lentiviral packaging system (LV003, Applied Biological Materials) using Lentifectin (Applied Biological Materials) in HEK293T cells. Lentiviral particles were purified and applied to D1 MSCs at passage 10 with 8 μg ml–1 polybrene (Sigma) for 3 days. Cells were expanded over a period of several days to reach ~80% confluency. Then, cells were sorted using a MoFlo Astrios (Beckman Coulter) based on their CD63–K2S signal compared to those of non-transduced cells of the same passage. Concentrated EV solutions were shown to be positive for CD63–K2S versus EVs from non-transduced cells using IVIS imaging (Living Image 4.0, Perkin Elmer).

Extracellular vesicle isolation and preparation

To isolate EVs from cells, the cells were washed twice with Hank's balanced salt solution (HBSS; Thermo) followed by incubation with serum-free growth medium for 1 h. Afterwards, the medium was exchanged with a medium that consisted of high-glucose DMEM supplemented

with 10% exosome-depleted FBS (Thermo) instead of 10% FBS. The next day, the medium was centrifuged at 2,000g for 10 min to remove cell debris followed by centrifugation at 10,000g to remove particles larger than 500 nm [130]. Afterwards, the solution was added to a 100 kDa MW-cutoff column (Amicon) and centrifuged at 5,000g for 20 min followed by washing with an equal volume of HBSS. The retentate was resuspended and confirmed to contain concentrated EVs using NanoSight NS300 (Malvern).

Lyophilization of EVs

Concentrated EVs were frozen at −80 °C overnight. If applicable, the preparations were treated with 4% trehalose (Sigma) before freezing. They were then placed in a lyophilization chamber operating at <0.1 mBar vacuum and <−100 °C temperature and allowed to sublimate overnight. The solid was reconstituted in HBSS and confirmed to contain EVs using NanoSight NS300.

Decellularization of lung tissues

All animal procedures were performed in compliance with National Institutes of Health and institutional guidelines approved by the ethical committee from UIC. Female C57BL/6 J mice were purchased from The Jackson Laboratory, housed in the UIC Biologic Resources Laboratory and killed 12 weeks after birth. Lung tissue was harvested and decellularized based on techniques described previously [173]. Briefly, the heart–lung bloc was exposed and the trachea cannulated with a blunted 18-gauge needle. Lungs were infused with 1 mL of deionized water that contained 5% P/S (wash solution). The heart–lung bloc was excised and washed

through the airway and the right ventricle, incubated in a 0.1% Triton-X wash solution overnight at 4 °C, washed and incubated in a 2% sodium deoxycholate wash solution overnight at 4 °C. It was then washed, incubated in a 1 M NaCl wash solution for 1 h at room temperature, washed and incubated in a wash solution that contained DNAase for 1 h at room temperature. The tissue was placed in a solution of liquified 5% low-melting-point agarose (GeneMate) and allowed to solidify at 4 °C overnight. Slices were prepared using a tissue slicer (Braintree) into 1 mm sections and punched into 5 mm discs using a punch (Integra). Discs were placed in HBSS, incubated at 42 °C for 30 min and washed several times.

Multiphoton microscopy

About 1×10^9 CD63-K2S EVs were incubated with a ~5 mm tissue slice at 37 °C for 3 days followed by washout. EV-loaded tissue slices were imaged using a ×20 1.00 NA water immersion objective (Olympus) with a multiphoton microscope (Bruker Fluorescence Microscopy) equipped with a Coherent Cameleon Ultra II laser that employed both second harmonic and two-photon excited fluorescence signal generation [174]. Backward-scattering second harmonic generation was obtained at 860 nm excitation to capture signals from collagen within tissue and two-photon excited fluorescence generation was performed at 760 nm excitation to capture signals from CD63-K2S. Three images were taken each for experimental and background (no loaded EVs) conditions. Images were processed by subtracting background fluorescence from the 760 nm channel. Then, three regions of interest were chosen for each background-subtracted image and Pearson's correlation coefficient was calculated. Next, the 760 nm channel signal was randomized using the MATLAB function RANDBLOCK, Pearson's correlation coefficient calculated again and the distributions compared.

Lung-tissue transport experiments

After loading ~1×10^9 CD63-K2S EVs onto a ~5 mm tissue slice for 3 days, the loading was confirmed using IVIS. The EV transport was determined by measuring tissue fluorescence before and after the indicated times. Imaging occurred with a 3 s exposure using a fluorescence excitation filter at 570 nm and an emission filter at 640 nm. IVIS software (Living Image 4.0, Perkin Elmer) was used to create a region of interest around the tissue pieces where the total fluorescent signal was counted.

Material preparation and hydrogel formation

Raw sodium alginates with different molecular weights, low (5/60, ~40 kDa) and medium (10/60, ~120 kDa), were obtained from FMC Corporation. Alginate was purified through dialysis in a 3.5 kDa membrane submerged in water, followed by treatment with activated charcoal (Sigma) 0.5 g per gram alginate. It was then filtered, frozen and lyophilized to obtain a solid polymer. Conjugation of click chemistry reagents or RGD (amino acid sequence GGGGRGDSP, Peptide 2.0) to alginate polymers was performed using a method described previously [126]. 1-bicyclo[2.2.1]hept-5-en-ylmethanamine (norbornene amine, Matrix Scientific) was conjugated to 10/60 alginate at degree of substitution (DS) 75–150 and tetrazine-amine (Conju-Probe) was conjugated to 5/60 alginate to achieve a DS18-36. For some experiments, RGD was conjugated to 10/60 alginate at DS10. Physically crosslinked hydrogels were formed as described previously [71]. Briefly, alginate solutions were mixed to be 1% 5/60 and 1% 10/60 (2% total), added to a syringe and locked to another syringe with CaSO4 (Sigma) to achieve final calcium

concentrations of 12 mM (soft) and 20 mM (stiff). After mixing, the solutions were deposited under glass for 2 h to form a hydrogel. For covalently crosslinked hydrogels, tetrazine-alginate and norbornene-alginate were mixed to be 1% each (2% total), and deposited under glass for 2 h to form a hydrogel. Interpenetrating network hydrogels of collagen-1 and alginate were created as described [175]. Briefly, hydrogels were prepared as physically crosslinked hydrogels, but the solution was mixed with collagen-I to achieve a final concentration of 0.75 or 0.375 mg mL–1 before mixing with CaSO4. To avoid drying, hydrogels were incubated in a 'retention medium': HEPES-buffered saline at pH 7.75 supplemented with 2 mM $CaCl_2$, an amount shown previously [67] to prevent the leaching of calcium from hydrogels without leading to further crosslinking.

Mechanical characterization of hydrogels and tissues

The mechanical properties of hydrogels or tissues were obtained using rheometry via Anton Paar MCR302. Storage (G′) and loss (G″) moduli were measured through a frequency sweep by lowering the geometry (Anton Paar PP08) to a 5% normal strain followed by a rotation that induced a 0.5% shear strain at an increasing frequency and finally measurement of the resulting shear stress. The complex shear modulus G* was calculated [128]:

$$G^* = \sqrt{G'^2 + G''^2} \qquad \text{(Equation 3.3.1)}$$

The loss tangent was defined as:

$$tan\delta = G''/G' \qquad \text{(Equation 3.3.2)}$$

determine the stress relaxation, the geometry was lowered at constant velocity (25 μm/s) through the linear elastic region until a 15% strain was reached. Swelling ratios were calculated by

leaving samples to dry or swell overnight followed by mass measurements. The swelling ratio *Q* was calculated through the volumes of hydrogels expressed as [176, 177]:

$$V_s = \frac{m_d}{m_s} = \frac{1}{Q}; V_r = \frac{m_d}{m_r} \qquad \text{(Equation 3.3.3)}$$

where *m* is the hydrogel weight and subscripts d, r and s denote dry, relaxed (before swelling) and swollen hydrogels. The average molecular weight between the crosslinks was calculated as:

$$1/\bar{M}_c = 2/\bar{M}_n - \frac{\left(\bar{\bar{v}}/V\right)\left[\ln(1-V_s) + V_s + \chi V_s^{\,2}\right]}{V_r\left[\left(V_s/V_r\right)^{\frac{1}{3}} - V_s/2V_r\right]} \qquad \text{(Equation 3.3.4)}$$

with $\bar{M}_n$ is the average molecular weight of polymers, $\bar{\bar{v}}/V$ the molar volume of hydrogel divided by the molar volume of water and χ the Flory interaction parameter. The values were used to calculate the average hydrogel mesh size ξ through the equation:

$$\xi = V_s^{-\frac{1}{3}}\left(\frac{2C\bar{M}_c}{\bar{M}_r}\right)^{\frac{1}{2}} l \qquad \text{(Equation 3.3.5)}$$

with *C* the polymer characteristic ratio, $\bar{M}_r$ the average molecular weight of the polymer repeating unit and l the carbon–carbon bond length. Differential scanning calorimetry was used to perform thermoporometry to measure the pore size distributions as described previously [178]. Briefly, samples ~10 mg were placed in a sealable aluminium pan inside the differential scanning calorimetry instrument (TA Instruments Q2000). Samples were cooled to −30 °C at a rate of 4 °C/min, held for 5 min, warmed to 15 °C at a rate of 4 °C/min, held for 5 min and then cooled again to −30 °C at 4 °C/min. Distributions were calculated by determining $\Delta V/\Delta R_p$ [179], where *Rp* is the pore radius, and then fitted to a frequency-normalized histogram.

Bulk transport experiments

Liposomes (FormuMax, no, F60103F-F) were obtained with a similar (~45% cholesterol, ~55% phospholipids) content as that of the EVs [180]. The encapsulation of particles or dextran in bulk alginate hydrogels was performed by mixing particles with alginate or click alginate followed by hydrogel formation. The hydrogels were punched into discs and placed into polystyrene plates with retention medium. If applicable, the hydrogels were treated with blebbistatin (Cayman 13013) or Y-27632 (Cayman 10005583). If necessary, gels were digested by adding medium with 3.4 mg/mL alginate lyase (Sigma) and placing at 37 °C for 30 min. Release was measured using fluorescence for polystyrene nanoparticles (SpheroTech) and FITC-dextran (500 kDa, Sigma). Percent release was determined at the indicated times as the number of particles in the medium P_M divided by P_M plus the number of particles in the digested hydrogel P_G as:

$$\%\ Release = \frac{P_M}{P_M + P_G} * 100\% \qquad \text{(Equation 3.3.6)}$$

For EVs and liposomes, P_M was measured as above using NanoSight NS300, but P_G was determined by calculating the initial number of particles added to the hydrogel using NanoSight NS300. Samples without encapsulated particles were used to account for background.

3D single-particle tracking

CD63-K2S EVs were encapsulated in hydrogels, placed on dishes of no. 1.5 coverslip thickness (MatTek), and imaged at ×60 with immersion oil of refractive index 1.518 (Cargille)

using a DeltaVision OMX microscope (GE). Single channel 1,024 × 1,024-pixel (81.92 × 81.92 μm) images were obtained in 2 μm thick stacks with 0.125 μm spacing (16 images per stack) using the conventional imaging mode. Over ~8 s, 30 stacks were acquired for a stack frequency of 3.75 Hz and image frequency of 60 Hz. After acquisition, the images were processed through deconvolution using softWoRx.

Using the IMARIS 'Spots' function, a custom particle tracking algorithm was created. Particles were determined using intensity thresholding over regions that measured 10 × 10 × 1 pixels followed by tracking their 3D position (*x, y, z*) over time (*t*). Tracks could continue if the particle was undetectable for a single timepoint within the track but not for two or more consecutive timepoints.

Analysis of particle-tracking data

Mathematical calculations and analysis were performed using MATLAB software. The particle MSD was calculated from the positional data as:

$$MSD(t) = [x(t) - x(t=0)]^2 + [y(t) - y(t=0)]^2 + [z(t) - z(t=0)]^2 . \quad \text{(Equation 3.3.7)}$$

Tracks with less than five measurements of MSD were removed from further analysis. For ensemble-averaged tracks, a lower limit of 20 points and an upper limit of 30 points were defined to constrain the tracks considered for analysis, as uneven track sizes can bias the results [181]. Owing to this, the data are shown only up to the lower limit of 20 points ($t \approx 5$ s). To account for static (or localization) error [182], for each particle type, particles were adhered to

glass using (3-aminopropyl)trimethoxysilane (Sigma) with a method described previously [94]. The *MSD* was tracked for adherent particles over time, and the static error was defined as the plateau *MSD*. This error was subtracted from all subsequent *MSD* measurements for each experimental group.

Ensemble-averaged track data were generated by averaging the *MSD* for each track *i* at every time *t* elapsed since the start of tracking:

$$< MSD(t) >= \frac{1}{N}\sum_{i=1}^{N} MSD_i(t) \qquad \text{(Equation 3.3.8)}$$

where *N* is number of tracks. The expected *D* for particles was determined based on the Stokes–Einstein relationship:

$$D = \frac{k_b T}{6\pi\eta r} \qquad \text{(Equation 3.3.9)}$$

where $k_b T$ is the Boltzmann constant multiplied by temperature, *r* is the particle radius and η is the solution viscosity. The viscosity of glycerol solutions was determined previously [183]. For each sample, simulations were performed to obtain an equal number of simulated tracks as the number of tracks measured for each sample. Each *MSD(t)* was drawn randomly from a zero-mean Gaussian distribution determined for each sample with variance $2D_{1.06s}t$ [181]. $D_{1.06s}$ was then calculated for simulated tracks as for experimental measurements. Tracks were evaluated for their ability to overcome 'cage' size by exceeding *c* (particles escaping) or not (particles not

escaping). The timepoint at which the particle exceeds *c* is defined as the escape time.R_g was defined as the time-averaged root mean square displacement of particle tracks as:

$$R_g = [{}^{1}/_{N} \sum_{i=1}^{N} MSD(t_i)]^{\frac{1}{2}} \quad \text{(Equation 3.3.10)}$$

over each measured timepoint t_i through the duration of the track.

ATP measurement and pharmacological depletion

ATP concentration was measured using a commercially available luciferase-based assay (Cayman, 700410). Briefly, samples were lysed followed by the addition of a mixture that catalyses a reaction to produce bioluminescence based on the concentration of ATP within the samples. Values of bioluminescence were compared to a standard curve with a known concentration of ATP. To deplete ATP, the cells were treated with 1 μg/mL oligomycin (Cayman, 1404-19-9) and 1 mM 2-deoxy-D-glucose (Cayman, 154-17-6) for 24 h.

siRNA transfection

Scrambled siRNA (Dharmacon) or siRNA against AQP1 (AM16708, Ambion) was diluted to 160 nM in unsupplemented Opti-MEM medium (Thermo) and combined 1:1 with Opti-MEM supplemented with 2% Lipofectamine RNAiMAX (Thermo) and incubated at room temperature for at least 20 min. Cells were washed with HBSS and fresh growth medium was added to cells. The transfection solution was added dropwise for a final siRNA concentration of 4 nM and cells were incubated for 3 days followed by EV isolation.

Gene expression analysis

Trizol (Thermo Fisher Scientific) was added directly to cells. Chloroform (200 µl) was added per 1 ml of Trizol followed by centrifugation for 15 min at 15,000 rpm and 4 °C. The top layer was collected and RNA precipitated with 500 µL of isopropanol for 20 min at 4 °C. Samples were centrifuged at 12,500 rpm for 15 min at 4 °C. The supernatant was removed, precipitated RNA was washed with 75% ethanol and centrifuged for 5 min at 7,500 rpm and 4 °C. Ethanol was removed and the purified RNA was resuspended in 15 µL of RNase-free water. The RNA concentration was quantified by NanoDrop. Complementary DNA was reverse transcribed by SuperScript-III (Thermo Fisher Scientific). qPCR was performed in the ViiA7 qPCR system with PowerSYBR Green master mix (Applied Biosystem). Samples were analyzed in triplicate with 50 ng of complementary DNA per well. Relative gene expression was computed by the delta-cycle-threshold method by comparing threshold cycle values to those of a reference gene (GAPDH). Table 3.S1 shows the list of primers for qPCR. See Appendix J for primers used for quantitative PCR.

Atomic force microscopy

Vesicles were adhered to freshly cleaved mica by incubation at room temperature for 15 min followed by washing [94]. Atomic force microscopy was performed using an MFP-3D-Bio model (Asylum Research) with a pyramidal tip (Bruker; MLCT, triangular, resonant frequency ~125 kHz) as described previously [184]. Briefly, vesicles with a size range between about 50 and 300 nm were found by scanning in a tapping (a.c.) mode and indented until they

reached 0.5 nN at 250 nm/s to generate a force–displacement curve. The data were analyzed and converted to Young's modulus (*E*) using MATLAB by modelling the EVs as thin elastic shells [185]. The slope of the approach curve was calculated over a sliding interval and the surface of the vesicle was determined by a high and sustained change in the slope. The linear region was used to calculate *E* via the equation

$$F(\delta) = \frac{aEt^2}{r}\delta \qquad \text{(Equation 3.3.11)}$$

with *F* as the measured cantilever force and δ as the tip displacement. The constant $^{at^2}/_{r}$ is determined by the vesicle geometry and assumed to be ~0.87 nm.

Western blot

Western blot was performed using conventional methods on samples prepared by RIPA buffer. For each lane, 20 μg of protein was added. Immunoblots were performed against AQP1 (sc-20810, SCBT, 1:2000) and GAPDH (600004-1-Ig, Proteintech, 1:5000) using an anti-rabbit or anti-mouse HRP-conjugate secondary antibody (rabbit: 115-035-003; mouse: 115-035-071, Jackson ImmunoResearch Laboratories) combined with Luminol (Santa Cruz) substrate for detection.

Statistical Evaluation

Statistics were performed as described in figure captions. All statistical analyses were performed using GraphPad Prism version 8.1.1. Unless otherwise noted, statistical comparisons were made

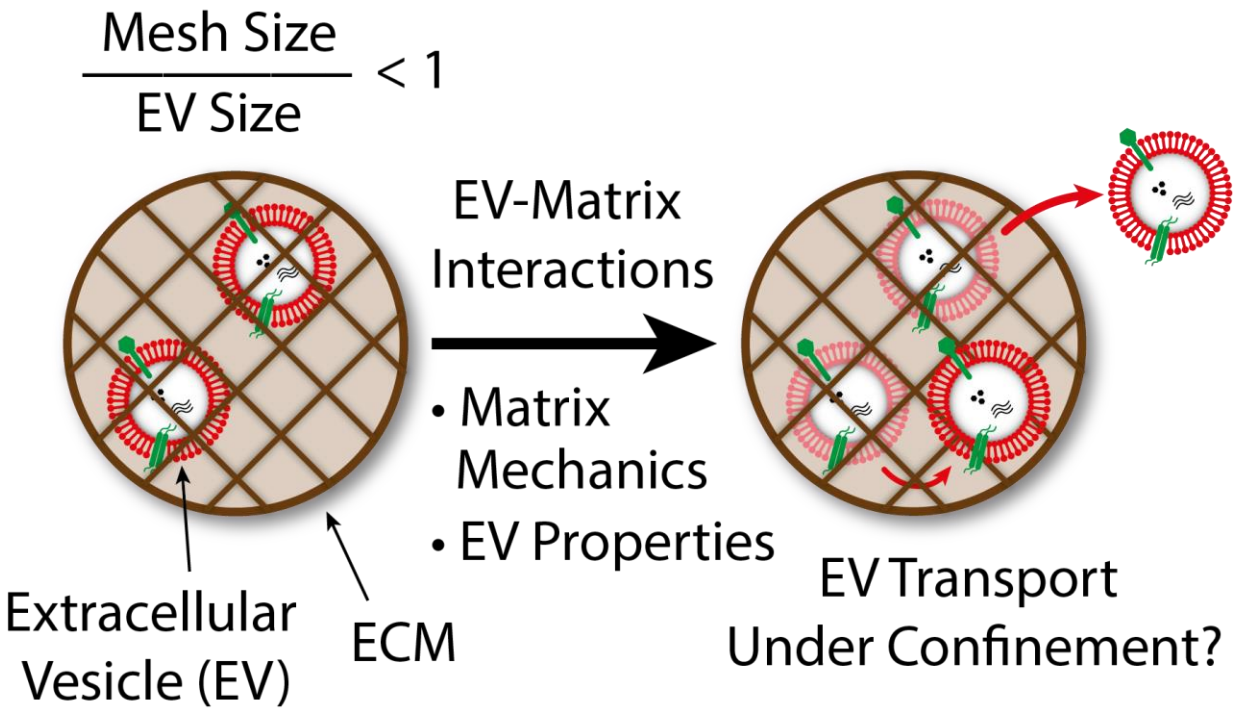

Figure 3.1. Hypothesis for EV transport within ECM. EVs exist within ECMs, where often the mesh size is smaller than the size of EVs. Mechanisms and dependencies directing their potential transport under confinement are unclear.

from at least three independent experiments by one-way ANOVA followed by Tukey's multiple comparison test, and then were considered significant if $p < 0.05$.

3.4 RESULTS

To evaluate the extent to which EVs transport through the interstitial ECM (Fig. 3.1), we engineered EVs from mouse mesenchymal stromal cells (MSCs) to contain the EV marker CD63 fused with Katushka2S (K2S, a far-red fluorescent protein [186]) to visualize them after passive loading by incubation in a decellularized matrix from lung tissue. MSCs were chosen as the source of EVs because in vivo they are often present in interstitial regions surrounded by matrix [187]. The expression of CD63–K2S in EVs (K2S–EVs) did not alter their expected size distribution (diameter [d] ≈ 50–150 nm) (Fig. 3.2a). Multiphoton second harmonic imaging analysis showed that the EVs were distributed throughout the collagen fibers within the matrix (Fig. 3.2b). Despite a nanoscale mean porosity (Fig. 3.2c,d) of the matrix, ~50% of the loaded CD63–K2S–EVs were released from the matrix within ~24.7 h (Fig. 3.2e,f), which suggests that EVs readily transport through naturally derived nanoporous matrices.

A decellularized matrix exhibited a complex shear modulus magnitude G^* of ~750 Pa with a loss tangent (viscous modulus/elastic modulus, G''/G') of ~0.15 (Fig. 3.3a,b), and a stress relaxation behavior ($t_{1/2} \approx 15$ s) (Fig. 3.3c). To determine whether the matrix mechanics mediates the EV transport, we engineered alginate-based hydrogels with a range of mechanical properties known to be present in tissues [70]. Importantly, alginate-based hydrogels are bio-inert, non-degradable and exhibit homogeneous nanoporous structures [67], which makes them ideal to model ECM without the influence of biochemical or degrading interactions. Hydrogels

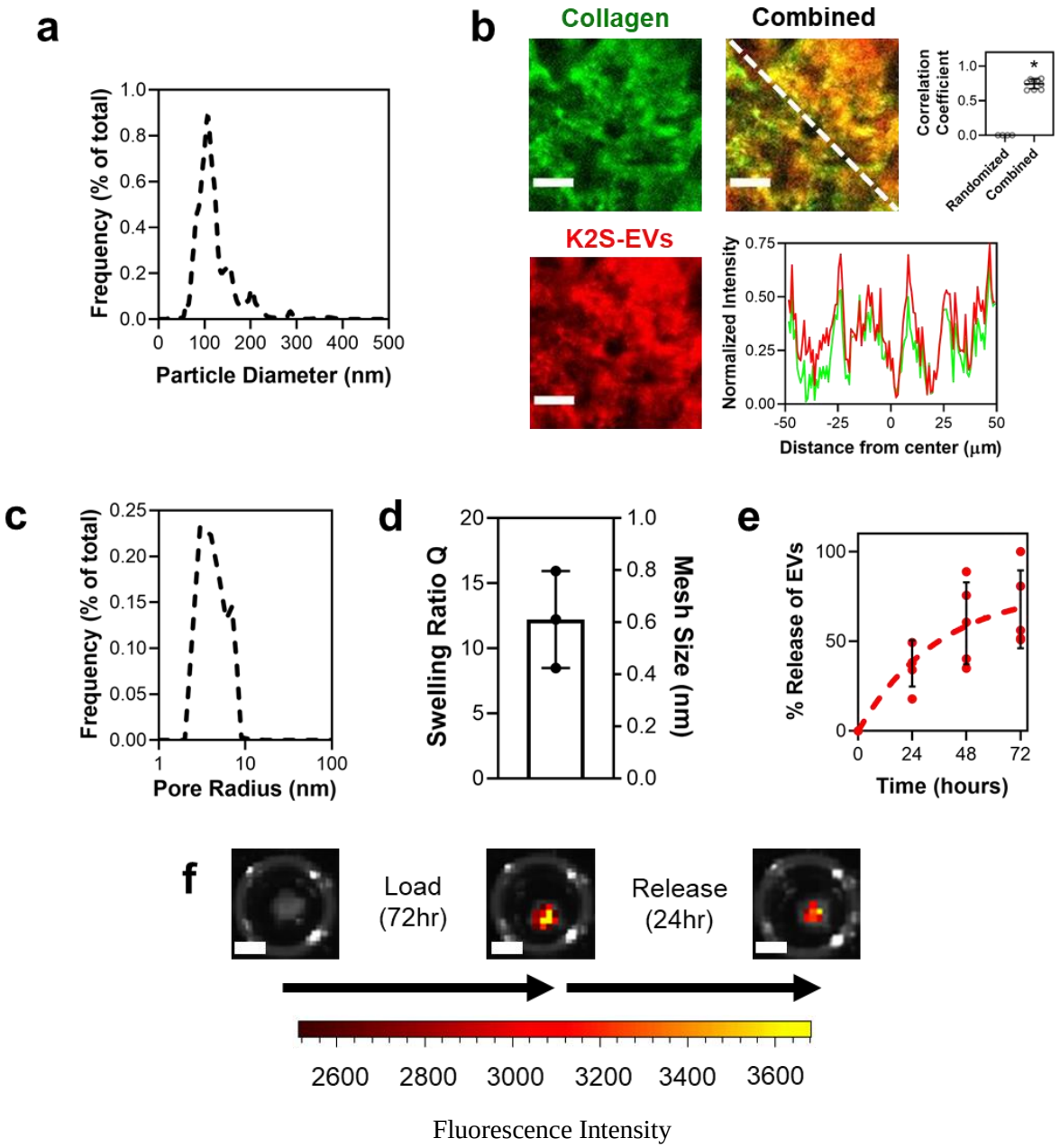
a
Frequency (% of total)
1.0
0.8
0.6
0.4
0.2
0.0
0
100
200
300
400
500
Particle Diameter (nm)
b
Collagen
Combined
Correlation Coefficient
1.0
0.5
0.0
*
Randomized
Combined
K2S-EVs
Normalized Intensity
0.75
0.50
0.25
0.00
-50
-25
0
25
50
Distance from center (μm)
c
Frequency (% of total)
0.25
0.20
0.15
0.10
0.05
0.00
1
10
100
Pore Radius (nm)
d
Swelling Ratio Q
20
15
10
5
0
Mesh Size (nm)
1.0
0.8
0.6
0.4
0.2
0.0
e
% Release of EVs
100
50
0
0
24
48
72
Time (hours)
f
Load
(72hr)
Release
(24hr)
2600
2800
3000
3200
3400
3600
Fluorescence Intensity

Figure 3.2. EVs transport within decellularized lung tissue. (a) Representative EV size distribution. Data represents the mean of $N = 3$ preparations. **(b)** Representative images of collagen (top left), K2S-EVs (bottom left) and combined (top middle) of decellularized lung tissue with EVs passively loaded. Scale bars, 15 μm. A pixel intensity chart (bottom right) drawn along the dotted line in the combined image demonstrates that EVs existed along fibers. The mean Pearson's correlation coefficient (top right) is reported for N = 9 regions of interest analyzed across 3 pairs of background-subtracted images. $^{*}P < 10^{-15}$ via an unpaired two-tailed t-test. Error bars denote the s.e.m. **(c)** Pore size distribution of decellularized lung tissue as measured by differential scanning calorimetry for N = 1 tissue slice. **(d)** Mean mesh size as calculated by equilibrium swelling theory for N = 3 tissue slices over 2 independent experiments. Error bars are SD. **(e)** Mean % of EV released from the decellularized lung tissue over time with $t_{1/2} = 24.7$ h. N = 5 tissue slices across 3 independent experiments. **(f)** Representative images of EV load (after 72 h) and release (after 24 h) in decellularized lung tissue. AU, arbitrary units. Scale bars, 2 mm. Error bars denote the SD.

can be crosslinked physically through divalent cations or covalently through click chemistry, and G^* is tunable for both (Fig. 3.3d,e). Physical crosslinking leads to stress relaxing hydrogels and covalent crosslinking leads to elastic hydrogels, as indicated by the loss tangent (Fig. 3.3f) and stress relaxation times (Fig. 3.3g) [69]. We consider $G^* \approx 500$ Pa as 'soft' and $G^* \approx 3{,}000$ Pa as 'stiff'. Alginate-based hydrogels are nanoporous, like the decellularized matrix (Fig. 3.4a), regardless of the crosslinking density or type. This is consistent with the egg-box model of crosslinking between alginate chains [188], in which increased crosslinking is not expected to dramatically alter the mesh size. As expected, after dextran–FITC (hydrodynamic radius ~15 nm [189]) molecules were encapsulated in the hydrogels, most released completely within 24 hours (Fig. 3.4b, left). In contrast, a minimal release was observed for polystyrene nanoparticles (NPs; $d \approx 80$–100 nm (Fig. 3.4c) (Fig. 3.4b, middle). As for decellularized tissue, some EVs released from the hydrogels; however, surprisingly, EV release was greater from stress relaxing hydrogels with a higher G^* (Fig. 3.4b, right). This effect occurred for EVs from other cells (Fig. 3.4d), which suggests its generalizability across cell type. Liposomes with a similar size (Fig. 3.4e) and lipid content as those of EVs [180] did not exhibit a higher release from stress relaxing hydrogels with a higher G^* (Fig. 3.4f). Hydrogels did not

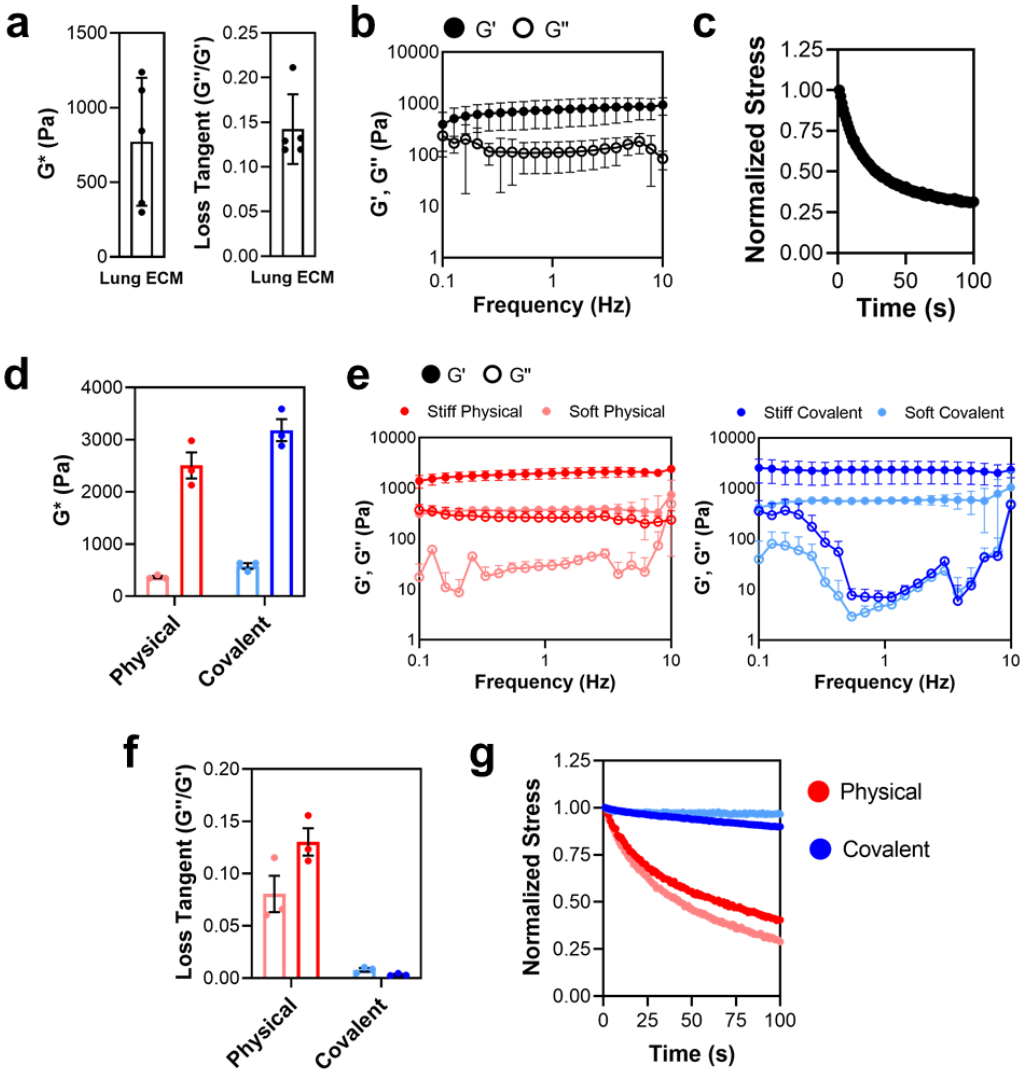

Figure 3.3. Physical properties of tissue ECM and engineered hydrogels with their effect on particle release. (a) Mean rheological properties of N = 5 decellularized lung tissue slices calculated at 1 Hz: complex shear (left) modulus and loss tangent (right). **(b)** Frequency sweep of storage and loss moduli for decellularized lung tissue. N = 3 tissue slices. **(c)** Decellularized lung tissue exhibited stress relaxation with t1/2 = 14.9 s. Data represent the mean of N = 3 tissue slices. **(d)** Complex shear modulus of N = 3 hydrogels calculated at 1 Hz. **(e)** Expanded rheological properties of N = 3 hydrogels. **(f)** Loss tangent of N = 3 hydrogels. **(g)** Stress relaxation properties of the hydrogels. Dots represent the mean of N = 3 hydrogels. Unless stated otherwise, bars represent the mean and error bars denote SEM.

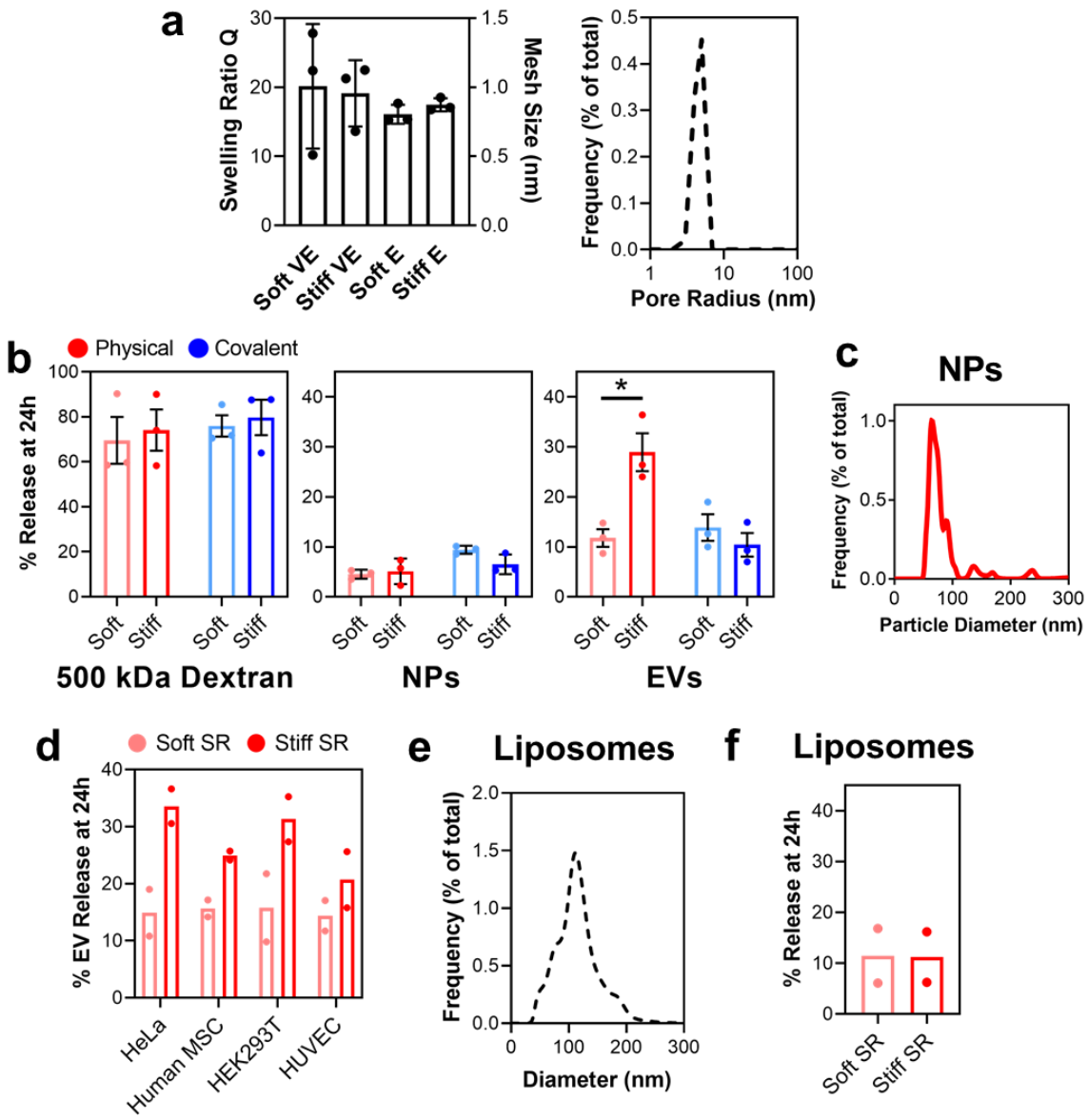

Figure 3.4. Complex shear modulus and stress relaxation time regulate the bulk release of EVs from nanoporous hydrogels. (a) Hydrogel mesh size calculations. (Left) Calculated by equilibrium swelling theory, N = 3 hydrogels for each condition. (Right) Calculated by differential scanning calorimetry for stiff stress relaxing hydrogel, N = 1 hydrogel. **(b)** The release of EVs, but not of dextran or NPs, was affected by the hydrogel complex shear modulus for hydrogels that exhibit stress relaxation: 500 kDa dextran release from hydrogels (left), NP release from hydrogels (middle) and EV release from hydrogels (right). **(c)** Representative NP size distribution. N = 3 preparations. **(d)** EVs derived from multiple cell types exhibit increased release from stiffer versus softer stress relaxing hydrogels. Each N = 2 hydrogels. **(e)** Size distribution of liposomes with similar lipid composition to EVs. N = 1 preparation. **(f)** Liposomes do not exhibit increased release from stiffer versus softer stress relaxing hydrogels. *N* = 2 hydrogels. Unless stated otherwise, data represent the mean of N = 3 experiments and error bars denote SEM.

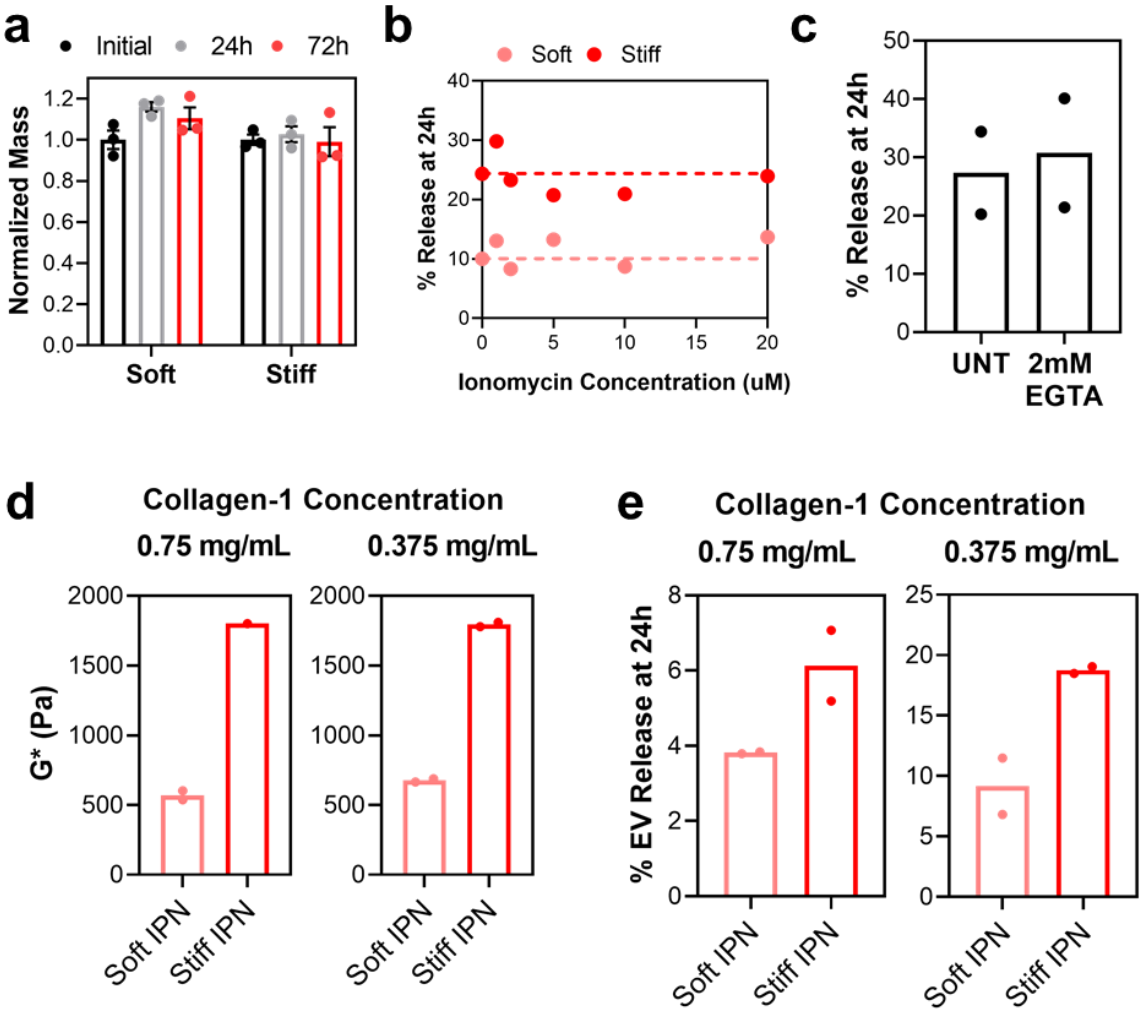

Figure 3.5. Examination of increased EV release from hydrogels. (a) Stress relaxing hydrogels do not lose mass over the tested time period. Mass is normalized to hydrogel initial mass after 1 hour. Data represents the mean of N = 3 hydrogels across one experiment. **(b)** Treatment of EVs encapsulated in hydrogels with ionomycin, a compound that facilitates calcium flux across membranes, does not affect EV release across a range of ionomycin concentrations. Dotted lines represent 0 mM ionomycin. N = 2 hydrogels across 2 independent experiments. **(c)** Treatment of hydrogels with 2 mM EGTA, a calcium chelator, does not affect EV release. Data represents the mean of N = 2 hydrogels within one experiment. **(d)** Interpenetrating network (IPN) hydrogels of collagen-1 and alginate exhibit tunable G* independent of collagen-1 concentration. Data represents the mean of N = 2 hydrogels for each condition. **(e)** Though EVs release less overall with increasing collagen-1 concentration, release is greater from stiffer versus softer IPN hydrogels. N = 2 hydrogels for each condition. Unless stated otherwise, error bars denote SD.

undergo degradation or loss of mass over the tested time period (Fig. 3.5a), which confirms the independence of degradation. Importantly, this observation is independent of Ca^{2+}, as treatment with ionomycin (Fig. 3.5b) or EGTA did not affect the release (Fig. 3.5c). To test whether the EV release is mechanosensitive in a more natural ECM composition, an interpenetrating network hydrogel of alginate and collagen-I polymers was fabricated [175] in which the hydrogel G^* was tunable independent of the collagen-I concentration (Fig. 3.5d). Although EV release from the interpenetrating network was generally lower, depending on the collagen concentration, the release remains mechanosensitive (Fig. 3.5e).

To study whether the EV release from engineered hydrogels corresponds to individual EV transport, we developed a three-dimensional (3D) particle-tracking approach that utilized high-speed 3D microscopy with deconvolution to visualize and calculate the mean square displacement (*MSD*) of the CD63–K2S–EVs over time in different environments. Particles were tracked immediately after hydrogel formation to capture the initial behaviors possibly affected by hydrogel swelling. Data were collected every $\Delta t = 0.267$ s over a total time $T \approx 8$ s. Next, data were ensemble-averaged over numerous tracks and fit to the power law form [152]:

$$< MSD(t) > = K_\alpha t^\alpha \qquad \text{(Equation 3.4.1)}$$

to calculate an effective ensemble exponent α and coefficient K_α. The effective diffusion coefficient:

$$D_\tau = {MSD(\tau)}/{6\tau} \qquad \text{(Equation 3.4.2)}$$

was calculated for each track over each interval $\tau = 4\Delta t \approx 1.06$ s [181] to give:

$$D_{1.06s} = {MSD(\tau = 1.06s)}/{6(1.06s)}\ . \qquad \text{(Equation 3.4.3)}$$

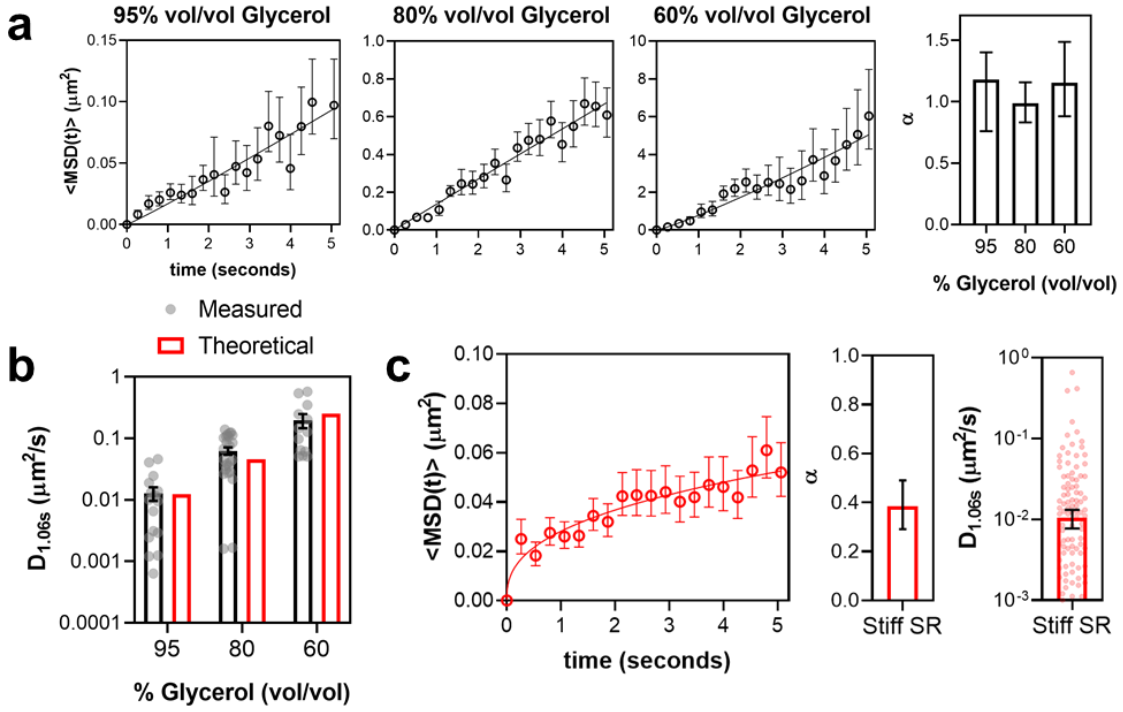

Figure 3.6. Validation of 3D particle tracking methods using nanoparticles. (a) (Left) Ensemble MSD curves for polystyrene nanoparticles transporting in solutions with various amounts of glycerol: 95% (N = 17), 80% (N = 32), 60% (N = 13). (Right) Values for effective transport exponent α by a non-linear fit of Equation 1 for curves presented in (a). Values are close to 1 as expected for particles transporting freely in solution. Error bars are 95% CI. **(b)** Mean diffusion coefficient $D_{1.06s}$ for nanoparticles transporting in each solution of glycerol matches that expected based on the theoretical Stokes-Einstein relationship. **(c)** (Left) Ensemble *MSD* curves for polystyrene nanoparticles transporting in stiff stress relaxing matrix. (Middle) The value of α for nanoparticles in matrix is less than 1, indicating sub-diffusion. Error bars are 95% CI. (Right) Mean diffusion coefficient $D_{1.06s}$ for nanoparticles in matrix. Data are for N = 343 tracks.

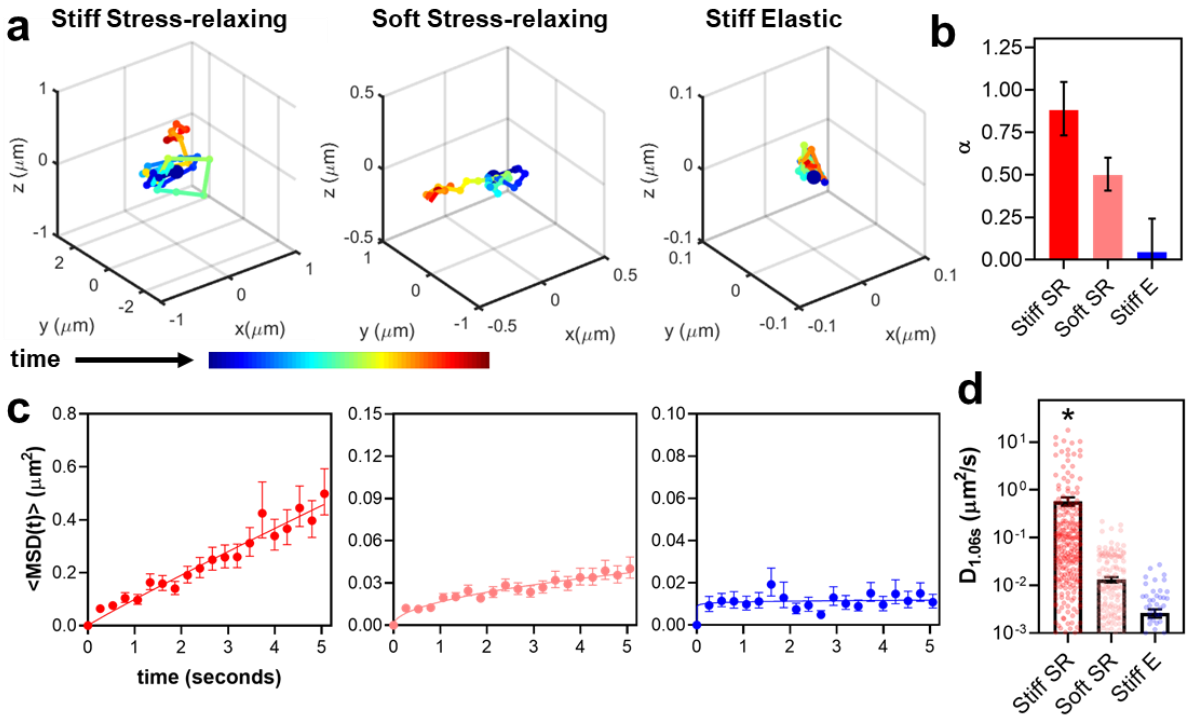

Figure 3.7. Individual EVs show more rapid and diffusive transport in a stiff stress relaxing matrix. (a) Representative 3D particle tracks for EVs in a matrix. **(b)** Values of α calculated for a non-linear fit of tracking data for EVs in the matrices. Error bars represent the 95% confidence interval. **(c)** EVs in a stiff stress relaxing matrix (left, $N = 279$) exhibit a more diffusive ensemble-averaged transport ($\alpha \approx 0.89$) relative to EVs in a soft stress relaxing (middle, $N = 263$) or stiff elastic matrix (right, $N = 89$). Data represent the mean and error bars represent SEM. **(d)** Mean $D_{1.06s}$ calculated for the tracks in (b). $^{*}P = 6.9 \times 10^{-7}$ via a one-way ANOVA with Tukey's test for multiple comparisons.

Multiple values for $D_{1.06s}(\tau)$ were obtained for a single track for each interval τ and averaged to obtain a single $D_{1.06s}$ for each track (see section 3.2). We validated our method by measuring the transport of NPs in glycerol solutions with different solution viscosities and thus different expected transport speeds. NPs in these solutions show an α of ~1 (Fig. 3.6a), which indicates diffusive transport. Furthermore, they exhibited diffusion coefficients $D_{1.06s}$ like those expected from conventional Stokes–Einstein theory (Fig. 3.6b). In contrast, NPs in a stiff stress relaxing matrix exhibited a subdiffusive ($\alpha \approx 0.39$), slower ($D_{1.06s} \approx 0.01$ μm^2/s) transport (Fig. 3.6c), which indicates confinement. Strikingly, EVs in a stiff stress relaxing matrix (Fig. 3.7a) showed α approaching that of NPs transporting in solution ($\alpha \approx 0.88$) (Fig. 3.7b. Fig. 3.7c). EVs in a soft stress relaxing matrix exhibited a significantly lower $D_{1.06s}$ (Fig. 3.7d) with subdiffusive transport ($\alpha \approx 0.49$), whereas EVs in a stiff elastic matrix showed a more pronounced subdiffusive transport ($\alpha \approx 0.045$), which indicates that the matrix stress relaxation allows EVs to overcome confinement.

Stress relaxing matrix systems can give rise to ‘dynamic heterogeneity’ [190] wherein particles can escape confinement or ‘cages’ formed by the matrix. To determine an expected SD of $D_{1.06s}$ for particles in a homogeneous system, tracks were simulated matched to measurement conditions (see section 3.2). Simulated tracks followed the measured tracks for NPs transporting in solutions (Fig. 3.8a). The standard deviation (SD) of experimentally determined $D_{1.06s}$ (σ_{meas}) was calculated and normalized to the SD of $D_{1.06s}$ for simulated trajectories (σ_{sim}) to measure the degree of heterogeneity of $D_{1.06s}$ [191]. Although NPs in solution followed their simulated trajectories with a lower degree of heterogeneity, $\sigma_{meas}/\sigma_{sim}$ (Fig. 3.8b), EVs in the matrix

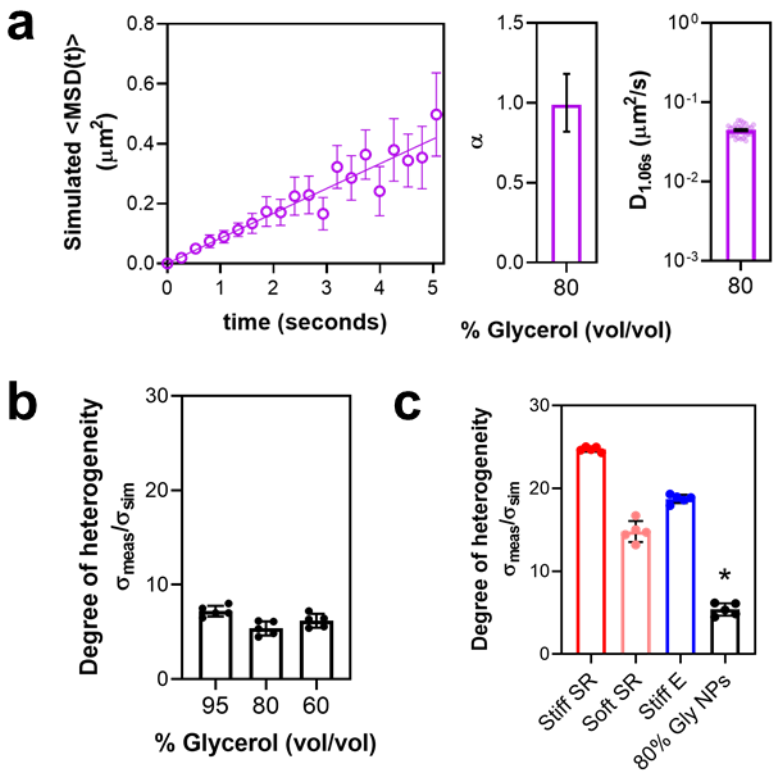

Figure 3.8. Analysis of degree of heterogeneity for particle tracks. (a) (Left) Simulated *MSD* curve for nanoparticles transporting in 80% vol/vol glycerol solution with (Middle) α value and (Right) $D_{1.06s}$. The curve and the values are similar to (Fig. 3.6a, Middle) as expected. N = 32 tracks. Error bars denote 95% CI. **(b)** Degree of heterogeneity $\sigma_{meas}/\sigma_{sim}$ for nanoparticles transporting in glycerol solutions. N = 5 simulations. Error bars denote SEM. **(c)** A higher SD of $D_{1.06s}$ for the measured tracks versus the simulated tracks, $\sigma_{meas}/\sigma_{sim}$. $N = 5$ simulations. $^*P < 10^{-15}$ via one-way ANOVA with Tukey's test for multiple comparisons.

showed a higher $\sigma_{meas}/\sigma_{sim}$ (Fig. 3.9c), which indicates a more heterogeneous distribution of $D_{1.06s}$. To investigate this behavior, we analyzed how individual EVs exhibited changes in transport motions over time by defining another 3D diffusion coefficient ($D_{0.53s}$) with shorter intervals $\tau = 2\Delta t \approx 0.53$ s to capture the local transport behaviors. $D_{0.53s}$ was calculated for each interval τ_i within the tracks to express each track as $D_{0.53s}(\tau)$. Next, the difference of $D_{0.53s}(\tau)$ between consecutive intervals τ_i and τ_{i+1} ($\tau_1 \approx 0.53$ s, $\tau_2 \approx 1.06$ s, …) was taken to calculate $\Delta D_{0.53s}$:

$$\Delta D_{0.53s}(\tau_i) = D_{0.53s}(\tau_{i+1}) - D_{0.53s}(\tau_i) \qquad \text{(Equation 3.4.4)}$$

which indicates the magnitude of changes in the diffusion coefficient over time within a track. To compare the spread of $\Delta D_{0.53s}$ between groups, values for $\Delta D_{0.53s}$ were normalized to the mean $\Delta D_{0.53s}$ for each group (normalized $\Delta D_{0.53s}$). From a theoretical perspective, particle motion is facilitated when $\Delta D_\tau > 0$, particle motion is hindered when $\Delta D_\tau < 0$ and particle motion remains constant when $\Delta D_\tau \approx 0$ (Fig. 3.9a). $\Delta D_{0.53s}$ values were close to zero for NPs transporting in solution (Fig. 3.9b), which suggests that $\Delta D_{0.53s} \approx 0$ for particles that undergo free diffusion. However, individual tracks of EVs in a stiff matrix showed a much broader distribution of $\Delta D_{0.53s}$ (Fig. 3.9c-e), which suggests that a stiff matrix drives the fluctuating transport motions within the tracks. Furthermore, $\Delta D_{0.53s}$ values were ~50% both positive and negative (Fig. 3.9f), which indicates that this behavior is associated with zero-mean fluctuations in transport motion.

To calculate the extent to which EVs escaped confinement, we modeled the matrix as a system of ‘cages’ with a defined size *c* that transporting particles must overcome (Fig. 3.10a)

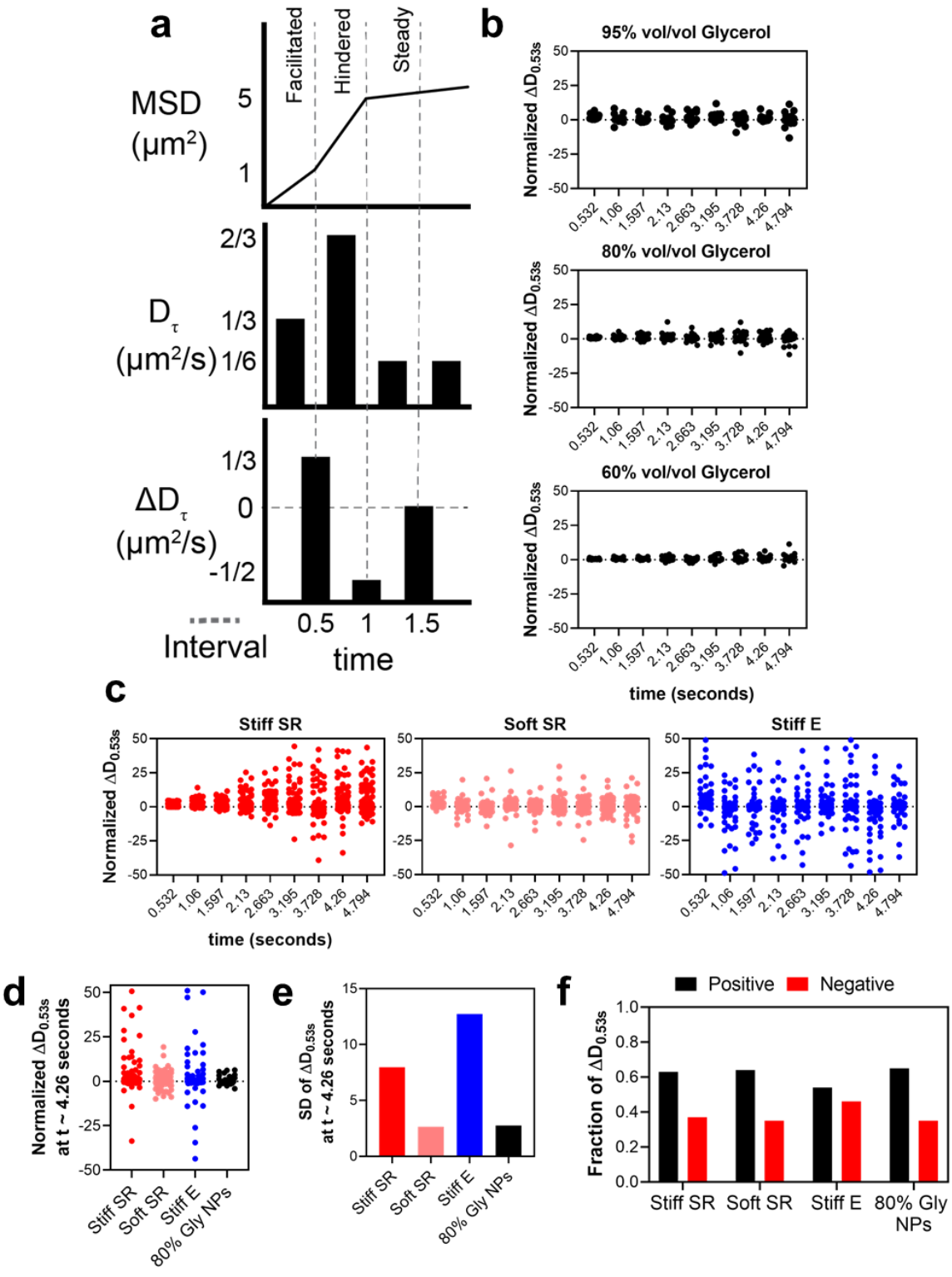
a
MSD (μm²)
5
1
Facilitated
Hindered
Steady
D_τ (μm²/s)
2/3
1/3
1/6
ΔD_τ (μm²/s)
1/3
0
-1/2
0.5
1
1.5
Interval
time
b
95% vol/vol Glycerol
80% vol/vol Glycerol
60% vol/vol Glycerol
Normalized ΔD0.53s
time (seconds)
c
Stiff SR
Soft SR
Stiff E
Normalized ΔD0.53s
time (seconds)
d
Normalized ΔD0.53s at t ~ 4.26 seconds
Stiff SR
Soft SR
Stiff E
80% Gly NPs
e
SD of ΔD0.53s at t ~ 4.26 seconds
f
Positive
Negative
Fraction of ΔD0.53s
Stiff SR
Soft SR
Stiff E
80% Gly NPs

Figure 3.9. Analysis of EV tracking data in terms of changes in D_τ over time. (a) Illustration of the relationship between *MSD(t)*, D_τ, and ΔD_τ values. Particle motion remains constant when $\Delta D_\tau \sim 0$, particle motion is facilitated when $\Delta D_\tau > 0$, and particle motion is hindered when $\Delta D_\tau < 0$. Values are arbitrary and for illustrative purposes only. **(b)** Values for $\Delta D_{0.53s}$ over the length of the track for nanoparticles transporting in glycerol, 95% (N = 17), 80% (N = 32), 60% (N = 13). **(c)** Values for $\Delta D_{0.53s}$ over the length of the track for EVs transporting in matrix, Stiff SR (N = 279), Soft SR (N = 263), Stiff E (N = 89). **(d)** The distributions of the change in diffusion coefficient $\Delta D_{0.53s}$ calculated at $t \approx 4$ s are broader for EVs in a stiff matrix, which indicates a fluctuating motion. **(e)** Standard deviation (SD) of $\Delta D_{0.53s}$ distributions for tracks in Fig. 3b measured at $t \sim 4.26$ seconds. **(f)** Fraction of all $\Delta D_{0.53s}$ values for particle tracks with positive or negative value.

[192-194]. As NPs in a stiff stress relaxing matrix were confined with $\alpha \approx 0.39$, c was defined as the plateau *MSD* for this condition ($c \approx 0.09\ \mu m^2$). Tracks were analyzed to determine whether their *MSD* exceeded c (the fraction of particles that escapes from the cages) and, if so, the elapsed time before the *MSD* exceeded c (the escape time). A significant amount of the EVs in a stiff stress relaxing matrix demonstrated the ability to escape cages and they did this more rapidly (~1.3 s) than the EVs in a soft stress relaxing matrix (Fig. 3.10b). In contrast, EVs in a stiff elastic matrix less readily escaped cages, which further shows that matrix stress relaxation is crucial to allow EV transport. Furthermore, we calculated the radius of gyration R_g [195] for each particle, defined as the time-averaged root mean square displacement over the particle trajectory. EVs in a stiff stress relaxing matrix explored more space than EVs in a soft stress relaxing matrix, as indicated as by a higher R_g (Fig. 3.10c).

As the EVs showed the ability to transport in confined spaces, we hypothesized that intrinsic EV properties also drive their transport. Although lyophilized (freeze-dried) EVs possessed the same size distribution as freshly isolated EVs (Fig. 3.11a), they did not exhibit a greater release from the stiff stress relaxing hydrogel (Fig. 3.11b)—this was further confirmed by a decrease in $D_{1.06s}$ by about tenfold and in α to ~0.25. (Fig. 3.11c). Non-lyophilized EVs with

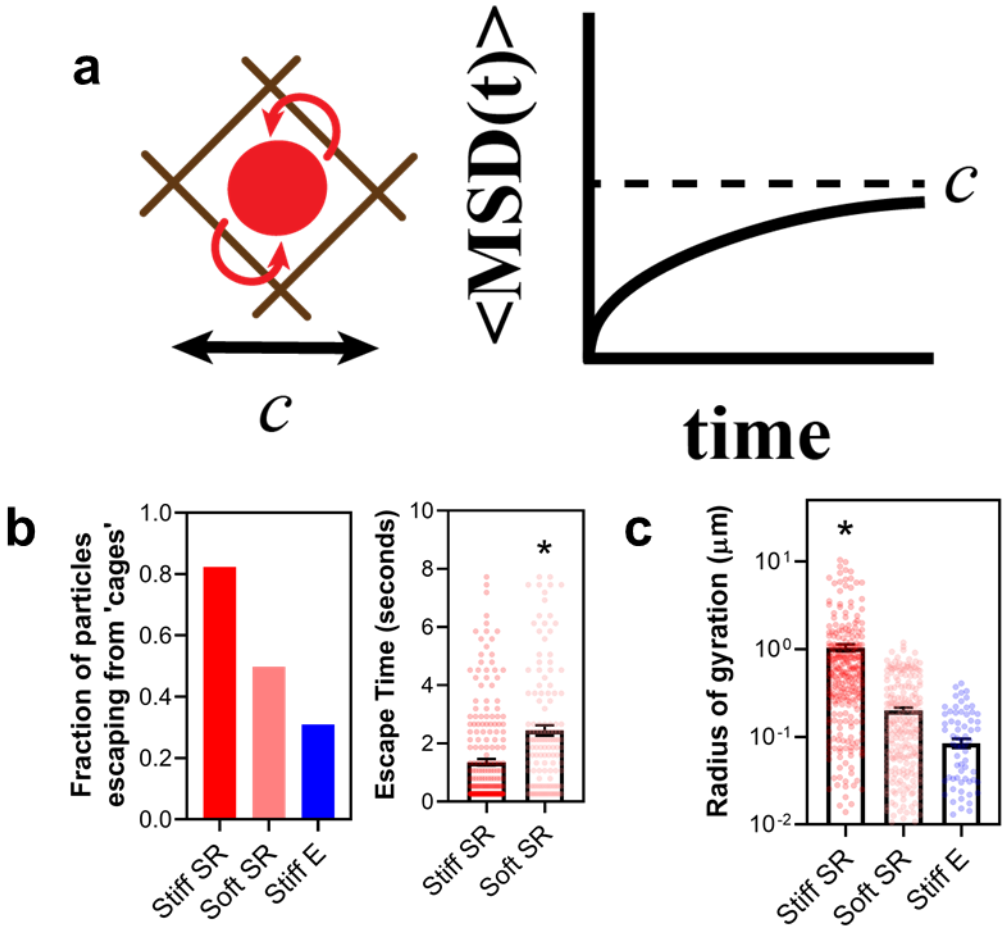

Figure 3.10. Analysis of EV tracking data in terms of escape from cages in the matrix. **(a)** Particles under confinement in matrix exhibit an *MSD* that can be used to model the system as a set of cages with size *c* defined by the *MSD* plateau. **(b)** Escape from the cages of confinement for EV tracks in Fig. 3.7: fraction of EVs able to escape cages (left) and time elapsed before the EVs escape the cages (right). $*P = 7.5 \times 10^{-8}$ via an unpaired two-tailed *t*-test. **(c)** R_g for EV tracks in (b). $*P < 10^{-15}$ via one-way ANOVA with Tukey's test for multiple comparisons. Unless stated otherwise, error bars denote SEM. SR, stress relaxing; E, elastic.

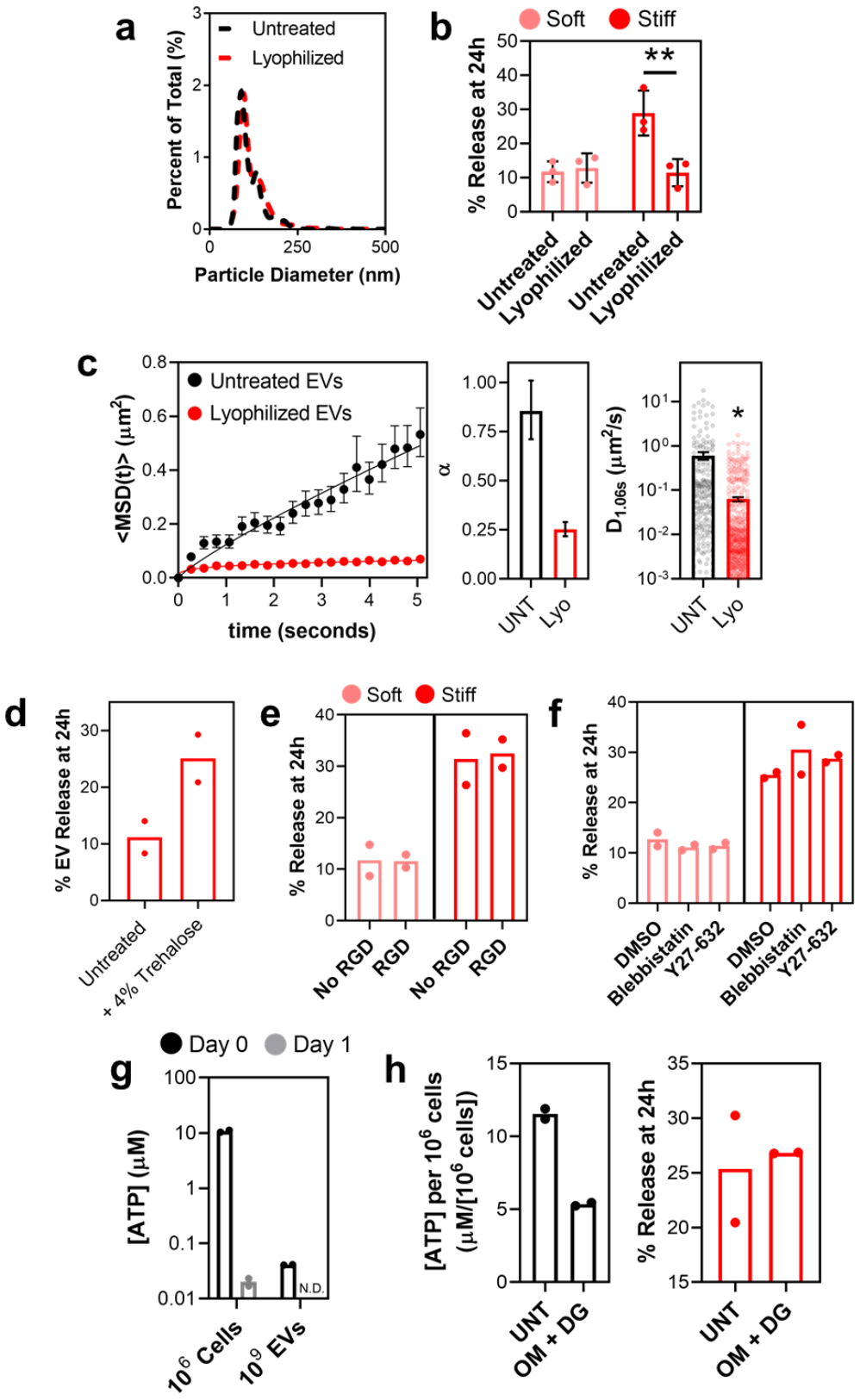
a
Untreated
Lyophilized
Percent of Total (%)
Particle Diameter (nm)
b
Soft
Stiff
% Release at 24h
**
Untreated
Lyophilized
Untreated
Lyophilized
c
Untreated EVs
Lyophilized EVs
<MSD(t)> (μm²)
time (seconds)
α
UNT
Lyo
D1.06s (μm²/s)
*
UNT
Lyo
d
% EV Release at 24h
Untreated
+ 4% Trehalose
e
Soft
Stiff
% Release at 24h
No RGD
RGD
No RGD
RGD
f
% Release at 24h
DMSO
Blebbistatin
Y27-632
DMSO
Blebbistatin
Y27-632
g
Day 0
Day 1
[ATP] (μM)
N.D.
10⁶ Cells
10⁹ EVs
h
[ATP] per 10⁶ cells (μM/[10⁶ cells])
UNT
OM + DG
% Release at 24h
UNT
OM + DG

Figure 3.11. Mechanisms of mechanosensitive EV release from hydrogels. (a) Lyophilization of EVs does not affect their size distribution after reconstitution. $N = 2$ preparations. **(b)** After lyophilization, the mean % EV release decreased from stiff stress relaxing hydrogels. N = 3 hydrogels for each condition. **P = 0.012 via two-way ANOVA followed by Tukey's test for multiple comparisons. **(c)** Ensemble MSD curves for untreated (Unt; N = 279) versus lyophilized (Lyo; N = 618) EV tracks in a stiff stress relaxing matrix (left). Values of α from a non-linear fit by Equation 3.4.1 (middle). Error bars represent the 95% confidence interval. Mean $D_{1.06s}$ (right). *P = 2.9×10^{-12} via an unpaired two-tailed t-test. **(d)** Addition of 4% trehalose to EVs during lyophilization recovers their mean % release in stiff stress relaxing matrix. $N = 2$ hydrogels each condition. **(e)** Presence of 0.8 μM RGD peptide tethered within stress relaxing hydrogels does not affect mean % EV release. **(f)** Treating RGD-hydrogels containing encapsulated EVs with cytoskeletal inhibitors does not affect mean % EV release. **(g)** EVs contain little ATP in comparison to their cells. The 10^9 EVs are isolated from the 10^6 cells over 24 hours. $N = 2$ preparations within one experiment**.** **(h)** (Left) Cells are depleted of ATP by ~50% with treatment with 1 μg/mL oligomycin (OM) and 1mM 2-deoxy-D-glucose (DG). (Right) EVs from cells depleted of ATP do not exhibit a different release after 24 hours from stiff stress relaxing hydrogels. $N = 2$ hydrogels for each condition. Unless stated otherwise, data represent the mean of N = 3 experiments and error bars denote SEM.

an integral membrane structure are probably required for mechanically sensitive transport, as lyophilizing EVs [196] can compromise their membrane integrity. This is supported by the addition of the cryoprotectant trehalose to EV preparations during lyophilization [197], which recovers release behavior (Fig. 3.11d). We speculated that transport may be regulated by EV surface interactions within hydrogels or actomyosin contractility within EVs. However, tethering the integrin binding ligand RGD (~0.8 μM) within hydrogels or treating hydrogels with drugs against myosin-II (blebbistatin) and Rho-associated protein kinase (Y27632) did not affect the EV release (Fig. 3.11e,f). Importantly, ATP within EV preparations existed at a concentration much less than that in cells (Fig. 3.11g), and EVs from cells partially (~50%) depleted of ATP do not release differently (Fig. 3.11h), which indicates that EV transport mechanisms are probably metabolically passive rather than active.

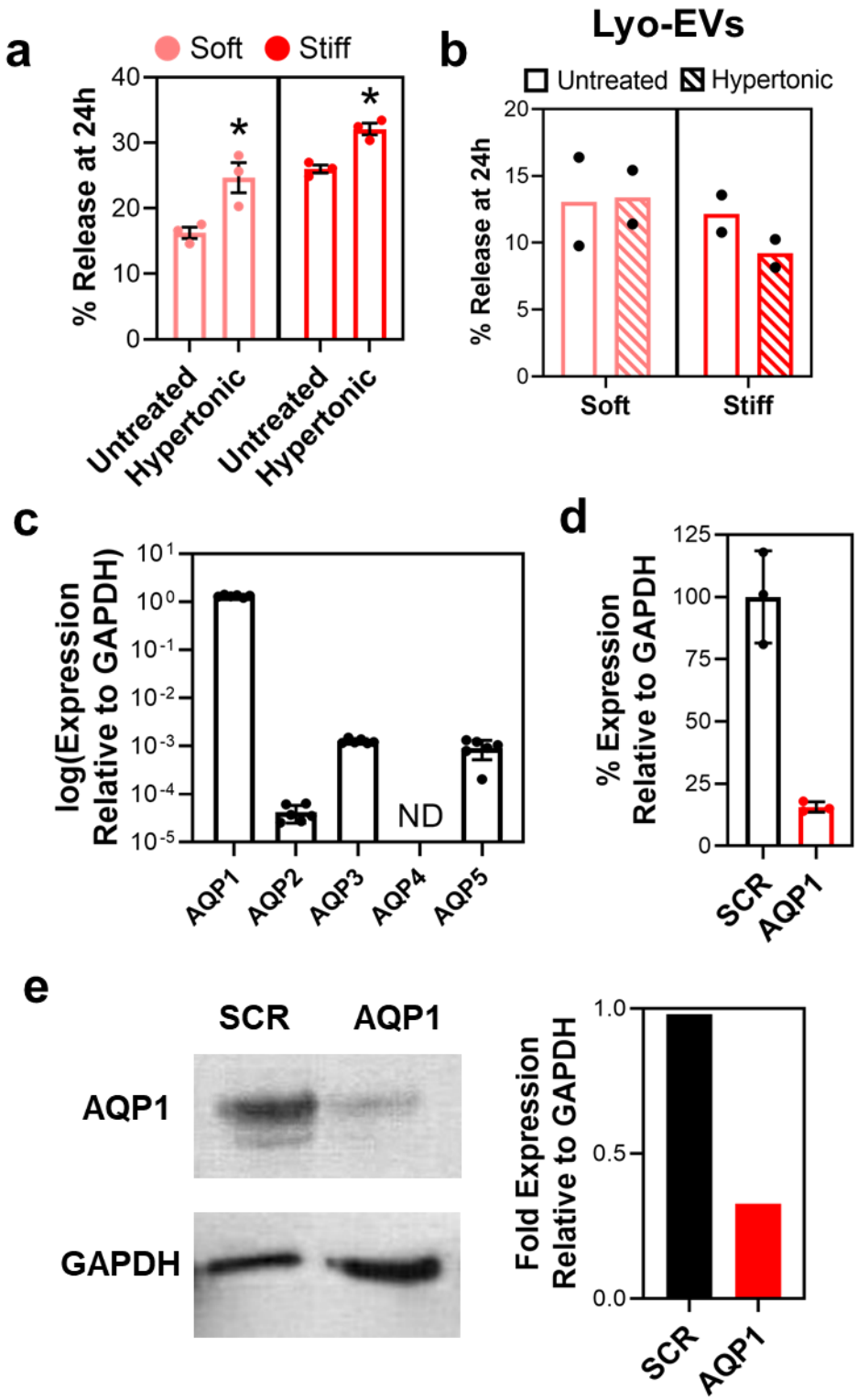
a
Soft
Stiff
% Release at 24h
40
30
20
10
0
*
*
Untreated
Hypertonic
Untreated
Hypertonic
b
Lyo-EVs
Untreated
Hypertonic
% Release at 24h
20
15
10
5
0
Soft
Stiff
c
log(Expression Relative to GAPDH)
10^{1}
10^{0}
10^{-1}
10^{-2}
10^{-3}
10^{-4}
10^{-5}
ND
AQP1
AQP2
AQP3
AQP4
AQP5
d
% Expression Relative to GAPDH
125
100
75
50
25
0
SCR
AQP1
e
SCR
AQP1
AQP1
GAPDH
Fold Expression Relative to GAPDH
1.0
0.5
0.0
SCR
AQP1

Figure 3.12. Evidence for water channels effect on EV release and aquaporin-1 knockdown in EVs. (a) Hypertonic medium (3% polyethylene glycol, 300 kDa) significantly increased the mean % EV released from stress relaxing hydrogels. N = 3 hydrogels for each condition. *P = 0.026 (soft), P = 5×10^{-3} (stiff) via an unpaired two-tailed t-test. **(b)** Treating lyophilized EVs encapsulated in stress relaxing hydrogels with hypertonic solution does not affect their mean % release. **(c)** *AQP1* is the dominant aquaporin isoform in mMSCs. The y-axis is expressed as the log fold change of RNA expression relative to *GAPDH* RNA expression. Data represent the mean of *N* = 3 reactions in one experiment. **(d)** Verification of RNA expression knockdown in cells by treatment with siRNA against *AQP1*. SCR = scrambled siRNA control. Data represent *N* = 3 reactions in one experiment. **(e)** EVs collected from cells treated with siRNA against *AQP1* express less AQP1 protein. (Left) Western blot of EVs from cells treated with siRNA against *AQP1* or a scrambled (SCR) control siRNA. (Right) Blot quantification. Unless stated otherwise, data represent the mean of N = 3 experiments and error bars denote SEM.

Water permeation via aquaporins drives the migration of spatially confined cells independent of myosin-II [198]. As aquaporins are partitioned into EVs [64], we hypothesized that water permeation through aquaporins regulates EV transport. EV release in both stiff and soft stress relaxing hydrogels was increased by the addition of 3% polyethylene glycol (Fig. 3.12a) but did not occur if the EVs were freeze-dried (Fig. 3.12b). We then tested whether aquaporins are required for EV release. AQP1 is the dominant aquaporin isoform expressed in MSCs (Fig. 3.12c). Treating cells with short interfering RNA (siRNA) against AQP1 leads to an ~80% mRNA knockdown in cells (Fig. 3.12d) and a ~60% reduction in the AQP1 protein packaged into EVs (Fig. 3.12e). AQP1 depletion in EVs significantly increased their Young's modulus (Fig. 3.13a-c), which suggests that water permeation makes the EVs more deformable. AQP1 depletion in EVs significantly decreased the EV release from hydrogels (Fig. 3.14a), and AQP1-depleted EVs showed an impaired release from decellularized matrices (Fig. 3.14b,c), which indicates that the greater deformability via AQP1 enhances the EVs ability to transport in the matrix. Although AQP1 depletion reduced $D_{1.06s}$ by about threefold, α remained unchanged for individual EVs (Fig. 3.14d). Consistent with these results, AQP1 depletion decreased the

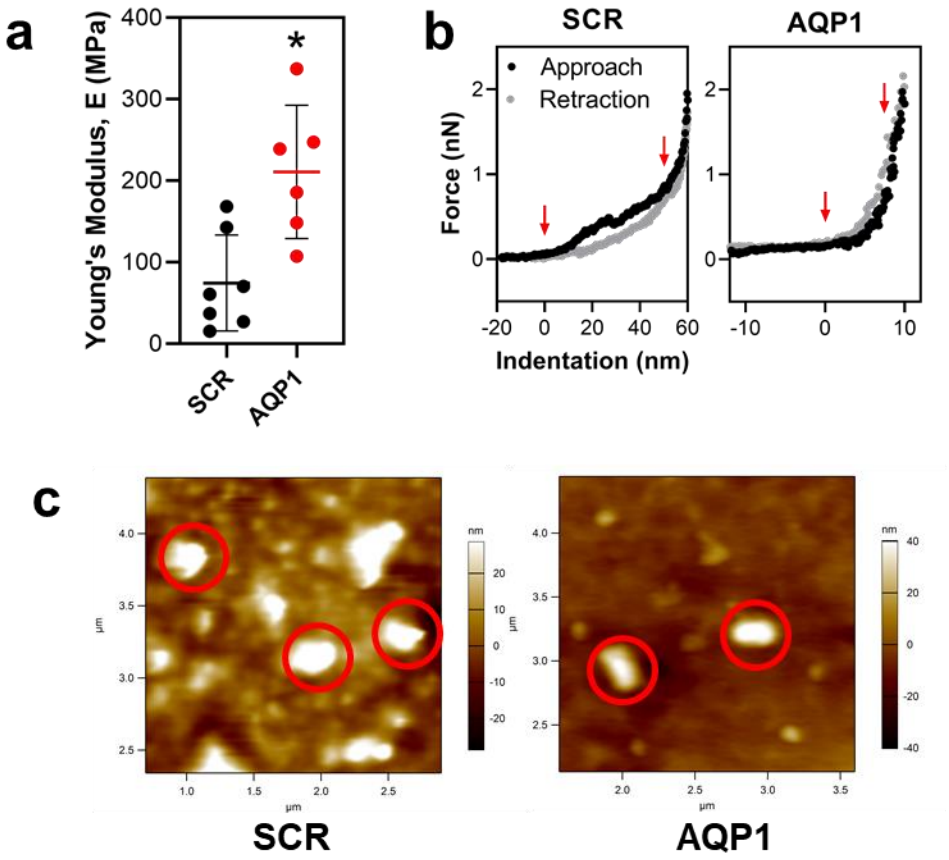

Figure 3.13. AQP1 in EVs mediates their deformability. (a) EVs from cells treated with siRNA against AQP1 (N = 6) exhibited a significantly higher mean Young's modulus (*E*) than EVs from cells treated with a scrambled siRNA control (SCR, N = 7). *P = 0.005 via an unpaired two-tailed t-test. Line represents the mean and error bars denote SD. **(b)** Representative force-displacement curves of EVs from cells treated with siRNA against *AQP1* versus a control. Red arrows indicate the range in which Young's modulus is calculated. **(c)** Representative images of EVs adhered to mica acquired using scanning mode with atomic force microscopy. Red circles indicate particles measuring 50-150 nm in height that are measured for Young's modulus.

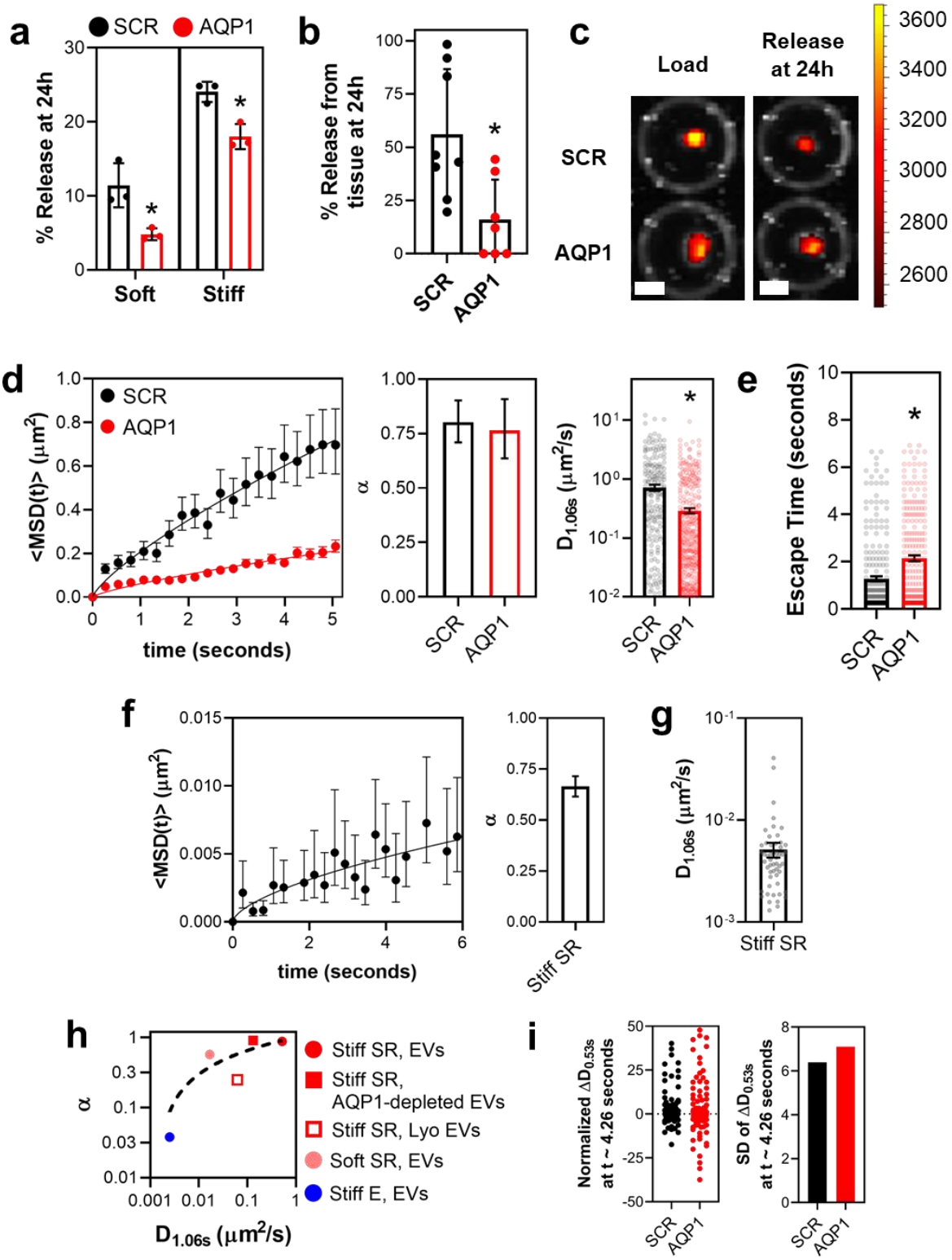
a
SCR
AQP1
% Release at 24h
Soft
Stiff
b
% Release from tissue at 24h
SCR
AQP1
c
Load
Release at 24h
SCR
AQP1
3600
3400
3200
3000
2800
2600
d
SCR
AQP1
<MSD(t)> (μm²)
time (seconds)
α
D1.06s (μm²/s)
e
Escape Time (seconds)
f
<MSD(t)> (μm²)
time (seconds)
Stiff SR
g
D1.06s (μm²/s)
Stiff SR
h
α
D1.06s (μm²/s)
Stiff SR, EVs
Stiff SR, AQP1-depleted EVs
Stiff SR, Lyo EVs
Soft SR, EVs
Stiff E, EVs
i
Normalized ΔD0.53s at t ~ 4.26 seconds
SD of ΔD0.53s at t ~ 4.26 seconds

Figure 3.14. AQP1 in EVs mediates their release from and transport within hydrogels. **(a)** EVs depleted of AQP1 exhibited a significantly lower mean % released from stress relaxing hydrogels. N = 3 hydrogels for each condition. *P = 0.021 (soft), P = 8.6×10^{-3} (stiff) via an unpaired two-tailed t-test. **(b)** The mean % release of AQP1-depleted EVs (N = 7) from decellularized lung tissue was significantly reduced versus a control (N = 8). *P = 0.010 via an unpaired two-tailed t-test. **(c)** Representative image of AQP1-depleted EVs largely remaining within decellularized lung tissue 24 hours after loading. The axis scale is fluorescence intensity counts (arbitrary units). Scale bars = 2 mm. **(d)** Ensemble MSD curves (left) for AQP1-depleted EV tracks (N = 613) versus control (N = 659) EV tracks. AQP1-depletion did not change the α values (middle). Error bars are the 95% confidence interval. AQP1-depletion significantly decreased the mean $D_{1.06s}$ (right). *P = 1.3×10^{-8} via an unpaired two-tailed t-test. **(e)** From an analysis of the tracks from (d), AQP1-depleted EVs exhibited a significantly slower mean escape time than that of the control EVs in a stiff stress relaxing matrix. *P = 2.1×10^{-7} via an unpaired two-tailed t-test. **(f)** (Left) Ensemble *MSD* curves for liposomes in stiff stress relaxing matrix. (Right) Value for transport exponent α for the *MSD* curve. Error bars denote 95% CI. Data are for N = 58 tracks. **(g)** Mean diffusion coefficient $D_{1.06s}$ for liposomes in stiff stress relaxing matrix from (f). **(h)** Values for α and mean $D_{1.06s}$ plot for all groups of EVs in matrix measured in this study fit to a standard one-phase association curve. **(i)** Distributions of the change in local transport coefficient $\Delta D_{0.53s}$ calculated at time ~4.26 seconds are similar for AQP1-depleted EVs (N = 613) versus a control (N = 659). Particles are analysed for $N \geq 180$ tracks for each condition. Unless stated otherwise, error bars denote SEM.

time required for EVs to escape cages (Fig. 3.14e). Liposomes encapsulated in the stiff stress relaxing matrix exhibited $\alpha \approx 0.65$ (Fig. 3.14f) with a much lower $D_{1.06s}$ (Fig. 3.14g), which suggests that the presence of lipid membrane alone is not sufficient for an enhanced EV transport. Pulling values from all the experimental groups of EVs in a matrix shows that α increases with increased $D_{1.06s}$, but becomes saturated near $\alpha \approx 1.0$ when $D_{1.06s}$ is higher than 0.1 μm^2/s (Fig. 3.14h), which suggests that a threefold decrease in $D_{1.06s}$ via AQP1 depletion is less likely to be sufficient to significantly decrease α. Finally, AQP1 depletion did not affect the spread of $\Delta D_{0.53s}$ (Fig. 3.14i), which indicates the independence of AQP1 with fluctuating transport motion.

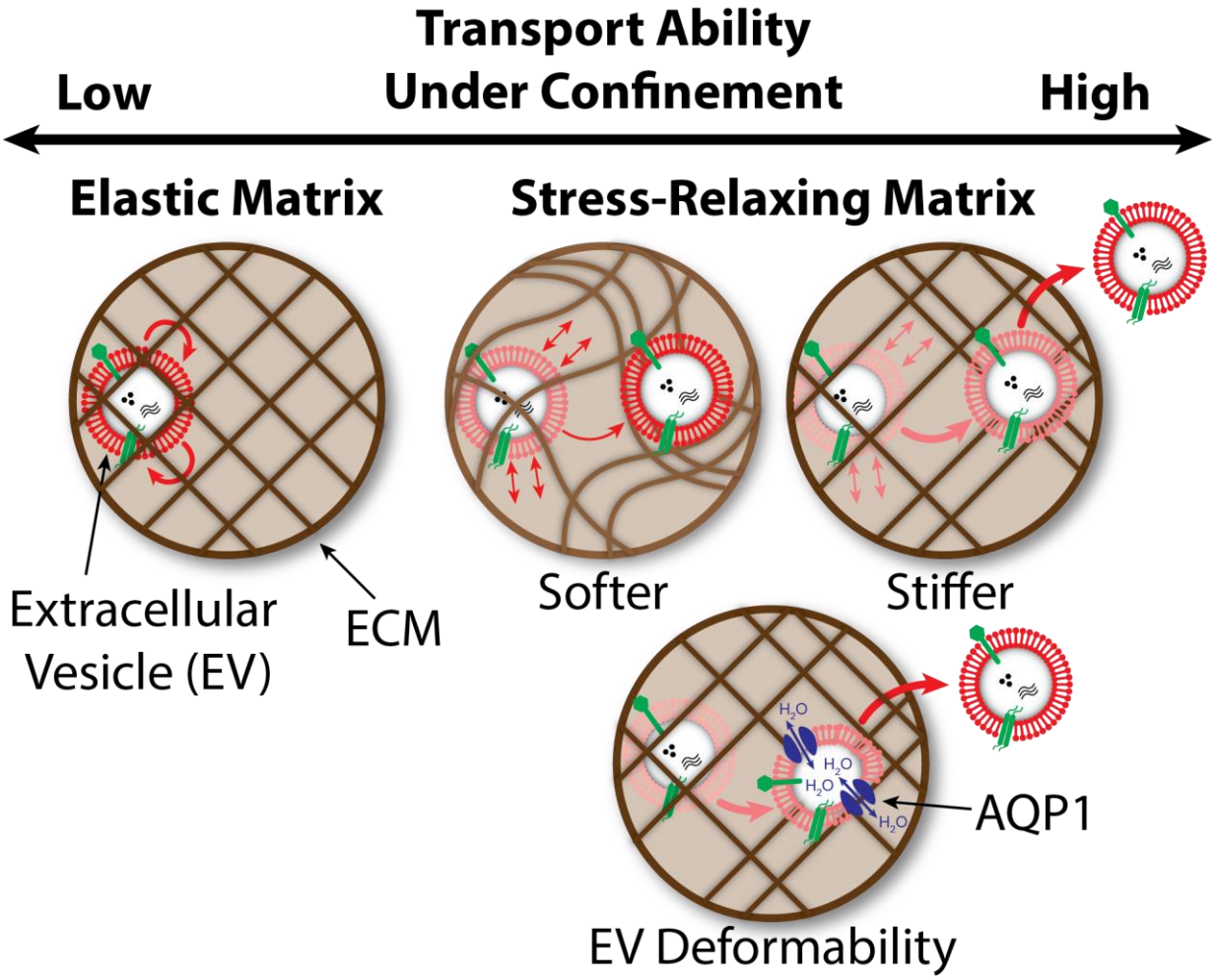

Figure 3.15. Model for EV transport under confinement. EVs exist trapped in an elastic matrix, whereas matrix stress relaxation allows EVs to escape confinement. Stiffness in a stress relaxing matrix leads to fluctuating transport motions, which further increases EVs ability to transport. Furthermore, AQP1 present on EVs mediates water permeation within the EVs, which leads to a greater EV deformability and enhanced transport under confinement.

3.5 DISCUSSION

The results describe the ability of EVs to transport in a polymer matrix with an absence of matrix degradation, despite EVs being larger than the average mesh size of the matrices. The matrix stress relaxation allowed the EVs to readily escape cages formed by the polymer network (Fig. 3.15). A stiff matrix increased the fluctuating EV transport motions, and thus the combination of stiffness and stress relaxation led to a greatly enhanced EV transport. EVs were also subjected to water permeation through AQP1, which allowed the EVs to become more deformable by altering their volume, which enabled their escape from confinement. This behavior is reminiscent of a model of the hopping diffusion of nanoparticles in entangled polymer matrices [199-201], in which it is hypothesized that nanoparticles show the ability to slide through a matrix under some conditions. The phospholipid content of EVs vary [105], and thus it will be interesting to determine whether and how these contents affect EV transport in matrix, as lipid asymmetry was shown to affect EV membrane stability [202]. The observation that AQP1 mediates EV deformability and the resulting transport in ECM is important because the deformability of synthetic nanoparticles with lipid bilayers was recently shown to dramatically affect their accumulation in tissues both in vitro and in vivo [184]. Future studies will test whether the presence of water channels on lipid vesicles alone is sufficient or if other membrane components are also necessary to facilitate EV transport under confinement in matrix. Furthermore, the 3D particle tracking approach utilized here can be extended to study EV transport in various environments, for investigating or treating diseases implicating EVs. Finally, the results may inform how therapeutic EVs can potentially be modified to better facilitate their delivery through tissue ECM. In summary, this study opens new avenues of investigations into EV transport behaviors that occur in the ECM.

4. MODELING OF EXTRACELLULAR VESICLE TRANSPORT IN MATRICES

4.1. ABSTRACT

Despite being ~10-fold larger in size than the average polymer mesh within a matrix, we recently reported the ability for extracellular vesicles (EVs) to transport within decellularized extracellular matrix and viscoelastic hydrogels. To better understand this unexpected phenomenon, we developed a model based on the theory of hopping diffusion of nanoparticles that interface with polymers. Using this model, we show that the ability of EVs to transport in a reversible network versus a permanent network is explained by a lower bond energy of crosslinks, which leads to a lower activation energy required for particles to slip through the mesh and undergo hopping diffusion. We show experimentally that the matrix stress relaxation properties impact this bond energy, suggesting that EVs impose a strain on the mesh. We also show that synthetic nanoparticles do not exhibit fast transport characteristics as EVs in the same matrix, and we quantify these and incorporate in the model by introducing a particle-type dependent parameter. In summary, we explain EV transport in a nanoporous matrix using a model of hopping diffusion, which has implications for further understanding complex interactions between biological nanoparticles and extracellular matrices.

4.2. INTRODUCTION

Some regions of the body are composed of a biological extracellular matrix (ECM) through which soluble factors must transport to maintain tissue homeostasis. Soluble factors such as small molecules and proteins oftentimes exhibit a hydrodynamic radius smaller than the mesh

size of ECM, which means that they can transport relatively freely through the ECM mesh. However, as factors become larger relative to the ECM mesh, transport is less well understood, as interactions between factors and the matrix become more important in determining transport – if transport is possible at all [95]. Studies have shown that ECMs can act as a selective barrier, 'filtering' larger particles based on properties such as size [203], charge [191, 204], pH [191], and stiffness [93], among others. However, it remains possible that larger particles such as nanoparticles can transport through the selective ECM barriers [93, 205], and some mathematical frameworks [206-208] have been established as nanoparticle transport through ECM is beginning to be studied in greater detail.

Extracellular vesicles (EVs), nano-sized particles composed of a lipid bilayer, are released by cells for the purpose of intercellular communication. EVs are present within interstitial regions in tissues, where they need to transport through matrix to avoid accumulation and reach target cells. We recently discovered the ability of EVs to transport in tissues and engineered viscoelastic hydrogel matrices despite the measured average matrix mesh size being ~10-fold smaller than the EVs diameter [132] (Chapter 3). However, EV transport only occurs to a significant extent if the matrix exhibits a stress relaxing versus elastic property. Furthermore, EV composition plays an important role, since lyophilized EVs or EVs depleted of the water channel aquaporin-1 on their surface show hindered transport under the same conditions. In contrast to nanoparticles transporting freely in solution, EVs exhibit erratic fluctuating transport motions in matrix, which suggests a unique mode of transport.

A recent study describes how nanoparticles encapsulated in polymer melts or matrices can navigate the mesh by transporting or 'hopping' through polymers [199]. A particle confined within a dense polymer solution or matrix can undergo 'hopping diffusion' by overcoming an

activation energy to slip through polymer loops existing within the solution or matrix. Absent any significant changes in EV size, navigating within the matrix through polymer loops by 'hopping diffusion' is a plausible potential mechanism by which EVs could transport in this circumstance, because it explains how a particle can transport within a matrix where it is confined with a diameter larger than the matrix mesh size. Furthermore, the mechanism explains how EVs can show differential transport due to matrix mechanical properties and EV composition. This model has been applied to partly explain molecular [209], protein [210], and nanoparticle [211] transport in dense polymer solutions and matrices [212]. Additionally, it has been applied to hydrogel systems controlling nanoparticle release for therapeutic applications [213, 214] . However, the relevance of hopping diffusion theory in describing EV transport in viscoelastic matrices remains unclear.

4.3. MATERIALS AND METHODS

Hydrogel Preparation

Raw sodium alginates with different molecular weights, low (5/60, ~40 kDa), medium (10/60, ~120 kDa), and high (LF200, ~240 kDa) were obtained from FMC Corporation. Hydrogels were formed as described in Chapter 3.3. The 'high'-MW hydrogel was formed by using 1% 10/60 and 1% LF200 with 15mM $CaSO_4$. The 'medium'-MW hydrogel was formed by using 2% 10/60 with 20mM $CaSO_4$. The 'low'-MW hydrogel was formed by using 1% 10/60 and 1% 5/60 with 20mM $CaSO_4$.

See Chapter 3.3 for other experimental methods used for this Chapter. Mathematical analyses were conducted using MATLAB R2020a. Data fitting was performed using a least-squares approach with GraphPad Prism 9.0.0.

4.4. RESULTS

We sought to develop a mathematical model of EV transport in hydrogel networks (Fig. 4.1a) based on the concept of hopping diffusion. As reported in Chapter 3, the mean size of EVs is around 100nm while the apparent average mesh size of synthetic alginate hydrogel matrix is ~10-fold smaller as measured by differential scanning calorimetry [178] (Fig. 4.1b). Despite being much larger than the mesh, EV transport does occur in this matrix but only if the hydrogel matrix is formed by reversible ionic bonds, which confer a stress relaxing bulk mechanical property (Fig. 3.7). If instead the matrix is composed of permanent covalent bonds, which leads to an elastic bulk mechanical property, the EVs do not transport (Fig. 3.7). To explain this phenomenon, we first sought to develop a mathematical model of a nanoporous hydrogel network consisting of permanent crosslinks with encapsulated EVs. After visualizing the motion of fluorescent EVs expressing CD63-Katushka2S (see Chapter 3.3) in matrix, particles can be tracked by measuring the mean square displacement (MSD) of particles over time (t)

$$MSD(t) = K_a t^{\alpha} \qquad \text{(Equation 4.4.1)}$$

with K_a as transport coefficient and α as transport exponent. The value of α indicates the ability of particles to transport, with $\alpha = 1$ indicating Brownian diffusion and $\alpha < 1$ indicating sub-diffusion. EV transport is significantly impaired in the elastic network, with value of α ~ 0.05 (Fig. 4.1c), suggesting that EVs are completely trapped in cages formed by the network.

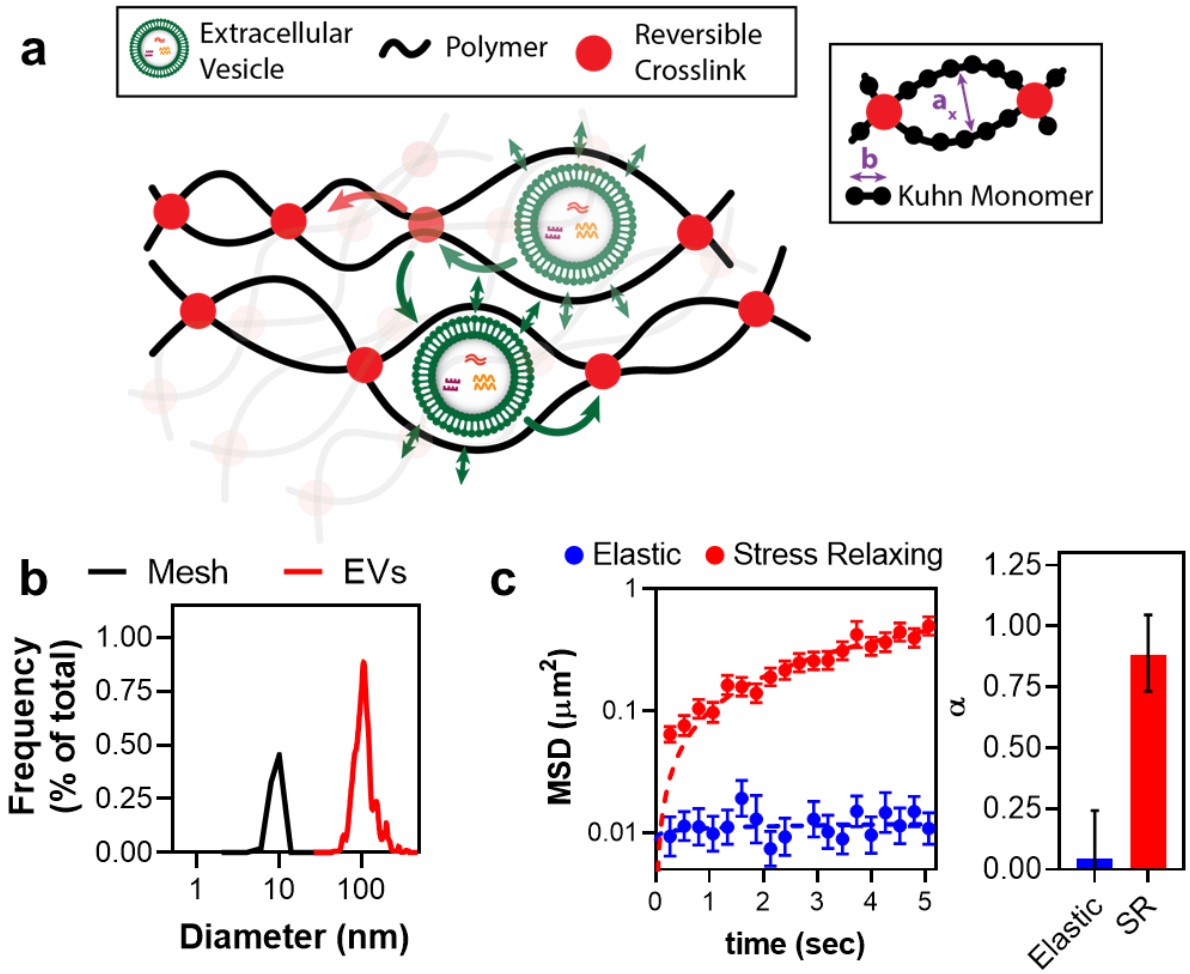

Figure 4.1. EVs are larger than alginate hydrogel matrix mesh, where mechanical properties determine EV transport. (a) EVs confined in a polymer matrix can undergo transport if crosslinks are reversible. Thermal fluctuations of EVs lead to a strain imposed on crosslinks of a viscoelastic material, leading to remodeling of crosslinks due to stress relaxation and subsequent transport of EVs through the mesh. a_x = average matrix mesh size. **(b)** Representative size distributions of matrix mesh diameter (a_x) versus EV diameter (d). Mesh is calculated by differential scanning calorimetry, N = 1 hydrogel. For EVs, data represents the mean of $N = 3$ preparations. **(c)** Stress relaxing (SR, N = 279 tracks) versus elastic (N = 89) matrix facilitates EV transport in terms of $MSD(t)$ (Left) and transport exponent α (Right). Error bars

To model the alginate hydrogel network used in our studies, we defined each polymer strand between two neighboring crosslinks with N_x Kuhn monomers [215] of size b. The mean distance between crosslinks in the network is the mesh size a_x (Fig. 4.1a). For this model, we chose b as 1.5 nm, which is on the order of reported previously for alginic acid [216, 217] and a_x (~10 nm) as the measured mesh size as shown in Fig. 4.1a. In this case, EV diameter d (~100 nm) is significantly greater than a_x and thus the network will form 'cages' of polymers around the EVs. We measured the stress relaxation properties of hydrogels as described in Chapter 3.3 to show the difference between permanent and reversible networks (Fig. 4.2a, i). We fit the normalized force (S_N) data over time to an equation for hydrogel stress relaxation [218, 219]

$$S_N(t) = \frac{S(t)}{S_0} = \frac{E_R}{S_0}\left(1 + \frac{\lambda_s - \lambda_e}{\lambda_e} e^{-\frac{t}{\lambda_e}}\right) \qquad \text{(Equation 4.4.2)}$$

where S is stress, S_0 is initial stress, E_R is the relaxed modulus, λ_s is the time of relaxation under constant load, and λ_e is the time of relaxation under constant strain. In this case, we hypothesize that λ_e is relevant since spatially confined, thermally fluctuating particles in a polymer mesh likely will apply a constant strain. As expected, the value for λ_e is much higher for the permanent network than the reversible network (Fig. 4.2a, ii). Polymers are likely strained due to thermal vibration of EVs, which is a key element of the model (Fig. 4.1a). EVs probe the local cage environment on a time scale of the monomer relaxation time [220]

$$\tau_0 = {\eta_s \xi^3}\Big/{k_b T} \qquad \text{(Equation 4.4.3)}$$

with ξ the polymer correlation length, η_s the solvent viscosity, k_b Boltzmann constant and T temperature. The correlation length ξ is related to polymer volume fraction φ with Flory exponent ν as [221]

$$\xi \cong b\varphi^{-\nu/(3\nu-1)}. \qquad \text{(Equation 4.4.4)}$$

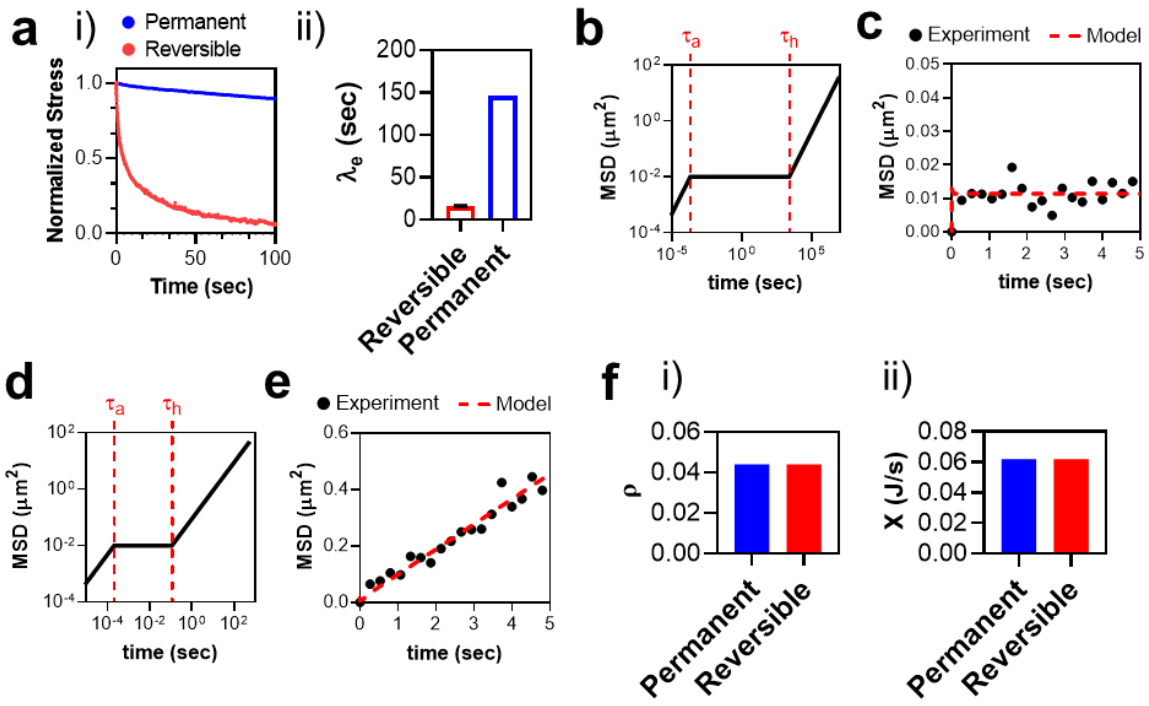

Figure 4.2. A model for EV transport in an alginate matrix with permanent or reversible crosslinks. (a) (i) Alginate hydrogels were created with different types of crosslinking, leading to differential stress relaxation properties. Data represent the mean of N = 3 hydrogels. (ii) Relaxation under constant strain λ_e fit for data in (i) using Equation 4.2. Error bars are 95% confidence interval (CI). **(b)** EVs encapsulated in alginate matrix with permanent crosslinks initially probe cages and remained trapped there for relevant time scales. **(c)** Model of EVs encapsulated in alginate matrix with permanent crosslinks closely follows experimental data shown in Fig. 4.1. **(d)** In contrast to (a), EVs in alginate matrix with reversible crosslinks undergo hopping diffusion more readily. **(e)** Model of EVs encapsulated in alginate matrix with reversible crosslinks closely follows experimental data shown in Fig. 4.1. **(f)** Values for (i) ρ and (ii) X are similar for both conditions, demonstrating robustness of the model.

Alginate hydrogels are dilute with $\varphi \sim 0.062$ if the density of alginate is 1.67 g/cm^3 [222], and we assume the solvent is a good athermal solvent ($v = 0.588$). Using these values, $\xi \sim a_x$ (~10 nm). On the time scale τ_0, particles transport with a linear *MSD* (α = 1) on the length scale of the cage volume ($a_x{}^3$) divided by particle diameter

$$MSD(t) = \frac{a_x{}^3}{d}\left(\frac{t}{\tau_0}\right) \qquad \text{(Equation 4.4.5)}$$

from ($0 < t < \tau_a$). At time τ_a, where particles reach the mesh size limit [221]

$$\tau_a = \tau_0 \left(\frac{a_x}{b}\right)^3, \qquad \text{(Equation 4.4.6)}$$

particles become coupled to the mesh and thus remain trapped at an MSD plateau determined by the size of cages $a_x{}^3$ with value $MSD(t = \tau_a)$:

$$MSD(t = \tau_a) = \frac{a_x{}^3}{d}. \qquad \text{(Equation 4.4.7)}$$

from ($\tau_a < t < \infty$). However, in a model including the potential of hopping diffusion, particles will gain the ability to transport between network cages through polymer loops. The likelihood of occurrence for this energetically unfavorable process has an energy barrier ΔU that is related to the squared ratio between particle and mesh size [199]

$$\Delta U \cong k_b T \frac{d^2}{a_x{}^2} + \gamma. \qquad \text{(Equation 4.4.8)}$$

We added the term γ to also consider the strength of the bonds between crosslinks within the hydrogel network. Since the key difference between covalently and ionically crosslinked matrix is the stress relaxation time of polymers, we sought to incorporate a matrix stress relaxation time in the γ term as

$$\gamma = \frac{E_b}{N_A} * X\lambda_e \qquad \text{(Equation 4.4.9)}$$

where E_b is the crosslink bond energy, N_A is the Avogadro constant, and X is a fit parameter with units Joules per second. The permanently crosslinked alginate hydrogels used in this study were crosslinked by tetrazine-norbornene click chemistry [126] with a covalent bond strength ($E_{b,P}$) we estimate as the sum of a bond component ($E_{b,C-C}$) and a ring strain component ($E_{b,RS}$) with estimated values of 485 [223] and 85 kJ/mol [224] respectively, to yield

$$E_{b,P} = 2E_{b,C-C} + E_{b,RS} = 2\left(485\frac{kJ}{mol}\right) + 85\frac{kJ}{mol} = 1055\frac{kJ}{mol}. \qquad \text{(Equation 4.4.10)}$$

The ΔU required for particles to commence hopping diffusion will determine the timescale τ_h that hopping occurs [199]

$$\tau_h = \tau_a \frac{a_x}{d} \exp\left(\rho * {}^{\Delta U}/_{k_b T}\right). \qquad \text{(Equation 4.4.11)}$$

We incorporated a particle-intrinsic factor ρ being the contribution by EVs to be able to transport in the matrix. For example, we reported that EVs are deformable in part by virtue of water channels existing within their membrane [132], which are partially necessary to facilitate their transport in the viscoelastic matrix. A more deformable particle will require less energy to move through polymer loops by hopping diffusion, and this should be captured in the model. In addition, it is possible that different types of particles may exhibit distinct intrinsic thermal fluctuations, which could differentially impact a strain on a polymer network. From $(\tau_h < t < \infty)$, particles will follow a linear MSD

$$MSD(t) = \frac{{a_x}^3}{d}\left(1 + {}^{t}/_{\tau_h}\right). \qquad \text{(Equation 4.4.12)}$$

Under these conditions, EVs in an alginate hydrogel network with permanent crosslinks do not commence hopping diffusion within the measured time (Fig. 4.2b) and the model closely follows reported experimental data for the permanent network (Fig. 4.2c).

We next considered a matrix with the same amount of crosslinking and elastic modulus but instead, the crosslinks are reversible ionic crosslinks and thus the hydrogel matrix recapitulates the stress relaxing matrix in Fig. 4.1c. In this case, crosslinks are formed between free calcium ions (Ca^{2+}) and carboxylic acid residues on the alginate chains [67]. These will have a lower reversible network bond energy ($E_{b,R}$) we estimate as ~250 kJ/mol [225]. As expected, this modification leads to a significantly less time for particles to begin transporting in the matrix (Fig. 4.2d) and follows experimental data accordingly (Fig. 4.2e) with the same values for ρ (Fig. 4.2f, i) and *X* (Fig. 4.2f, ii) as in the case of the permanent network, suggesting that these parameters are independent of crosslinking type. Importantly, the mesh size a_x is still constant as measured experimentally.

Next, we wanted to determine whether the fit parameters ρ and *X* are truly independent of matrix stress relaxation properties. Thus, we created additional alginate hydrogels by increasing the polymer molecular weight (MW) while holding the total amount of polymer constant and measured their stress relaxation properties (Fig. 4.3a, i). We named these hydrogels by their relative polymer MW: 'high', 'medium', and 'low', where 'low' is the hydrogel used in Chapter 3 and Fig. 4.2c. Importantly, the 'high'- and 'medium'-MW hydrogels exhibit the same storage modulus *G'* as the 'low'-MW hydrogel (Fig. 4.3b, i), but the ratio between storage and loss modulus G''/G' is expectedly decreasing with higher polymer MW (Fig. 4.3b, ii). Fitting the data for EVs transporting in these matrices against the model demonstrated that the *MSD* vs time curves follow the model as expected with similar values of the fit parameters ρ (Fig. 4.3d, i) and *X* (Fig. 4.3d, ii). Thus, matrix stress relaxation determines EV transport ability and a decreasing λ_e is associated with an increased ability for EVs to transport.

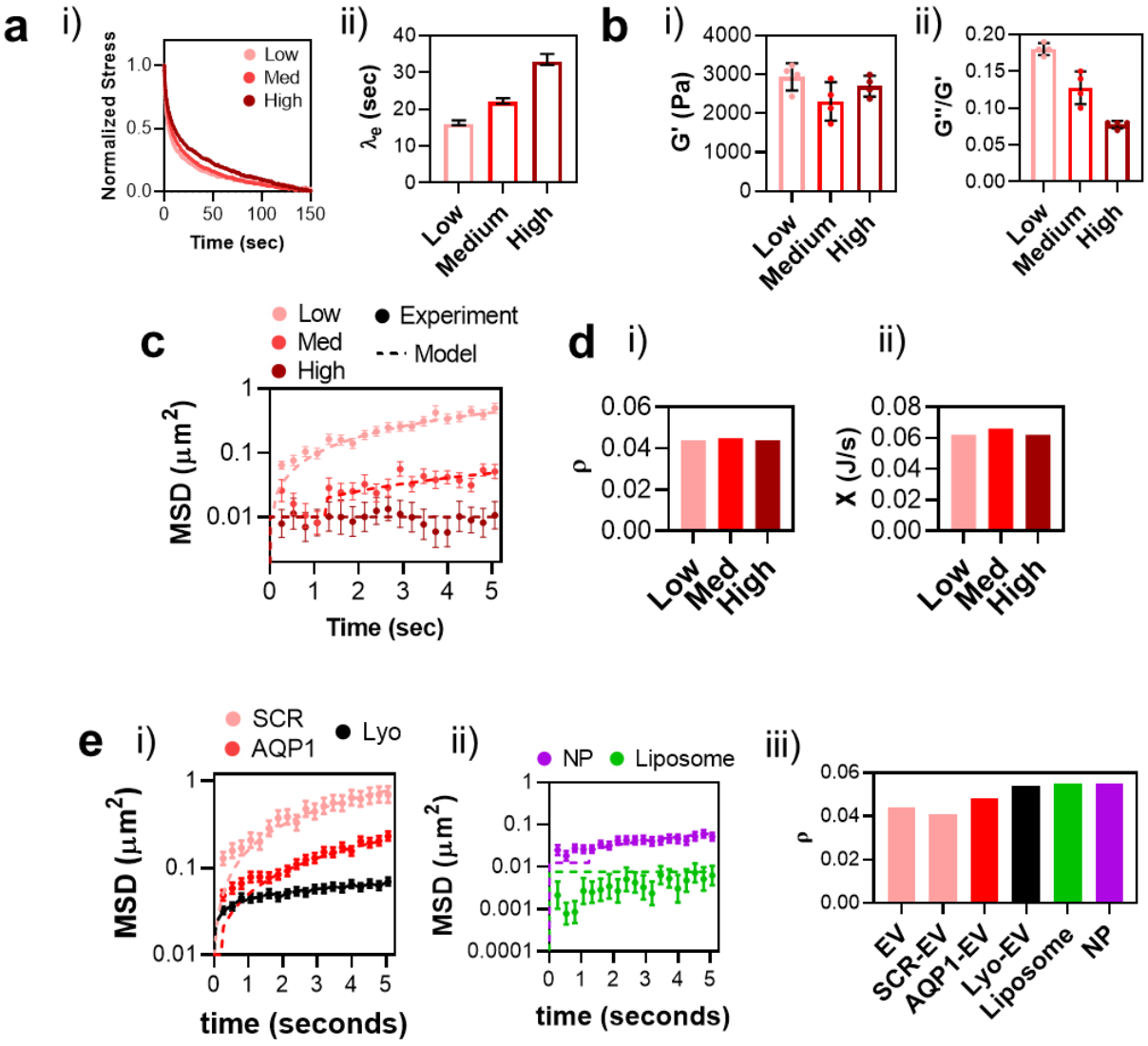

Figure 4.3. Dependence of the model on matrix stress relaxation and particle type. (a) (i) Alginate hydrogels were created with different molecular weight, leading to differential stress relaxation properties. Data represent the mean of N = 3 hydrogels. (ii) Relaxation under constant strain λ_e fit for data in (i) using Equation 4.2. Error bars are 95% confidence interval (CI). **(b)** (i) Storage modulus *G'* for hydrogels with different MW and λ_e measured at 1 Hz. N = 4 hydrogels. (ii) *G"/G'* for hydrogels with different MW and λ_e. N = 4 hydrogels measured at 1 Hz. **(c)** EVs encapsulated in hydrogels with different MW and λ_e fit using the model. N = 27 tracks ('High'), N = 54 tracks ('Med'), N = 279 tracks ('Low'). **(d)** Fit values for (i) ρ and (ii) *X* using data in (c). **(e)** (i) EVs depleted of AQP1 (AQP1) or lyophilized (Lyo) tracked in the 'low'-MW hydrogel fit the model by increasing ρ. SCR = scrambled siRNA control. N = 613 (SCR), N = 659 (AQP1), N = 618 (Lyo). (ii) Synthetic polystyrene nanoparticles (NP) and liposomes fit the model by increasing ρ. (iii) Values for ρ used in (i) and (ii). Error bars denote SEM.

Since the parameter X directly modifies the contribution of matrix stress relaxation time λ_e, we sought to determine whether the parameter ρ can account for intrinsic particle-dependent contributions on their ability to transport in a matrix, such as particle rigidity and particle fluctuation [226], including the ability of EVs to become more deformable partly through water channels such as AQP1 present on their surface (Fig. 3.13). Thus, we depleted AQP1 on the surface of EVs using siRNA, tracked their transport over time versus a control in the 'low'-MW stress relaxing matrix, and fit the MSD vs time curves using the model (Fig. 4.3e, i) by holding X constant as determined in Fig. 4.3d. We also tracked lyophilized EVs as a comparison. This shows that a higher ρ value captures the effect of AQP1 depletion (scrambled vs AQP1 siRNA = 0.041 *vs.* 0.048), but other unknown factors may play a role as well, since lyophilized EVs (ρ = 0.055) still show a higher ρ value than AQP1-depleted EVs (ρ = 0.048). Next, we tested whether ρ captures particle type-dependent effects while maintaining the integrity of the model. Thus, we tested the transport of synthetic polystyrene nanoparticles and liposomes with a similar lipid composition as EVs in the stress-relaxing matrix (Fig. 4.3e, ii). Polystyrene nanoparticles are known to exhibit an order of magnitude higher Young's modulus [227] than EVs [185, 228], which potentially accounts for the increased ρ (~0.055) for these particles. In contrast, liposomes exhibit a similar or perhaps even lower Young's modulus than EVs [185, 229], suggesting that other factors, such as decreased particle fluctuation, can potentially increase the ρ parameter (~ 0.055). With all else equal, an increasing ρ means a decreasing ability for particles to transport. Importantly, the model accounts for transport behaviors for six different particles (Fig. 4.3e, iii) with different ρ values, demonstrating the robustness of the model.

4.5. DISCUSSION

These results illustrate how mathematical modeling of the polymer matrix with an account of the potential for hopping diffusion of nanoparticles can explain how EV transport within matrices with a mesh size smaller than the diameter of encapsulated particles. Here, we illustrate the key properties of a reversible network, as opposed to a permanent network, in how it leads to an unexpected amount transport for EVs confined within a crosslinked polymer matrix. This occurs in part due to a difference in bond energy of crosslinks between a covalently-crosslinked (permanent) network and an ionically-crosslinked (reversible) network. Furthermore, we characterize the ability for EVs to transport in terms of stress relaxation times and particle-intrinsic factors, the latter which are related to an intrinsic property of particles to transport within a matrix. We show that with decreasing matrix time of relaxation under constant strain applied by thermally fluctuating particles, particles show an enhanced ability to transport. EVs that are lyophilized or depleted of the water channel AQP1 fit the model with a higher particle-dependent constant ρ. We also compared the transport of synthetic polystyrene nanoparticles and liposomes versus EVs and calculated the resulting particle-dependent constant, demonstrating that EVs have a lower ρ than nanoparticles and liposomes.

Though transport of nano-sized particles is important to understanding fundamental biology as well as for therapeutic applications, the factors affecting if and how nano-sized particles transport through a matrix environment remain mostly unclear [95]. Thus, the mathematical framework presented in this study can be useful for studying particle transport in matrix by incorporating other materials, material properties, and particles in future studies. Additional data will better inform the model to become more generalizable for particle transport in different types of matrices. In particular, the relationship between bond energy and

characteristic stress relaxation time is assumed to be independent in the present study, but they may in fact be related. The stress relaxation properties of matrices manifest in part due to the nature of crosslinks, but as shown here, other parameter such as polymer molecular weight also play a role. Future studies should more robustly explore the relationship between crosslink bond energy and material stress relaxation and incorporate any relevant results into the model. Additionally, it remains possible that particles transporting in matrix alter the local mechanical properties – this possibility can be addressed in future studies employing microrheology or similar methods.

As currently presented, the framework remains to be further developed to explain exactly why EVs impose an enough strain on the mesh to transport through a matrix with a faster stress relaxation property than other nanoparticles or lyophilized EVs. Other nanoparticles such as gold nanorods [226] exhibit thermally driven deformations. It is possible that EVs undergo similar thermally driven deformations by dynamic regulation of their internal water contents or membrane structure. Furthermore, the mechanism of reversible crosslink displacement by EV motions remains to be explained. Application of various mathematical models that address the 'narrow escape problem' [230], which have been applied to explain transport and chemical reactions within cells, may help elucidate the potential interactions between particle transport and polymer crosslinks. The results also suggest that particles and matrices can potentially be engineered to tune particle transport, which can be relevant for various controlled release applications. In sum, this study quantitatively explains the unique ability for EVs to transport in a nanoporous polymer matrix and highlights the contributions of matrix stress relaxation and particle type in facilitating this transport.

5. CONCLUSIONS AND FUTURE DIRECTIONS

5.1 CONCLUSIONS

Cells exist in a microenvironment with biophysical properties that regulate their phenotypes. To communicate with other cells, they readily secrete nano-sized lipid bilayer particles called extracellular vesicles (EVs). However, it is unclear how biophysical properties of the environment regulate EV production by cells. Furthermore, once EVs are produced, it is likely that they must navigate the extracellular matrix (ECM) which is often a dense mesh with an average mesh size smaller than the EV diameter. It also remains unclear whether EVs can transport through this mesh, and if so, whether biophysical properties of the matrix or the EVs themselves affects transport. This thesis sought to understand and describe the biophysical characteristics of extracellular vesicle production by cells and transport through the matrix to better understand the biology of EVs as well as to improve their potential for clinical applications.

In Chapter 2, synthetic hydrogels were designed with various stiffnesses and stress relaxation properties to recapitulate salient aspects of the endogenous environment. MSCs cultured on softer hydrogels produce significantly more exosomes than MSCs on stiffer hydrogels, which takes place due to less outside-in integrin signaling occurring on softer hydrogels. Importantly, exosomes derived from cells cultured on substrates of different stiffness have similar size, morphology, and presence of membrane markers, suggesting that substrate stiffness regulates number of exosomes produced without changing other properties. Additionally, exosomes from substrates of different stiffness retain similar amounts of therapeutic cargoes and are similarly efficacious against a model of acute lung injury. MSCs

cultured on softer substrates show enhanced MVB transport which is correlated with a greater number of events where MVBs fuse with the plasma membrane. Decreased MVB transport and fusion on stiffer substrates is likely due to a denser actin mesh within cells since inhibition of Arp2/3 restores MVB transport and exosome release. These results demonstrate the dependence of therapeutic exosome production by MSCs on biophysical properties of the environment. Although the results suggest more optimal conditions for functional EV production by MSCs, the fundamental concepts presented in this study can be adapted and scaled to different EV production systems that require cells to interface with materials.

In Chapter 3, it was shown that EVs isolated from MSCs can transport readily within a decellularized lung matrix that exhibits a mesh size smaller than that of EVs. This finding was extended by demonstrating that EVs release to a greater extent than nanoparticles or liposomes of a similar size after encapsulation in synthetic alginate hydrogels. Tracking individual EVs in the matrix confirmed that EV transport is possible only in hydrogels with a stress relaxing property; surprisingly, transport was greatly increased in stiffer stress relaxing hydrogels. Lyophilized EVs did not show increased transport in stress relaxing hydrogels, suggesting that membrane integrity of EVs is likely important in driving their transport in matrix. Knockdown of the water channel AQP1 made EVs less deformable with a higher stiffness, leading to a decreased transport in matrix. Thus, matrix mechanics and water permeation through AQP1 significantly affect the unexpected ability for EVs to transport in nanoporous matrix. In sum, these results demonstrate the unique ability for EVs, as opposed to nanoparticles and liposomes, to transport under confinement within a matrix and highlight a striking dependence on matrix properties and vesicle composition. The findings are important since they suggest that EVs can

be cleared from and transported through matrices in the body, thereby opening new avenues of investigation into EV biology and therapeutics.

In Chapter 4, a mathematical model for EV transport through nanoporous matrices was proposed based on a nanoparticle ‘hopping’ diffusion model through entangled polymers. The model accounts for greatly enhanced transport for EVs in reversible versus irreversible crosslinking networks by considering the relative bond energy between reversible and irreversible crosslinks. Matrices exhibiting faster stress relaxation properties show lower bond energy, thereby enabling EVs to more readily overcome an energy barrier. Transport is also particle-dependent, as synthetic nanoparticles or liposomes do not transport to the same great extent as EVs, which is likely due to both intrinsic ability of thermally fluctuating particles to overcome threshold bond energy and deformability of particles.

Findings presented in this thesis are significant because they lend insight into potential issues in effectively translating EVs as therapies used in the clinical settings. By demonstrating that EV production depends on the biophysical properties of the environment, culture environments used for production of EVs for therapeutic purposes can be better designed to increase EV yield by biomaterial design. Understanding mechanisms behind this process is of fundamental importance to advance both the basic science of exosome-mediated intercellular communication and the manufacturing of therapeutic exosomes from cells using biomaterials, especially because cell-material interactions have largely been overlooked in these contexts. By demonstrating that EVs can transport through nanoporous matrices, interactions between EVs and interstitial tissues in the body can be studied to determine the extent of EV trafficking within the environment. Additionally, other aspects of EV compositions can be studied to further elucidate their dependence on EV transport behaviors. With knowledge presented in this thesis,

several engineering projects can be conducted to improve EVs as therapeutics; for example, hydrogel carrier systems can be designed so that encapsulated therapeutic EVs can release from them after delivery to deep tissues, prolonging EV release to treat disease.

Together, this thesis states that biophysical properties of the environment control EV production by cells and regulate their anomalous transport through nanoporous matrix. Cells produce more EVs when the substrate is softer but will likely accumulate EVs locally because they are not as readily transported in a softer matrix. In contrast, EVs are less available around cells in a stiffer matrix because they are produced in a less quantity and are more readily dispersed. Since MSCs around a soft matrix are also more likely to be near the vasculature [231], it is possible that MSCs would produce more EVs there since there are more opportunities to communicate with effector cells that exist within vascular regions [232, 233]. Furthermore, in these regions EVs will be more likely to enter the vasculature, where they can be transported for delivery to distant regions of the body. Additionally, if EVs are cleared through the vasculature, there is less need for their transport through matrix, as their accumulation is more likely offset by clearance into the vasculature. MSCs in a denser and stiffer interstitial matrix are likely sparser, since matrix is deposited by cells, which on average will tend to separate cells. So, if EVs are produced in a stiffer matrix where cells are more distant, it seems plausible that EVs should be able to better navigate the matrix to reach distant cells. It follows that if EVs transport more readily within a stiffer matrix region, there is less need to produce as many EVs since their efficiency in reaching targets is higher on a per EV basis. In contrast, in softer matrix where EV transport is impaired, a higher production level of EVs would be required to offset less efficient transport to distribute EVs to recipient cells. These ideas are summarized in Figure 5.1. Taken as

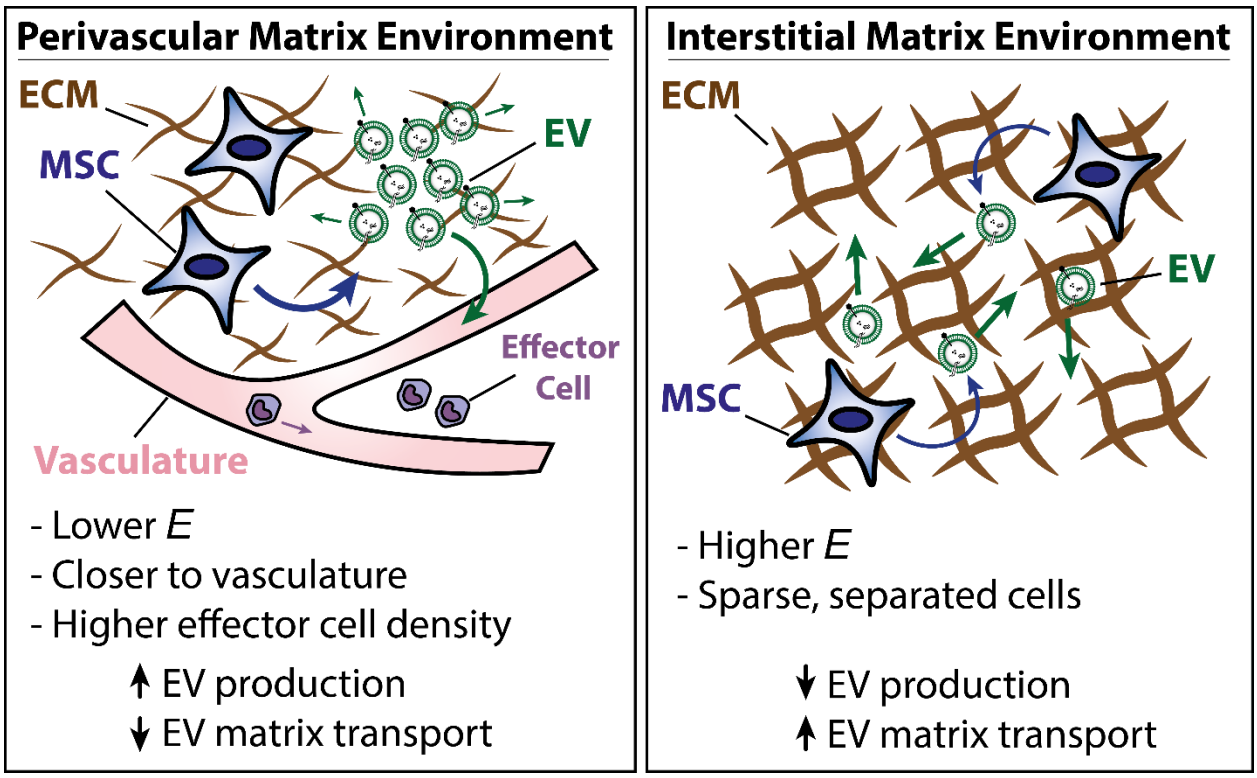

Figure 5.1. The biophysical characteristics of EV production and transport. Physiological environments from which MSCs are derived can be broadly categorized into perivascular environments, which tend to be softer and near vasculature, and interstitial environments, which tend to be stiffer with sparser cell distributions. Results presented in this thesis support the idea that MSCs produce more EVs in a softer perivascular environment, where EVs are less able to transport longer distances through matrix. In contrast, in a stiffer interstitial environment, EVs are produced less but have a greater ability to transport longer distances through matrix.

a whole, this thesis introduces significant insight on the interactions between cells and the extracellular matrix in the regulation of EV production and transport.

5.2 FUTURE DIRECTIONS

The work describes the biophysical relationship between EV production by cells and EV transport through the matrix. From a biological standpoint, the work opens new avenues of investigations into EV biology by further describing their production mechanisms and introducing a novel concept of EV transport through nanoporous matrix. It will be interesting to further delineate the mechanisms behind matrix mechanics-mediated EV production. For example, the results suggest that actin branching mediated by Arp2/3 in cells is less on a softer substrate leading to enhanced MVB transport and fusion; however, the actin branching pattern and morphology itself can affect cellular functions [234]. Thus, it will be important to study the character of the actin networks within cells, potentially by imaging live actin distributions at the same time as measuring transport and fusion of MVBs. Furthermore, the various contributions of membrane tension, MCAs, and cytoskeletal tension on exosome release by cells remains to be elucidated. Measuring these will require simultaneous physical manipulation of cellular tension and tracking or measurement of MVB fusion, potentially by using fluorescent imaging combined with atomic force microscopy. Other options include utilizing micropipette systems to directly interface with the cell membrane and apply fluid pressure. An ambitious direction would be to pursue microrheology using optical tweezers to probe regions of the cytoplasm that are currently undergoing MVB fusion to test how fusion affects the regional tension and the underlying contributions of the MCAs. Though in this study the substrate stiffness did not significantly alter the therapeutic contents in EVs relevant to lung injury, it remains possible that EV composition

is affected by the cell response to various chemomechanical properties. For example, mechanics regulate MSC response to TNFα [235], an inflammatory cytokine that can potentially alter content within exosomes.

Along these lines, it will be useful to the field to perform molecular profiling studies to broadly determine potential differences in EV content as a function of differences in EV secretion due to matrix stiffness. Both RNA profiling studies using RNAseq methods and protein profiling studies using mass spectrometry can be performed. Single-cell RNA sequencing has become a popular method in recent years, and single-EV profiling methods are beginning to be reported, such as a method that can profile the surface markers existing on single EVs [236]. Though possible in theory, however, the potential for single-EV RNA sequencing is yet to be realized. Furthermore, other new techniques such as asymmetric flow field-flow fractionation have elucidated more distinct vesicle subsets when isolated based on density and hydrodynamic properties [237]. It will thus be interesting to measure differences in vesicle density and hydrodynamic properties as a function of the substrate mechanical properties from which EVs were derived. This can also potentially be combined with a profiling approach, by separating EVs using asymmetric flow field-flow fractionation and following up with molecular profiling of resulting vesicle subsets. Furthermore, it will be possible to utilize the EV encapsulation methods used in Chapter 3 and Appendix D to separate subsets of EVs that release from hydrogels versus remaining trapped in hydrogels. It is likely that these EV subsets may express or exhibit different compositions based on their transport abilities. Results could provide a clue to whether some endogenous EVs are naturally engineered by cells to travel deeper into tissues to deliver different cargoes.

Because the present study used TIRF imaging to visualize MVBs within cells, the reported transport and fusion events occurred near to the cell membrane as it interfaces with the underlying hydrogel substrate. This suggests that fusion events can occur at the membrane interfacing with the matrix. It remains to be studied how a three-dimensional environment will affect EV release from cells. In a three-dimensional environment, cells will be surrounded by matrix, so they must regulate their membrane totally in relation to its interfacing with the matrix, as opposed to presenting part of the membrane to fluid. It is possible that cells exhibit a different vesicle release behavior depending on whether the interface is fluid or solid, as vesicles have been shown to be directly deposited in the matrix secreted by cells [109]. It will be further interesting to determine whether the mechanism by which cells secrete EVs directly into the matrix provides some force that may propel vesicles to transport through the matrix. Cells can potentially tune EV secretion based on the intended fate of EVs: to be matrix-bound or fluid-phase. A more rigorous investigation of these ideas may shed light on the different populations of EVs that may become matrix-bound or fluid-phase.

Furthermore, since EVs have been shown to sometimes contain matrix degradation proteins, it may be possible that EVs can release themselves from the matrix by degrading the surrounding matrix. This study primarily used alginate hydrogels to encapsulate EVs to precisely study the effects of matrix mechanics on EV transport, since alginate hydrogels are unable to be degraded by any proteins expressed by mammalian cells. Given EVs ability to transport over longer distances in matrix, as described here, it is possible that EVs act as a medium to distribute matrix-degrading proteins throughout the ECM. Furthermore, the matrix stiffness could direct cellular packaging of matrix degrading enzymes into EVs so that they can degrade surrounding matrix after secretion. This seems plausible, since the regulation of matrix degradation by cells is

important for ECM homeostasis, and dysregulation can sometimes lead to diseases such as fibrosis [238].

Based on the results from the present study, it can be hypothesized that material properties and EV deformability are key properties that will affect whether EVs are retained in a matrix-bound form or are able to transport through and release from matrix to exist in the fluid phase. This is a key distinction, since EVs embedded in the matrix have shown the ability to be taken up by cells and induce changes in cell behavior such as driving an M2-phenotype in macrophages [37] and also promotion of directional cell migration [109]. Since cell migration has also been associated with matrix stiffness [239], in the future it can be determined whether differences in cell migration can be associated with differences in EV production as a result of ECM properties. In the case of primary dermal fibroblasts, stiffness-dependent cell migration requires CD44 [240], which was shown here to be expressed in EVs at similar levels independent of substrate stiffness. It will be interesting to determine whether CD44 on EVs regulates matrix stiffness-dependent cell migration phenotypes. Because cell adhesion through integrins is negatively associated with EV production in this work, it is possible that greater EV production under lower adhesion conditions lead to greater amounts of adhesion molecules present within EVs other than CD44. Additionally, the present study did not include the potential for cells to bind to matrix through CD44, and thus it remains possible that given the opportunity to bind CD44, cells will package differential amounts of CD44 in their EVs as a function of matrix mechanical properties.

Showing that water channels present on the surface of EVs regulate their transport in matrix suggests that other channels on the surface of EVs may similarly be regulating their transport or performing other biological functions previously not considered. For example, it is

likely that ion channels work in tandem with water channels on the EV surface to regulate EV volume as occurs in cells [63, 198]. It will be possible to study contributions of different channels on particle volume by creating liposomes with similar lipid compositions as EVs that include one or more transmembrane protein channels and studying the contributions of the channels to particle transport. Additionally, direct measurement of EV water content and efflux rates will be important to measure in determining relative contributions of these channels in regulating volume and deformability. One potential method to measure water content and efflux is through using deuterium oxide, which can be detected by techniques such as Raman microspectroscopy [241]. It is further possible that EVs can secrete different types of their cargoes other than water after they are secreted by cells, thereby serving as delivery vehicles over the course of a given transport route. Lastly, the recent findings that EVs can become embedded in tissues in a matrix-bound form [37] suggests the interesting hypothesis that EVs themselves can contribute to the mechanical properties of matrix within tissues. This can potentially occur if EVs are acting as a crosslinking agent through the presence of moieties on their surface. Indeed, nanoparticles have been functionalized to act as crosslinking agents within hydrogels to form nanocomposite hydrogels [242]. In some cases, these nanocomposite hydrogels can exhibit novel properties that do not exist by virtue of either the nanoparticle or hydrogel component but emerge when the two components are combined [243]. This raises an interesting hypothesis that EVs could alter the properties of matrices in a functional way, and furthermore these properties can potentially be regulated by relative amounts of EVs transporting or remaining matrix-bound, which is likely dependent on their membrane channel compositions.

From an engineering standpoint, the work implies that there may exist optimal environments for cells to produce EVs and optimal environments for EVs to transport.

Bioreactor systems that incorporate cell culture to produce biological products are useful partly because they possess a flow component to scale up production more efficiently. This study showed that EV production rate also depends on the time that cells adhere to a substrate; thus, designing a bioreactor that can periodically attach and detach cells from a surface with defined mechanical properties and ligand density may have the ability to dramatically increase EV yield from a cell culture setting. Furthermore, the flow rates within the bioreactor can be tuned precisely to match EV production kinetics, which will be dependent on cell adhesion time, in order to maximize EV production per cell within the bioreactor. Initial studies can be performed using microfluidic devices [244], which could be scaled up to larger systems eventually. A recent study showed that fibronectin bound on the EV surface facilitates their activation of FAK within ESCs thereby maintaining pluripotency [245]. Since it is likely that free matrix molecules are present within interstitial matrices, this suggests that transport through matrix may induce a supplementary effect to EV bioactivity by introducing matrix molecules on the EV surface. Furthermore, this suggests the possibility to load fibronectin or other matrix molecules on the surface of EVs to further enhance their ability to modify phenotypes of recipient cells. The EV tracking method used in Chapter 3 could be adapted to study the extent of EV transport occurring in tissues endogenously, for example, as a diagnostic tool, since EVs are known to be involved in various pathologies such as cancer. For example, based on the results shown here, tissues which are known to exhibit a more stress-relaxing behavior are predicted to show more EV transport, which can be investigated using the EV tracking method used here. This can be extended to hypothesize phenotypes existing within tissues that may be affected by EV transport behaviors.

EVs can also potentially be engineered to contain different amounts of channel proteins, which may allow their transport ability to become tunable. It is possible that significant increases

in EV deformability will enhance their potential to enter tissues from the bloodstream, which will significantly improve their outlook as potential therapeutics. These insights are particularly important for cases where administered EVs will require transport through a matrix or a vitreous fluid. Recently, it has been shown that MSC exosomes show therapeutic effects against eye diseases [246] such as retinal detachment [247]. Since the eye contains a vitreous fluid, EV transport is likely to be impaired similar to as if it they are encapsulated in a matrix. Thus, a strategy for the treatment of retinal disease can be to tune EV transport properties so that they are better able to transport within vitreous fluid and eventually reach the retina to deliver therapeutic contents. In fact, it was recently shown that the eye vitreous fluid endogenously contains vesicles resembling EVs [248], though it is yet to be determined whether these exist bound within the vitreous or show the capability to transport there.

Some efforts to utilize hydrogel delivery systems for delivering EVs for therapeutic purposes have been reported previously [249]. This is an attractive strategy, because it offers the possibility to control release of EVs over time, which will address the issue of EVs clearing rapidly after systemic administration. Based on the results presented here, a hydrogel delivery system can be engineered with mechanical properties that are optimal for EV transport. The system can be at the bulk scale for implantation, or also be designed at the micrometer scale for injection, which will add the ability for the carrier system and the delivered EVs to reach deeper into tissues such as the vasculature, airways, or lymph nodes. Once trafficked to deep tissues, the hydrogel can release therapeutic EVs over time, substantially increasing the delivery of EVs to target tissues versus a bolus injection or instillation of EVs alone.

In sum, this work that interfaces biology and engineering of EV production and transport suggests numerous avenues for further research and development of novel technologies that explore EV biology and utilize it for potential therapeutic purposes.

APPENDIX A

EXTRACELLULAR VESICLE ISOLATION METHODS

There are two main methods used in this thesis to isolate and concentrate extracellular vesicles: filtration and ultracentrifugation. Filtration is a less time-consuming and easier process, but ultracentrifugation (using a sucrose gradient) will produce higher yields. Note: using the ultracentrifugation method without a sucrose cushion as described here will lead to isolated vesicles degrading over time in solution.

Materials

- Exosome-depleted fetal bovine serum (Thermo, A2720801)
- Base culture medium (without FBS)
- Phosphate-buffered saline (PBS) or Hank's buffered salt solution (HBSS)

Filtration

- Amicon Ultra-15 100kDa MWCO filter unit (Millipore, UFC910024)
- Sodium azide

Ultracentrifugation

- 14mL ultracentrifuge tube (Beckman, 331374)
- Sucrose
- Ethanol

Methods

1. Obtain a conditioned medium containing EVs.
    - Note: this medium cannot contain FBS, otherwise, the product will be contaminated with bovine EVs.

- If the medium must contain FBS for cells to not die (as is the case for D1 cells), one can supplement with exosome-depleted fetal bovine serum.
- If one must change medium on existing cells to a medium lacking FBS or EVs within FBS, follow this brief method:

1. Aspirate medium.
2. Wash cells with HBSS twice.
3. Add serum-free medium and incubate for 20min.
4. Aspirate medium.
5. Add a desired medium lacking FBS or FBS containing EVs.
2. Centrifuge medium at 2000xg 4C for 10min.
3. Collect supernatant; centrifuge medium at 10,000xg 4C for 20min.
    - Note: this step will remove particles larger than ~500nm.
4. Collect supernatant and proceed below.

Filtration

1. Add the conditioned medium to the Amicon filter column and centrifuge at 5000xg 4C for 10-30min.
    - Note: the spin time can be modified depending on the goal, i.e. remaining liquid in the column at any point.
    - Note: invert the column a few times after spinning to avoid accumulation on the filter.
2. Repeat step #1 until all medium has passed through the column.
3. Run an equal volume as the sample of PBS or HBSS (depending on final application) through the column.
4. Once a desirable final volume is achieved, resuspend the sample directly in the filter unit using a pipette.
5. To re-use columns, add PBS or HBSS containing 0.05% sodium azide to avoid drying the filter.
    - Note: wash out sodium azide with PBS or HBSS before next use.

Ultracentrifugation

1. Add 1.5mL 30% sucrose in PBS or HBSS (depending on final application) to each 14mL ultracentrifuge tube.
2. Add the conditioned medium to the ultracentrifuge tubes.
    - Note: for 14mL tubes, do not add medium higher than ~10mL.
3. Add tubes to ultracentrifuge buckets and precisely balance partner buckets.
    - Note: for reference, I always used the Beckman Coulter SW40Ti rotor.
4. Load buckets onto rotor and rotor into ultracentrifuge.
5. Run 280,000rpm (100,000xg) for 90min at 4C.
6. Aspirate supernatant down to the original line of the sucrose cushion.

7. Wash the sucrose cushion thoroughly with 8.5mL of PBS or HBSS.
8. Repeat step #5.
9. Aspirate all supernatant (leave only pellet).
10. Resuspend pellet in PBS or HBSS.
    - Note: practically, I find the lowest volume that can be used here per 14mL tube is ~25uL.
11. To re-use tubes, wash with water followed by ethanol, dry overnight, and autoclave.

APPENDIX B

ANALYSIS OF EXTRACELLULAR VESICLES: SIZE, MORPHOLOGY, AND CONTENT

(portions adapted from Sing Wan Wong)

Nanoparticle tracking analysis (NTA) by Malvern using NS300 is the preferred method to measure EV number and size. To measure morphology, one can use transmission electron microscopy – I do not have an expertise directly here, and I simply prepared samples as in Appendix A (ultracentrifugation) with the assistance of the Electron Microscopy Core at UIC. For content, one can perform an enzyme-linked immunosorbent assay (ELISA) or western blot to detect protein, and reverse transcription (RT) followed by quantitative polymerase chain reaction (qPCR) to detect mRNA/miRNA.

Materials

Nanosight

- Normject 1mL luer-slip syringe (53548-001)
- Samples with volume 1mL
- Buffer(s) by which samples are prepared (referred to as ‘buffer’)

ELISA

- ELISA Wash Buffer: 1X PBS, 0.05% Tween 20
- Blocking Buffer: 1X PBS, 1% bovine serum albumin (BSA, Roche)
- Sample Buffer: 1X PBS, 0.01% Tween 20, 1% BSA
- Nunc MaxiSorp™ flat-bottom coated plates (Invitrogen, 44-2404-21)
- 5X Coating Buffer B (BioLegend)
- anti-human CD63 (BioLegend, 353014)

- anti-human CD9 (BioLegend, 312102)
- recombinant human CD63 standard (Sino Biological)
- recombinant human CD9 standard (Sino Biological)
- biotin anti-human CD63 (GeneTex, GTX52381)
- biotin anti-human CD9 (Miltenyi, 130-103-989)
- Streptavidin-HRP (R&D Systems)
- ELISA substrate (R&D Systems)
- 1M hydrochloric acid (HCl)

Western Blot

- 10X RIPA buffer (Cell Signaling, 9806S)
- Protease inhibitor cocktail (Millipore, 539131)
- BCA Assay kit (Thermo)
- 4X Laemelli dye (Bio-Rad, 1610747)
- DTT (Goldbio, DTT10)

RT/qPCR

- DNase I (NEB, M0303S)
- RNeasy Mini kit (Qiagen, 74104)
- DNeasy Blood & Tissue kit (Qiagen, 69504)
- Isopropanol
- RNAase-free water
- Molecular biology grade ethanol
- Superscript III Enzyme (Thermo, 18080093)
- RNAse Out (Thermo, 10777019)
- qPCR forward and reverse primers for each target (IDT)
- qPCR 96-well plates
- SYBR Green (Thermo, 4367659)

Methods

Nanosight

Note: The instrument I used for the entirety of this thesis was the Nanosight NS300 by Malvern.

Note: the instrument has a precise detection range from ~1e7 particles/mL to ~1e9 particles/mL. This can be determined empirically for specific samples by dilution, etc. As a working rule, concentrated preparations as those from Appendix A should be diluted in the range 1:100 to 1:1000. Other samples may need dilution appropriately.

1. Using a syringe, prime the microfluidic chamber by running buffer through the inlet.
2. Attach the chamber to the laser module with the provided screws.
3. Carefully fill the chamber with buffer.
4. Attach the module to the instrument and increase camera level to 14.

- Note: depending on samples, this may change – however, it can not be changed after acquisition, and samples are not comparable at different camera levels.

5. Visualize the buffer – the viewing area is clearly illuminated by rays of light – check that it is clean – if not, repeat #2-4.
6. Load ~400-600uL of the sample and visualize its presence on the screen – attach syringe to
7. Run a script titled 'Stephen'; briefly, it should load syringe at flow rate 100µl/min, capture 30sec, repeat twice (for 3 videos total), process data, and export.
8. Once capture finishes, set detection threshold as 7 or whatever is best for your sample.
   - Note: this can be changed later (leading to different results), as long as one keeps videos.
9. Export data.
   - Note: data (either PDF or Excel) will contain both concentration data and size data.
10. Clean-up by running 10% ethanol once, followed by air a few times.

ELISA

This assay sometimes is sold in kit form – in that case, follow the kit instructions. I developed a couple of assays myself (human CD63 and human CD9), and I will detail them here. Practically speaking, EV samples will not differ from a typical protein sample.

1. Mix 5X Coating Buffer B (BioLegend) with distilled water and add 50µl to each well. Rock overnight at 4C.
   - mouse anti-human CD63 (BioLegend, 353014) final concentration of 5µg/mL.
   - mouse anti-human CD9 (BD) final concentration of 5µg/mL.
2. Wash 4x with ELISA wash buffer.
3. Block wells for >1 hour at room temperature (RT) with 100µL of 1X PBS with 1% BSA.
4. Wash 4x with ELISA wash buffer.
5. Add 100µL recombinant standard (I recommend a serial dilution from 500ng/mL to 10ng/mL) in 1X PBS with 1% BSA, 0.01% Tween 20. Add 100µL of EV samples. Incubate overnight at 4C. Be sure to add buffer blank for each sample buffer used.
6. Wash 4x with ELISA wash buffer.
7. Add 100µL of 2µg/mL biotin antibody in 1X PBS with 1% BSA, 0.01% Tween 20 and rock at RT for 2 hours.
   - biotin anti-human CD63 (GeneTex, GTX52381)
   - biotin anti-human CD9 (Miltenyi, 130-103-989)
8. Wash 4x with ELISA wash buffer.
9. Add 100µL of strep-HRP (1:200 dilution) in 1X PBS with 1% BSA, 0.01% Tween 20 and rock at RT for 30min.
10. Wash 4x with ELISA wash buffer.
11. Mix 1:1 ELISA substrate buffer A and B (R&D Systems), add 100µL and observe color change (clear to blue) over 20min.
12. After sufficient development (~20min), add 100µL 1M HCl and observe color change (blue to yellow) instantly.
13. Read plate at 450nm (yellow) or 650nm (blue).

Western blot

Downstream of sample preparation, this procedure is highly standardized and thus I will not detail it here. For those, refer to the internet (sites such as Thermo, Bio-Rad, etc.) or experienced colleagues. For preparation of EV samples:

Note: it is very important to remove all exogenous protein that will be involved in the sample. This can best be done by either not having any serum in the medium in the first place, and/or by using the ultracentrifugation method in Appendix A.

1. Prepare EVs using any method with final volume as small as possible.
2. Add 1:10 10X RIPA buffer (i.e. 10µL to 90µL).
3. Add 1:100 protease inhibitor cocktail.
5. Maintain constant agitation for 30min at 4C.
6. Centrifuge 12,000rpm 20min at 4C.
7. Take supernatant. At this point proceed with protocol or store at -80C long-term, -20C short-term.

Perform BCA assay to determine protein content:

1. Take eight tubes -- add 30µL water to each.
2. Add 30µL 2% BSA and dilute it down the line of tubes (each is ½ of previous).
   - Last tube (8th) – do not add BSA – keep as water (assay blank)
3. Samples – depends on how much you have. Minimum to test is 10µL, but you can add up to 30µL per tube.
4. Mix 50:1 solutions A:B together – need enough for 8*(180µL), give yourself room with 9*(180µL) = 1620µL (1588µL A, 32µL B) plus whatever you need for samples. E.g. for 4 samples 30µL each, need 4*(180µL), now it becomes 2340µL (2293µL A, 47µL B)
5. Add solution A:B to all solutions at 7:1 (e.g. add 180µL to 30µL; 60µL to 10µL).
   - Note: this ratio can be changed depending on desired sensitivity, but minimum vol/96-well plate well should be 70µL.
6. Incubate samples at 37C for 20-30min.
7. Read absorbance at 562nm.

Prepare samples for SDS-PAGE:

Note: Prepare ~1.5x of each sample.

1. Prepare dye/reducing solution; need 0.25µL/µL of sample + extra room (~50µL); in other words, for 4 samples 45µL each, one should prepare 5*45µL *0.25µL/µL = 56µL + 50µL = 106µL.
2. Use 1:120 final DTT from stock (stock is 1.2M; final is 10mM)
3. Add 1:30 DTT to 4X Laemelli dye.
   - Example: For 106µL: add 3.5µL stock DTT, 102.5µL 4X dye.
4. Mix dye/reducing solution into samples 1:4.
   - Example: for a 45µL sample, add 11.25µL dye/reducing solution

5. Boil samples at 95C for 5min.
6. Move to load samples immediately after boil.

RT/qPCR

This method can be used to detect DNA, RNA, or micro-RNA (miRNA) within EVs. In each case, the method will differ slightly as described. To isolate nucleic acids, one can also use either a Trizol method or a spin-column method – I will describe both methods here.

1. Prepare EV samples as detailed in Appendix A – ideally, try to get less than or equal to 100µL of sample volume.
2. For all samples, treat with 1:100 DNAse I for 60min at 37C followed by inactivation for 15min at 65C.
3. Proceed with RNeasy kit or DNeasy kit (follow kit instructions) to isolate nucleic acids.

For Trizol nucleic acid extraction:

1. Add 1mL of Trizol per sample.
2. Vortex each sample for 10-15 seconds.
   - Note: at this point, samples can be stored at -80C – resume protocol accordingly.
3. Add 200uL chloroform to 1mL Trizol containing digested cell contents. Invert/shake several times and vortex ~20sec.
4. Incubate 2-3min at RT.
5. Spin 12,000rpm for 10min at 4C.
6. Collect top (clear) layer (~400-500µL) in new tube. Add 500µL isopropanol and invert a couple times.
7. Incubate at room temperature for 20min or on ice for 1hr+.
8. Spin 12,000rpm for 10min at 4C.
9. Slowly pour isopropanol out of tube.
10. Add 1 mL cold 75% molecular biology grade ethanol in RNAase-free water directly to RNA pellet: vortex for 10 seconds.
11. Spin 7500rpm, for 5min, at 4C.
12. Pour out the EtOH, use 200µL pipette tip to aspirate remaining EtOH: do not disturb pellet.
13. Let pellet air dry but not completely.
14. Add 15µL of RNAase-free water.
15. Incubate at 65C for 10min.
16. Incubate on ice for 3min.
17. Briefly spin down then measure nucleic acid concentration via NanoDrop.

At this point, samples are isolated nucleic acids. For RNA and miRNA, proceed with reverse transcription. For DNA, proceed to qPCR.

For reverse transcription:

Note: For miRNA, at this point one needs to add the stem loop RT primer for each target (see ref [131]. These should not interfere (unless there is target overlap), and thus in theory one can add as many as they want.

1. One reaction corresponds to 500ng of RNA. In practice, add 900ng RNA per 2 reactions.
2. Add 500 or less ng RNA to a new PCR tube and bring up to 11µL with RNAase-free water.
3. Add 1µL random primer (0.2µg/mL) and 1uL 10mM dNTP mix (for miRNA, add the stem loop primers at this point [final concentration 100nM each]).
4. Incubate at 65C for 5min (using thermocycler).
5. Incubate on ice for 3min.
6. Per reaction, add 15µL of a master mix solution containing:
    - 4µL 5X FS buffer
    - 4µL 0.1M DTT
    - 1µL RNAase out
    - 0.5µL Superscript III enzyme
7. Run one PCR cycle:
    - 25C for 10min
    - 50C for 50min
    - 85C for 5min
    - 4C for ∞
8. Store product at -20C or proceed with qPCR.

qPCR

Note: Aim to add as much as 50ng RNA/miRNA or 10ng DNA per qPCR reaction.

Note: For miRNA, there will be a universal reverse primer (corresponding to the stem-loop design), but there will still be unique forward primers for each target.

1. Add 3µL DNA x 3 wells, per gene per sample (in other words, do everything in triplicate: 3 reactions per sample per gene).
2. Per target gene, create a master mix containing 27µL x (# samples) x 3 (i.e. 1 sample = 81 µL) containing, per 1x reaction, the following formula is correct:
    - 15µL SYBR Green
    - 0.3µL (100µM) forward primer (final concentration: 1µM)
    - 0.3µL (100µM) reverse primer (final concentration: 1µM)
    - 11.4µL RNAase-free water
3. Add 27µL master mix (of corresponding gene target) to each well.
4. Seal top with film.
5. Run plate on Viia7.

APPENDIX C

MECHANICAL CHARACTERIZATION OF HYDROGELS

In this thesis I have performed measurements of hydrogel mechanical properties in the form of complex modulus G*, storage modulus G', loss modulus G'', stress relaxation, and swelling ratio Q. For G*, G', and G'', I used Rheometers: both an Anton Paar MCR302 and a Malvern Kinexus. Here, I will describe how to obtain those property measurements.

Methods

Rheometer

1. Form hydrogels in a preferred method and create 8mm discs; for more details, see Appendix D or Appendix G.
2. To retain hydrogels before measurement, add a small amount of an appropriate buffer.
3. Use an 8mm geometry.
4. Calibrate the instrument by determining the zero gap.
5. Load hydrogels onto the stage.

Measurement of G, G', G''*

1. Use an established protocol to lower the geometry to a ~15% strain – if hydrogels are 1mm thick, this is a gap of 0.85mm.
2. Apply a logarithmic frequency sweep from 0.01 Hz to 10 Hz.
3. G*, G', and G'' will be reported within the table of data that is acquired during the sweep.

Measurement of stress relaxation

1. Use an established protocol to lower the geometry to a ~15% strain – if hydrogels are 1mm thick, this is a gap of 0.85mm.
2. Allow hydrogels to equilibrate for ~5-10sec.
3. Measure the normal force over a time period of ~180sec.
4. Fit the normal force vs. time curve with an equation to calculate the half-time $t_{1/2}$.

Measurement of swelling ratio Q

1. Form hydrogels in a preferred method and create 8mm discs; for more details, see Appendix D or Appendix G.
2. Weigh a weigh-boat and record the mass value.
3. Add hydrogels to the weigh-boat and record the mass value – this is the ‘relaxed’ mass.
4. Swell hydrogels overnight by adding an excess of appropriate buffer.
5. The next day, remove all the buffer so that only the hydrogel remains.
6. Weigh the weigh-boat and record the mass value – this is the ‘swollen’ mass.
7. Allow the hydrogel to dry overnight.
8. The next day, weigh the weigh-boat and record the mass value – this is the ‘dry’ mass.
9. Swelling ratio Q is equal to swollen mass divided by dry mass.

For more complicated mesh size measurements, etc. refer to Section 3.3.

APPENDIX D

ENCAPSULATION OF EXTRACELLULAR VESICLES WITHIN SYNTHETIC HYDROGELS

In this thesis, I encapsulated EVs within alginate hydrogels. These hydrogels can be formed by ionic crosslinking or covalent crosslinking. To encapsulate EVs in covalently crosslinked hydrogels, the alginate chains must first be modified by to contain 'click' chemicals – in this case, norbornene and tetrazine [126]. Thus, I will cover how to add chemical groups to alginate chains generally (conjugation) and then discuss how EVs can be encapsulated in either ionically or covalently crosslinked hydrogels.

Materials

Conjugation

- Dialysis membranes (3.5 kDa) (Spectrapor)
- Activated charcoal (Sigma, 05105)
- N-(3-Dimethylaminopropyl)-N′-ethylcarbodiimide hydrochloride (EDC) (Sigma, E1769)
- Sulfo-NHS (Thermo, 24510)
- Alginate polymer (FMC Corporation)
- NaCl (Fisher)
- Norbornene-amine (Matrix Scientific)

EV Encapsulation

- Solution of EVs as prepared from Appendix A.
- HBSS
- Calcium sulfate (Sigma)
- 1mm glass slides
- 8mm or 5mm tissue punches (Integra)
- Spatula
- luer-lok 3mL syringe (BD, 1219C23)
- luer-lok adapter (female-female) (Cole-Parmer, UX-45508-22)

Methods

Conjugation

This method can be followed generally for any chemical containing a single primary amine functional group, but I will use norbornene-amine conjugation to alginate as an example.

First, purify the alginate of ash and other contaminants:

1. Dissolve X grams of alginate at 1% w/v (I recommend 2g in 200mL) in distilled water overnight.
2. Add the solution to dialysis membranes and dialyze with a decreasing salt (NaCl) gradient (in a 2L distilled water bath), changing the bath 3-4 times per day: 15g, 12.5g, 10g, 7.5g, 5g, 2.5g, 0g, 0g, 0g, 0g, 0g.
3. Transfer the contents into a fresh beaker and stir.
4. Add activated charcoal: 0.5g per 1g of alginate.
5. Stir for 30min, then, let it sit (no stirring) for 30min+.
6. Run the solution through a sterile filter in the tissue culture (TC) hood, removing the charcoal.
7. Place the solution in -20C freezer overnight.
8. Place the solution in -80C freezer overnight.
9. Lyophilize the solution over several days to obtain a solid – it should be white.

Next, proceed with conjugation:

1. Dissolve X moles of purified alginate at 1% w/v in MES buffer pH 5.5-6.5.
   - Note: use a higher pH for more sensitive materials such as peptides; for chemicals, pH 5.5 should be used.
2. Add (DS)*X moles of norbornene-amine to 1mL of MES buffer pH 5.5-6.5, and then transfer into the alginate solution.
   - DS = degree of substitution – this is how many molecules will be present per alginate chain. In practice, I used DS75-150 for norbornene-amine on “10/60” alginate, which I estimate is ~120,000 g/mol.
3. Stir for 1 hour.
4. Add 2.5*X moles of sulfo-NHS in 1mL MES buffer pH 5.5-6.5.
5. Add 10*X moles of EDC in 1mL MES buffer pH 5.5-6.5.
   - Note: for better conjugation efficiency, one can split this into three separate additions of reagents each occurring 8 hours apart.
6. Stir for 24 hours.
7. Add the solution to dialysis membranes and dialyze with a decreasing salt (NaCl) gradient (in a 2L distilled water bath), changing the bath 3-4 times per day: 15g, 12.5g, 10g, 7.5g, 5g, 2.5g, 0g, 0g, 0g, 0g, 0g.
8. Run the solution through a sterile filter in the TC hood.
9. Place the solution in -20C freezer overnight.
10. Place the solution in -80C freezer overnight.
11. Lyophilize the solution over several days to obtain a solid.

EV Encapsulation

As stated above, this can be performed for either ionically crosslinked or covalently crosslinked hydrogels.

For an ionically crosslinked alginate hydrogel:

It is most helpful to define the total volume of gel and fill in components as we proceed. In this example, I will use a 600µL total final volume and 1% hydrogel:

<u>600µL</u>
150µL of 4% alginate
100µL of EV solution
150µL of 80mM calcium sulfate
200µL of appropriate buffer (I recommend HBSS)

Note: this example uses 20mM calcium sulfate as a final concentration, but this can vary.

1. Prepare an alginate solution from the above formula, without EV solution or calcium sulfate yet.
2. Mix the EV solution within the alginate solution thoroughly.
3. Transfer this solution (450µL) into a luer-lok 3mL syringe.
4. Add a luer-lok adapter to the syringe and drive the solution to fill the entire syringe plus the adapter.
5. To another 3mL syringe, add 150µL of 80mM calcium sulfate dissolved in an appropriate buffer (I recommend HBSS).
6. Join the syringes through the adapter and mix vigorously for ~20-30sec.
7. Deposit the solution on a glass plate and between glass slides so that a gel disc with 1mm thickness will be formed.
8. Wait for 2 hours for the gel to fully form.
9. Punch gel with tissue punches as appropriate.

For a covalently crosslinked alginate hydrogel:

In this example, I will use a 600µL total final volume and 2% hydrogel (1% alginate with tetrazine and 1% alginate with norbornene):

<u>600µL</u>
150µL of 4% alginate-norbornene
150uL of 4% alginate-tetrazine
100µL of EV solution
200µL of appropriate buffer (I recommend HBSS)

1. Prepare an alginate-norbornene solution from the above formula, without EV solution or alginate-tetrazine yet.
2. Mix the EV solution within the alginate-norbornene solution thoroughly.

3. Add the alginate-tetrazine solution and mix thoroughly with a pipette.
    - Note: work quickly as gelation will begin upon mixing.
4. Using a pipette, deposit the solution on a glass plate and between glass slides so that a gel disc with 1mm thickness will be formed.
5. Wait for 2 hours for the gel to fully form.
6. Punch gel with tissue punches as appropriate.

For a hydrogel with both covalent crosslinks and ionic crosslinks, the above methods can be combined logically. I will do it here:

<u>600µL</u>
150µL of 4% alginate
150uL of 4% alginate-tetrazine
100µL of EV solution
150µL of 80mM calcium sulfate
50µL of appropriate buffer (I recommend HBSS)

1. Prepare an alginate-norbornene solution from the above formula, without EV solution or alginate-tetrazine yet.
2. Mix the EV solution within the alginate-norbornene solution thoroughly.
3. Add the alginate-tetrazine solution and mix thoroughly with a pipette.
    - Note: work quickly as gelation will begin upon mixing.
4. Transfer this solution (450µL) into a luer-lok 3mL syringe.
5. Add a luer-lok adapter to the syringe and drive the solution to fill the entire syringe plus the adapter.
6. To another 3mL syringe, add 150µL of 80mM calcium sulfate dissolved in an appropriate buffer (I recommend HBSS).
7. Join the syringes through the adapter and mix vigorously for ~20-30sec.
8. Deposit the solution on a glass plate and between glass slides so that a gel disc with 1mm thickness will be formed.
9. Wait for 2 hours for the gel to fully form.
10. Punch gel with tissue punches as appropriate.

APPENDIX E

LENTIVIRUS-MEDIATED RECOMBINANT PROTEIN EXPRESSION IN D1 MSCS

Expression of recombinant proteins in mammalian cells (such as for the cell line D1 MSCs) can be achieved by transfer of a lentiviral vector to the mammalian cells using a lentivirus. In this Appendix, I will detail how to insert a gene of choice into a lentiviral vector using conventional restriction enzyme-based 'cut-and-paste' cloning techniques. I will then describe how to produce lentivirus containing this vector, and how to use lentivirus to integrate the vector into a mammalian cell genome to produce a stable cell line.

Note: all techniques described in this Appendix are conventional and described thoroughly elsewhere (see for example resources through Addgene or Thermo websites); I intend to detail my methods here merely as a guide.

Materials

Restriction cloning

- Forward and reverse PCR primers
- Taq PCR kit (NEB, E5000S)
- Restriction enzymes (NEB is preferred)
- CutSmart buffer (NEB)
- rAPid alkaline phosphatase kit (Roche, 4898133001)
- Agarose powder (Bio-Rad)
- DNA gel electrophoresis dye (NEB)
- 1kb DNA ladder (NEB)
- Gel extraction kit (Qiagen, 28704)
- TaKaRa DNA Ligation Kit LONG (TaKaRa, 6024)
- NEB® Stable Competent E. coli (C3040H)
- Antibiotic selection agar plates
- Luria broth (LB)

Lentivirus production

- Lentiviral vector
- HEK293T cells (ATCC®, CRL-3216™)
- 10cm tissue culture dish
- 2nd generation lentiviral packaging mix (ABM, LV003)
- LentiFectin (ABM, G074)
- Fetal bovine serum (FBS)
- Cell growth medium
- HBSS
- 0.45μm sterile filter
- Amicon Ultra-15 100kDa MWCO filter unit (Millipore, UFC910024)

Lentivirus transduction

- D1 MSCs (ATCC®, CRL-12424™)
- Polybrene (Millipore)
- Puromycin (Sigma)

Methods

Restriction cloning

Prepare the DNA using standard antibiotic selection and Miniprep kit (Qiagen).

Typically, one will PCR amplify an 'insert' to be placed in a lentiviral 'backbone' using the method I describe here. In this example, we will assume that the desired restriction sites to 'paste' the insert in the backbone are NheI and XbaI.

First, amplify the insert using PCR:

1. Prepare PCR primers to amplify the insert. These will contain 15-30 nucleotides with 10-25 bases homologous to the insert, and thus a ~5 base 'overhang'. The overhang must contain the restriction sites – in this case, NheI on the forward primer, and XbaI on the reverse primer.
    - Note: for best results, perform a no template control.
2. Prepare a 25μL PCR reaction:
    - 2.5μL 10X standard Taq buffer
    - 0.5μL 10mM dNTPs
    - 0.5μL 10uM forward primer
    - 0.5μL 10uM reverse primer
    - 0.125μL Taq polymerase
    - X μL template (optimize from 50-500ng – start with 50ng)
    - Makeup with water
3. Perform the PCR using a thermocycler; the cycle is:
    - 95C 30s

- Cycle 25 times:
  - 95C 15s (denature)
  - 60C 30s (anneal)
  - 70C 2min (extend)
- 72C 5min
- 4C remainder
- Note: temperatures and times may need to be optimized, these values are a guide

Second, digest the PCR product (insert) and backbone:

Note: use the whole PCR product and ~1µg of the backbone.

1. Prepare the digestion reaction:
   - 43µL DNA made up with water
   - 1µL NheI enzyme
   - 1µL XbaI enzyme
   - 5µL CutSmart buffer
2. Run at 37C for 1-18 hours (longer is better).
3. Treat vector with alkaline phosphatase:
   1. Add 5.5µL ALP buffer and 2.1µL ALP enzyme.
   2. Run 10min at 37C, followed by 2min at 75C, cool on ice.
4. Run an agarose gel to separate bands:
   1. Prepare 1% gel in TAE buffer.
   2. Microwave 50mL TAE buffer + 0.5g agarose for 1min – until boil – mix well.
   3. Add ethidium bromide – 2µL (10mg/mL solution) per 50mL gel.
   4. Pour and wait for gel to form (~20-30min).
   5. Prepare samples: Add 6X dye to be 1X (in other words, add 10µL to 50µL).
   6. Prepare 1kb ladder: 24uL per ladder lane.
      - 4µL ladder
      - 4µL 6X dye
      - 16µL water
   7. Load lanes with ladder (usually just one lane) or samples
   8. Run gel 120V for 60min.
   9. Cut desired lanes and weigh them in tubes.
5. Use the gel extraction kit with included protocol.

Third, ligate the digested insert and backbone.

Note: for best results, perform ligation at different molar ratios insert:backbone, for example: 3:1, 7:1, 10:1.

1. Prepare a ligation reaction (49µL total):
   - X µL vector DNA (use 50ng)
   - Y µL insert DNA (using molar ratio as above)
   - 5µL 10X ligation buffer
   - Makeup with water
2. Heat for 3min at 65C and immediately cool on ice.

3. Add 1µL of the ligase enzyme.
4. Incubate overnight at 16C.

Fourth, transform the ligation mixture into a competent cell:

Note: be very gentle with this cell; never pipette up and down to mix.

Note: one does not need to use the whole tube, one only needs ~30-50µL per reaction.

1. Thaw a tube of cells on ice.
2. Add 2µL of ligation mixture.
3. Place on ice for 30min.
4. Heat shock at exactly 42C for exactly 30 sec.
5. Add 950µL of SOC medium – shake at 37C for 1hr -- meanwhile, warm the antibiotic selection plates.
6. Spread 50-100µL of mixture on the plate and incubate at 37C overnight.
7. Pick colonies and grow overnight in LB.
8. Sequence clones for the presence of the insert.
9. Store the positive clone in a glycerol stock.

Lentivirus production

First, prepare a large quantity of lentiviral vector DNA by Miniprep from the glycerol stock.

Day 1

1. Seed 1 million HEK293T cells in a 10cm dish, place in tissue culture (TC) incubator overnight.

Day 2

2. Add 10µg lentiviral vector and 10µg (20µL) 2nd generation packaging mix to 1mL serum-free antibiotic-free medium.
3. Add 80µL LentiFectin to 1 mL serum-free antibiotic-free medium.
4. Mix above solutions and incubate 20min at RT.
5. Add 4.5mL serum-free medium to the solution.
6. Remove medium from 10cm dish, wash with 10mL HBSS, and add the 6.5mL packaging medium.
7. Incubate for 5-8 hours at 37C.
8. Add 0.65mL FBS and incubate overnight at 37C.

Day 3

9. Remove packaging medium, add 10 mL complete medium to cells.
10. Incubate for 24 hours at 37C.

Day 4

1. Collect medium and centrifuge at 450xg for 15min at 4C.
2. Filter medium with a 0.45µm sterile filter.

3. Concentrate 10X using Amicon Ultra-15 100K spin-filter column.
4. Store at -80C.
5. A second harvest can be performed (by repeating steps #1-4) 24h later, if desired.

Lentivirus transduction

Day 1

1. Plate 5,000 D1 cells each in 10 wells of a 24-well plate.
2. Add 500mL growth medium and incubate overnight at 37C.

Day 2

3. Prepare complete medium with 8μg/mL polybrene, remove medium, and add 500mL polybrene medium to cells.
4. Infect cells at increasing dilutions of maximum viral medium (for example: 1:1, 1:2, 1:5, 1:30). Bring each condition up to 1mL total with complete medium and add to cells. Perform two replicates for each dilution condition.

Note: it is important to perform dilutions in the case that cells become sick with too much virus.

5. Incubate overnight at 37C.

Day 3

6. Check to see if cells are growing and/or dying. Leave in the incubator until wells become confluent.

Day 4+

7. When cells become confluent, split cells 1:3 (6 wells each condition) in a new 24-well plate and incubate 48 hours in complete medium.

Day 6+

8. Take 4 wells for each dilution condition and analyze via flow cytometry for the fluorescent marker present within your vector (if applicable).
9. To the remaining wells, add complete medium with an amount of puromycin determined previously by a killing curve (try 5μg/mL as previously determined from a killing experiment for D1 cells. Incubate overnight at 37C (or longer if necessary, as determined by a new killing experiment).

Day 7+

10. If necessary, combine wells of different dilutions to obtain higher cell number. Analyze via flow cytometry. If suitable expression is obtained, take cells for growth in larger surface area containers (i.e. T-75 flask followed by T-175 flask). Keep treating with puromycin until desirable expression and/or cell number is obtained.
11. If desired, perform limiting dilution or cell sorting via FACS on any conditions in the previous step and sequentially take for growth in larger surface area containers (i.e. T-75 flask followed by T-175 flask).

APPENDIX F

ANALYSIS OF EXTRACELLULAR VESICLE TRANSPORT WITHIN A MATRIX

Chapter 3 included encapsulating extracellular vesicles in alginate hydrogel matrix and tracking their transport over time. This section will describe how to image EVs in a matrix and track and analyze their transport.

Note: for imaging experiments I used the DeltaVision OMX instrument by GE.

Materials

- Compatible 60X oil-immersion imaging objective (I used Olympus PlanApo N 60X 1.42)
- Immersion oil with refractive index 1.518 (Cargille)
- #1 thickness cover glass slides
- Hank's balanced salt solution (HBSS) (or other appropriate buffer)
- Matrix with encapsulated fluorescent EVs (created as described in Chapter 3.2).

Methods

Imaging

1. Encapsulate EVs in a matrix as described in Appendix D or otherwise.
2. To keep the matrix from drying, add a few drops of HBSS or another appropriate buffer.
3. Start the imaging instrument as appropriate.
4. Load the immersion oil on the objective.
5. Place the EV-containing matrix on a cover glass slide and load it onto the objective.
6. Focus the sample to the glass-matrix interface.
7. By moving the focal plane up into the sample, one should be able to see particles.

Note: I used the following settings with the DeltaVision OMX GE:

- Imaging Mode: Sequential
- Light Path: Conventional
- Size: 1024 x 1024
- Binning: 1 x 1
- Channel: A568
- Mode: Fast 286 MHz
- Exposure: 5msec
- Excitation: 568
- Laser power: 100%

- Experiment Type: Conventional
- Sectioning
  - ‘Focus point when scan starts’: middle
  - ‘Optical section spacing’: 0.125 µm
  - ‘Number of optical sections’: 17
  - ‘Sample thickness’: 2µm
- Time-lapse
  - ‘Time points’: 30
  - ‘Time-lapse’: 50msec
  - ‘Total time’: 8sec

8. Acquire several image sets.
9. Pass the image sets through standard deconvolution (I used softWoRx 7.0.0).
10. Clean the microscope and objective appropriately.

Tracking

Note: I used IMARIS 9.5.0 for this section.

1. Upload the files into IMARIS 9.5.0.
2. Analyze the image set using a new ‘Spots’ method.
1. Choose ‘Algorithm Settings’, ‘Track Spots (over time)’. Move forward (blue right arrow).
2. For ‘Estimated XY Diameter’, input 0.8µm.
3. Select ‘Background Subtraction’. Move forward.
4. Create a filter: ‘Quality’. This should be adjusted to capture the particles in the image set. I recommend a value around 10. Move forward.
5. Move forward.
6. Choose:
   - ‘Algorithm’: ‘Brownian Motion’
   - ‘Max Distance’: 2µm
   - ‘Max Gap Size’: 1
7. Move forward.
8. Move forward.
3. Export the data corresponding to ‘Displacement^2’, ‘Time’, and ‘Track Length’ (choose others as well if desired).

Note: ideally one will obtain a single excel file with all exported data – if one wants to analyze several images sets at once, this can be done using IMARIS ‘batch processing’.

Analysis

Note: I used MATLAB 2019b for this section.

1. Import the Excel data exported from IMARIS.

2. Create a single matrix that combines all tracks. The matrix should have vertical dimension time and horizontal dimension track #. Entries will then be MSD, as calculated from IMARIS.
3. Remove tracks with less than 5 timepoint measurements.
4. Remove tracks with less than 20 timepoint measurements.
5. Remove tracks with greater than 30 timepoint measurements (if you followed the above strictly, there will not be more than 30 timepoints).
6. As tracks will not always be starting and ending at the same time, shift tracks in time to be consistent.
7. As tracks will vary in # timepoints between 20 and 30, one needs to change unassigned values to NaN to preserve the integrity of the matrix.
8. Subtract the static error MSD (determined previously) from each MSD value in the matrix.

Note: The MATLAB script below is an example of how to do all of this, it will achieve steps #1-8 above:

```
%% import file, load data

files = dir;
files = {files.name};
files = files(contains(files, '.xls'));

m_master = cell(length(files),1);

for ii = 1:length(files)
    data_d2 = xlsread(files[ii],'Displacement^2');
    data_d = xlsread(files[ii],'Track Displacement Length');
    t = zeros(30,1);
    for jj = 1:29
        [e,~] = find(data_d2(:,4)>t(jj));
        if ~isempty(e)
            t(jj+1) = data_d2(e(1),4);
        else
            t(jj+1) = data_d2(end,5);
        end
    end
    [sz_d,~] = size(data_d);
    id = zeros(sz_d,1);
    id(:,1) = data_d(:,4);
    m_it = zeros(length(t), length(id));
    for jj = 1:length(id)
        idt = id(jj);
        [a,~] = find(data_d2==idt);
        for kk = 1:length(a)
            time = data_d2(a(kk),4);
            time_it = abs(time-t);
            [~,g] = min(time_it);
            m_it(g,jj) = data_d2(a(kk),1);
        end
    end
    m_master[186] = m_it;
```

```
end

%% full displacement (cells) / time (row) matrix; tracks are columns

m = [];

for ii = 1:length(m_master)
    it = m_master[186];
    m = [m it];
end

%% remove tracks with less measurements than tol

%throw away tracks with less than this #timepoints
tol = 5;

[~,sz_m] = size(m);
m_r = zeros(length(t),1);

for ii = 1:sz_m
    it = m(:,ii);
    num_d = length(find(it));
    if num_d >= tol
        m_r = [m_r it];
    end
end

[~,sz_mr] = size(m_r);
m_r(:,1:sz_mr-1) = m_r(:,2:sz_mr);
m_r(:,sz_mr) = [];

[~,sz_mr] = size(m_r);
y = zeros(4,1);
t_init = zeros(4,2);
t_init(:,1) = 1;

m_work = m_r;

num_init = 4;

for ii = 1:sz_mr
    it = m_r(:,ii);
    [a,~] = find(it);
    st = a(1);
    fin = a(1)+num_init-2;
    y(2:num_init) = m_r(st:fin,ii);
    t_init(2:num_init,2) = t(st:fin,1);
    param = t_init\y;
    m_work(1,ii) = 0.001;
end

%% create MSD vs time matrices

[~,sz_m_work] = size(m_work);
```

```
%lower (N) and upper (M) bounds (in #timepoints) for considered tracks
N = 20;
M = 30;

%cut m_work to rid of <N or >M
alpha_init_id = 1:1:sz_m_work;
alpha_init_id = alpha_init_id';
alpha_cut_id = [];
a_work = zeros(length(t),1);

for ii = 1:sz_m_work
    it = m_work(:,ii);
    [a,~] = find(it);
    st = a(2);
    fin = a(end);
    len = fin-st+2;
    if len >= N && len <= M
        a_work = [a_work it];
        alpha_cut_id = [alpha_cut_id; alpha_init_id(ii)];
    end
end

a_work(:,1) = [];

%% shift all tracks to be consistent with t=0

[~,sz_a_work] = size(a_work);

alpha_full_ne = zeros(M,sz_a_work);
alpha_full = zeros(M,sz_a_work);

for ii = 1:sz_a_work
    it = a_work(:,ii);
    [a,~] = find(it);
    st = a(2);
    fin = a(end);
    len = fin-st+2;
    alpha_full_ne(1,ii) = it(1);
    alpha_full_ne(2:len,ii) = it(st:fin);
end

%% remove untracked points at ends of tracks

[rows_a_full,sz_a_full] = size(alpha_full_ne);

for ii = 1:sz_a_full
    it = alpha_full_ne(:,ii);
    [a,~] = find(it);
    fin = a(end);
    if fin ~= length(it)
        number = length(it)-fin;
        for jj = 1:number
            alpha_full_ne(fin+jj,ii) = NaN;
        end
```

```
    end
end

% remove static error

% static error in um^2
static_error = 0.004;

for ii = 1:sz_a_full
    for jj = 1:rows_a_full
        it = alpha_full_ne(jj,ii);
        if ~isnan(it)
            new_it = it-static_error;
            if new_it < 0
                new_it = 0;
            end
            alpha_full(jj,ii) = new_it;
        end
    end
end
```

9. Calculate the diffusion coefficient D as described in Chapter 3.2.

Note: The MATLAB script below is an example of how to do this: it will achieve step #9 above (the product vector containing all coefficients will be 'D'):

```
%% calculate D based on moving average method, num intervals == tau

%interval (in #timepoints) for calculating D
tau = 4;

D = zeros(sz_a_full,1);

tt_temp = zeros(length(t)-1,1);
for ii = 1:length(t)-1
    tt_temp(ii) = t(ii+1)-t(ii);
end

tau_time = tau*mean(tt_temp);

for ii = 1:sz_a_full
    it = alpha_full(:,ii);
    [a,~] = find(~isnan(it));
    len = a(end);
    num = len/tau;
    %round down
    if ~isinteger(num)
        num2 = round(num);
        if num2-num <= 0.5
            num2 = num - 0.5;
            num2 = round(num2);
        end
        num = num2;
    end
        d_temp = zeros(num,1);
```

```
        temp = zeros(tau,1);
        temp(1) = it(1);
        for jj = 2:tau
            temp(jj) = it(1+jj-2);
        end
        d_temp(1) = mean(temp)/(6*tau_time);
        for jj = 2:length(d_temp)
            temp2 = zeros(tau,1);
            for kk = 1:tau
                iter = 1 + ((jj-1)*tau)+ (kk-2);
                temp2(kk) = it(iter);
            end
            d_temp(jj) = mean(temp2)/(6*tau_time);
        end
    D(ii) = mean(d_temp);
end
```

10. Calculate the ensemble MSD curves.

Note: The MATLAB script below is an example of how to do this: it will achieve step #9 above (the product matrix containing the ensemble curve data will be ‘ens’):

```
%% calculate ensemble curves

%create log version of MSD/time matrices
%change 0 values to NaN

a_full_log = alpha_full;

for ii = 1:sz_a_full
    it = alpha_full(:,ii);
    for jj = 1:length(it)
        it2 = it(jj);
        if it2 == 0 || it2 < 0
            a_full_log(jj,ii) = NaN;
        else
            a_full_log(jj,ii) = log10(alpha_full(jj,ii));
        end
    end
end

%cut out t=0 MSD

alpha_full(1,:) = [];

ens_data = zeros(4,3);

%column1 = time; column2  = MSD value,
%column3 = lower limit (error [s.e.m.]), column4 = upper limit (error
[s.e.m.])

ens = zeros(length(t),4);

[sz_a_full,~] = size(alpha_full);
```

```
for ii = 2:sz_a_full
    ens(ii,1) = t(ii);
    ens(ii,2) = 10^(nanmean(a_full_log(ii,:)));
    ens(ii,3) = 10^((nanmean(a_full_log(ii,:))-
(nanstd(a_full_log(ii,:)))/sqrt(sum(~isnan(a_full_log(ii,:))))));
    ens(ii,4) =
10^((nanmean(a_full_log(ii,:))+(nanstd(a_full_log(ii,:)))/sqrt(sum(~isnan(a_f
ull_log(ii,:))))));
end

%trim down to N

for ii = 1:length(ens)
    ens((N+1):end,:) = [];
end
```

APPENDIX G

PREPARING 2D HYDROGEL SUBSTRATES AND SEEDING CELLS ON THEIR SURFACE

Chapter 4 included seeding cells on 2-D substrates. I did this using alginate hydrogel substrates or PEG hydrogel substrates. In the case of PEG hydrogel substrates, I coated a thin layer of PEG hydrogel over a coverslip (PEG-hydrogel-coverslips) to facilitate imaging of cells. This section will describe how prepare each type of substrate as well as how to seed cells on the substrates.

Materials

Substrate Preparation: Alginate hydrogels

- Hank's buffered salt solution (HBSS)
- High-MW alginate (Manugel, FMC)
- Medium-MW alginate (10/60, FMC)
- Calcium sulfate (Sigma)
- Adipic acid dihydrazide (Santa Cruz, sc-257072)
- N-(3-Dimethylaminopropyl)-N′-ethylcarbodiimide hydrochloride (EDC) (Sigma, E1769)
- 1-Hydroxybenzotriazole (HOBt) (Sigma, 157260)
- RGD peptide (sequence GGGRGDSP, Peptide 2.0)
- MES buffer pH 6.5 (Sigma)
- 1mm glass slides
- 14mm, 9mm or 5mm tissue punches
- Spatula
- luer-lok 3mL syringe (BD, 1219C23)
- luer-lok adapter (female-female) (Cole-Parmer, UX-45508-22)
- ultra-low binding well plate (Corning)

Substrate Preparation: PEG-coverslip-hydrogels

- 12mm diameter #1 coverslips (Fisher)
- Methanol (Fisher)
- Ethanol (Fisher)
- Potassium Hydroxide (KOH) (Fisher)

- Acetic Acid (Fisher)
- 3-(Trimethoxysilyl)propyl Acrylate (TCI, A1597)
- Lens paper (Fisher)
- Scotch tape
- SYLGARD™ 184 Silicone Elastomer Kit (PDMS) (Ellsworth)
- PEGDA 700 (Sigma, 455008)
- Sodium ascorbate (Sigma, PHR1279)
- Lithium phenyl(2,4,6-trimethylbenzoyl)phosphinate (LAP) (TCI, L0290)
- CRGD peptide (sequence CGGGRGDSP, Peptide 2.0)
- Tris(2-carboxyethyl)phosphine hydrochloride (TCEP) (Sigma, C4706)
- 1X PBS (Sigma)
- 365nm light source

Seeding cells

- Trypsin to detach cells
- Complete growth medium (containing FBS)
- Appropriate wash buffer (I used HBSS)
- 40µm mesh cell strainer (Corning, 352340)

Methods

Substrate Preparation: Alginate hydrogels

1. Synthesize alginate (medium-MW) conjugated with DS10 RGD as described in Appendix D to obtain medium-MW alginate DS10 RGD.

Note: make sure to prepare all materials that will contact the hydrogels by autoclaving or otherwise sterilizing beforehand.

Hydrogels can be made either with physical crosslinking or covalent crosslinking. For physically crosslinked hydrogels, we can use an example as follows:

1000µL
250µL of 4% medium-MW alginate DS10 RGD dissolved in appropriate buffer (I used HBSS)
250uL of 4% high-MW alginate dissolved in appropriate buffer (I used HBSS)
200µL of 125mM calcium sulfate in appropriate buffer (I used HBSS)
300µL of appropriate buffer (I used HBSS)

Note: this example uses 25mM calcium sulfate as a final concentration, but this can vary.

1. Prepare the solution as described above – all components except the calcium sulfate solution.
2. Transfer this solution (800µL) into a luer-lok 3mL syringe.

3. Add a luer-lok adapter to the syringe and drive the solution to fill the entire syringe plus the adapter.
4. To another 3mL syringe, add 200μL of 125mM calcium sulfate dissolved in an appropriate buffer (I recommend HBSS).
5. Join the syringes through the adapter and mix vigorously for ~20-30sec.
6. Deposit the solution on a glass plate and between glass slides so that a gel disc with 1mm thickness will be formed.
7. Wait for 2 hours for the gel to fully form.
8. Punch gel with tissue punches as appropriate.
9. Plate them into an ultra-low binding plate.

For covalently crosslinked hydrogels, we can use an example as follows:

<u>1000μL</u>
250μL of 4% medium-MW alginate DS10 RGD dissolved in MES Buffer pH 6.5
250uL of 4% high-MW alginate dissolved in MES Buffer pH 6.5
200μL of crosslinker solution (30mM AAD)
300μL of MES buffer pH 6.5

1. Prepare the solution as described above – all components except the crosslinking solution.
2. Prepare the crosslinking solution as follows (note: this example uses a final concentration of 6mM AAD):
    1. Dissolve 4.6mg/mL HOBt in MES buffer pH 6.5.
    2. Dissolve 50mg/mL EDC in the above solution.
    3. Dissolve 30mM AAD in the above solution.
    4. Sterile filter this solution.
3. Mix well the 200μL of crosslinker solution (30mM AAD) with the solution from #1 and deposit the solution on a glass plate and between glass slides so that a gel disc with 1mm thickness will be formed.

Note: work quickly in the above step since the gel will begin to form over time.

4. Leave overnight at room temperature for 15-20 hours.
5. While still under the glass, soak the hydrogel discs with an appropriate buffer (I used HBSS) for ~30min.
6. Remove the glass from the hydrogels and punch them with tissue punches as appropriate.
7. Plate them into an ultra-low binding plate.

Note: be sure to wash hydrogels for at least 3 days using an appropriate buffer (I used HBSS) before seeding cells.

Substrate Preparation: PEG-coverslip-hydrogels
First, we need to prepare coverslips by silanizing their surface as follows:

1. Sonicate coverslips in a solution of 1M KOH in water for 20min.

2. Rinse coverslips with water three times.
3. Rinse coverslips with methanol one time.
4. Prepare a reaction mixture and place coverslips in the solution:
    - 100mL methanol
    - 5mL acetic acid
    - 3mL 3-(Trimethoxysilyl)propyl Acrylate

Note: once coverslips are treated with this solution, it is important that they are not allowed to dry until the end.

5. Incubate for 20min at room temperature.
6. Rinse coverslips with methanol three times.
7. Rinse coverslips with ethanol three times.

Note: be careful to remove as much solution as possible from coverslips while drying them with lens paper.

Next, we can prepare PEG-coverslip hydrogels as follows:

Note: these parameters will affect hydrogel mechanical properties (primarily PEG and LAP concentrations, and light power); the following is just one example:

1. Prepare a PEG solution in 1X PBS as follows:
    - 10% PEG
    - 10mM sodium ascorbate
    - 4mM TCEP
    - 0.8mM CRGD
    - 0.5mg/mL LAP

2. Prepare PDMS-coated glass slides by putting a thin layer of PDMS mixed well with 1:10 crosslinker ratio (make sure to remove air with a vacuum chamber) and baking overnight at 65C.
3. Using scotch tape, tape a PDMS-coated glass slide to another glass surface on each side. I use 4 pieces of tape, which should provide a thickness of ~100µm.
4. Clean coverslips with ethanol.
5. Place a coverslip on the PDMS-coated glass slide.
6. Place 10-15µL of the PEG solution on the coverslip.
7. Place another PDMS-coated glass slide on top to create a thin layer of PEG solution on the coverslip.

Note: for help with the preparation, see the following diagram (not precisely to scale):

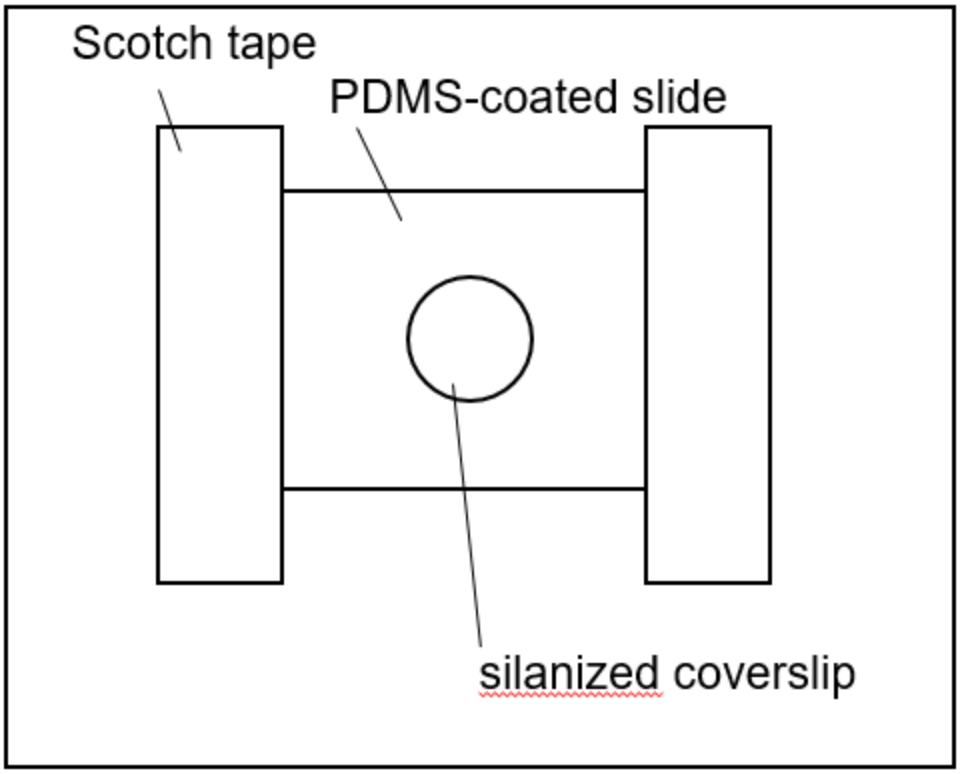

8. Apply the 365nm light source for some time (I used ~60sec).
9. Remove the top PDMS-coated glass slide.
10. Place the PEG-coverslip-hydrogel in an ultra-low binding plate.

Note: be sure to wash hydrogels for at least 3 days using an appropriate buffer (I used HBSS) before seeding cells.

Seeding cells

Note: this method seeks to seed cells without FBS – however, this may not be possible depending on the application – thus, I refer to the medium in which cells are seeded as the 'desired medium'.

1. Detach cells using trypsin.
2. Neutralize trypsin with complete growth medium (containing FBS)
3. Centrifuge cells to obtain a pellet.
4. Wash cells in the desired medium.
5. Pass cells through the 40µm mesh cell strainer twice.
6. Centrifuge cells to obtain a pellet.
7. Resuspend cells in desired medium.
8. Add as dilute as possible of a cell solution to the hydrogels, in order to obtain an appropriate cell number per hydrogel. For example, I recommend using 2mL of cell solution per 24-well plate well.

9. Rock the plate for 4 hours.
10. If applicable, allow cells to adhere for a further amount of time at 37C.
11. At this point, remove the medium from the well.
12. Wash the hydrogel with HBSS twice.
13. Add a desired medium to the cells.

APPENDIX H

ANALYSIS OF MVB TRANSPORT WITHIN CELLS ON A 2D HYDROGEL SURFACE

Chapter 4 included visualizing CD63-Katushka2S^{+} MVBs within D1 cells and tracking their transport over time. This section will describe how to image D1 cells seeded on substrates (seeding as described in Appendix G) and how to track and analyze their transport.

Note: for imaging experiments I used the DeltaVision OMX instrument by GE.

Materials

Imaging

- CellMask Green (Thermo, C37608)
- Compatible 60X TIRF oil-immersion imaging objective (I used Olympus Apo N 60X 1.49)
- Immersion oil with refractive index 1.518 (Cargille)
- Square #1 thickness cover glass slides (12mm x 12mm)
- Rectangular #1 thickness cover glass slides (24mm x 60mm)
- Forceps
- Double-sided tape (Scotch)
- Krazy glue
- Bulb transfer pipette

Methods

Imaging

1. Seed CD63-Katushka2S-expressing D1 cells on a PEG-coverslip-hydrogel as described in Appendix H or otherwise.
2. Stain the cells with CellMask Green (1000X) for 5min at 37C.
3. Wash the cells.
4. Bring all materials to the imaging instrument.
5. Start the imaging instrument as appropriate.
6. Prepare the sample as follows:
    1. Glue two 12 x 12 cover slips to a 24 x 60 cover slip with a space in-between that will support the 12mm diameter PEG-hydrogel-coverslip. Note: do not use too much glue.

2. Place a drop of the medium which the cells are in, in-between the 12 x 12 cover slips.
3. Using forceps, pick up the PEG-coverslip-hydrogel with seeded cells and place it upside-down on top of the medium and the 12 x 12 cover slips.
4. Cut small pieces of double-sided tape and place one on top of each 12 x 12 cover slip (do not have them touch the sample)
5. Take another 24 x 60 cover slip and place it flush on top of the entire preparation, pressing down on the double-sided tape to seal it.
6. Mark this side (the bottom) with a marker.
7. Flip the preparation over (so that now cells on facing up).

Note: see the following diagram for assistance with the preparation (not drawn precisely to scale):

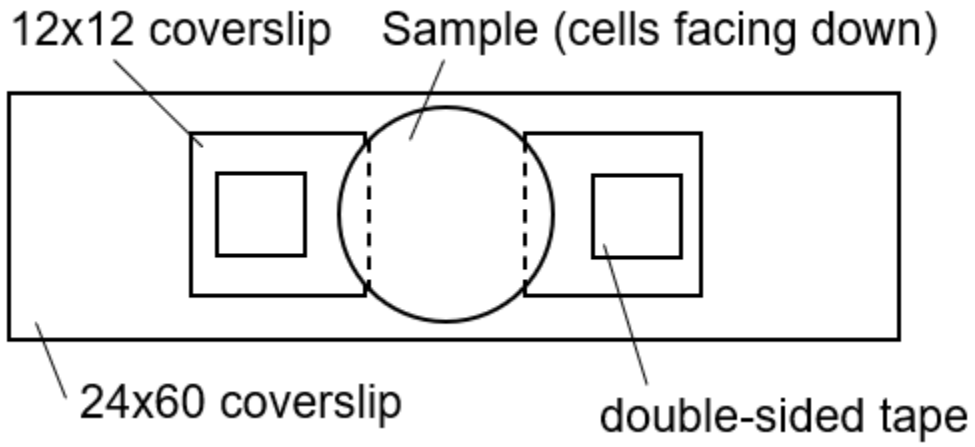

7. Load the immersion oil on the objective.
8. Load the entire sample preparation on the objective.
9. Focus the sample to the matrix-cell interface.

Note: for experiments done here (using GE DeltaVision OMX), I found z-height of 5500-5700µm to work best.

10. Find a cell.
11. Turn on TIRF mode.
12. Calibrate the TIRF mode (‘Instrument’->’TIRF’->’Calibrate TIRF’).

Note: I used the following settings with the DeltaVision OMX:

- Imaging Mode: Sequential
- Light Path: TIRF
- Size: 512 x 512
- Binning: 1 x 1
- Channel: A568
  - Mode: Fast 286 MHz
  - Exposure: 75msec
  - Excitation: 568
  - Laser power: 100%

- Channel: A488
  - Mode: Fast 286 MHz
  - Exposure: 12msec
  - Excitation: 488
  - Laser power: 100%
- Experiment Type: TIRF
- Sectioning: unselected
- Time-lapse
  - ‘Time points’: 250
  - ‘Time-lapse’: 100msec
  - ‘Total time’: 25sec
- TIRF settings (Instrument->TIRF)
  - Angle (A488): 80-90
  - Angle (A568): 80-90

13. Acquire several image sets.
14. Clean up the instrument and objective as appropriate.

Tracking

Note: I used IMARIS 9.5.0 for this section.

1. Upload the files into IMARIS 9.5.0.
2. Analyze the image set using a new ‘Surfaces’ method.
    1. Select under ‘Algorithm Settings’:
        - ‘Segment only a Region of Interest’
        - ‘Track Surfaces (over time)’.
    2. Move forward (blue right arrow).
    3. Select the region of interest corresponding to the cell.
    4. Move forward.
    5. Select ‘Smooth’; ‘Surfaces Detail’: 0.1µm.
    6. Select ‘Background Subtraction (Local Contrast)’; ‘Diameter of largest Sphere which fits into the Object’: 0.4µm.
    7. Move forward.
    8. Use automatic thresholding.
    9. Move forward.
    10. Create a filter: ‘Number of Voxels Img=1’. This should be adjusted to capture the MVBs in the image set. I recommend a value around 12. Move forward.
    11. Move forward.
    12. Choose:
        - ‘Algorithm’: ‘Brownian Motion’
        - ‘Max Distance’: 1µm
        - ‘Max Gap Size’: 1
    13. Move forward.
    14. Move forward.

3. Export the data corresponding to ‘Displacement^2’, ‘Area’, and ‘Track Length’ (choose others as well if desired).

Analysis

Note: I used MATLAB R2020a for this section.

1. Import the Excel data exported from IMARIS.
2. Create a single matrix that combines all tracks. Do this for both MSD and Area. The matrix should have vertical dimension time and horizontal dimension track #. Entries will then be MSD or Area, as calculated from IMARIS.
3. Remove tracks with less than 20 timepoint measurements.
4. Remove tracks with greater than 30 timepoint measurements (if you followed the above strictly, there will not be more than 30 timepoints).
5. As tracks will not always be starting and ending at the same time, shift tracks in time to be consistent.
6. As tracks will vary in # timepoints between 20 and 30, one needs to change unassigned values to NaN to preserve the integrity of the matrices.
7. Calculate the mean area per track, and the mean diffusion coefficient D as described in Chapter 2.2.
8. Create output matrices for both D (Da_matrix) and area (area_matrix).
9. Create ensemble curves.
10. Export parameters into the workspace.

Note: ‘Da_matrix’ and ‘area_matrix’ should include all parameters (D, ensemble curves, and area) on a per-file basis. For a concatenation of parameters for all files, see ‘D_vector’, ‘total_ens’ and ‘area_vector’.

Note: The MATLAB script below is an example of how to do all of this: it will achieve steps #1-10 above. It is acceptable to include an excel sheet for each sample, as this example script will handle several excel sheets:

```
%%import file, load data

N = 15; %cut by time, number*0.1s, e.g. N=50 is N=5s
M = 180; %cut by last time, number*0.1s, e.g. M=500 is N=50s


files = dir;
files = {files.name};
files = files(contains(files, '.xls'));


f_master = cell(length(files),1);


%m is area in um^2; rows are particles and columns are time
%x is displacement in um^2; rows are particles and columns are time
```

```
m_raw = [];
area_matrix = cell(length(files)+1,5);
area = [];
area_vector = [];


x_raw = [];
Da_matrix = cell(length(files)+1,4);
D = [];
D_vector = [];
ens = [];
total_tracks = [];
track_per_time = zeros(N,length(files));


for ii = 1:length(files)
    m_raw = [];
    x_raw = [];
    data_a = xlsread(files[186],'Area');
    data_d = xlsread(files[186],'Displacement^2');
    [sz_a,~] = size(data_a);
    [sz_d,~] = size(data_d);
    id_a_temp = zeros(sz_a,1);
    id_a_temp(:,1) = data_a(:,5);
    id_d_temp = zeros(sz_d,1);
    id_d_temp(:,1) = data_d(:,5);
    id_a = [];
    id_d = [];
    for jj = 1:length(id_a_temp)
        it = id_a_temp(jj);
        if isempty(find(id_a==it,1))
            id_a = [id_a; it];
        end
    end
    for jj = 1:length(id_d_temp)
        it = id_d_temp(jj);
        if isempty(find(id_d==it,1))
            id_d = [id_d; it];
        end
    end




%%calculate track per time

    for jj = 1:N
        a = find(data_d(:,4)==jj);
```

```
        track_per_time(jj,ii) = length(a);
    end

%%create matrices based on id vectors

    id = id_d;
    t_max = max(data_a(:,4));
    m_raw_t = zeros(length(id),t_max);
    x_raw_t = zeros(length(id),t_max);
    for jj = 1:length(id)
        idt = id(jj);
        [a,~] = find(data_a(:,5)==id(jj));
        [b,~] = find(data_d(:,5)==id(jj));
        for kk = 1:length(a)
            it = data_a(a(kk),1);
            t_it = data_a(a(kk),4);
            m_raw_t(jj,t_it) = it;
        end
        for kk = 1:length(b)
            it = data_d(b(kk),1);
            t_it = data_d(b(kk),4);
            x_raw_t(jj,t_it) = it;
        end
    end

    sz_mr_temp = size(m_raw);
    sz_mr_t_temp = size(m_raw_t);
    if sz_mr_temp(2) ~= sz_mr_t_temp(2)
        if sz_mr_temp(2) < sz_mr_t_temp(2)
            diff = sz_mr_t_temp(2)-sz_mr_temp(2);
            temp = zeros(sz_mr_temp(1),diff);
            m_raw = [m_raw temp];
        elseif sz_mr_temp(2) > sz_mr_t_temp(2)
            diff = sz_mr_temp(2)-sz_mr_t_temp(2);
            temp = zeros(sz_mr_t_temp(1),diff);
            m_raw_t = [m_raw_t temp];
        end
    end

    m_raw = [m_raw; m_raw_t];
    sz_mr = size(m_raw);

    sz_xr_temp = size(x_raw);
    sz_xr_t_temp = size(x_raw_t);
    if sz_xr_temp(2) ~= sz_xr_t_temp(2)
        if sz_xr_temp(2) < sz_xr_t_temp(2)
            diff_x = sz_xr_t_temp(2)-sz_xr_temp(2);
            temp = zeros(sz_xr_temp(1),diff_x);
            x_raw = [x_raw temp];
        elseif sz_xr_temp(2) > sz_xr_t_temp(2)
```

```
            diff_x = sz_xr_temp(2)-sz_xr_t_temp(2);
            temp = zeros(sz_xr_t_temp(1),diff_x);
            x_raw_t = [x_raw_t temp];
        end
    end

    x_raw = [x_raw; x_raw_t];
    sz_xr = size(x_raw);


    for jj = 1:sz_mr(1)
        for kk = 1:sz_mr(2)
            it = m_raw(jj,kk);
            if it == 0
                m_raw(jj,kk) = NaN;
            end
        end
    end


    for jj = 1:sz_xr(1)
        for kk = 2:sz_xr(2)
            it = x_raw(jj,kk);
            if it == 0
                x_raw(jj,kk) = NaN;
            end
        end
    end



%%cut based on N and M

    %cut m_raw to rid of <N or >M
    m = [];
    id_m = [];


    for jj = 1:sz_mr(1)
        it = m_raw(jj,:);
        [~,a] = find(~isnan(it));
        len = length(a);
        if len >= N && len <=M
            m = [m; m_raw(jj,:)];
        end
    end


    m_old = m;
    sz_m_old = size(m_old);
```

```
    m_new = m;
    m_new(:) = NaN;


    x = [];


    for jj = 1:sz_xr(1)
        it = x_raw(jj,:);
        [~,b] = find(~isnan(it));
        len = length(b);
        if len >= N && len <=M
            x = [x; x_raw(jj,:)];
        end
    end


    x_old = x;
    sz_x_old = size(x_old);


    x_new = x;
    x_new(:) = NaN;
    x_new(:,1) = 0;


%%shift all tracks to be consistent with t=0

    for jj = 1:sz_m_old(1)
        it = m_old(jj,:);
        [~,a] = find(~isnan(it));
        it_work = it(a(1):a(end));
        len = length(it_work);
        m_new(jj,1:len) = it_work;
    end


    m = m_new;


    for jj = 1:sz_x_old(1)
        it = x_old(jj,:);
        it(1) = [];
        [~,b] = find(~isnan(it));
        it_work = it(b(1):b(end));
        len = length(it_work);
        x_new(jj,2:(len+1)) = it_work;
    end
```

```
    x = x_new;
    sz_x_new = size(x_new);

    for jj = 1:sz_x_new(2)
        for kk = 1:sz_x_new(1)
            it = x_new(kk,jj);
            if ~isnan(it)
                new_it = it;
                if new_it < 0
                    new_it = 0;
                end
                x_new(kk,jj) = new_it;
            end
        end
    end


%%calculate mean area per track

    area = zeros(sz_m_old(1),1);


    for jj = 1:sz_m_old(1)
        it = m_new(jj,:);
        area(jj) = nanmean(it);
    end

%%calculate mean D per track

    t = linspace(0,sz_x_old(2)/10,sz_x_old(2));
    D = zeros(sz_m_old(1),1);
    tau = 4; %parameter for calculating D in #timepoints


    tt_temp = zeros(length(t)-1,1);
    for jj = 1:length(t)-1
        tt_temp(jj) = t(jj+1)-t(jj);
    end


    tau_time = tau*mean(tt_temp);


    for jj = 1:sz_x_old(1)
        it = x_new(jj,:)';
        [a,~] = find(~isnan(it));
        len = a(end);
        num = len/tau;
```

```
        %round down
        if ~isinteger(num)
            num2 = round(num);
            if num2-num <= 0.5
                num2 = num - 0.5;
                num2 = round(num2);
            end
            num = num2;
        end
            d_temp = zeros(num,1);
            temp = zeros(tau,1);
            temp(1) = it(1);
            for kk = 2:tau
                temp(kk) = it(1+kk-2);
            end
            d_temp(1) = mean(temp)/(6*tau_time);
            for kk = 2:length(d_temp)
                temp2 = zeros(tau,1);
                for ll = 1:tau
                    iter = 1 + ((kk-1)*tau)+ (ll-2);
                    temp2(ll) = it(iter);
                end
                d_temp(kk) = mean(temp2)/(6*tau_time);
            end
        D(jj) = nanmean(d_temp);
    end

%%create ensemble matrix

    ens = zeros(M,3);

    for jj = 1:M
        ens(jj,1) = nanmean(t(jj));
        ens(jj,2) = nanmean(x_new(:,jj));
        ens(jj,3) = nanstd(x_new(:,jj))/sum(~isnan(x_new(:,jj)));
        ens(jj,4) = sum(~isnan(x_new(:,jj)));
    end



%%create output matrix

    area_matrix{ii+1,1} = files[186];
    area_matrix{ii+1,2} = area;
    area_vector = [area_vector; area];

    Da_matrix{ii+1,1} = files[186];
    Da_matrix{ii+1,2} = D;
    Da_matrix{ii+1,4} = ens;
    D_vector = [D_vector; D];
    D_mean = nanmean(D_vector);
```

```
    total_tracks = [total_tracks; x_new(:,1:N)];
    end
%%calculate total ens matrix

total_ens_uncut = zeros(M,4);


for jj = 1:N
    total_ens(jj,1) = nanmean(t(jj));
    total_ens(jj,2) = nanmean(total_tracks(:,jj));
    total_ens(jj,3) = nanstd(total_tracks(:,jj));
    total_ens(jj,4) = sum(~isnan(total_tracks(:,jj)));
end


%%export area matrix

area_matrix{1,1} = 'file_name';
area_matrix{1,2} = 'area_vector';
area_matrix{1,3} = 'mean_area';
area_matrix{1,4} = 'total_area';
area_matrix{1,5} = 'number_bodies';
for ii = 1:length(files)
    it = area_matrix{ii+1,2};
    area_matrix{ii+1,3} = nanmean(it);
    area_matrix{ii+1,4} = sum(it);
    area_matrix{ii+1,5} = length(it);
end



%%export Da matrix

Da_matrix{1,1} = 'file_name';
Da_matrix{1,2} = 'D_vector';
Da_matrix{1,3} = 'mean_D';
Da_matrix{1,4} = 'ens_matrix';
for ii = 1:length(files)
    it = Da_matrix{ii+1,2};
    Da_matrix{ii+1,3} = nanmean(it);
end
```

APPENDIX I

ANALYSIS OF MVB FUSION WITHIN CELLS ON A 2D HYDROGEL SURFACE

Chapter 4 included visualizing CD63-pHLuorin2^{+} D1 cells and counting their fusion events. This section will describe how to image CD63-pHLuorin2^{+} D1 cells seeded on substrates (as described in Appendix G) and how to analyze the data to determine fusion events.

Note: for imaging experiments I used the DeltaVision OMX instrument by GE.

Materials

Imaging

- CellMask Deep Red (Thermo, C10046)
- Compatible 60X TIRF oil-immersion imaging objective (I used Olympus Apo N 60X 1.49)
- Immersion oil with refractive index 1.518 (Cargille)
- Square #1 thickness cover glass slides (12mm x 12mm)
- Rectangular #1 thickness cover glass slides (24mm x 60mm)
- Forceps
- Double-sided tape (Scotch)
- Krazy glue
- Bulb transfer pipette

Methods

Imaging

1. Seed CD63-pHLuorin2-expressing D1 cells on a PEG-coverslip-hydrogel as described in Appendix H or otherwise.
2. Stain the cells with CellMask Deep Red (1000X) for 5min at 37C.
3. Wash the cells.
4. Bring all materials to the imaging instrument.
5. Start the imaging instrument as appropriate.
6. Prepare the sample as follows:
    1. Glue two 12 x 12 cover slips to a 24 x 60 cover slip with a space in-between that will support the 12mm diameter PEG-hydrogel-coverslip. Note: do not use too much glue.

2. Place a drop of the medium which the cells are in, in-between the 12 x 12 cover slips.
3. Using forceps, pick up the PEG-coverslip-hydrogel with seeded cells and place it upside-down on top of the medium and the 12 x 12 cover slips.
4. Cut small pieces of double-sided tape and place one on top of each 12 x 12 cover slip (do not have them touch the sample)
5. Take another 24 x 60 cover slip and place it flush on top of the entire preparation, pressing down on the double-sided tape to seal it.
6. Mark this side (the bottom) with a marker.
7. Flip the preparation over.

7. Load the immersion oil on the objective.
8. Load the entire sample preparation on the objective.
9. Focus the sample to the matrix-cell interface.

Note: for experiments done here (using GE DeltaVision OMX), I found z-height of 5500-5700µm to work best.

10. Find a cell.
11. Turn on TIRF mode.
12. Calibrate the TIRF mode (‘Instrument’->’TIRF’->’Calibrate TIRF’).

Note: I used the following settings with the DeltaVision OMX:

- Imaging Mode: Sequential
- Light Path: TIRF
- Size: 512 x 512
- Binning: 1 x 1
- Channel: A488
  - Mode: Fast 286 MHz
  - Exposure: 75msec
  - Excitation: 568
  - Laser power: 50%
- Channel: Cy5
  - Mode: Fast 286 MHz
  - Exposure: 12msec
  - Excitation: 640
  - Laser power: 40%
- Experiment Type: TIRF
- Sectioning: unselected
- Time-lapse
  - ‘Time points’: 250
  - ‘Time-lapse’: 100msec
  - ‘Total time’: 25sec
- TIRF settings (Instrument->TIRF)
  - Angle (A488): 80-90
  - Angle (A568): 80-90

13. Acquire several image sets.
14. Clean up the instrument and objective as appropriate.

Analysis

Note: I used ImageJ and MATLAB R 2020a for this section.

1. Using ImageJ, process the images by cropping the image to contain only the cell.
2. Split the channels.
3. Save the green channel as an image sequence of JPEG images (i.e. you will obtain 250 image files).
4. Place these into a folder in MATLAB.
5. Process all images in the sequence by fitting their pixel intensities to a gaussian curve (this will clean up image noise.
6. For each image, create a 'mean image' of previous images (I used 5) by which to compare each current image.
7. For each image, subtract the above image and the mean image across the entire sequence, weighted by a threshold.
8. Binarize the resulting image and search for regions that are larger (~20 pixels or so).
9. Evaluate these regions by cross-referencing them with their state in the current image: calculate the total intensity during the potential event (current time) versus the total intensity before the potential event.
10. Count events only if they exceed a certain fold value of the above parameter.
11. Document important parameters of each event, such as its centroid, area, intensity, etc.
12. Export the number of events that occurred and their important parameters.

Note: The MATLAB script below is an example of how to do all of this: it will achieve steps #1-12 above.

Note: the parameters 'prev_num', 'threshold', 'ind_filter_fc', 'gauss_filt_std', and 'event_size' will affect event calling.

Note: 'event_log' contains a log of all called events with important parameters as described in the script.

```
%% define some parameters

prev_num = 5; % number of images in rolling average
threshold = 0.4; % background subtraction threshold
ind_filter_fc = 3; % fold change filter
gauss_filt_std = 2; % determines smoothing
event_size = 20; % number of pixels for event to be counted

%% process image sequence

ext_length = 10; % event extension in space
preallocate_num = 1000; % for speed
num_time = 0.1; % number to time conversion (sec per timepoint)
```

```
raw_images = cell(length(im_sequence),2);
gauss_images = cell(length(im_sequence),2); % clear previous sample processed
images
prev_image_means = cell(length(im_sequence),2);
processed_images_diff1 = cell(length(im_sequence)-(prev_num+1),2);
processed_images_diff2 = cell(length(im_sequence)-(prev_num+1),2);

for ii = 1:length(im_sequence)
    % process current image
    current_num = ii;
    it = im_sequence[186];
    it = imread(it);
    it = it(:,:,2);
    it_gfilt = imgaussfilt(it,gauss_filt_std); % filter gaussian

    gauss_images{ii,1} = it_gfilt; % store in processed_images
    gauss_images{ii,2} = current_num*num_time; % store time of image

    raw_images{ii,1} = it; % store
    raw_images{ii,2} = current_num*num_time; % store time of image
end

for ii = 1:length(gauss_images)
    it = double(gauss_images{ii,1});
    if ii == 1
        m_temp = it;
    else
        m_temp = m_temp+it;
    end
end

m_image = m_temp./length(gauss_images); % average by number of images
mean_image = uint8(m_image); % make back to uint8

for ii = (prev_num+1):length(im_sequence)


    current_image = gauss_images[186];
    current_num = ii;

    prev_image_mean_it = zeros(size(gauss_images{1,1}));

    for jj = 1:prev_num
        prev_image_mean_temp = double(gauss_images{ii-jj});
        prev_image_mean_it = prev_image_mean_it + prev_image_mean_temp;
    end

    prev_image_mean_it = prev_image_mean_it./prev_num;
    prev_image_mean_it = uint8(prev_image_mean_it);
    prev_image_means{ii,1} = prev_image_mean_it;

    diff_1 = 2.*current_image - prev_image_mean_it - mean_image;
    diff_1 = diff_1-threshold.*mean(current_image(:));
    diff_2 = diff_1;
```

```
    diff_2(diff_2 > 0) = 1;
    diff_2(diff_2 < 0) = 0;
    diff_2 = logical(double((diff_2)));

    processed_images_diff1{ii,1} = diff_1;
    processed_images_diff2{ii,1} = diff_2;

    prev_image_means{ii,2} = current_num*num_time;
    processed_images_diff1{ii,2} = current_num*num_time;
    processed_images_diff2{ii,2} = current_num*num_time;
end

im_sequence_adj = im_sequence;

for ii = 1:(prev_num)
    im_sequence_adj(1) = [];
    raw_images(1,:) = [];
    gauss_images(1,:) = [];
    prev_image_means(1,:) = [];
    processed_images_diff1(1,:) = [];
    processed_images_diff2(1,:) = [];
end
%% evaluate individual events

num_events = 0; % set number of events to 0

event_centroids = zeros(preallocate_num,2);
event_intensities = zeros(preallocate_num,1);
event_foldchanges = zeros(preallocate_num,1);
event_areas = zeros(preallocate_num,1);

% event_sequence = zeros(1,event_sequence_num*2+1);
event_log = cell(preallocate_num,6); % c1 = event num, c2 = time (sequence
number), c3 = centroid, c4 = area, c5 = intensity, c6 = FC, c7 = [xmin xmax
ymin ymax], c8 = pixellist
event_log2 = zeros(preallocate_num,3);

time_event = zeros(length(processed_images_diff2),2);

for ii = 1:length(processed_images_diff2)

    current_num = ii;
    current_im = processed_images_diff2{ii,1};
    current_time = processed_images_diff2{ii,2};
    time_event(ii,1) = current_time;

    o = regionprops(current_im,'Area','Centroid','PixelList');
    a = find([o.Area]>event_size); % filter objects less than event_size
parameter

    event_areas_temp = zeros(length(a),1);
    event_centroids_temp = zeros(length(a),2);
    list_temp1 = cell(length(a),1);
```

```
    for jj = 1:length(a)
         event_areas_temp(jj) = o(a(jj)).Area;
         event_centroids_temp(jj,:) = o(a(jj)).Centroid;
         list_temp1{jj} = o(a(jj)).PixelList;
    end

    real_image = gauss_images{ii,1};

    if ~isempty(event_centroids_temp)
        [sz,~] = size(event_centroids_temp);
        for kk = 1:sz
            list_temp2 = list_temp1{kk};
            ymin_ex = min(list_temp2(:,1))-ext_length; ymin =
min(list_temp2(:,1));
            ymax_ex = max(list_temp2(:,1))+ext_length; ymax =
max(list_temp2(:,1));
            xmin_ex = min(list_temp2(:,2))-ext_length; xmin =
min(list_temp2(:,2));
            xmax_ex = max(list_temp2(:,2))+ext_length; xmax =
max(list_temp2(:,2));
            size_image = size(real_image);
            if xmin_ex < 1
                xmin_ex = 1;
            end
            if ymin_ex < 1
                ymin_ex = 1;
            end
            if xmax_ex > size_image(1)
                xmax_ex = size_image(1);
            end
            if ymax_ex > size_image(2)
                ymax_ex = size_image(2);
            end

            temp_image = real_image;
            temp_image2 = prev_image_means{ii,1};

            temp_image_int = double(temp_image(xmin:xmax,ymin:ymax));
            temp_image_int = temp_image_int-min(temp_image_int(:));

            temp_image_int2 = double(temp_image2(xmin:xmax,ymin:ymax));
            temp_image_int2 = temp_image_int2-min(temp_image_int2(:));

            intensity_temp = sum(temp_image_int(:));
            intensity_temp2 = sum(temp_image_int2(:));

            fc_min_temp = sum(temp_image_int2(:));
            fc_max_temp = sum(temp_image_int(:));
            fold_change_temp = fc_max_temp/fc_min_temp;

            if fold_change_temp > ind_filter_fc
                event_centroids(num_events+1,:) = event_centroids_temp(kk,:);
                event_areas(num_events+1) = event_areas_temp(kk);
                event_intensities(num_events+1) = intensity_temp;
                event_foldchanges(num_events+1) = fold_change_temp;
```

```
                event_log_list_temp = [xmin_ex xmax_ex ymin_ex ymax_ex];
                event_log_list_temp2 = [xmin xmax ymin ymax];
                event_log{num_events+1,1} = num_events+1;
                event_log{num_events+1,2} = current_num;
                event_log{num_events+1,3} = event_centroids_temp(kk,:);
                event_log{num_events+1,4} = event_areas_temp(kk);
                event_log{num_events+1,5} = intensity_temp;
                event_log{num_events+1,6} = fold_change_temp;
                event_log{num_events+1,7} = event_log_list_temp;
                event_log{num_events+1,8} = event_log_list_temp2;
                event_log{num_events+1,9} = list_temp2;
                event_log2(num_events+1,1) = current_num;
                event_log2(num_events+1,2:3) = event_centroids_temp(kk,:);
                time_event(ii,2) = 1;
                new_event = 1;
                num_events = num_events + 1;
            end
        end
    end
end

event_centroids((num_events+1):preallocate_num,:) = [];
event_intensities((num_events+1):preallocate_num,:) = [];
event_foldchanges((num_events+1):preallocate_num,:) = [];
event_areas((num_events+1):preallocate_num,:) = [];
event_log((num_events+1):preallocate_num,:) = [];
event_log2((num_events+1):preallocate_num,:) = [];
```

APPENDIX J
QUANTITATIVE PCR PRIMERS

Table 1. Reverse transcription and quantitative PCR primers used in Chapter 2.

Target	**Sequence**
Human *GAPDH* (NM_002046)	Forward (F): ACATCGCTCAGACACCATG Reverse (R): TGTAGTTGAGGTCAATGAAGGG
Human *PTK2* (*FAK*) (NM_001199649.2)	F: CTTGGCCCTGAGGACATTATT R: CACCCAGGTCAGAGTTCAATAG
Human *TLN1* (NM_006289.4)	F: GGGACTTCAGACCCAAGTTATT R: CAGACAGGTGAGCTGATTGTAG
Mouse *GAPDH* (NM_001289726.1)	F: AGCAGCCGCATCTTCTTGTGCAGTG R: GGCCTTGACTGTGCCGTTGAATTT
Mouse *Fgf7* (*KGF*) (NM_008008.4)	F: GTCCTAGCCTCTTTCCAATAACA R: GCATCTTCCCAGATGAGAGTAAA
Mouse *IL6* (NM_001314054.1)	F: GTCTGTAGCTCATTCTGCTCTG R: GAAGGCAACTGGATGGAAGT
Mouse *ND1* (NC_005089.1)	F: CTAGAAACCCCGAACCAAA R: CCAGCTATCACCAAGCTCGT
Mouse *mt-Atp6* (NC_005089.1)	F: GCTCTCACTCGCCCACTTCCTTCC R: GCCGGACTGCTAATGCCATTGGTT
Mouse Rnu6 (U6) (NR_003027.2)	F: CTCGCTTCGGCAGCACA R: AACGCTTCACGAATTTGCGT
SLRT for mouse miR-146A (NR_029701.1)	GTCGTATCCAGTGCAGGGTCCGAGGTATTCGCACTGG ATACGACAACCCA
SLRT for mouse miR-30b-3p (NR_029534.1)	GTCGTATCCAGTGCAGGGTCCGAGGTATTCGCACTGG ATACGACGACGTA
SLRT for mouse miR-27a-3p (NR_029746.1)	GTCGTATCCAGTGCAGGGTCCGAGGTATTCGCACTGG ATACGACGCGGAA
Mouse miR-146A Forward	CGGCGGTGAGAACTGAATTCCAT
Mouse miR-30b-3p Forward	CGCCGTCTGGGATGTGGA
Mouse miR-27a-3p Forward	CGCCCGTTCACAGTGGCT
miRNA Universal reverse qPCR primer	CCAGTGCAGGGTCCGAGGTA

Table 2. Reverse transcription and quantitative PCR primers used in Chapter 3.

Target	**Sequence**
GAPDH	F: ACATCGCTCAGACACCATG R: TGTAGTTGAGGTCAATGAAGGG
AQP1	F: CTGGCGATTGACTACACTGG R: AAGTCATAGATGAGCACTGCC
AQP2	F: TTGGTTTCTCTGTTACCCTGG R: AACGGGCTGGATTCATGG
AQP3	F: CTTTGCCACCTATCCCTCTG R: CCACAGTGAAAGCCTCCAG
AQP4	F: GCTTAGATCTGGCTTTCAAAGG R: AATGTCCACACTTACCCCAC
AQP5	F: CTCCCCAGCCTTATCCATTG R: ACCCAGAAGACCCAGTGAG

APPENDIX K

COPYRIGHT STATEMENTS

Lenzini S., Devine D., and Shin J.-W. Leveraging biomaterial mechanics to improve pluripotent stem cell applications for tissue engineering. Front. Bioeng. Biotechnol. 2019; 10.

From: https://www.frontiersin.org/about/policies-and-publication-ethics

"Frontiers allows the inclusion of content which first appeared in an author's thesis so long as this is the only form in which it has appeared, is in line with the author's university policy, and can be accessed online. If the thesis is not archived online, it is considered original, unpublished data and is subject to the unpublished data restrictions of some article types. Inclusion of material from theses or dissertations should be noted in the Acknowledgements section of the manuscript AND cited accordingly in the reference list. For some examples, please check our Manuscript Formatting Guidelines."

Wong, S.W., Lenzini, S., Cooper, M.H., Mooney, D.J., Shin, J.-W. Soft extracellular matrix enhances inflammatory activation of mesenchymal stromal cells to induce monocyte production and trafficking. Science Advances, 2020. 6(15): p. eaaw0158.

From: https://advances.sciencemag.org/content/6/15/eaaw0158?intcmp=trendmd-adv

"This is an open-access article distributed under the terms of the Creative Commons Attribution-NonCommercial license, which permits use, distribution, and reproduction in any medium, so long as the resultant use is not for commercial advantage and provided the original work is properly cited."

Devine, D., Vijayakumar, V., Wong, S.W., Lenzini, S., Newman, P., Shin, J.-W. Hydrogel Micropost Arrays with Single Post Tunability to Study Cell Volume and Mechanotransduction. Adv Biosyst, 2020. 4(11): p. e2000012.

From: https://www.wiley.com/network/researchers/latest-content/how-to-clear-permissions-for-a-thesis-or-dissertation

“If you are the author of a published Wiley article, you have the right to reuse the full text of your published article as part of your thesis or dissertation. In this situation, you do not need to request permission from Wiley for this use.”

Lenzini, S., Bargi, R., Chung, G., Shin, J.-W. Matrix mechanics and water permeation regulate extracellular vesicle transport. Nat Nanotechnol 2020; 15: 217-223.

From: https://www.nature.com/nature-research/reprints-and-permissions/permissions-requests

"Authors have the right to reuse their article’s Version of Record, in whole or in part, in their own thesis. Additionally, they may reproduce and make available their thesis, including Springer Nature content, as required by their awarding academic institution. Authors must properly cite the published article in their thesis according to current citation standards.”

CITED LITERATURE

1. Pan, B.-T. and R.M. Johnstone, *Fate of the transferrin receptor during maturation of sheep reticulocytes in vitro: Selective externalization of the receptor.* Cell, 1983. **33**(3): p. 967-978.
2. Harding, C., J. Heuser, and P. Stahl, *Receptor-mediated endocytosis of transferrin and recycling of the transferrin receptor in rat reticulocytes.* Journal of Cell Biology, 1983. **97**(2): p. 329-339.
3. Harding, C., J. Heuser, and P. Stahl, *Endocytosis and intracellular processing of transferrin and colloidal gold-transferrin in rat reticulocytes: demonstration of a pathway for receptor shedding.* Eur J Cell Biol, 1984. **35**(2): p. 256-63.
4. Wolf, P., *The Nature and Significance of Platelet Products in Human Plasma.* British Journal of Haematology, 1967. **13**(3): p. 269-288.
5. Kalluri, R. and V.S. LeBleu, *The biology, function, and biomedical applications of exosomes.* Science, 2020. **367**(6478).
6. El Andaloussi, S., et al., *Extracellular vesicles: biology and emerging therapeutic opportunities.* Nature Reviews Drug Discovery, 2013. **12**(5): p. 347-357.
7. Raposo, G., et al., *B lymphocytes secrete antigen-presenting vesicles.* Journal of Experimental Medicine, 1996. **183**(3): p. 1161-1172.
8. Valadi, H., et al., *Exosome-mediated transfer of mRNAs and microRNAs is a novel mechanism of genetic exchange between cells.* Nature Cell Biology, 2007. **9**(6): p. 654-659.
9. Zomer, A., et al., *In Vivo imaging reveals extracellular vesicle-mediated phenocopying of metastatic behavior.* Cell, 2015. **161**(5): p. 1046-1057.
10. Liang, X., et al., *Paracrine mechanisms of mesenchymal stem cell-based therapy: current status and perspectives.* Cell Transplant, 2014. **23**(9): p. 1045-59.
11. Volarevic, V., et al., *Ethical and Safety Issues of Stem Cell-Based Therapy.* International journal of medical sciences, 2018. **15**(1): p. 36-45.
12. Esensten, J.H., J.A. Bluestone, and W.A. Lim, *Engineering Therapeutic T Cells: From Synthetic Biology to Clinical Trials.* Annual Review of Pathology: Mechanisms of Disease, 2017. **12**(1): p. 305-330.
13. Fu, W., et al., *CAR exosomes derived from effector CAR-T cells have potent antitumour effects and low toxicity.* Nature Communications, 2019. **10**(1): p. 4355.
14. Zhu, X., et al., *Comprehensive toxicity and immunogenicity studies reveal minimal effects in mice following sustained dosing of extracellular vesicles derived from HEK293T cells.* J Extracell Vesicles, 2017. **6**(1): p. 1324730.
15. Ha, D., N. Yang, and V. Nadithe, *Exosomes as therapeutic drug carriers and delivery vehicles across biological membranes: current perspectives and future challenges.* Acta Pharmaceutica Sinica B, 2016. **6**(4): p. 287-296.
16. Jeyaram, A. and S.M. Jay, *Preservation and Storage Stability of Extracellular Vesicles for Therapeutic Applications.* The AAPS journal, 2017. **20**(1): p. 1-1.
17. Mendt, M., K. Rezvani, and E. Shpall, *Mesenchymal stem cell-derived exosomes for clinical use.* Bone Marrow Transplant, 2019. **54**(Suppl 2): p. 789-792.
18. Abraham, A. and A. Krasnodembskaya, *Mesenchymal stem cell-derived extracellular vesicles for the treatment of acute respiratory distress syndrome.* Stem Cells Transl Med, 2020. **9**(1): p. 28-38.

19. Mansouri, N., et al., *Mesenchymal stromal cell exosomes prevent and revert experimental pulmonary fibrosis through modulation of monocyte phenotypes.* JCI Insight, 2019. **4**(21).
20. Li, T., et al., *Exosomes Derived from Human Umbilical Cord Mesenchymal Stem Cells Alleviate Liver Fibrosis.* Stem Cells and Development, 2012. **22**(6): p. 845-854.
21. Grange, C., et al., *Stem cell-derived extracellular vesicles inhibit and revert fibrosis progression in a mouse model of diabetic nephropathy.* Scientific Reports, 2019. **9**(1): p. 4468.
22. Alibhai, F.J., et al., *Emerging roles of extracellular vesicles in cardiac repair and rejuvenation.* American Journal of Physiology-Heart and Circulatory Physiology, 2018. **315**(4): p. H733-H744.
23. Galieva, L.R., et al., *Therapeutic Potential of Extracellular Vesicles for the Treatment of Nerve Disorders.* Frontiers in neuroscience, 2019. **13**: p. 163-163.
24. Wiklander, O.P.B., et al., *Advances in therapeutic applications of extracellular vesicles.* Sci Transl Med, 2019. **11**(492).
25. Kordelas, L., et al., *MSC-derived exosomes: a novel tool to treat therapy-refractory graft-versus-host disease.* Leukemia, 2014. **28**(4): p. 970-973.
26. Whitford, W. and P. Guterstam, *Exosome manufacturing status.* Future Med Chem, 2019. **11**(10): p. 1225-1236.
27. Meldolesi, J., *Exosomes and ectosomes in intercellular communication.* Current Biology, 2018. **28**(8): p. R435-R444.
28. Colombo, M., et al., *Analysis of ESCRT functions in exosome biogenesis, composition and secretion highlights the heterogeneity of extracellular vesicles.* Journal of Cell Science, 2013. **126**(24): p. 5553.
29. Hessvik, N.P. and A. Llorente, *Current knowledge on exosome biogenesis and release.* Cellular and molecular life sciences : CMLS, 2018. **75**(2): p. 193-208.
30. Lai, C.P., et al., *Dynamic Biodistribution of Extracellular Vesicles in Vivo Using a Multimodal Imaging Reporter.* ACS Nano, 2014. **8**(1): p. 483-494.
31. Gangadaran, P., et al., *A new bioluminescent reporter system to study the biodistribution of systematically injected tumor-derived bioluminescent extracellular vesicles in mice.* Oncotarget, 2017. **8**(66): p. 109894-109914.
32. Wiklander, O.P.B., et al., *Extracellular vesicle in vivo biodistribution is determined by cell source, route of administration and targeting.* Journal of extracellular vesicles, 2015. **4**: p. 26316-26316.
33. Smyth, T., et al., *Biodistribution and delivery efficiency of unmodified tumor-derived exosomes.* Journal of Controlled Release, 2015. **199**: p. 145-155.
34. Kooijmans, S.A.A., et al., *PEGylated and targeted extracellular vesicles display enhanced cell specificity and circulation time.* Journal of Controlled Release, 2016. **224**: p. 77-85.
35. Antes, T.J., et al., *Targeting extracellular vesicles to injured tissue using membrane cloaking and surface display.* Journal of Nanobiotechnology, 2018. **16**(1): p. 61.
36. Li, Y., et al., *EV-origin: Enumerating the tissue-cellular origin of circulating extracellular vesicles using exLR profile.* Computational and Structural Biotechnology Journal, 2020. **18**: p. 2851-2859.
37. Huleihel, L., et al., *Matrix-bound nanovesicles within ECM bioscaffolds.* Science Advances, 2016. **2**(6): p. e1600502.

38. Nawaz, M., et al., *Extracellular Vesicles and Matrix Remodeling Enzymes: The Emerging Roles in Extracellular Matrix Remodeling, Progression of Diseases and Tissue Repair.* Cells, 2018. **7**(10).
39. Bidarimath, M., et al., *Extracellular vesicle mediated intercellular communication at the porcine maternal-fetal interface: A new paradigm for conceptus-endometrial cross-talk.* Scientific Reports, 2017. **7**(1): p. 40476.
40. Saint-Pol, J., et al., *Targeting and Crossing the Blood-Brain Barrier with Extracellular Vesicles.* Cells, 2020. **9**(4).
41. Miyazawa, B., et al., *Regulation of endothelial cell permeability by platelet-derived extracellular vesicles.* The journal of trauma and acute care surgery, 2019. **86**(6): p. 931-942.
42. Ma, Y., et al., *Role of Neutrophil Extracellular Traps and Vesicles in Regulating Vascular Endothelial Permeability.* Frontiers in Immunology, 2019. **10**(1037).
43. Ivanovska, I.L., et al., *Stem cell mechanobiology: diverse lessons from bone marrow.* Trends in Cell Biology, 2015. **25**(9): p. 523-532.
44. Streuli, C.H., *Integrins as architects of cell behavior.* Molecular Biology of the Cell, 2016. **27**(19): p. 2885-2888.
45. Pelham, R.J., Jr. and Y. Wang, *Cell locomotion and focal adhesions are regulated by substrate flexibility.* Proc Natl Acad Sci U S A, 1997. **94**(25): p. 13661-5.
46. McBeath, R., et al., *Cell shape, cytoskeletal tension, and RhoA regulate stem cell lineage commitment.* Dev Cell, 2004. **6**(4): p. 483-95.
47. Engler, A.J., et al., *Matrix elasticity directs stem cell lineage specification.* Cell, 2006. **126**(4): p. 677-89.
48. Sun, M., et al., *Effects of matrix stiffness on the morphology, adhesion, proliferation and osteogenic differentiation of mesenchymal stem cells.* International journal of medical sciences, 2018. **15**(3): p. 257.
49. Peyton, S.R., et al., *Marrow-Derived stem cell motility in 3D synthetic scaffold is governed by geometry along with adhesivity and stiffness.* Biotechnology and Bioengineering, 2011. **108**(5): p. 1181-1193.
50. Nikkhah, M., et al., *Engineering microscale topographies to control the cell–substrate interface.* Biomaterials, 2012. **33**(21): p. 5230-5246.
51. Uroz, M., et al., *Regulation of cell cycle progression by cell–cell and cell–matrix forces.* Nature Cell Biology, 2018. **20**(6): p. 646-654.
52. Lee, G., et al., *Cancer Mechanobiology: Microenvironmental Sensing and Metastasis.* ACS Biomaterials Science & Engineering, 2019. **5**(8): p. 3735-3752.
53. Tschumperlin, D.J., et al., *Mechanosensing and fibrosis.* The Journal of Clinical Investigation, 2018. **128**(1): p. 74-84.
54. Han, Y., et al., *Mechanobiology in vascular remodeling.* National Science Review, 2018. **5**(6): p. 933-946.
55. Diz-Muñoz, A., D.A. Fletcher, and O.D. Weiner, *Use the force: membrane tension as an organizer of cell shape and motility.* Trends in cell biology, 2013. **23**(2): p. 47-53.
56. Guo, M., et al., *Cell volume change through water efflux impacts cell stiffness and stem cell fate.* Proceedings of the National Academy of Sciences, 2017. **114**(41): p. E8618.
57. Gauthier, N.C., T.A. Masters, and M.P. Sheetz, *Mechanical feedback between membrane tension and dynamics.* Trends in Cell Biology, 2012. **22**(10): p. 527-535.

58. Fletcher, D.A. and R.D. Mullins, *Cell mechanics and the cytoskeleton.* Nature, 2010. **463**(7280): p. 485-492.
59. Chugh, P., et al., *Actin cortex architecture regulates cell surface tension.* Nature Cell Biology, 2017. **19**(6): p. 689-697.
60. Panciera, T., et al., *Mechanobiology of YAP and TAZ in physiology and disease.* Nature Reviews Molecular Cell Biology, 2017. **18**(12): p. 758-770.
61. Oakes, P.W., et al., *Lamellipodium is a myosin-independent mechanosensor.* Proc Natl Acad Sci U S A, 2018. **115**(11): p. 2646-2651.
62. Zhao, Q., et al., *Structure and mechanogating mechanism of the Piezo1 channel.* Nature, 2018. **554**(7693): p. 487-492.
63. Schwab, A., et al., *Role of Ion Channels and Transporters in Cell Migration.* Physiological Reviews, 2012. **92**(4): p. 1865-1913.
64. Blanc, L., et al., *The water channel aquaporin-1 partitions into exosomes during reticulocyte maturation: implication for the regulation of cell volume.* Blood, 2009. **114**(18): p. 3928-34.
65. Huebert, R.C., et al., *Aquaporin-1 facilitates angiogenic invasion in the pathological neovasculature that accompanies cirrhosis.* Hepatology, 2010. **52**(1): p. 238-248.
66. Wong, S.W., S. Lenzini, and J.-W. Shin, *Perspective: Biophysical regulation of cancerous and normal blood cell lineages in hematopoietic malignancies.* APL Bioengineering, 2018. **2**(3): p. 031802.
67. Lee, K.Y. and D.J. Mooney, *Alginate: Properties and biomedical applications.* Progress in Polymer Science, 2012. **37**(1): p. 106-126.
68. Lenzini, S., D. Devine, and J.W. Shin, *Leveraging Biomaterial Mechanics to Improve Pluripotent Stem Cell Applications for Tissue Engineering.* Front Bioeng Biotechnol, 2019. **7**: p. 260.
69. Chaudhuri, O., et al., *Hydrogels with tunable stress relaxation regulate stem cell fate and activity.* Nature Materials, 2016. **15**(3): p. 326-334.
70. Vining, K.H., A. Stafford, and D.J. Mooney, *Sequential modes of crosslinking tune viscoelasticity of cell-instructive hydrogels.* Biomaterials, 2019. **188**: p. 187-197.
71. Chaudhuri, O., et al., *Substrate stress relaxation regulates cell spreading.* Nature Communications, 2015. **6**(1): p. 6365.
72. Li, L., J. Eyckmans, and C.S. Chen, *Designer biomaterials for mechanobiology.* Nature materials, 2017. **16**(12): p. 1164-1168.
73. Liu, Z., et al., *Looking into the Future: Toward Advanced 3D Biomaterials for Stem-Cell-Based Regenerative Medicine.* Advanced Materials, 2018. **30**(17): p. 1705388.
74. Baker, B.M. and C.S. Chen, *Deconstructing the third dimension – how 3D culture microenvironments alter cellular cues.* Journal of Cell Science, 2012. **125**(13): p. 3015.
75. Bao, M., et al., *3D microniches reveal the importance of cell size and shape.* Nature Communications, 2017. **8**(1): p. 1962.
76. Gauthier, N.C., et al., *Temporary increase in plasma membrane tension coordinates the activation of exocytosis and contraction during cell spreading.* Proceedings of the National Academy of Sciences, 2011. **108**(35): p. 14467.
77. Goud, B. and P.A. Gleeson, *TGN golgins, Rabs and cytoskeleton: regulating the Golgi trafficking highways.* Trends in Cell Biology, 2010. **20**(6): p. 329-336.
78. Rogers, S.L. and V.I. Gelfand, *Membrane trafficking, organelle transport, and the cytoskeleton.* Current Opinion in Cell Biology, 2000. **12**(1): p. 57-62.

79. Granger, E., et al., *The role of the cytoskeleton and molecular motors in endosomal dynamics.* Seminars in cell & developmental biology, 2014. **31**(100): p. 20-29.
80. Tomlins, P., et al., *Measurement of Pore Size and Porosity of Tissue Scaffolds.* Journal of ASTM International, 2004. **1**(1): p. 1-8.
81. Xu, Z., et al., *Spatiotemporal Characterization of Extracellular Matrix Microstructures in Engineered Tissue: A Whole-Field Spectroscopic Imaging Approach.* Journal of Nanotechnology in Engineering and Medicine, 2013. **4**(1).
82. DiDomenico, C.D., M. Lintz, and L.J. Bonassar, *Molecular transport in articular cartilage - what have we learned from the past 50 years?* Nat Rev Rheumatol, 2018. **14**(7): p. 393-403.
83. van Zijl, F., G. Krupitza, and W. Mikulits, *Initial steps of metastasis: cell invasion and endothelial transmigration.* Mutation research, 2011. **728**(1-2): p. 23-34.
84. Beekhuizen, H. and R.v. Furth, *Diapedesis*, in *Encyclopedia of Immunology (Second Edition)*, P.J. Delves, Editor. 1998, Elsevier: Oxford. p. 757-760.
85. Suh, J., M. Dawson, and J. Hanes, *Real-time multiple-particle tracking: applications to drug and gene delivery.* Advanced Drug Delivery Reviews, 2005. **57**(1): p. 63-78.
86. Mason, T.G., et al., *Particle Tracking Microrheology of Complex Fluids.* Physical Review Letters, 1997. **79**(17): p. 3282-3285.
87. Wirtz, D., *Particle-Tracking Microrheology of Living Cells: Principles and Applications.* Annual Review of Biophysics, 2009. **38**(1): p. 301-326.
88. Ensign, L.M., et al., *Ex vivo characterization of particle transport in mucus secretions coating freshly excised mucosal tissues.* Molecular pharmaceutics, 2013. **10**(6): p. 2176-2182.
89. Yáñez-Mó, M., et al., *Biological properties of extracellular vesicles and their physiological functions.* Journal of Extracellular Vesicles, 2015. **4**(1): p. 27066.
90. Hussey, G.S., et al., *Lipidomics and RNA sequencing reveal a novel subpopulation of nanovesicle within extracellular matrix biomaterials.* Science Advances, 2020. **6**(12): p. eaay4361.
91. Hoshino, A., et al., *Tumour exosome integrins determine organotropic metastasis.* Nature, 2015. **527**(7578): p. 329-35.
92. Lai, R.C., et al., *MSC secretes at least 3 EV types each with a unique permutation of membrane lipid, protein and RNA.* J Extracell Vesicles, 2016. **5**: p. 29828.
93. Yu, M., et al., *Rapid transport of deformation-tuned nanoparticles across biological hydrogels and cellular barriers.* Nature Communications, 2018. **9**(1): p. 2607.
94. Vorselen, D., et al., *The fluid membrane determines mechanics of erythrocyte extracellular vesicles and is softened in hereditary spherocytosis.* Nature Communications, 2018. **9**(1): p. 4960.
95. Witten, J. and K. Ribbeck, *The particle in the spider's web: transport through biological hydrogels.* Nanoscale, 2017. **9**(24): p. 8080-8095.
96. Friedl, P. and K. Wolf, *Plasticity of cell migration: a multiscale tuning model.* Journal of Cell Biology, 2009. **188**(1): p. 11-19.
97. Brábek, J., et al., *The role of the tissue microenvironment in the regulation of cancer cell motility and invasion.* Cell Communication and Signaling, 2010. **8**(1): p. 22.
98. Wolf, K., et al., *Multi-step pericellular proteolysis controls the transition from individual to collective cancer cell invasion.* Nature Cell Biology, 2007. **9**(8): p. 893-904.

99. Trappmann, B., et al., *Matrix degradability controls multicellularity of 3D cell migration.* Nature Communications, 2017. **8**(1): p. 371.
100. Dolo, V., et al., *Matrix-degrading proteinases are shed in membrane vesicles by ovarian cancer cells in vivo and in vitro.* Clinical & Experimental Metastasis, 1999. **17**(2): p. 131-140.
101. Chanda, D., et al., *Fibronectin on the Surface of Extracellular Vesicles Mediates Fibroblast Invasion.* American journal of respiratory cell and molecular biology, 2019. **60**(3): p. 279-288.
102. Arasu, U.T., et al., *Human mesenchymal stem cells secrete hyaluronan-coated extracellular vesicles.* Matrix Biology, 2017. **64**: p. 54-68.
103. Wiklander, O.P.B., et al., *Advances in therapeutic applications of extracellular vesicles.* Science translational medicine, 2019. **11**(492): p. eaav8521.
104. Van Niel, G., G. d'Angelo, and G. Raposo, *Shedding light on the cell biology of extracellular vesicles.* Nature reviews Molecular cell biology, 2018. **19**(4): p. 213.
105. Mathieu, M., et al., *Specificities of secretion and uptake of exosomes and other extracellular vesicles for cell-to-cell communication.* Nature Cell Biology, 2019. **21**(1): p. 9-17.
106. Shao, C., et al., *Role of hypoxia-induced exosomes in tumor biology.* Molecular Cancer, 2018. **17**(1): p. 120.
107. Verweij, F.J., et al., *Quantifying exosome secretion from single cells reveals a modulatory role for GPCR signaling.* J Cell Biol, 2018. **217**(3): p. 1129-1142.
108. Messenger, S.W., et al., *A Ca2+-stimulated exosome release pathway in cancer cells is regulated by Munc13-4.* Journal of Cell Biology, 2018. **217**(8): p. 2877-2890.
109. Sung, B.H., et al., *Directional cell movement through tissues is controlled by exosome secretion.* Nature Communications, 2015. **6**(1): p. 7164.
110. Santoso, M.R., et al., *Exosomes From Induced Pluripotent Stem Cell-Derived Cardiomyocytes Promote Autophagy for Myocardial Repair.* J Am Heart Assoc, 2020. **9**(6): p. e014345.
111. Feng, Y., et al., *Human bone marrow mesenchymal stem cells rescue endothelial cells experiencing chemotherapy stress by mitochondrial transfer via tunneling nanotubes.* Stem cells and development, 2019. **28**(10): p. 674-682.
112. van Balkom, B.W.M., et al., *Endothelial cells require miR-214 to secrete exosomes that suppress senescence and induce angiogenesis in human and mouse endothelial cells.* Blood, 2013. **121**(19): p. 3997-4006.
113. Pittenger, M.F., et al., *Mesenchymal stem cell perspective: cell biology to clinical progress.* npj Regenerative Medicine, 2019. **4**(1): p. 22.
114. Phinney, D.G. and M.F. Pittenger, *Concise Review: MSC-Derived Exosomes for Cell-Free Therapy.* Stem Cells, 2017. **35**(4): p. 851-858.
115. Tang, X.D., et al., *Mesenchymal stem cell microvesicles attenuate acute lung injury in mice partly mediated by Ang-1 mRNA.* Stem cells, 2017. **35**(7): p. 1849-1859.
116. Ahn, S.Y., et al., *Vascular endothelial growth factor mediates the therapeutic efficacy of mesenchymal stem cell-derived extracellular vesicles against neonatal hyperoxic lung injury.* Experimental & molecular medicine, 2018. **50**(4): p. 1-12.
117. Zhu, Y.g., et al., *Human mesenchymal stem cell microvesicles for treatment of Escherichia coli endotoxin-induced acute lung injury in mice.* Stem cells, 2014. **32**(1): p. 116-125.

118. Shah, T., et al., *Alk5/Runx1 signaling mediated by extracellular vesicles promotes vascular repair in acute respiratory distress syndrome.* Clinical and translational medicine, 2018. **7**(1): p. 19.
119. Monsel, A., et al., *Therapeutic effects of human mesenchymal stem cell–derived microvesicles in severe pneumonia in mice.* American journal of respiratory and critical care medicine, 2015. **192**(3): p. 324-336.
120. Park, J., et al., *Therapeutic effects of human mesenchymal stem cell microvesicles in an ex vivo perfused human lung injured with severe E. coli pneumonia.* Thorax, 2019. **74**(1): p. 43-50.
121. Chaubey, S., et al., *Early gestational mesenchymal stem cell secretome attenuates experimental bronchopulmonary dysplasia in part via exosome-associated factor TSG-6.* Stem cell research & therapy, 2018. **9**(1): p. 1-26.
122. Morrison, T.J., et al., *Mesenchymal stromal cells modulate macrophages in clinically relevant lung injury models by extracellular vesicle mitochondrial transfer.* American journal of respiratory and critical care medicine, 2017. **196**(10): p. 1275-1286.
123. Weaver, V.M., *Cell and tissue mechanics: the new cell biology frontier.* Mol Biol Cell, 2017. **28**(14): p. 1815-1818.
124. Smith, L.R., S. Cho, and D.E. Discher, *Stem cell differentiation is regulated by extracellular matrix mechanics.* Physiology, 2018. **33**(1): p. 16-25.
125. Wong, S.W., S. Lenzini, and J.W. Shin, *Perspective: Biophysical regulation of cancerous and normal blood cell lineages in hematopoietic malignancies.* APL Bioeng, 2018. **2**(3): p. 031802.
126. Desai, R.M., et al., *Versatile click alginate hydrogels crosslinked via tetrazine-norbornene chemistry.* Biomaterials, 2015. **50**: p. 30-7.
127. Zhao, X., et al., *Stress-relaxation behavior in gels with ionic and covalent crosslinks.* J Appl Phys, 2010. **107**(6): p. 63509.
128. Courtney, T.H., *Mechanical behavior of materials*. 2005: Waveland Press.
129. Askeland, D.R. and W.J. Wright, *The science and engineering of materials*. Seventh edition. ed. 2016, Boston, MA: Cengage Learning. xx, 870 pages.
130. Lobb, R.J., et al., *Optimized exosome isolation protocol for cell culture supernatant and human plasma.* J Extracell Vesicles, 2015. **4**: p. 27031.
131. Yang, L.-h., et al., *Universal stem-loop primer method for screening and quantification of microRNA.* PLoS One, 2014. **9**(12): p. e115293.
132. Lenzini, S., et al., *Matrix mechanics and water permeation regulate extracellular vesicle transport.* Nat Nanotechnol, 2020. **15**(3): p. 217-223.
133. Devine, D., et al., *Hydrogel Micropost Arrays with Single Post Tunability to Study Cell Volume and Mechanotransduction.* Adv Biosyst, 2020. **4**(11): p. e2000012.
134. Knezevic, N., et al., *The G protein betagamma subunit mediates reannealing of adherens junctions to reverse endothelial permeability increase by thrombin.* J Exp Med, 2009. **206**(12): p. 2761-77.
135. Humphries, J.D., A. Byron, and M.J. Humphries, *Integrin ligands at a glance.* Journal of cell science, 2006. **119**(19): p. 3901-3903.
136. Diduch, D.R., et al., *Two cell lines from bone marrow that differ in terms of collagen synthesis, osteogenic characteristics, and matrix mineralization.* JBJS, 1993. **75**(1): p. 92-105.

137. Nolte, M.A., E.N.M. Nolte-'t Hoen, and C. Margadant, *Integrins Control Vesicular Trafficking; New Tricks for Old Dogs.* Trends Biochem Sci, 2020.
138. Gumbiner, B.M., *Regulation of cadherin-mediated adhesion in morphogenesis.* Nat Rev Mol Cell Biol, 2005. **6**(8): p. 622-34.
139. Kim, C., F. Ye, and M.H. Ginsberg, *Regulation of integrin activation.* Annu Rev Cell Dev Biol, 2011. **27**: p. 321-45.
140. Kong, F., et al., *Demonstration of catch bonds between an integrin and its ligand.* J Cell Biol, 2009. **185**(7): p. 1275-84.
141. Mas-Moruno, C., F. Rechenmacher, and H. Kessler, *Cilengitide: the first anti-angiogenic small molecule drug candidate design, synthesis and clinical evaluation.* Anticancer Agents Med Chem, 2010. **10**(10): p. 753-68.
142. Hong, S., et al., *Real-time analysis of cell-surface adhesive interactions using thickness shear mode resonator.* Biomaterials, 2006. **27**(34): p. 5813-20.
143. Matthay, M.A., *Extracellular Vesicle Transfer from Mesenchymal Stromal Cells Modulates Macrophage Function in Acute Lung Injury. Basic Science and Clinical Implications.* Am J Respir Crit Care Med, 2017. **196**(10): p. 1234-1236.
144. Zhu, Y.G., et al., *Human mesenchymal stem cell microvesicles for treatment of Escherichia coli endotoxin-induced acute lung injury in mice.* Stem Cells, 2014. **32**(1): p. 116-25.
145. Ragni, E., et al., *Extracellular Vesicle-Shuttled mRNA in Mesenchymal Stem Cell Communication.* Stem Cells, 2017. **35**(4): p. 1093-1105.
146. Ma, S., et al., *Immunobiology of mesenchymal stem cells.* Cell Death & Differentiation, 2014. **21**(2): p. 216-225.
147. Morrison, T.J., et al., *Mesenchymal Stromal Cells Modulate Macrophages in Clinically Relevant Lung Injury Models by Extracellular Vesicle Mitochondrial Transfer.* Am J Respir Crit Care Med, 2017. **196**(10): p. 1275-1286.
148. Song, Y., et al., *Exosomal miR-146a Contributes to the Enhanced Therapeutic Efficacy of Interleukin-1β-Primed Mesenchymal Stem Cells Against Sepsis.* Stem Cells, 2017. **35**(5): p. 1208-1221.
149. Yi, X., et al., *Exosomes derived from microRNA-30b-3p-overexpressing mesenchymal stem cells protect against lipopolysaccharide-induced acute lung injury by inhibiting SAA3.* Exp Cell Res, 2019. **383**(2): p. 111454.
150. Wang, J., et al., *Mesenchymal Stem Cell–Derived Extracellular Vesicles Alleviate Acute Lung Injury Via Transfer of miR-27a-3p*.* Critical Care Medicine, 2020. **48**(7): p. e599-e610.
151. Sinha, S., et al., *Cortactin promotes exosome secretion by controlling branched actin dynamics.* J Cell Biol, 2016. **214**(2): p. 197-213.
152. Metzler, R., et al., *Anomalous diffusion models and their properties: non-stationarity, non-ergodicity, and ageing at the centenary of single particle tracking.* Physical Chemistry Chemical Physics, 2014. **16**(44): p. 24128-24164.
153. Luby-Phelps, K., et al., *Hindered diffusion of inert tracer particles in the cytoplasm of mouse 3T3 cells.* Proc Natl Acad Sci U S A, 1987. **84**(14): p. 4910-3.
154. Gupta, M., et al., *Adaptive rheology and ordering of cell cytoskeleton govern matrix rigidity sensing.* Nat Commun, 2015. **6**: p. 7525.
155. Serrels, B., et al., *Focal adhesion kinase controls actin assembly via a FERM-mediated interaction with the Arp2/3 complex.* Nat Cell Biol, 2007. **9**(9): p. 1046-56.

156. Bazzoni, R., et al., *Extracellular Vesicle-Dependent Communication Between Mesenchymal Stromal Cells and Immune Effector Cells.* Front Cell Dev Biol, 2020. **8**: p. 596079.
157. Zhou, R., et al., *The decade of exosomal long RNA species: an emerging cancer antagonist.* Molecular Cancer, 2018. **17**(1): p. 75.
158. Jeppesen, D.K., et al., *Reassessment of Exosome Composition.* Cell, 2019. **177**(2): p. 428-445.e18.
159. Mogre, S., A.I. Brown, and E.F. Koslover, *Getting around the cell: physical transport in the intracellular world.* Phys Biol, 2020.
160. Li, J., et al., *Dependence of Membrane Tether Strength on Substrate Rigidity Probed by Single-Cell Force Spectroscopy.* J Phys Chem Lett, 2020. **11**(10): p. 4173-4178.
161. Neisch, A.L. and R.G. Fehon, *Ezrin, Radixin and Moesin: key regulators of membrane–cortex interactions and signaling.* Current Opinion in Cell Biology, 2011. **23**(4): p. 377-382.
162. Burdick, J.A. and W.L. Murphy, *Moving from static to dynamic complexity in hydrogel design.* Nat Commun, 2012. **3**: p. 1269.
163. Wang, J., et al., *Boosting the Biogenesis and Secretion of Mesenchymal Stem Cell-Derived Exosomes.* Cells, 2020. **9**(3): p. 660.
164. Colao, I.L., et al., *Manufacturing Exosomes: A Promising Therapeutic Platform.* Trends in Molecular Medicine, 2018. **24**(3): p. 242-256.
165. Watson, D.C., et al., *Scalable, cGMP-compatible purification of extracellular vesicles carrying bioactive human heterodimeric IL-15/lactadherin complexes.* Journal of Extracellular Vesicles, 2018. **7**(1): p. 1442088.
166. Patel, D.B., et al., *Enhanced extracellular vesicle production and ethanol-mediated vascularization bioactivity via a 3D-printed scaffold-perfusion bioreactor system.* Acta Biomater, 2019. **95**: p. 236-244.
167. Yang, Z., et al., *Large-scale generation of functional mRNA-encapsulating exosomes via cellular nanoporation.* Nature Biomedical Engineering, 2020. **4**(1): p. 69-83.
168. van der Pol, E., et al., *Classification, functions, and clinical relevance of extracellular vesicles.* Pharmacol Rev, 2012. **64**(3): p. 676-705.
169. Colombo, M., G. Raposo, and C. Théry, *Biogenesis, secretion, and intercellular interactions of exosomes and other extracellular vesicles.* Annu Rev Cell Dev Biol, 2014. **30**: p. 255-89.
170. Rani, S., et al., *Mesenchymal Stem Cell-derived Extracellular Vesicles: Toward Cell-free Therapeutic Applications.* Mol Ther, 2015. **23**(5): p. 812-823.
171. Rilla, K., et al., *Extracellular vesicles are integral and functional components of the extracellular matrix.* Matrix Biol, 2019. **75-76**: p. 201-219.
172. McGinley, L., et al., *Lentiviral vector mediated modification of mesenchymal stem cells & enhanced survival in an in vitro model of ischaemia.* Stem Cell Res Ther, 2011. **2**(2): p. 12.
173. Bonenfant, N.R., et al., *The effects of storage and sterilization on de-cellularized and re-cellularized whole lung.* Biomaterials, 2013. **34**(13): p. 3231-45.
174. Pena, A.M., et al., *Three-dimensional investigation and scoring of extracellular matrix remodeling during lung fibrosis using multiphoton microscopy.* Microsc Res Tech, 2007. **70**(2): p. 162-70.

175. Branco da Cunha, C., et al., *Influence of the stiffness of three-dimensional alginate/collagen-I interpenetrating networks on fibroblast biology.* Biomaterials, 2014. **35**(32): p. 8927-36.
176. Carr, D.A. and N.A. Peppas, *Molecular structure of physiologically-responsive hydrogels controls diffusive behavior.* Macromolecular bioscience, 2009. **9**(5): p. 497-505.
177. Berger, J., et al., *Structure and interactions in covalently and ionically crosslinked chitosan hydrogels for biomedical applications.* Eur J Pharm Biopharm, 2004. **57**(1): p. 19-34.
178. Boontheekul, T., H.J. Kong, and D.J. Mooney, *Controlling alginate gel degradation utilizing partial oxidation and bimodal molecular weight distribution.* Biomaterials, 2005. **26**(15): p. 2455-65.
179. Iza, M., et al., *Determination of pore size distribution for mesoporous materials and polymeric gels by means of DSC measurements: thermoporometry.* Polymer, 2000. **41**(15): p. 5885-5893.
180. Skotland, T., et al., *Exosomal lipid composition and the role of ether lipids and phosphoinositides in exosome biology.* J Lipid Res, 2019. **60**(1): p. 9-18.
181. Etoc, F., et al., *Non-specific interactions govern cytosolic diffusion of nanosized objects in mammalian cells.* Nature Materials, 2018. **17**(8): p. 740-746.
182. Backlund, M.P., R. Joyner, and W.E. Moerner, *Chromosomal locus tracking with proper accounting of static and dynamic errors.* Phys Rev E Stat Nonlin Soft Matter Phys, 2015. **91**(6): p. 062716.
183. Segur, J.B. and H.E. Oberstar, *Viscosity of Glycerol and Its Aqueous Solutions.* Industrial & Engineering Chemistry, 1951. **43**(9): p. 2117-2120.
184. Guo, P., et al., *Nanoparticle elasticity directs tumor uptake.* Nature Communications, 2018. **9**(1): p. 130.
185. Calò, A., et al., *Force measurements on natural membrane nanovesicles reveal a composition-independent, high Young's modulus.* Nanoscale, 2014. **6**(4): p. 2275-2285.
186. Luker, K.E., et al., *Comparative study reveals better far-red fluorescent protein for whole body imaging.* Sci Rep, 2015. **5**: p. 10332.
187. Rakian, R., et al., *Native extracellular matrix preserves mesenchymal stem cell "stemness" and differentiation potential under serum-free culture conditions.* Stem Cell Research & Therapy, 2015. **6**(1): p. 235.
188. Grant, G.T., et al., *Biological interactions between polysaccharides and divalent cations: The egg-box model.* FEBS Letters, 1973. **32**(1): p. 195-198.
189. Armstrong, J.K., et al., *The hydrodynamic radii of macromolecules and their effect on red blood cell aggregation.* Biophys J, 2004. **87**(6): p. 4259-70.
190. Schirmacher, W., G. Ruocco, and V. Mazzone, *Heterogeneous Viscoelasticity: A Combined Theory of Dynamic and Elastic Heterogeneity.* Physical Review Letters, 2015. **115**(1): p. 015901.
191. Lieleg, O., I. Vladescu, and K. Ribbeck, *Characterization of Particle Translocation through Mucin Hydrogels.* Biophysical Journal, 2010. **98**(9): p. 1782-1789.
192. Goiko, M., J.R. de Bruyn, and B. Heit, *Short-Lived Cages Restrict Protein Diffusion in the Plasma Membrane.* Sci Rep, 2016. **6**: p. 34987.
193. Weigel, A.V., et al., *Ergodic and nonergodic processes coexist in the plasma membrane as observed by single-molecule tracking.* Proceedings of the National Academy of Sciences, 2011. **108**(16): p. 6438-6443.

194. Manzo, C., et al., *Weak Ergodicity Breaking of Receptor Motion in Living Cells Stemming from Random Diffusivity.* Physical Review X, 2015. **5**(1): p. 011021.
195. Parry, B.R., et al., *The bacterial cytoplasm has glass-like properties and is fluidized by metabolic activity.* Cell, 2014. **156**(1-2): p. 183-94.
196. Kusuma, G.D., et al., *To Protect and to Preserve: Novel Preservation Strategies for Extracellular Vesicles.* Frontiers in Pharmacology, 2018. **9**(1199).
197. Frank, J., et al., *Extracellular vesicles protect glucuronidase model enzymes during freeze-drying.* Scientific Reports, 2018. **8**(1): p. 12377.
198. Stroka, K.M., et al., *Water permeation drives tumor cell migration in confined microenvironments.* Cell, 2014. **157**(3): p. 611-23.
199. Cai, L.-H., S. Panyukov, and M. Rubinstein, *Hopping Diffusion of Nanoparticles in Polymer Matrices.* Macromolecules, 2015. **48**(3): p. 847-862.
200. Wong, I.Y., et al., *Anomalous Diffusion Probes Microstructure Dynamics of Entangled F-Actin Networks.* Physical Review Letters, 2004. **92**(17): p. 178101.
201. Ritchie, K., et al., *Detection of Non-Brownian Diffusion in the Cell Membrane in Single Molecule Tracking.* Biophysical Journal, 2005. **88**(3): p. 2266-2277.
202. Manno, S., Y. Takakuwa, and N. Mohandas, *Identification of a functional role for lipid asymmetry in biological membranes: Phosphatidylserine-skeletal protein interactions modulate membrane stability.* Proc Natl Acad Sci U S A, 2002. **99**(4): p. 1943-8.
203. Zámecník, J., et al., *Extracellular matrix glycoproteins and diffusion barriers in human astrocytic tumours.* Neuropathology and Applied Neurobiology, 2004. **30**(4): p. 338-350.
204. Lieleg, O., R.M. Baumgärtel, and A.R. Bausch, *Selective filtering of particles by the extracellular matrix: an electrostatic bandpass.* Biophysical journal, 2009. **97**(6): p. 1569-1577.
205. Lai, S.K., Y.Y. Wang, and J. Hanes, *Mucus-penetrating nanoparticles for drug and gene delivery to mucosal tissues.* Adv Drug Deliv Rev, 2009. **61**(2): p. 158-71.
206. Hansing, J., et al., *Particle Diffusion in Polymeric Hydrogels with Mixed Attractive and Repulsive Interactions.* Nano Letters, 2018. **18**(8): p. 5248-5256.
207. Stylianopoulos, T., et al., *Diffusion of particles in the extracellular matrix: the effect of repulsive electrostatic interactions.* Biophys J, 2010. **99**(5): p. 1342-9.
208. Zhang, X., et al., *Particle Transport through Hydrogels Is Charge Asymmetric.* Biophysical Journal, 2015. **108**(3): p. 530-539.
209. Kanduč, M., et al., *Selective Molecular Transport in Thermoresponsive Polymer Membranes: Role of Nanoscale Hydration and Fluctuations.* Macromolecules, 2018. **51**(13): p. 4853-4864.
210. Feng, X., et al., *Understanding Protein Diffusion in Polymer Solutions: A Hydration with Depletion Model.* The Journal of Physical Chemistry B, 2016. **120**(38): p. 10114-10123.
211. Wang, L., et al., *Nanoscale Diffusion of Polymer-Grafted Nanoparticles in Entangled Polymer Melts.* Macromolecules, 2020. **53**(19): p. 8393-8399.
212. Chen, Y., et al., *Nanoparticle Mobility within Permanently Cross-Linked Polymer Networks.* Macromolecules, 2020. **53**(11): p. 4172-4184.
213. Thalhauser, S., et al., *Silica particles incorporated into PLGA-based in situ-forming implants exploit the dual advantage of sustained release and particulate delivery.* European Journal of Pharmaceutics and Biopharmaceutics, 2020. **156**: p. 1-10.
214. Wang, Y., et al., *Controlled release of entrapped nanoparticles from thermoresponsive hydrogels with tunable network characteristics.* Soft Matter, 2020. **16**(20): p. 4756-4766.

215. Flory, P.J., *Principles of polymer chemistry*. 1953: Cornell University Press.
216. Astbury, W.T., *Structure of Alginic Acid.* Nature, 1945. **155**(3944): p. 667-668.
217. Smidsrød, O., *Solution properties of alginate.* Carbohydrate Research, 1970. **13**(3): p. 359-372.
218. Wong, S.W., et al., *Controlled Deposition of 3D Matrices to Direct Single Cell Functions.* Advanced Science, 2020. **7**(20): p. 2001066.
219. Darling, E.M., S. Zauscher, and F. Guilak, *Viscoelastic properties of zonal articular chondrocytes measured by atomic force microscopy.* Osteoarthritis and Cartilage, 2006. **14**(6): p. 571-579.
220. Tamm, M.V. and K. Polovnikov, *Dynamics of Polymers: Classic Results and Recent Developments*, in *Order, Disorder and Criticality*. p. 113-172.
221. Rubinstein, M. and R.H. Colby, *Polymer physics*. Vol. 23. 2003: Oxford university press New York.
222. Moya, M.L., et al., *Stability of alginate microbead properties in vitro.* Journal of materials science. Materials in medicine, 2012. **23**(4): p. 903-912.
223. Zavitsas, A.A., *The Relation between Bond Lengths and Dissociation Energies of Carbon−Carbon Bonds.* The Journal of Physical Chemistry A, 2003. **107**(6): p. 897-898.
224. Eising, S., et al., *Highly Stable and Selective Tetrazines for the Coordination-Assisted Bioorthogonal Ligation with Vinylboronic Acids.* Bioconjugate Chemistry, 2018. **29**(9): p. 3054-3059.
225. Bala, T., et al., *Interaction of Different Metal Ions with Carboxylic Acid Group: A Quantitative Study.* The Journal of Physical Chemistry A, 2007. **111**(28): p. 6183-6190.
226. Gerbal, F. and Y. Wang, *Optical detection of nanometric thermal fluctuations to measure the stiffness of rigid superparamagnetic microrods.* Proceedings of the National Academy of Sciences, 2017. **114**(10): p. 2456-2461.
227. Guo, D., et al., *Elastic Properties of Polystyrene Nanospheres Evaluated with Atomic Force Microscopy: Size Effect and Error Analysis.* Langmuir, 2014. **30**(24): p. 7206-7212.
228. Lenzini, S., et al., *Matrix mechanics and water permeation regulate extracellular vesicle transport.* Nature Nanotechnology, 2020. **15**(3): p. 217-223.
229. Benne, N., et al., *Atomic force microscopy measurements of anionic liposomes reveal the effect of liposomal rigidity on antigen-specific regulatory T cell responses.* Journal of Controlled Release, 2020. **318**: p. 246-255.
230. Schuss, Z., A. Singer, and D. Holcman, *The narrow escape problem for diffusion in cellular microdomains.* Proceedings of the National Academy of Sciences, 2007. **104**(41): p. 16098-16103.
231. Jansen, L.E., et al., *Mechanics of intact bone marrow.* Journal of the Mechanical Behavior of Biomedical Materials, 2015. **50**: p. 299-307.
232. Mangialardi, G., A. Cordaro, and P. Madeddu, *The bone marrow pericyte: an orchestrator of vascular niche.* Regenerative medicine, 2016. **11**(8): p. 883-895.
233. Pinho, S. and P.S. Frenette, *Haematopoietic stem cell activity and interactions with the niche.* Nature Reviews Molecular Cell Biology, 2019. **20**(5): p. 303-320.
234. Roper, S.I., et al., *B cells extract antigens using Arp2/3-generated actin foci interspersed with linear filaments.* bioRxiv, 2019: p. 792481.

235. Wong, S.W., et al., *Soft extracellular matrix enhances inflammatory activation of mesenchymal stromal cells to induce monocyte production and trafficking.* Science Advances, 2020. **6**(15): p. eaaw0158.
236. Lee, K., et al., *Multiplexed Profiling of Single Extracellular Vesicles.* ACS Nano, 2018. **12**(1): p. 494-503.
237. Zhang, H., et al., *Identification of distinct nanoparticles and subsets of extracellular vesicles by asymmetric flow field-flow fractionation.* Nature Cell Biology, 2018. **20**(3): p. 332-343.
238. Cox, T.R. and J.T. Erler, *Remodeling and homeostasis of the extracellular matrix: implications for fibrotic diseases and cancer.* Disease models & mechanisms, 2011. **4**(2): p. 165-178.
239. Bangasser, B.L., et al., *Shifting the optimal stiffness for cell migration.* Nature communications, 2017. **8**: p. 15313-15313.
240. Razinia, Z., et al., *Stiffness-dependent motility and proliferation uncoupled by deletion of CD44.* Scientific Reports, 2017. **7**(1): p. 16499.
241. Berry, D., et al., *Tracking heavy water (D₂O) incorporation for identifying and sorting active microbial cells.* Proceedings of the National Academy of Sciences, 2015. **112**(2): p. E194-E203.
242. Dannert, C., B.T. Stokke, and R.S. Dias, *Nanoparticle-Hydrogel Composites: From Molecular Interactions to Macroscopic Behavior.* Polymers, 2019. **11**(2): p. 275.
243. Memic, A., et al., *Hydrogels 2.0: improved properties with nanomaterial composites for biomedical applications.* Biomed Mater, 2015. **11**(1): p. 014104.
244. Tehranirokh, M., et al., *Microfluidic devices for cell cultivation and proliferation.* Biomicrofluidics, 2013. **7**(5): p. 051502.
245. Hur, Y.H., et al., *Embryonic Stem Cell-Derived Extracellular Vesicles Maintain ESC Stemness by Activating FAK.* Dev Cell, 2021. **56**(3): p. 277-291.e6.
246. Harrell, C.R., et al., *Therapeutic Potential of Mesenchymal Stem Cell-Derived Exosomes in the Treatment of Eye Diseases*, in *Cell Biology and Translational Medicine, Volume 2: Approaches for Diverse Diseases and Conditions*, K. Turksen, Editor. 2018, Springer International Publishing: Cham. p. 47-57.
247. Ma, M., et al., *Therapeutic effects of mesenchymal stem cell-derived exosomes on retinal detachment.* Experimental Eye Research, 2020. **191**: p. 107899.
248. Zhao, Y., et al., *Liquid Biopsy of Vitreous Reveals an Abundant Vesicle Population Consistent With the Size and Morphology of Exosomes.* Translational vision science & technology, 2018. **7**(3): p. 6-6.
249. Riau, A.K., et al., *Sustained Delivery System for Stem Cell-Derived Exosomes.* Frontiers in Pharmacology, 2019. **10**(1368).

VITA

NAME: Stephen B. Lenzini

EDUCATION:

University of Illinois at Chicago, College of Engineering *2016 – 2021*
PhD Candidate in Bioengineering (Advisor: Dr. Jae-Won Shin)
PhD Thesis title: The biophysical characteristics of extracellular vesicle production and transport

Northwestern University, McCormick School of Engineering and Applied Sciences *2011 – 2016*
Master of Science in Chemical Engineering (Advisor: Dr. Joshua Leonard)
Bachelor of Science in Chemical Engineering

HONORS:

UIC Dean's Scholar Fellowship Award	*2020*
UIC W.C. & May Preble Deiss Award for Biomedical Graduate Research	*2020*
BMES Advanced Biomanufacturing Graduate Student Research Award	*2020*
American Heart Association Predoctoral Fellowship Award	*2019*
NIH T32 Predoctoral Fellowship Award, UIC Department of Pharmacology	*2017*
ASCB | EMBO Travel Grant Recipient	*2019*

PUBLICATIONS:

Lenzini, S., Bargi, R., Chung, G., Shin, JW. (2020) Matrix mechanics and water permeation regulate extracellular vesicle transport. *Nature Nanotechnology 15,* 217–223. doi.org/10.1038/s41565-020-0636-2. Featured in News & Views.

Wong S.W., Lenzini S., Bargi R., Feng Z., Macaraniag C., Lee J.C., Peng Z., and Shin J.W. (2020) Controlled deposition of three-dimensional matrices to direct single cell functions. *Advanced Science 7(20),* 2001066.

Wong, S., Lenzini, S., Cooper, M., Mooney, DJ., Shin, JW. (2020) Soft extracellular matrix enhances inflammatory activation of mesenchymal stromal cells to induce monocyte production and trafficking. *Science Advances 6(15),* eaaw0158. doi.org/10.1126/sciadv.aaw0158.

Devine D.*, Vijayakumar V.*, Wong S.W.*, Lenzini S., Newman P., Shin J.W. (2020) Hydrogel micropost arrays with single post tunability to study cell volume and mechanotransduction. *Advanced Biosystems* (In Press), 2000012.

Lenzini, S., Devine, D. & Shin, J. W. (2019) Leveraging Biomaterial Mechanics to Improve Pluripotent Stem Cell Applications for Tissue Engineering. *Front. Bioeng. Biotechnol 7*, 260. doi.org/10.3389/fbioe.2019.00260

Wong, S.*, Lenzini, S.*, Shin, JW (2018). Biophysical regulation of cancerous and normal blood cell lineages in hematopoietic malignancies. *APL Bioengineering 3*(2), 030812. doi.org/10.1063/1.5025689. *authors contributed equally

Hung, M.E.*, Lenzini, S.*, Stranford, D.M. & Leonard, J.N. (2018). Enrichment of extracellular vesicle subpopulations via affinity chromatography. In *Methods in Molecular Biology* (Vol. 1740, pp. 109-124). *authors contributed equally

Moura, M., Pertusi, D., Lenzini, S., Bhan, N., Broadbelt, L.J. & Tyo, K.E.J. (2016). Characterizing and predicting carboxylic acid reductase activity for diversifying bioaldehyde production. *Biotechnology and Bioengineering 113*(5), 944-952. doi.org/10.1002/bit.25860

CONFERENCE PRESENTATIONS:

Matrix mechanics and water permeation regulate extracellular vesicle transport
Oral Presentation.
UIC GEMS Symposium. Chicago, IL (2019).

Matrix mechanics and water permeation regulate extracellular vesicle transport
Poster Presentation.
BMES Annual Meeting. Philadelphia, PA (2019).
ASCB | EMBO Annual Meeting. Washington, DC (2019).

Biophysical Control of Extracellular Vesicle Production and Transport
Poster Presentation
BMES Cellular and Molecular Bioengineering Conference. San Diego, CA (2019).
UIC Bioengineering Research Symposium. Chicago, IL (2019).
UIC GEMS Symposium. Chicago, IL (2018).
UIC Pharmacology Department Research Retreat. Oak Brook, IL (2018).
UIC College of Medicine Research Forum. Chicago, IL (2018).

Mechanics and Crosslinking Network Regulate Extracellular Vesicle Transport in Nanoporous Hydrogels
Oral Presentation.
Functional and Regenerative Materials Workshop. Chicago, IL (2018).

Biomaterial Design for Controlled Delivery of Extracellular Vesicles
Oral Presentation.
UIC Bioengineering Research Symposium. Chicago, IL (2018).

Bioengineering approaches for biophysical control of synthetic and biologically-derived particles
Poster Presentation.
UIC College of Medicine GEMS Research Symposium. Chicago, IL (2017).
UIC Pharmacology Department Research Retreat. Oak Brook, IL (2017).
UIC College of Medicine Research Forum. Chicago, IL (2017).

Biophysical Control of Extracellular Vesicle (EV) Production and Release
Poster Presentation.
Center of Stem Cell and Regenerative Medicine Opening Convention. Chicago, IL (2017).